UC Berkeley
UC Berkeley Electronic Theses and Dissertations

Title

Multiscale Damage Characterization of Hybrid Fiber-Reinforced Concrete Composites under Seismic and Environmental Conditions

Permalink

https://escholarship.org/uc/item/8647j5wq

Author

Nguyen, Wilson Linh Nam

Publication Date

2017

Peer reviewed|Thesis/dissertation

eScholarship.org Powered by the California Digital Library
University of California

Multiscale Damage Characterization of Hybrid Fiber-Reinforced Concrete Composites under Seismic and Environmental Conditions

By

Wilson Linh Nam Nguyen

A dissertation submitted in partial satisfaction of the

requirements for the degree of

Doctor of Philosophy

in

Engineering – Civil and Environmental Engineering

in the

Graduate Division

of the

University of California, Berkeley

Committee in charge:

Professor Claudia P. Ostertag, Chair
Professor Paulo J.M. Monteiro
Professor Kenneth N. Raymond

Summer 2017

Abstract

Multiscale Damage Characterization of Hybrid Fiber-Reinforced Concrete Composites under Seismic and Environmental Conditions

by

Wilson Linh Nam Nguyen

Doctor of Philosophy in Engineering – Civil and Environmental Engineering

University of California, Berkeley

Professor Claudia P. Ostertag, Chair

The deteriorating quality of the United States' infrastructure will result in the construction of new civil engineering structures, particularly bridges, in the coming decades. This future construction presents an opportunity to modify current designs with novel materials that are more damage-resistant and durable than conventional materials.

Hybrid fiber-reinforced concrete (HyFRC) is proposed for implementation in reinforced concrete structures. This material utilizes a multiscale crack control scheme to achieve greater ductility and toughness than plain concrete, allowing for progressive crack resistance from microcrack initiation to macrocrack propagation. In this dissertation, reinforced HyFRC (i.e. HyFRC with embedded steel reinforcing bars) was investigated to evaluate realistic expectations of mechanical and durability performance of constructed structural elements.

Two primary sources of damage in reinforced HyFRC bridge structures were considered for study. The first source relates to earthquake events while the second source relates to corrosion of embedded steel reinforcing bars. Regarding earthquakes, which induce high deformations on reinforced concrete, reinforced HyFRC was investigated for its fracture behavior under direct uniaxial tension. Prismatic samples with a low longitudinal reinforcement ratio were tested to evaluate the feasibility of reducing reinforcing bar congestion in construction through the use of fiber-reinforced concrete. The overall deformation capacity of the reinforced composite was largely dependent on HyFRC cracking characteristics, which generally consisted of localized dominant cracking and longitudinal splitting crack suppression. For ductility enhancement, sufficient load capacity from strain hardening of steel reinforcement is required to offset load softening from fiber pull-out processes at a dominant crack.

A 1:4.5 scale bridge column utilizing a precast HyFRC tube, which contained all of the column's steel reinforcement, was laterally loaded to evaluate simulated seismic damage behavior. The experimental column was subjected to static, unidirectional, cyclic loading and utilized a base-rocking design for further ductility enhancement. At the conclusion of the test, the column reached a peak drift ratio of 13.1% and showed minor damage, including elimination of cover spalling. The HyFRC tube column design contributed effective resistance against longitudinal reinforcing bar buckling, allowing the column to maintain 93% of its peak load capacity at 9.5% drift. Compared to a monolithic HyFRC column, the precast HyFRC tube design showed no reduction in seismic performance despite being fabricated with 43% less HyFRC volume.

Steel reinforcement corrosion is an additional source of severe reinforced concrete bridge damage. Because cracking can occur in a structure prior to corrosion activity, as from seismic loads or other service loads, corrosion studies in this dissertation considered the effect of both preexisting (i.e. applied load-induced) and corrosion-induced cracks on corrosion activity. In a study focused on electrochemical polarization, samples with a single steel reinforcing bar were exposed to a chloride environment for 2.5 years while in a continuous tensile stress state or in a nonloaded condition, and were periodically monitored for electrochemical behavior. Electrochemical impedance spectroscopy (EIS) was additionally preformed at the conclusion of the test program. The severity of corrosion-induced splitting matrix cracks along the length of embedded steel reinforcing bars and subsequent formation of anodic surfaces were found to be the primary factors dictating the magnitude of corrosion current. Cathodic and anodic Tafel coefficients and Stern-Geary coefficients for passive and active samples are also reported.

Corrosion activity monitoring of reinforced HyFRC was further extended to beam elements containing a steel reinforcing bar of interest and a larger secondary reinforcing bar, which lumped the galvanic corrosion effects of electrically connected reinforcing bars expected in a steel reinforcement cage on the bar of interest. Samples were mechanically loaded to induce varied matrix cracking characteristics prior to a 2.2-year chloride exposure duration. When precracked, time to corrosion initiation was governed by flexural stiffness degradation. After corrosion initiation, HyFRC restricted corrosion-induced cracking, caused more extensive diffusion of corrosion products into the bulk cement paste, and lowered overall steel reinforcing bar mass loss. Any corrosion damage incurred by reinforced HyFRC had negligible effects on flexural stiffness.

To visualize the progressive in-situ corrosion damage of reinforced fiber-reinforced cementitious composites, X-ray micro-computed tomography (μCT), a non-destructive, 3D imaging technique, was performed. Similar to larger scale experiments, samples in this study were preloaded to induce cracking prior to environmental conditioning for 44 weeks. Corrosion damage of embedded steel bars was monitored at different environmental exposure times, with plain cementitious composites exhibiting splitting cracks that caused widespread corrosion of the steel bar. In contrast, the high splitting crack resistance of the fiber-reinforced cementitious composite restricted corrosion propagation to near the initial site of corrosion. The localized corrosion rate was determined based on actual steel mass loss and actual corroded surface area.

The experimental results and conclusions reported in this dissertation indicate that HyFRC composites can significantly enhance the damage resistance and durability of reinforced concrete structures, though HyFRC performance is most optimized under certain conditions.

Dedication

To my mother, Ngoc Ha Thi Nguyen, who placed the happiness of her children before her own. You did everything you could to give me the best life possible.

To my father, Long Nguyen, who received his doctoral degree from the University of California, Berkeley, in 1974. I hope I completed your wish.

To Irene, Michael, and Steven. I wanted to be like all of you, and you have always taken care of me.

To Elisha. I can’t return the days and nights that I needed to finish this dissertation. I promise the next years of our lives will be our happiest.

Table of Contents

1 Introduction 1
1.1 Current condition of United States infrastructure 1
1.2 Reinforced concrete damage 2
1.3 Hybrid fiber-reinforced concrete (HyFRC) 3
1.4 Organization of the dissertation 4
2 Tensile behavior of HyFRC composites 7
2.1 Introduction 7
2.2 Materials and methods 9
2.2.1 Concrete materials 9
2.2.2 Specimen design 10
2.2.3 Instrumentation and testing 10
2.3 Results 11
2.3.1 Global response 11
2.3.2 Local response 12
2.4 Discussion 14
2.4.1 Rebar plasticity development 14
2.4.2 Material load distribution 16
2.4.3 Comparison to composites with greater reinforcement ratio 19
2.5 Summary and conclusions 24
3 Seismic behavior of a rocking bridge column using a precast HyFRC tube 26
3.1 Introduction 26
3.2 Materials and methods 27
3.2.1 Specimen design 27
3.2.2 Concrete materials 29
3.2.3 Specimen construction 31
3.2.4 Lateral loading 32
3.3 Results and discussion 34
3.3.1 Damage mitigation 34
3.3.2 Measured response 36
3.3.3 Comparison to a cast-in-place HyFRC rocking column 40
3.4 Summary and conclusions 42
4 Electrochemical polarization behavior of HyFRC composites 43
4.1 Introduction 43
4.2 Materials and methods 47
4.2.1 Concrete materials 47
4.2.2 Specimen design 47
4.2.3 Tensile loading 48
4.2.4 Environmental conditioning 49
4.2.5 Electrochemical measurements 50
4.2.6 Destructive testing 50
4.3 Results 51
4.3.1 Observed damage 51
4.3.2 Tafel polarization 55
4.3.3 Corrosion rate monitoring 58
4.3.4 Electrochemical impedance spectroscopy 59

4.4 Discussion 62
4.4.1 Early-age corrosion propagation 62
4.4.2 Late-age corrosion propagation 64
4.5 Summary and conclusions 66
5 Corrosion behavior of HyFRC beam elements 68
5.1 Introduction 68
5.2 Materials and methods 71
5.2.1 Concrete materials 71
5.2.2 Specimen design 71
5.2.3 Flexural preloading 72
5.2.4 Environmental conditioning 73
5.2.5 Electrochemical measurements 73
5.2.6 Destructive testing 74
5.2.7 X-ray diffraction 76
5.3 Results 76
5.3.1 Mechanical preloading 76
5.3.2 Chloride permeation 77
5.3.3 Corrosion rate monitoring 79
5.4 Discussion 83
5.4.1 Corrosion initiation 83
5.4.2 Corrosion products 84
5.4.3 Electrochemical and physical damage 87
5.4.4 Post-corrosion composite mechanical properties 90
5.5 Summary and conclusions 91
6 Corrosion behavior of microfiber-reinforced cementitious composites using by X-ray micro-computed tomography 93
6.1 Introduction 93
6.2 Materials and methods 99
6.2.1 Mortar materials 99
6.2.2 Specimen design 100
6.2.3 Tensile preloading 101
6.2.4 X-ray micro-computed tomography 102
6.2.5 Image analysis 102
6.3 Results and discussion 103
6.3.1 Preload response 103
6.3.2 Visualized corrosion damage 105
6.3.3 Corrosion propagation behavior 107
6.3.4 Corrosion rate 112
6.4 Summary and conclusions 113
7 Final remarks 115
7.1 Conclusions 115
7.2 Recommendations for future research 116
8 References 118

List of Figures

Figure 1-1: Relation of structurally deficient bridge statistics to bridge age: (a) Number of bridges; (b) Percentage of bridges. 1
Figure 1-2: Percentage of structurally deficient bridges in each state of the United States. 2
Figure 1-3: Multiscale crack control of a hybrid fiber-reinforced concrete (HyFRC): (a) Showing smaller fibers (microfibers) resisting microcracks prior to crack coalescence; (b) Showing longer fibers resisting larger cracks 4
Figure 2-1: Proposed classification of high-performance fiber-reinforced concrete composites (HPFRCC) based on tensile response. 7
Figure 2-2: Typical 30 mm-long hooked-end steel fiber batched in HyFRC. 9
Figure 2-3: Specimen design: (a) Materials and measurements; (b) Global view of specimen prior to testing, showing external instrumentation; (c) Strain-gauged specimen prior to casting. 10
Figure 2-4: Load P versus average specimen strain ε response of R/C, R/HyFRC, and bare rebar: (a) Up to ε=0.4%; (b) Complete response. 11
Figure 2-5: (a) Rebar strain profile of R/C sample; Surface observations of sample at R/C average specimen strain $\varepsilon_{R/C}$: (b) $\varepsilon_{R/C}$=0.4%; (c) $\varepsilon_{R/C}$=1%; (d) $\varepsilon_{R/C}$=2%; (e) After failure. . 12
Figure 2-6: (a) Rebar strain profile of R/HyFRC sample; Surface observations of sample at R/HyFRC average specimen strain $\varepsilon_{R/HyFRC}$: (b) $\varepsilon_{R/HyFRC}$ =0.4%; (c) $\varepsilon_{R/HyFRC}$ =1%; (d) $\varepsilon_{R/HyFRC}$ =2%; (e) After failure. 13
Figure 2-7: Surface observations of two R/C samples ((a)-(b) and (c)-(d)) without strain gauge instrumentation at R/C average specimen strain $\varepsilon_{R/C}$ =0.4% and $\varepsilon_{R/C}$ =2%. 13
Figure 2-8: Surface observations of two R/HyFRC samples ((a)-(b) and (c)-(d)) without strain gauge instrumentation at R/HyFRC average specimen strain $\varepsilon_{R/HyFRC}$ =0.4% and $\varepsilon_{R/HyFRC}$ =2%. 14
Figure 2-9: Rebar strain ε_r versus: (a) Average R/C specimen strain $\varepsilon_{R/C}$; (b) Average R/HyFRC specimen strain $\varepsilon_{R/HyFRC}$. 15
Figure 2-10: Load P distribution of materials versus average specimen strain $\varepsilon_{R/C}$ or $\varepsilon_{R/HyFRC}$ (up to 0.4% strain) at select cross-sections: (a)-(b) R/C; (c)-(d) R/HyFRC.. 17
Figure 2-11: Load P distribution of materials versus average specimen strain $\varepsilon_{R/C}$ or $\varepsilon_{R/HyFRC}$ (up to 4% strain) at select cross-sections: (a)-(b) R/C; (c)-(d) R/HyFRC. 18
Figure 2-12: Designated tensile regimes for R/HyFRC based on representative samples. 20
Figure 2-13: Load P distribution of materials versus average R/HyFRC specimen strain $\varepsilon_{R/HyFRC}$ (up to 1.5% strain) at select cross-sections of R/HyFRC$_{1.2}$: (a) First dominant cracking section; (b) Secondary dominant cracking section. 21
Figure 2-14: Surface observation of a R/HyFRC$_{1.2}$ specimen just prior to fracture. 22
Figure 2-15: Load P versus average specimen strain ε of R/HyFRC$_{0.6}$ and R/ECC$_{1.2}$. 23
Figure 3-1: Crack localization in reinforced high-performance fiber-reinforced concrete bridge column specimen S2 at a drift of 2.6%. 26
Figure 3-2: Tube column design: (a) Structural details (units in mm); (b) Representative visualization of precast tube element.. 28
Figure 3-3: Slump flow test result of fresh HyFRC. 30
Figure 3-4: 4-point bending test results of HyFRC. 30
Figure 3-5: Tensile test results of reinforcing steel. 31

Figure 3-6: Tube column during construction: (a) Steel reinforcement prior to casting of tube, showing duct tape used for rebar debonding; (b) Precast HyFRC tube aligned prior to casting of foundation; (c) Overhead view of specimen prior to casting of its hollow interior. 32
Figure 3-7: Column test setup: (a) Plan view details; (b) Global view. 33
Figure 3-8: Observed state of southeast (SE) face of tube column at neutral position after completion of peak drift ratio θ: (a) θ=1.2%; (b) θ=4.8%; (c) θ=9.5%; (d) θ=13.1%. 34
Figure 3-9: Observed local state of tube column at neutral position after completion of peak drift ratio θ: (a) Southeast (SE) face, θ=4.8%; (b) SE face, θ=6%; (c) SE face, θ=9.5%; (d) Northwest (NW) face, θ=9.5%. 35
Figure 3-10: Specimen Base45 after reaching a drift ratio of 3.9%. 35
Figure 3-11: Lateral load versus drift ratio response: (a) Up to θ=6.0%; (b) Complete response. 36
Figure 3-12: Base rotation versus drift ratio response up to θ=7.1%. 37
Figure 3-13: Strain measurements plotted as a function of testing time: (a) From strain gauges placed on longitudinal rebar T10; (b) From displacement transducers placed on west column face. 38
Figure 3-14: Strain profile of spiral steel transverse reinforcement. 39
Figure 3-15: Observed final state of rebar T3 after manual removal of HyFRC cover. 39
Figure 3-16: Lateral load versus drift ratio response of HyFRC tube column and cast-in-place HyFRC column. 41
Figure 4-1: Schematic of corrosion process in reinforced concrete. 43
Figure 4-2: Photograph of a reinforced concrete bridge in the state of Delaware with corrosion-induced damage. 44
Figure 4-3: Details of specimen design: (a) Geometric drawing; (b) Plan view of specimen with ponding dam fixed to concrete surface; (c) Specimen in loading frame. 48
Figure 4-4: Specimen with loading frame: (a) During tensile loading, showing a hydraulic pump applying load onto the free end of the extruded reinforcing bar; (b) Loading schematic highlighting transfer of load on rebar from hydraulic pump to nut upon tightening of the nut. 49
Figure 4-5: Electrochemical measurement setup using a 3-electrode setup. 50
Figure 4-6: Schematic showing top, ponded surface of prism and coring locations of a loaded sample. 51
Figure 4-7: Schematic detailing prism extraction used for optical imaging. 51
Figure 4-8: Representative surface cracking after applied tensile loading and prior to environmental conditioning: (a) C-L; (b) HyFRC-L. 52
Figure 4-9: Sectional images of reinforced concrete specimens at the conclusion of environmental conditioning: (a)-(c) C-0; (d)-(f) C-L. 53
Figure 4-10: Sectional images of reinforced HyFRC specimens at the conclusion of environmental conditioning: (a)-(c) HyFRC-0; (d)-(f) HyFRC-L. 54
Figure 4-11: Typical fitting result of Tafel polarization curves for a passive sample and an active sample. 55
Figure 4-12: Tafel coefficients versus corrosion potential E_{corr}: (a) Cathodic Tafel coefficient β_c; (b) Anodic Tafel coefficient β_a. 56
Figure 4-13: Correlation between corrosion current obtained between Stern-Geary equation $I_{corr,S.-G.}$ and Tafel polarization extrapolation $I_{corr,T.}$ 57

Figure 4-14: Corrosion current of samples: (a) During initial 12 weeks of environmental conditioning; (b) Complete experimental duration. 58
Figure 4-15: Chloride content profiles: (a) Concrete; (b) HyFRC. 59
Figure 4-16: Equivalent electrical circuit model used for EIS results: (a) Reinforced concrete; (b) Reinforced HyFRC. 60
Figure 4-17: Bode plots showing EIS results and fitted results with a domain of frequency f: (a) Modulus of impedance $|Z|$; (b) Phase shift $-\Phi$. 61
Figure 4-18: Tafel polarization responses of select specimens over elapsed active corrosion time, up to 40 weeks: (a) C-0, additionally showing influence of factors on polarization curvature; (b) C-L; (c) HyFRC-L; (d) Superposition of I_{corr}-E_{corr} relations from (a)-(c). .. 63
Figure 4-19: Tafel polarization responses of select specimens over elapsed active corrosion time, up to 90 or 130 weeks: (a) C-0; (b) C-L; (c) HyFRC-L; (d) Superposition of I_{corr}-E_{corr} relations from (a)-(c). 65
Figure 4-20: I_{corr}-E_{corr} relations at 90 weeks, showing select fitted cathodic and anodic reaction curves from Tafel polarization responses. The corrosion current of HyFRC-L in the plot is referred to as $I_{corr,HyFRC\text{-}L}$. 66
Figure 5-1: Preparation and testing of specimen: (a) Sample after casting and prior to any testing; (b) Schematic for 4-point flexural preloading, with rebar of interest placed under tensile stress during preloading; (c) Sample during environmental exposure, with rebar of interest located near adhered ponding dam. 72
Figure 5-2: Typical electrochemical measurement setup for corrosion potential and linear polarization resistance. 74
Figure 5-3: Schematic showing top, ponded surface of beam. 75
Figure 5-4: Schematic showing the extraction of transverse section slices of rebar of interest and surrounding matrix from the beam sample. 75
Figure 5-5: Flexural preloading response prior to environmental conditioning: Applied load P versus midpoint deflection Δ. 76
Figure 5-6: Observed representative surface crack characteristics after preloading: (a) C-fs; (b) HyFRC-f. 77
Figure 5-7: Chloride content $C_{Cl\text{-}}$ determined at depth d from beam ponding surface: (a) Considering all sample types, taken at noncracked surfaces only; (b) Considering only sample types with preload-induced flexural macrocrack, with chloride contents reported at cracked and noncracked surfaces for each considered sample. 78
Figure 5-8: Corrosion current I_{corr} of the rebar of interest versus environmental conditioning time t: (a) -(b) Response of samples without macrocracks prior to exposure; (c)-(d) Response of samples with macrocracks prior to exposure. 80
Figure 5-9: Galvanic current I_g versus electrochemical parameter: (a) and (c) versus corrosion current I_{corr} of the rebar of interest in C and HyFRC samples, respectively; (b) and (d) versus the difference between corrosion potential of the rebar of interest E_{corr} and corrosion potential of secondary rebar E_{corr}' in C and HyFRC samples, respectively. 81
Figure 5-10: Corrosion initiation time t_{int} versus flexural stiffness retention K_{cr}/K_{el}. 83
Figure 5-11: Optical imaging of representative transverse sections of rebar of interest and surrounding matrix: (a) C-0; (b) C-fs; (c) HyFRC-0; (d) HyFRC-f. 85
Figure 5-12: X-ray powder diffractograms of C-0 and HyFRC-0. 86

Figure 5-13: Adjusted expected steel mass loss $\Delta m'$ versus corrosion propagation time t_{prop}: (a) All samples for entire experimental duration; (b) Nonloaded samples C-0 and HyFRC-0 for initial 10 weeks of corrosion propagation time; (c) Reinforced concrete samples C-0 and C-fs for initial 10 weeks of corrosion propagation time. 88
Figure 5-14: Observed representative ponding surfaces of samples lacking preload damage at conclusion of environmental conditioning: (a) C-0, showing a corrosion-induced splitting crack; (b) HyFRC-0, showing no observable surface splitting cracks. 89
Figure 5-15: Observed representative surfaces of extracted steel rebar of interest after manual extraction from specimens and removal of corrosion products: (a) C-0; (b) HyFRC-0. 89
Figure 5-16: Residual flexural loading response after environmental conditioning: Applied load P versus midpoint deflection Δ. 90
Figure 6-1: Effect of microfibers on HyFRC flexural response compared to conventional FRC. 93
Figure 6-2: Microtomography experimental setup at beamline 8.3.2 at Advanced Light Source. 94
Figure 6-3: Schematic showing an object and its projection. 95
Figure 6-4: Schematic of projections taken at different angles. 96
Figure 6-5: Possible image analysis sequence: (1) Obtain X-ray radiographs from µCT experimentation; (2) Reconstruct radiographs into horizontal cross-section tomograms; (3) Use tomogram image stack to obtain 3D information. 97
Figure 6-6: 3D visualization of corroded steel within reinforced cementitious composites in the literature. 98
Figure 6-7: Typical load-machine displacement response of SHCC. 100
Figure 6-8: Specimen design: (a) Geometric detailing; (b) Visualization of sample; (c) Visualization of sample with loading encasements. 100
Figure 6-9: Mechanical test setup: (a) Loading apparatus; (b) Specimen within apparatus. 101
Figure 6-10: Method of quantifying µCT data: (a) Reconstructed tomogram; (b) Phase segmentation of steel and corrosion products occupying original steel volume; (c) Conversion to geometric object for MATLAB analysis; (d) Determination of corroded surface of section after centroid alignment with reference images taken prior to environmental exposure. 102
Figure 6-11: Tensile preloading response of samples. 103
Figure 6-12: Tomograms of preload-induced cracking prior to environmental conditioning: (a) PCC; (b) SHCC. 104
Figure 6-13: 3D visualization of preload-induced cracking prior to environmental conditioning: (a) PCC; (b) SHCC. 104
Figure 6-14: 3D visualization of steel bar and corrosion products in PCC sample at increasing exposure durations: (a) 0 weeks; (b) 5.3 weeks; (c) 13.1 weeks; (d) 25.0 weeks; (e) 43.6 weeks. 105
Figure 6-15: 3D visualization of steel bar in PCC sample at 5.3 weeks, showing corrosion damage of the bar at the matrix crack location. 106
Figure 6-16: 3D visualization of steel bar and corrosion products in SHCC sample at increasing exposure durations: (a) 0 weeks; (b) 5.3 weeks; (c) 13.1 weeks; (d) 25.0 weeks; (e) 43.6 weeks. 107
Figure 6-17: Corrosion propagation of R/PCC: (a) Steel bar cross-section area A at steel bar height h; (b)-(e) Change in steel bar cross-section area. (f) 3D visualization of sample at 43.6 weeks. 108
Figure 6-18: Tomograms of select cross-sections. 109

Figure 6-19: Corrosion propagation of R/SHCC: (a) Steel bar cross-section area *A* at steel bar height *h*; (b)-(e) Change in steel bar cross-section area. 110
Figure 6-20: Tomograms of select cross-sections. 111
Figure 6-21: Proportion of corroded height h_{corr}/H versus elapsed exposure time *t*..... 112
Figure 6-22: Mean corrosion current density $i_{corr,mean}$ of steel cross-section at height *h*. 113

List of Tables

Table 1-1: Overview of experimental scales considered in this dissertation. 5
Table 2-1: Batch proportions of HyFRC. 9
Table 2-2: Properties of fibers in HyFRC. 9
Table 3-1: Summary of column design parameters. 28
Table 3-2: Batch proportions of HyFRC and concrete. 30
Table 3-3: Loading protocol. 33
Table 4-1: Oxidation and reduction reactions for steel corrosion. 43
Table 4-2: Survey of Tafel coefficients and Stern-Geary coefficients of reinforced concrete. 46
Table 4-3: Batch proportions of HyFRC. 47
Table 4-4: Specimen type designation. 48
Table 4-5: Summary of Tafel coefficients and Stern-Geary coefficient. 57
Table 4-6: Element values for equivalent electrical circuit used for EIS results fitting. 62
Table 5-1: Survey of select studies on the corrosion behavior of reinforced fiber-reinforced cementitious composite beam elements subjected to applied flexural loading prior to, or during, chloride exposure. 69
Table 5-2: Batch proportions of HyFRC. 71
Table 5-3: Specimen name designation and intended preload damage characteristics. 73
Table 5-4: Summary of specimen deformation and cracking characteristics. 77
Table 5-5: Comparison of expected and actual mass loss of rebar of interest. 82
Table 5-6: Presence of corrosion products on rebar surface as identified by XRD. 86
Table 5-7: Summary of specimen mechanical characteristics after residual flexural loading. 90
Table 6-1: Survey of X-ray computed tomography studies on corrosion behavior of reinforced cementitious composites.. 98
Table 6-2: Batch proportions of SHCC and PCC. 99

Acknowledgements

The work reported in this dissertation would not be possible without the help and support of many individuals who I was fortunate to collaborate with.

I would like to thank my advisor, Professor Claudia Ostertag, who allowed me the oppourtunity to return to school and pursue my doctoral degree. I benefitted from many long conversations I had with her about my research, and I hope the work presented herein becomes impactful for future researchers and engineers.

I would also like to thank my other dissertation committee members. Professor Paulo Monteiro provided steady support for my work. The enthusiasm he showed me while taking his CE 60 class in the Fall of 2007 remains with me to this day. Professor Kenneth Raymond first introduced me to the Advanced Light Source, where I spent numerous nights collecting experimental data.

Many mentors shaped my research skills and views. Gabe Jen has been as a consisent source of advice for me since I was an undergraduate student. I received further guidance from Will Trono, Phil Wong, Cruz Carlos, Rae Taylor, Daniel Hernández-Cruz, Lev Stepanov, Tim Teague, Alistair MacDowell, and Dula Parkinson.

My labmates, colleagues, and friends were a collective source of daily motivation, and included Alex Lin, Rotana Hay, Jake Duncan, Ian Williams, Parham Aghdasi, Kemal Celik, Jiaqi Li, Guoqing Geng, Daniela Martinez, and Andrew Wagner.

Several undergraduate students assisted my research activities and allowed me to become a better teacher. I am especially grateful to Tamika Bassman, Matt Landberg, Jack Wegleitner, Caroline Evans, and Ellen Heile for their commitments.

The studies detailed in Chapter 2 and Chapter 3 of this dissertation were supported by the Pacific Earthquake Engineering Research (PEER) Center.

The studies detailed in Chapter 4, Chapter 5, and Chapter 6 of this dissertation were supported by the Federal Highway Administration (FHWA) under grant DTFH61-09-R-00017.

1 Introduction

1.1 Current condition of United States infrastructure

The deteriorating quality of infrastructure in the United States is a major engineering and economic issue. Recent reported statistics by the Federal Highway Administration [1] revealed that 9.1% of 614,000 cataloged United States bridges were classified as structurally deficient in 2016. A structurally deficient is a bridge that has damage of load-carrying structural elements or has ineffective waterway openings such that traffic would be severely impacted. The condition of a bridge is highly correlated to its age. As shown in Figure 1-1a, the total number of structurally deficient bridges is generally greater as the age of the structure increases up to approximately 89 years of age, while the proportion of structurally deficient bridges within an age group generally increases up to 109 years of age (Figure 1-1b).

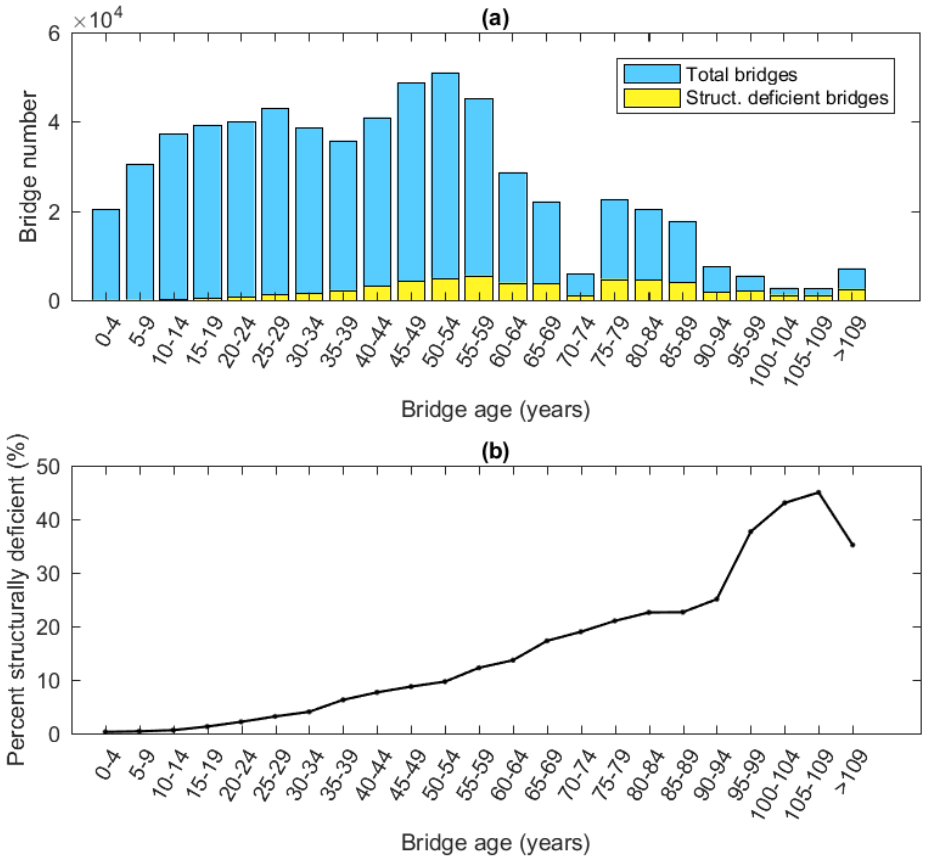


Figure 1-1: Relation of structurally deficient bridge statistics to bridge age: (a) Number of bridges; (b) Percentage of bridges. Values are based on 2016 statistics reported by the Federal Highway Administration [1].

The estimated replacement cost of all structurally deficient national highway system (NHS) bridges in 2016 was reported to be $25.1 billion United States dollars while rehabilitation of these structures was estimated to be $17.1 billon [1]. Replacement or rehabilitation of non-NHS bridges was estimated to cost an additional $21.9 billion or $14.9 billion, respectively. Once identified as damaged, treatment of affected structures is often not immediate. In a 2010 report prepared by the

United States Department of Transportation [2], an annual investment of $20.5 billion was projected to eliminate the backlog of deficient bridges by 2028, based on rehabilitation of individual bridge elements. In 2008, only $12.8 billion was spent on such rehabilitation.

Figure 1-2 shows the proportion of structurally deficient bridges relative to all cataloged bridges in each state of the United States. Greater deficiency was generally concentrated in the Midwest and Atlantic coastal regions of the country, coinciding with states that rely heavily on deicing salts placed on ice- or snow-covered roadways during winter seasons. Runoff from these salts can corrode the surfaces of exposed structural steel or penetrate porous reinforced concrete (R/C), resulting in corrosion of embedded steel reinforcing bars (rebar). The economic burden related to corrosion damage of bridge structures was estimated in 2001 to be $8.3 billion [3], which accounted for 37% of industrial costs within the infrastructure spending category at that time.

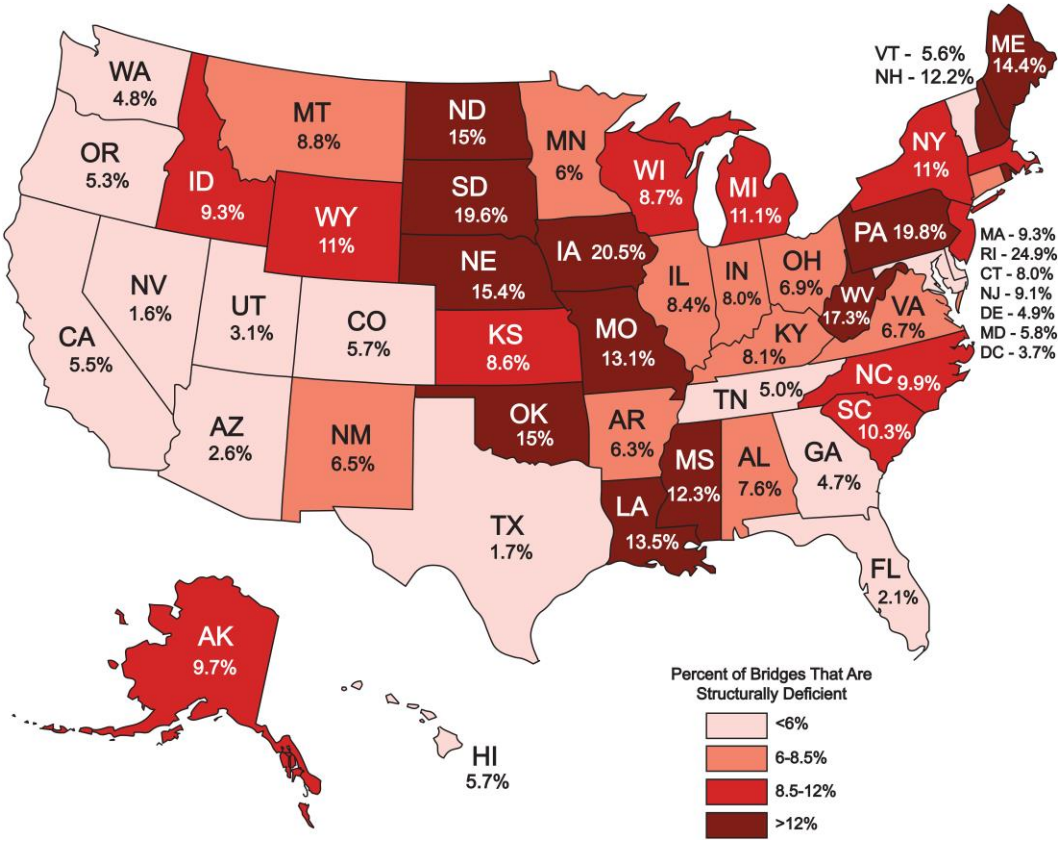


Figure 1-2: Percentage of structurally deficient bridges in each state of the United States. Values are based on 2016 statistics reported by the Federal Highway Administration [1].

1.2 Reinforced concrete damage

As the current damage state of structurally deficient bridges worsens over time, the replacement of these structures provides an opportunity to modify current, conventional bridge designs towards more sustainable designs that achieve greater durability and service life. Such a change should consider and evaluate the primary causes of bridge deterioration from both physical and chemical processes. Reinforced concrete structures located in seismic regions are highlighted herein. In the state of California, where considerable seismic activity can occur, bridge structures are designed

by the California Department of Transportation (CalTrans) seismic design criteria (SDC) to deform in a ductile manner while preventing collapse of the structure during an earthquake [4]. During less than design-level seismic events, concrete cracking and cover spalling can occur [5]. Damage from higher-intensity events may include longitudinal steel reinforcing bar (rebar) buckling and fracture, transverse rebar fracture, and concrete crushing.

Prior to seismic loading, reinforced concrete structures may accumulate long-term damage as a result of several chemical processes that can take place internally within the concrete. Corrosion of embedded steel rebar in reinforced concrete has major implications on the structural performance and sustainability of global infrastructure. In mild environments, low-carbon steel reinforcing bars (rebar) embedded within concrete form a passive film due to the high pH (ca. 13 to 13.5) of the concrete pore solution and are not generally expected to exhibit any significant corrosion activity during the designed service life of the structure. However, Cl^-, available from sources such as ocean saltwater or deicing salts placed on roadways, may permeate though the porous concrete cover and reach the steel rebar surface. When a sufficient concentration of local chlorides is present relative to the pH of the concrete pore solution, depassivation and corrosion of the steel reinforcing bar may begin [6, 7]. Because the volume of corrosion products is greater than the volume of the parent steel, the internal expansion of these products may cause concrete cracking [8], subsequently increasing the chloride solution permeability of the concrete [9, 10]. Corrosion-induced cracks can lower the structural capacity of a reinforced concrete structural element, which may result in poor performance during an earthquake [11-13]. Forensic investigations of damaged reinforced concrete structures found preexisting corrosion after the 1998 Adana-Ceyhan (Turkey) [14], 1999 İzmit (Turkey) [14], 2010 Haiti [15], and 2011 Lorca (Spain) [16] earthquakes, though poor structural performance may be attributed to a number of causes that also includes corrosion damage.

1.3 Hybrid fiber-reinforced concrete (HyFRC)

Due to multiple avenues of degradation, reinforced concrete structures require a robust solution towards durability improvement. Considering that a primary functional purpose of reinforced concrete is to resist load and that rehabilitation of structures does not occur immediately after structural deficiency detection, retention of structural load capacity even when damaged is a desired design property. As the development of concrete cracks is often an initial precursor to extensive structural damage, solutions aimed at restricting crack propagation in a controlled manner are worth exploring. In recent decades, high-performance fiber-reinforced cementitious composites (HPFRCC) have been investigated for partial or total replacement of conventional concrete [17-21]. HPFRCC constitutes a class of construction composite materials that contain short (e.g., 8 mm to 60 mm), discontinuous fibers randomly dispersed within a cement-based matrix. When properly designed, the fibers significantly toughen the overall composite by bridging cracks and restricting the cracks' opening and propagation [22]. Compared to plain concrete, HPFRCC matrix damage is often characterized by more diffuse cracking with smaller crack widths rather than less numerous cracks with larger crack widths, and can exhibit ductile tensile strain-hardening and flexural deflection-hardening behaviors after matrix cracking has occurred [23].

While a variety of fiber-reinforced concrete designs have been investigated and reported in the literature [17-21], hybrid fiber-reinforced concrete (HyFRC) is highlighted herein. HyFRC broadly refers to a fiber-reinforced concrete that utilizes multiple fiber types varying in material and geometry (i.e., hybridization) within the same composite. When designing HyFRC with a

gradation of fibers sizes, a multiscale crack control approach may be achieved. Loading of HyFRC results in the formation of numerous microcracks, which are resisted by microfibers, and is subsequently followed by microcrack coalescence into larger macrocracks, which are then resisted by macrofibers. Figure 1-3 schematically shows the multiscale crack control. Specifically, the HyFRC developed by Blunt and Ostertag [24] utilizes such an approach with the inclusion of 8-mm long, 0.04-mm diameter polyvinyl alcohol (PVA) fibers, 30-mm long, 0.55-mm diameter steel fibers, and 60-mm long, 0.75-mm diameter steel fibers. For the remainder of this report, the term HyFRC will generally refer to the composite designed by, or derived directly from [25], Blunt and Ostertag [24].

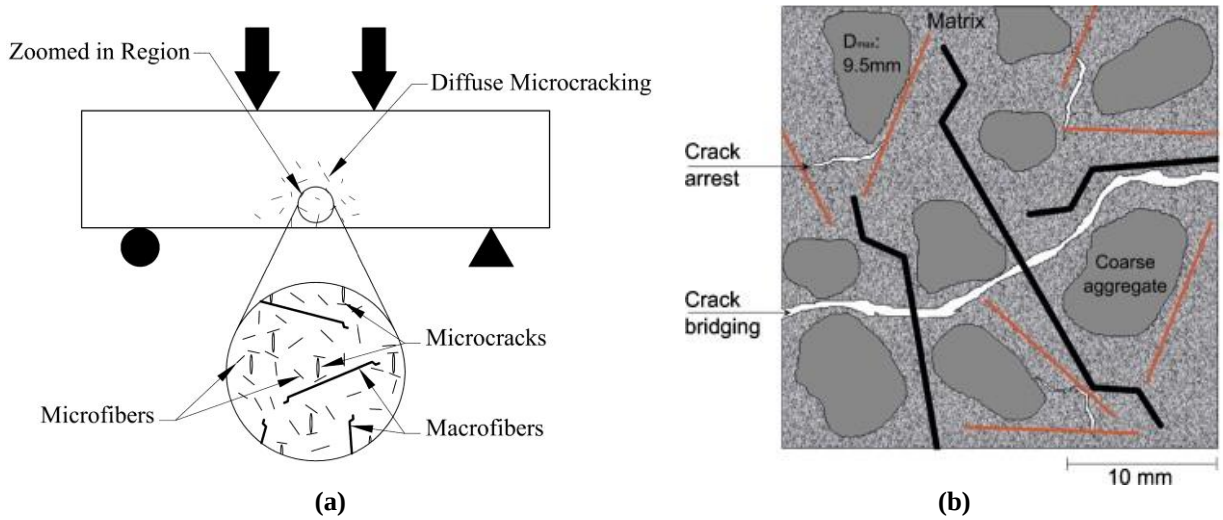


Figure 1-3: Multiscale crack control of a hybrid fiber-reinforced concrete (HyFRC): (a) Showing smaller fibers (microfibers) resisting microcracks prior to crack coalescence, as reported by Blunt and Ostertag [24]; (b) Showing longer fibers resisting larger cracks, as reported by Rambo et al. [26]

Continued investigation of HyFRC is motivated in part by its past large-scale structural validation in bridge columns [27, 28] and shear wall boundary elements [29]. Further application of HyFRC materials has been extended to building façade systems [30, 31]. However, details on the manner of damage control provided by hybrid fiber reinforcement under tensile and flexural loading are not yet completely elucidated. While HyFRC has also been observed to reduce corrosion-related physical and electrochemical damage [32-34], previous experiments generally did not have an experimental duration that caused embedded rebar in HyFRC composites to exhibit substantial corrosion damage. Other research has relied on methods to artificially induce corrosion in a short period of experimental time [35-37]. Thus, long-term corrosion propagation damage of HyFRC composites remains largely uninvestigated despite proposed use of HyFRC materials for more durable reinforced concrete structures with longer service lives [33].

1.4 Organization of the dissertation

To further advance the understanding of HyFRC and related fiber-reinforced cementitious composites, a multiscale experimental approach was taken to identify key mechanisms governing the damage characteristics of HyFRC. An overview of the broadly-defined experimental scales considered in this dissertation is presented in Table 1-1. Large-scale tests considered the effects of

multiple reinforcing bars within an individual HyFRC composite specimen, with experimental results correspondingly considering multiple damage effects to be incurred by structural elements in field conditions. Medium-scale tests considered the effects of a single reinforcing bar within an individual HyFRC composite specimen, with experimental results focusing on specific fundamental behaviors. Finally, microscale tests considered the effect of a single reinforcing bar within an individual reinforced fiber-reinforced cementitious composite specimen, with experimental results focusing on fundamental behaviors. As a whole, the experiments directly considered one of two primary causes of reinforced concrete bridge damage, which were seismic events or steel reinforcing bar corrosion. Details and discussion of the experimental results are provided in five distinct chapters.

Table 1-1: Overview of experimental scales considered in this dissertation.

Scale of study	Specimen design	Specimen cross-sectional diameter or width	Experimental results
Large-scale	Reinforced HyFRC with multiple steel reinforcing bars	150 – 400 mm	Considers multiple effects as incurred by a structural element in the field
Medium-scale	Reinforced HyFRC with a single steel reinforcing bar	130 – 180 mm	Considers specific fundamental behavior
Microscale	Reinforced microfiber-reinforced cementitious composite with a single steel reinforcing bar	< 10 mm	Considers specific fundamental behavior using X-ray micro-computed tomography (μCT)

In Chapter 2, the direct tensile response of reinforced HyFRC (i.e., HyFRC composites with steel reinforcing bars) is presented as a medium-scale experiment. Damage mechanisms related to crack formation and subsequent fiber pull-out processes are detailed, along with parameters dictating the promotion of ductile behavior in reinforced HyFRC. These parameters are important considerations when designing structural elements subjected to large applied displacements, such as those incurred during earthquakes.

In Chapter 3, the quasi-static seismic response of a bridge column constructed with a filled precast HyFRC tube element is presented as a large-scale experiment. This test directly considered design aspects of the CalTrans SDC [4]. The precast tube element contains all of the column's steel reinforcing bars. Such a design was investigated to synergistically incorporate practical economic considerations, namely accelerated bridge construction, and the crack-resisting benefits of HyFRC into a single structural design.

In Chapter 4, the electrochemical polarization behavior of reinforced HyFRC under sustained tensile stress and a chloride-based corrosive environment is presented as a medium-scale experiment. Samples were studied over a 2.5-year duration. The influence of cracking was related to the measured electrochemical behavior of tested samples.

In Chapter 5, the monitored corrosion activity of reinforced HyFRC beams from a 2.2-year study is presented as a large-scale experiment. These tests considered the behavior of steel rebar in contact with other steel rebar, as in rebar cage assemblies. The beams were subjected to flexural loading prior to chloride exposure. Corrosion initiation and propagation behaviors were affected by the presence of cracking in samples. At the conclusion of environmental exposure, the mechanical properties of corroded samples were evaluated.

In Chapter 6, progressive in-situ, 3D damage visualization of corrosion damage in microfiber-reinforced cementitious composites over a 44-week period is presented as a microscale

experiment. Hard X-ray micro-computed tomography (μCT) was used to acquire images for visualization. Similar to medium- and large-scale experiments, samples in this study were studied for the influence of matrix cracking prior to, and during, active corrosion.

While current reinforced concrete structures may safely operate up to a certain level of accumulated damage, the research results reported herein indicate that replacement of conventional concrete with HyFRC in certain conditions greatly improves the crack resistance of bridge structural elements and may improve its functional service life. Such an effect would minimize rehabilitation, reduce the frequency of structural element replacement, and result in more sustainable reinforced concrete structures.

2 Tensile behavior of HyFRC composites

2.1 Introduction

High-performance fiber-reinforced cementitious composites (HPFRCC) have emerged in recent decades as a potential alternative to conventional concrete in structural applications due to their greater crack resistance and enhanced toughness. Short, discontinuous fibers in the matrix bridge and transmit load across cracks, strengthening the cracked section and allowing for additional cracks to form elsewhere within the cementitious composite. The diffuse, multiple cracking behavior of HPFRCC delays the coalescence of microcracks into a dominant crack to greater strains and improves the overall ductility of the composite. HPFRCC research has historically emphasized the ability of these composites to exhibit tensile strain hardening behavior, with Naaman and Reinhardt [23] proposing the high-performance classification be based primarily on the ability of a fiber-reinforced cementitious composite to exhibit such behavior, as shown in Figure 2-1. A strain hardening HPFRCC is able to achieve a greater tensile strength than the cracking strength of its matrix. However, isolation of the mechanical properties of HPFRCC alone in determining the apparent advantages of the material may not result in more damage-tolerant structures due to the presence of steel reinforcing bars (rebar) in reinforced concrete design and construction. In contrast, the proposition of a high-performance concrete (not specific to fiber-reinforced cementitious composites) by the United States Department of Transportation [38] focused on materials that were more durable than conventional concrete, with strength enhancement achieved only if necessary. This designation further emphasized the use of similar materials as conventional concrete, promoting a more economic and sustainable mix design.

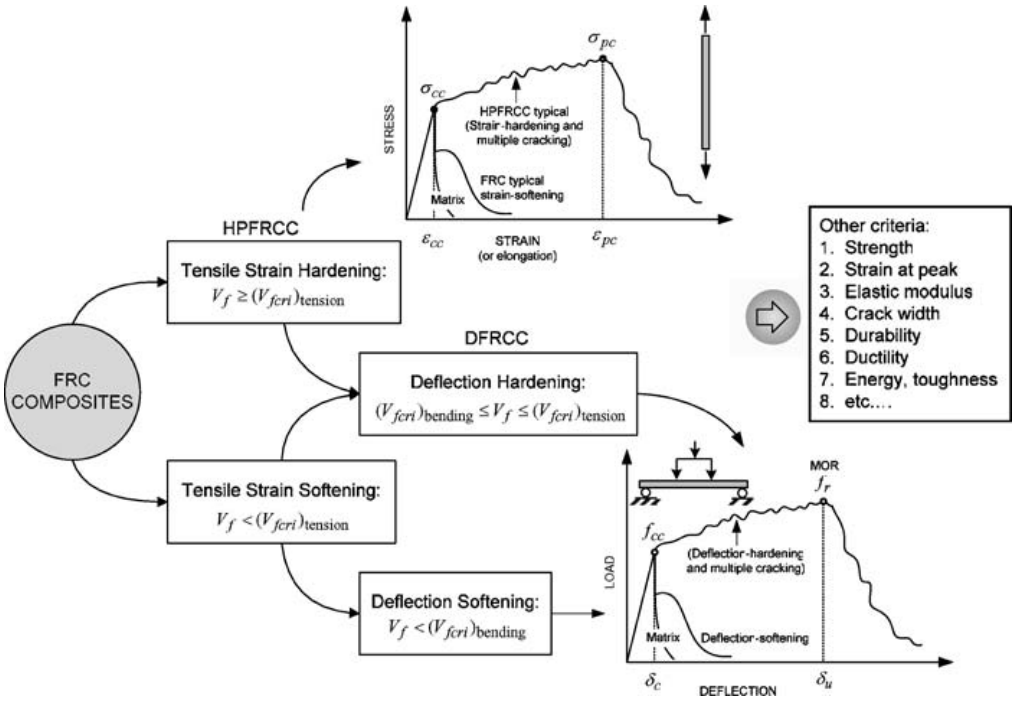


Figure 2-1: Proposed classification of high-performance fiber-reinforced concrete composites (HPFRCC) based on tensile response. Proposition is by Naaman and Reinhardt [23].

When reinforced concrete is placed under tensile stress, concrete exhibits strain compatibility with rebar prior to macrocracking, and contributes both tensile load resistance and stiffness to the reinforced composite. After cracking, concrete between cracks continues to stiffen the response of rebar. This effect is known as tension stiffening [39]. Differential slipping of rebar against concrete near crack surfaces may result in the formation of longitudinal splitting cracks [40], which degrades the rebar-matrix interfacial bond and subsequently relieves tension stiffening effects where those cracks occur [41].

Because fibers can carry tensile load across cracks, tension stiffening may be maintained in fiber-reinforced concrete composites at greater member strains than would be possible for conventional reinforced concrete. Several researchers have reported that tension stiffening remains present for reinforced fiber-reinforced concrete after matrix cracking, with fiber reinforcement allowing the composite load resistance to exceed that of the rebar yield load upon rebar yielding [42-49]. Under the same conditions, R/C load resistance is typically limited to the rebar yield load. Particular to reinforced HyFRC (R/HyFRC), Moreno et al. [44] tested prismatic samples in direct tension until failure and reported that a strengthening effect occurred when the composite load exceeded the rebar yield load. Compared to R/C, R/HyFRC generally achieved a greater load resistance for a given value of specimen strain, though exhibited a reduction in ultimate strain capacity. The ultimate strains of other types of reinforced HPFRCC have been reported to be lower than that of reinforced concrete, owed in part to the fibers' high resistance towards splitting crack propagation [42, 44].

Due to the contribution of HyFRC towards reinforced composite tensile load capacity, motivation exists to lower the longitudinal rebar reinforcement ratio of R/HyFRC. The ratio is defined herein as the quotient of longitudinal rebar volume to gross R/HyFRC volume. This design change is intended to partially relieve rebar congestion in heavily reinforced structural members, which would ease construction practices related to the casting of fresh fiber-reinforced concrete. While reducing the reinforcement ratio of R/HyFRC is expected to alter the rebar-matrix interfacial bond strength [50], Fischer and Li [49] reported that interfacial bond properties were not impactful on the macroscale tensile response of reinforced engineered cementitious composites (reinforced ECC, or R/ECC) due to the multiple cracking behavior of the fiber-reinforced ECC. Strain compatibility between steel and cracked ECC was mentioned to be maintained even when the rebar was plastically deformed. The conclusion suggests reinforcement ratio may have negligible effects on the deformation behavior of R/ECC up to tested specimen strains of 4% to 5%. However, variation of the longitudinal reinforcement ratio has been reported to be influential on the ultimate deformation capacity of R/ECC. Kang et al. [42] subjected R/ECC to direct tension and reported a decrease in ultimate strain capacity when the longitudinal reinforcement ratio decreased. Similarly, Bandelt and Billington [51] subjected R/ECC to flexure and reported a decrease in beam drift (i.e., deformation) capacity when the longitudinal reinforcement ratio decreased. Because HyFRC and ECC differ in design methodologies and mechanical behavior [20, 24], the effect of reinforcement ratio on R/HyFRC cannot be assumed based on R/ECC experimental characteristics.

In this chapter, the tensile response of R/HyFRC with a low reinforcement ratio of 0.6% is investigated. Conventional reinforced concrete is also considered for comparison. Prismatic samples with a single steel reinforcing bar were tested in direct uniaxial tension until fracture of the rebar was achieved. The results are compared to reported tensile results of R/HyFRC and R/ECC available in the literature to further identify key parameters dictating the behavior of reinforced HPFRCC under tensile stress.

2.2 Materials and methods

2.2.1 Concrete materials

Batch proportions for the hybrid fiber-reinforced concrete (HyFRC) tested in this study are presented in Table 2-1 and are based on the design reported by Blunt and Ostertag [52]. Fiber hybridization consisted of 8 mm-long polyvinyl alcohol (PVA) fibers, 30 mm-long hooked-end steel fibers, and 60 mm-long hooked-end steel fibers. The hooked-end geometry of the steel fibers, as shown in Figure 2-2, results in greater pull-out resistance while under tensile load compared to smooth fibers [53]. Additional fiber properties are presented in Table 2-2. The total fiber volume fraction, based on HyFRC volume, was set to 1.5%. During casting, fibers were randomly distributed within the sample mold and were not preferentially aligned. A plain concrete lacking fiber reinforcement was also studied and had the same water-binder mass ratio as the HyFRC. Both composites were cast with coarse aggregates with a maximum size of 9.5 mm, which provided matrix shrinkage restraint, and fine aggregates with a fineness modulus of 3.2. Samples were cured for 7 days within formwork and covered with wetted burlap, demolded, and then cured in ambient laboratory conditions (approximately 23.5° C, 45% relative humidity) until mechanical testing. This curing protocol (i.e. wet curing followed by dry curing) followed the same methods performed by Blunt and Ostertag [52] for the development of HyFRC. The mean compressive strength of concrete and HyFRC was 42 MPa and 40 MPa, respectively.

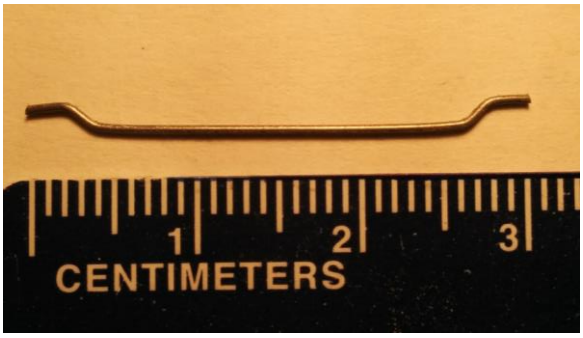


Figure 2-2: Typical 30 mm-long hooked-end steel fiber batched in HyFRC.

Table 2-1: Batch proportions of HyFRC.

Composite	Mass proportions (kg/m^3)				Fiber volume fraction (vol. % composite)		
	Cement	Water	Coarse aggregate	Fine aggregate	PVA	Steel (30-mm length)	Steel (60-mm length)
HyFRC	423	228	775	853	0.2	0.5	0.8

Table 2-2: Properties of fibers in HyFRC, as reported by Blunt and Ostertag [52].

Material	Surface texture	Diameter (mm)	Length (mm)	Tensile strength (MPa)	Elastic modulus (GPa)	Proportion in HyFRC (% vol. HyFRC)
PVA	Smooth	0.04	8	1600	42	0.2
Steel	Smooth, with hooked ends	0.55	30	1100	200	0.5
Steel	Smooth, with hooked ends	0.75	60	1050	200	0.8

2.2.2 Specimen design

Experimental details of the prismatic test specimens are presented in Figure 2-3a and are based on the specimen design used by Moreno et al. [44] The samples in this study had a square cross-section with a side length of 178 mm and an 813 mm-long region of interest where matrix cracking was allowed to occur. The total length of a sample was 1040 mm. A single United States number 5 (16 mm diameter) A706 [54] steel reinforcing bar with extruded ribs was embedded centrally along the specimen length, resulting in a volumetric longitudinal reinforcement ratio of ρ=0.6%. To dictate rebar fracture within the region of interest, each end of the rebar was friction-welded onto a steel coupler, which was then attached to a 25 mm-diameter, threaded steel rod. The yield load of the threaded rod was greater than the ultimate load of the R/HyFRC or R/C specimens. Pull-out action of the threaded rod from the cementitious matrix was prevented by strengthening portions of the sample excluded from the region of interest with an internal steel reinforcement cage and an external application of epoxied carbon fiber-reinforced polymer (CFRP) wrapping, as shown in Figure 2-3a. During testing, damage of the CFRP was not observed, indicating that the additionally reinforced sections of the specimen remained elastic.

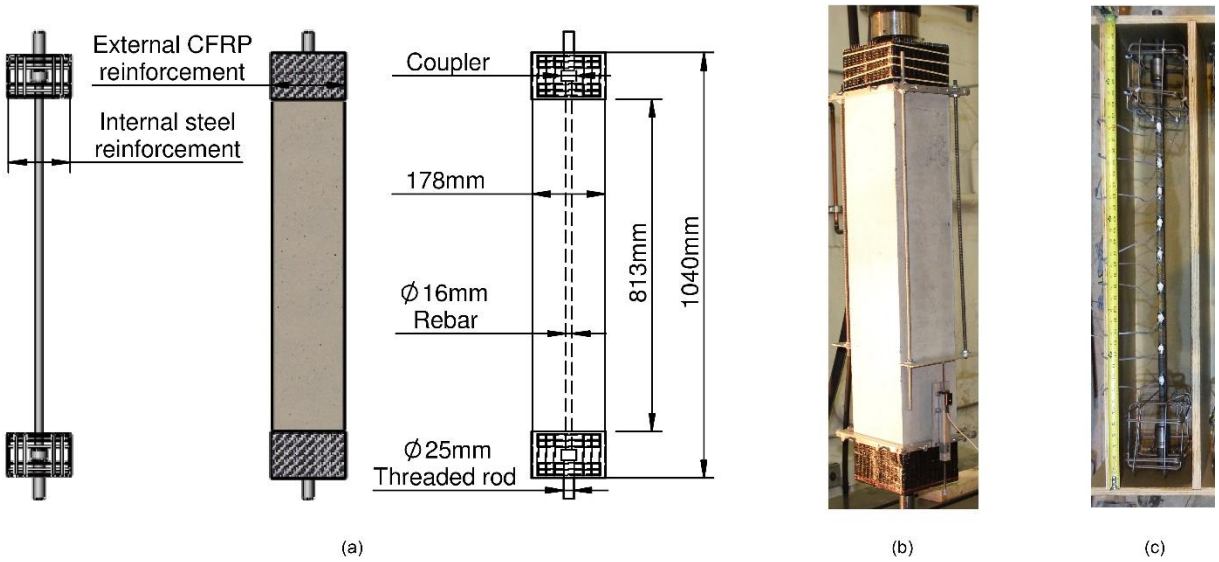


Figure 2-3: Specimen design: (a) Materials and measurements; (b) Global view of specimen prior to testing, showing external instrumentation; (c) Strain-gauged specimen prior to casting.

2.2.3 Instrumentation and testing

Four R/C and three R/HyFRC samples were prepared for experimentation. Linear variable displacement transducers were placed on opposite sides of the specimen and measured the displacement over the full length of the region of interest (Figure 2-3b). One specimen from each composite type had its reinforcing bar fitted with nine strain gauges, each spaced 76 mm apart, as shown in Figure 2-3c. The treated surfaces of the rebar required for strain gauge application were minimized to reduce defects at the rebar-matrix interface. A displacement-controlled protocol, with a rate of 0.6 mm per minute, was selected for testing and ceased upon fracture of the steel

reinforcing bar. Uniaxial tensile load was applied directly to the extruded threaded rods, which developed load in the composite samples through interfacial bond stress.

2.3 Results

2.3.1 Global response

Measured load-average specimen strain responses of the R/C and R/HyFRC composite samples are presented in Figure 2-4 for strains up to ε=0.4% and for the complete responses of samples. The average specimen strain is based on a gauge length of 813 mm, which spans the entire region of interest length, and is explicitly described as being averaged due to the nonuniform deformation that occurred during testing. Also included in the plots is the load-strain response of a bare 16 mm-diameter A706 [54] steel rebar, which was of the same type used in the reinforced composite samples. All samples, regardless of fiber inclusion, exhibited an initial elastic composite response at low strains (e.g., ε<0.01% to 0.02%) prior to matrix cracking (Figure 2-4a). After crack initiation, R/C samples exhibited one to two discrete, prominent load reductions prior to the specimen load stabilizing near the yield load of the rebar. The load reductions are indicative of matrix cracking events. Additional displacement of the R/C specimens resulted in increasing load resistance until a mean peak load of 124 kN was reached, which was nearly equivalent to the peak load of the bare rebar (121 kN).

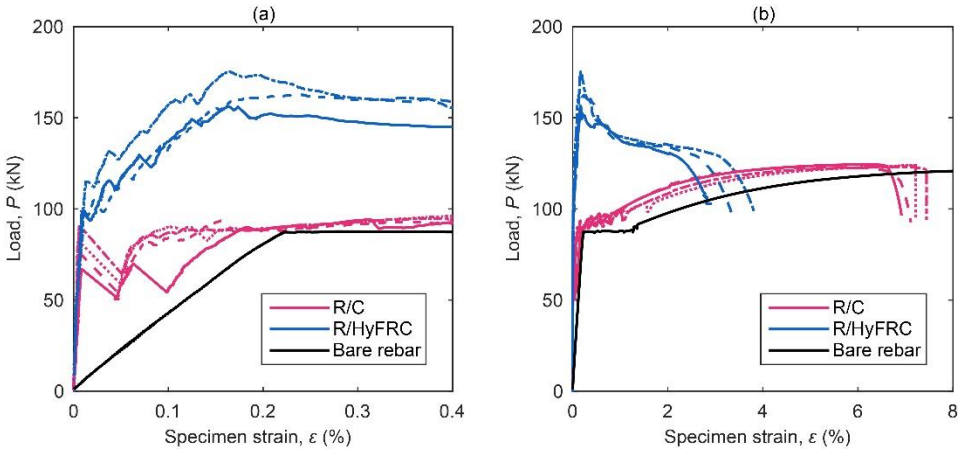


Figure 2-4: Load P versus average specimen strain ε response of R/C, R/HyFRC, and bare rebar: (a) Up to ε=0.4%; (b) Complete response.

Due to bridging action of fibers across matrix cracks, R/HyFRC samples exhibited an increase in load resistance after cracking. Based on the mean response of the three samples, this load increase occurred up to a mean strain of 0.19% and a mean peak load of 165 kN. Compared to the mean load of R/C samples at the same specimen strain of ε=0.19%, the R/HyFRC mean load was greater by a factor of 1.86. While R/HyFRC retained an average of 81% of peak load resistance at ε=2%, significant load softening occurred upon further applied displacement until a mean specimen fracture strain of 3.4% was reached (Figure 2-4b). The specimen failure strains of R/HyFRC were noticeably lower than the average failure strains measured for R/C (ε=7.2%), which is generally consistent with similar experiments performed elsewhere for the direct tensile response of reinforced high-performance fiber-reinforced cementitious composites [42, 44].

2.3.2 Local response

Strain gauge measurements of the steel rebar embedded within a R/C and a R/HyFRC specimen are presented in Figure 2-5 and Figure 2-6, respectively. The ordinate of the plots is labeled as the distance from midheight ΔH_{mid} of the sample and the plot range (-406 to 406 mm versus ΔH_{mid}) spans the entire region of interest where cracking was allowed and observed to occur. Surface damage of the gauged samples at select specimen strains and after failure is also presented. Black pens were used to trace the propagation of observed surface cracks, though the marking widths were not indicative of the actual crack widths formed.

Localized strain development of the rebar correlated well with surface crack locations. For the R/C sample, sections 2 and 8 exhibited noticeable nonuniform rebar strain at a specimen strain of $\varepsilon_{R/C}$=0.4%, being greater than other measured strains along the bar. Through-thickness cracks could be identified near these locations (Figure 2-5b). Additional applied displacement of the sample resulted in greater intensification of strain at these and some adjacent gauged locations. Though not seen on the presented R/C sample images, a longitudinal splitting crack was initially observed on an adjacent prism face at $\varepsilon_{R/C}$=0.38% between transverse cracks located near section 2 and section 4. Other tested R/C samples also exhibited surface splitting cracks by $\varepsilon_{R/C}$=0.4% (Figure 2-7a and c). Fracture of the gauged specimen occurred in the region where the adjacent splitting crack formed (Figure 2-5e). Concrete in sections of the sample sufficiently far from a transverse or splitting crack, such as section 6, continued to resist load while the rebar exhibited insignificant strain increases compared to plastically developed sections.

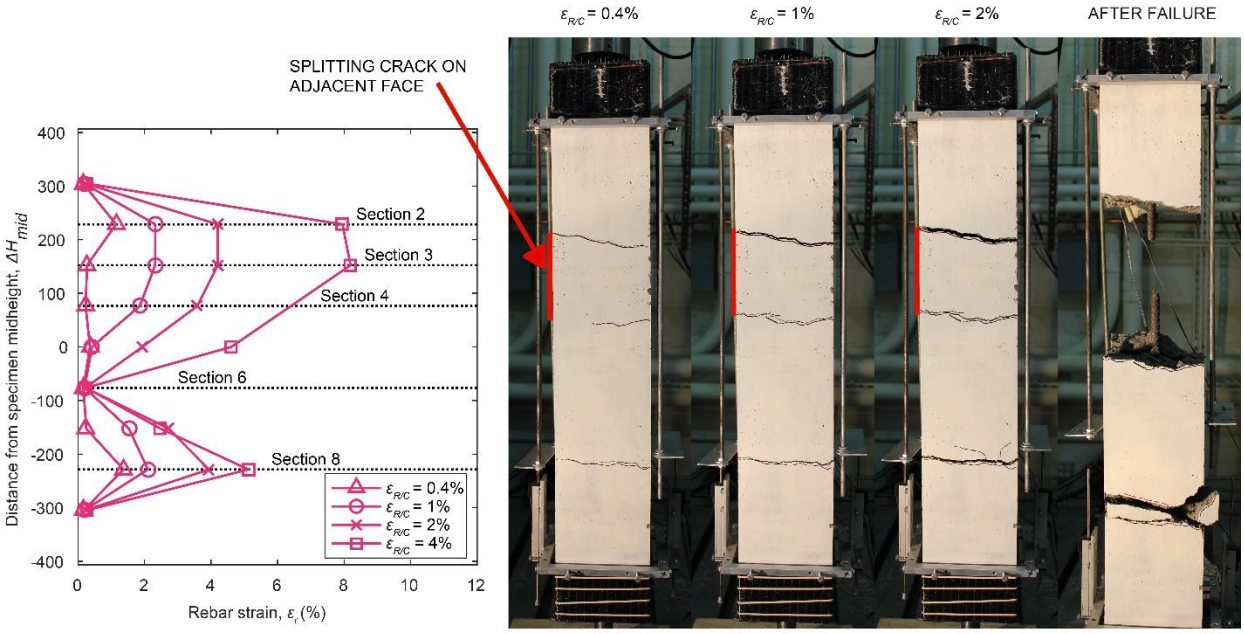


Figure 2-5: (a) Rebar strain profile of R/C sample; Surface observations of sample at R/C average specimen strain $\varepsilon_{R/C}$: (b) $\varepsilon_{R/C}$=0.4%; (c) $\varepsilon_{R/C}$=1%; (d) $\varepsilon_{R/C}$=2%; (e) After failure. Portions of concrete spalled from the specimen upon failure. A splitting crack (not seen) developed on an adjacent face between transverse cracks each located near section 2 and section 4.

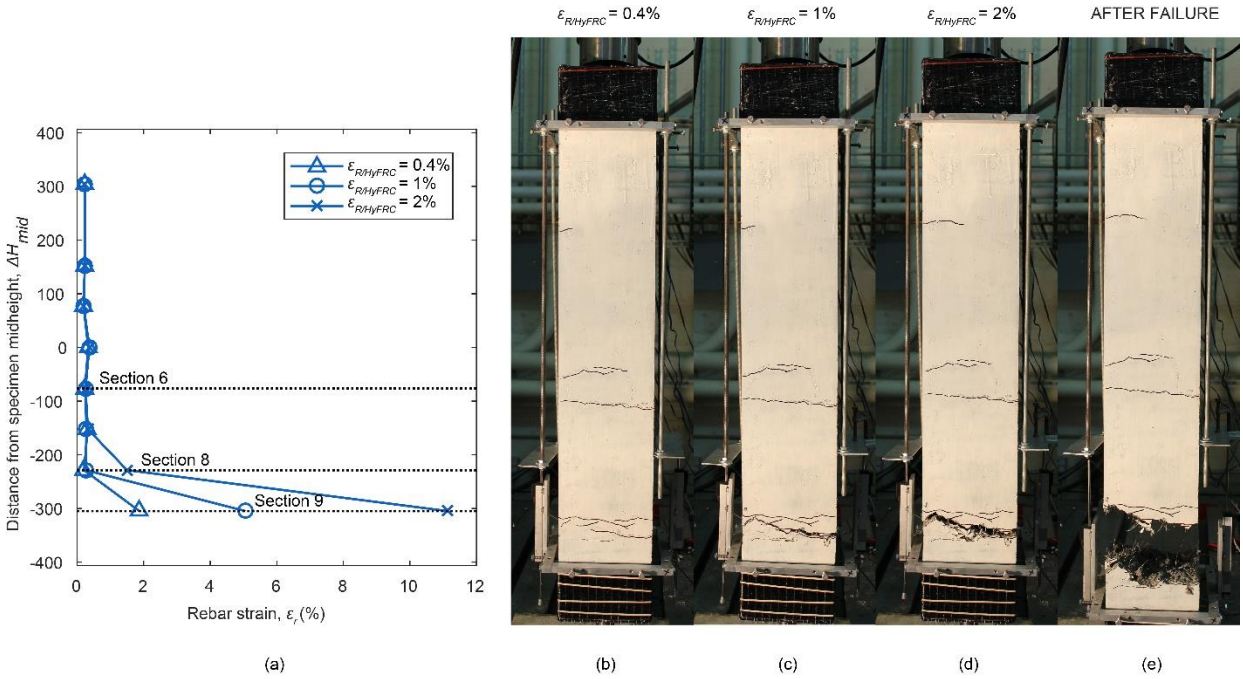


Figure 2-6: (a) Rebar strain profile of R/HyFRC sample; Surface observations of sample at R/HyFRC average specimen strain $\varepsilon_{R/HyFRC}$: (b) $\varepsilon_{R/HyFRC}$ =0.4%; (c) $\varepsilon_{R/HyFRC}$ =1%; (d) $\varepsilon_{R/HyFRC}$ =2%; (e) After failure.

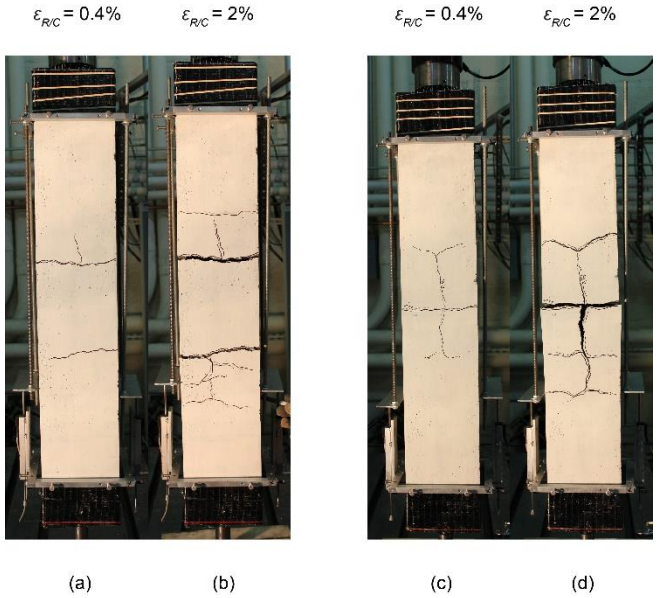


Figure 2-7: Surface observations of two R/C samples ((a)-(b) and (c)-(d)) without strain gauge instrumentation at R/C average specimen strain $\varepsilon_{R/C}$ =0.4% and $\varepsilon_{R/C}$ =2%.

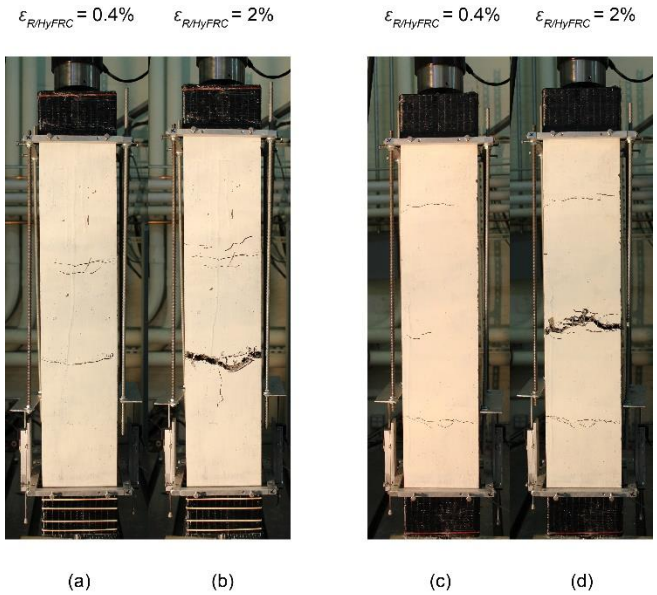


Figure 2-8: Surface observations of two R/HyFRC samples ((a)-(b) and (c)-(d)) without strain gauge instrumentation at R/HyFRC average specimen strain $\varepsilon_{R/HyFRC}$ =0.4% and $\varepsilon_{R/HyFRC}$ =2%.

The R/HyFRC sample similarly exhibited rebar strain localization at a specimen strain of $\varepsilon_{R/HyFRC}$=0.4%, as shown in Figure 2-6a. However, localization occurred only at section 9 despite the presence of other transverse cracks within the sample, such as those near section 6 (Figure 2-6b). Upon further loading, deformation of the sample continued to concentrate at and near section 9 within a coalesced dominant crack, while the rebar strain in secondary cracked sections (e.g., section 6) marginally increased. Visual observations of the sample (Figure 2-6b-d) revealed negligible transverse crack propagation or opening on the HyFRC surface aside from the single dominant crack, which was consistent with the damage behavior of other tested R/HyFRC samples (Figure 2-8). Furthermore, surface splitting cracks were either absent or did not significantly propagate on the surfaces of the individual samples. Rebar fracture for all R/HyFRC samples occurred within the dominant crack, as shown in Figure 2-6e.

2.4 Discussion

2.4.1 Rebar plasticity development

Inelastic deformation of the steel rebar resulted in considerable nonuniform strain distribution considering the full length of the rebar within the region of interest. The nonuniform deformation was related to the presence of transverse cracks and splitting cracks, if any. Figure 2-9 plots the measured rebar strain ε_r at select sections of the instrumented R/C and R/HyFRC samples as a function of specimen strain $\varepsilon_{R/C}$ and $\varepsilon_{R/HyFRC}$, respectively. The locations of the sections were previously designated in Figure 2-5 or Figure 2-6, and were selected for being at or near the site of final rebar fracture. For R/C, section 2 was located at or near a transverse crack while a transverse crack did not occur at the adjacent section 3. However, a splitting crack was observed between these sections. Similarly, for R/HyFRC, section 9 was located at or near a transverse crack while a transverse crack did not occur at adjacent section 8. Rebar strains at which yielding (ε_{yield})

and strain hardening ($\varepsilon_{hardening}$) initially occur are indicated in the plots, with the strain bounded between ε_{yield} and $\varepsilon_{hardening}$ being the strain range where the steel yield plateau occurs.

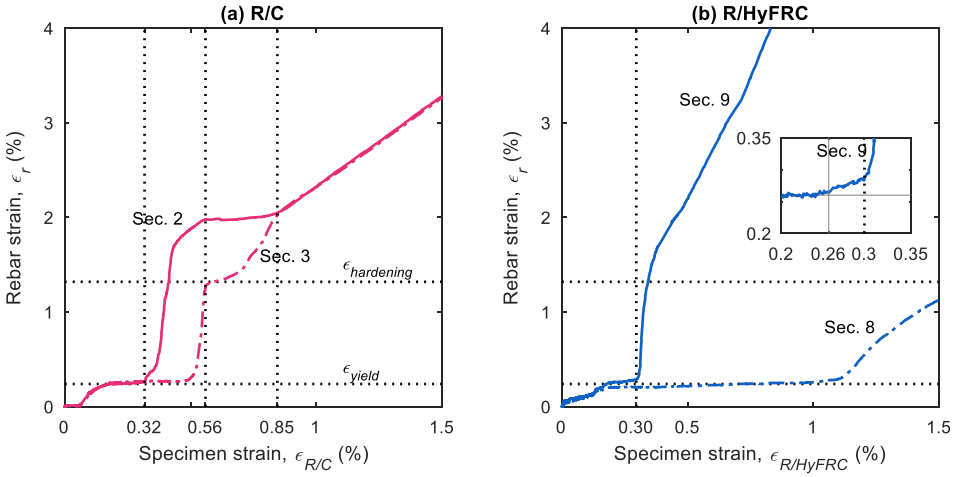


Figure 2-9: Rebar strain ε_r versus: (a) Average R/C specimen strain $\varepsilon_{R/C}$; (b) Average R/HyFRC specimen strain $\varepsilon_{R/HyFRC}$. Rebar strains are measured at select cross-sections (sec.) of a sample, which were designated in Figure 2-5 and Figure 2-6 for R/C and R/HyFRC, respectively. Rebar strains at which yielding (ε_{yield}) and strain hardening ($\varepsilon_{hardening}$) initially occur are explicitly marked as dotted horizontal lines in the plots.

For R/C, plasticity was developed in a series of events where final fracture of the rebar occurred (i.e., at section 2 and section 3). First, rapid rebar strain increase occurred at section 2 at $\varepsilon_{R/C}$=0.32%, as indicated by the steep slope in Figure 2-9a, from ε_{yield} to $\varepsilon_{hardening}$. Sample section 8, which is not shown in Figure 2-9a, exhibited a similar rapid strain increase at an earlier specimen strain of $\varepsilon_{R/C}$=0.23%. At a through-thickness cracked section, the specimen load is carried solely by the rebar across the crack opening. Because the rebar exhibits no tangential stiffness within the yield plateau regime (i.e., between ε_{yield} and $\varepsilon_{hardening}$), displacement of the specimen is localized at the rebar within the crack opening. Shortly after section 2 surpasses $\varepsilon_{hardening}$, its strain rate is decreased. In this context, strain rate refers to the strain change of a rebar section relative to the strain change of the composite specimen ($\Delta\varepsilon_r/\Delta\varepsilon_{R/C}$ or $\Delta\varepsilon_r/\Delta\varepsilon_{R/HyFRC}$). Between $\varepsilon_{R/C}$=0.56% and 0.85%, the rebar strain of section 2 does not significantly increase as specimen deformation becomes concentrated at the adjacent section 3, which also exhibited a rapid strain increase while deforming within the rebar yield plateau regime prior to reaching $\varepsilon_{R/C}$=0.56%. Plasticity in this section is developed through concrete splitting cracks, which were first observed at this section at $\varepsilon_{R/C}$=0.38% and debond the rebar from the concrete. These splitting cracks are caused by strain incompatibility (i.e. slippage) between the rebar and the matrix near transverse cracks, as the concrete is unloaded at a cracked section while the rebar carries the entire composite specimen load. For strains greater than $\varepsilon_{R/C}$=0.85%, debonding of section 3 is complete and the rate of plastic deformation is equivalent between section 2 and 3. Tension stiffening is no longer present where the rebar is fully debonded.

The plasticity development of R/HyFRC was noticeably different compared to R/C. While two to three observable transverse cracking sites were present when R/HyFRC reached a specimen strain of $\varepsilon_{R/HyFRC}$=0.4% (Figure 2-6b, and Figure 2-8a and c), only a single crack localization occurred for all R/HyFRC samples. Significant strain localization of the rebar within R/HyFRC occurred at $\varepsilon_{R/HyFRC}$=0.30% at section 9 (Figure 2-9b), though plastic deformation of the rebar

initially occurred at a lower rate and started at an earlier strain of $\varepsilon_{R/HyFRC}$=0.26%, as indicated in the subplot in Figure 2-9b. The initial low plastic strain rate suggests a resistance towards rebar deformation was present and is attributed to crack-bridging fibers providing a stiffening effect on the rebar, though the effect may have been less effective with increasing specimen strain. Additional discussion on the relationship between the influence of fibers on the plastic strain development of the rebar at $\varepsilon_{R/HyFRC}$=0.26% is provided in Section 2.4.2. Upon section 9 reaching $\varepsilon_{hardening}$, the strain rate is partially reduced, though remains locally high compared to plastic sections of R/C. When R/HyFRC section 9 deformed from ε_r=0.5% to 6%, its strain rate was $\Delta\varepsilon_r/\Delta\varepsilon_{R/HyFRC}$=5.75. In comparison, the average strain rate of R/C at sections 2 and 3 from ε_r=1% to 6% was $\Delta\varepsilon_r/\Delta\varepsilon_{R/C}$=1.89.

Considering other available strain measurements along the rebar in R/HyFRC, one additional location at section 8 exhibited plasticity. Surface cracking was not observed at this section (Figure 2-6). The strain rate of section 8 was not as great as other plastically deformed R/C sections due to sustained tension stiffening effects and high splitting crack resistance. Load is maintained within the HyFRC by crack-bridging fibers at section 9 and is not entirely redeveloped into the matrix by the rebar through interfacial bonding at section 8, reducing differential material slippage and hoop stresses required for splitting crack propagation. The localized plastic deformation of R/HyFRC compared to the more widespread plastic behavior of R/C resulted in lower specimen strain capacity, as previously presented in Figure 2-4b.

2.4.2 Material load distribution

Figure 2-10 and Figure 2-11 show the load carried by the entire specimen, rebar, or cementitious composite at select sections of samples with strain gauge instrumentation for specimen strains up to 0.4% and 4%, respectively. For each composite type, two sections were selected where separate transverse cracks occurred. Equation 2-1 describes the force equilibrium that must be satisfied at any cross-section within a reinforced concrete sample.

$$P_{R/C} = P_{Concrete} + P_{Rebar} \qquad \text{Equation 2-1}$$

$P_{R/C}$ is the measured load carried by the R/C specimen and is constant for all sections at a given specimen strain. P_{Rebar} is the load carried by the rebar and is estimated by directly correlating the measured rebar section strain to a load resistance based on the monotonic response of a steel rebar with the same size and steel alloy as in the R/C specimens. $P_{Concrete}$ is the sectional load carried by the concrete and is determined by calculating the difference between $P_{R/C}$ and P_{Rebar}. Similar calculations were made for R/HyFRC using the same methodology.

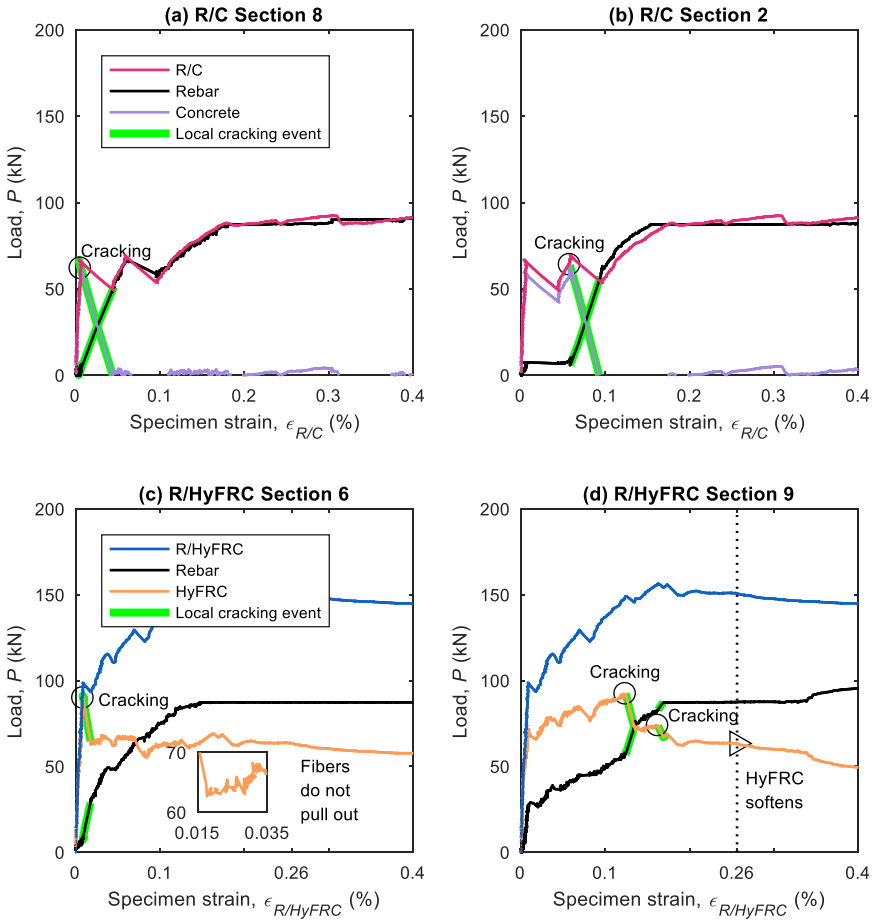


Figure 2-10: Load *P* distribution of materials versus average specimen strain $\varepsilon_{R/C}$ or $\varepsilon_{R/HyFRC}$ (up to 0.4% strain) at select cross-sections: (a)-(b) R/C; (c)-(d) R/HyFRC. Section locations were designated in Figure 2-5 and Figure 2-6 for R/C and R/HyFRC, respectively. Cracking events are highlighted in green.

Local cracking events at or near a presented section are highlighted in green in Figure 2-10. These cracking events are identified by both a decrease in concrete or HyFRC load resistance and an increase in rebar load resistance. As expected, after transverse matrix cracking of a R/C section, load in the concrete is completely relieved while load in the rebar significantly increases (Figure 2-10a and b). Continued loading after cracking reveals the specimen load being equivalent to the rebar load until failure, as indicated by Figure 2-11a and b.

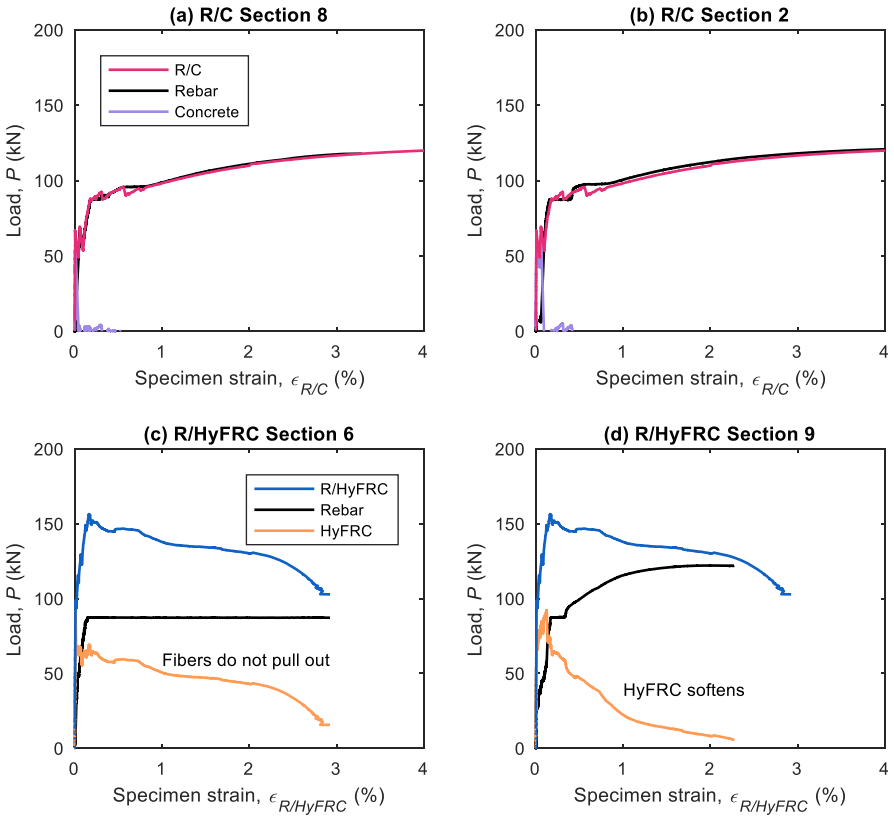


Figure 2-11: Load P distribution of materials versus average specimen strain $\varepsilon_{R/C}$ or $\varepsilon_{R/HyFRC}$ (up to 4% strain) at select cross-sections: (a)-(b) R/C; (c)-(d) R/HyFRC. Section locations were designated in Figure 2-5 and Figure 2-6 for R/C and R/HyFRC, respectively.

The load-specimen strain responses of R/HyFRC section 6 and section 9, which were both located near transverse cracks, are presented in Figure 2-10c and Figure 2-10d, respectively. Immediately after matrix cracking at section 6, an increase in rebar load occurred, as well as partial unloading of HyFRC. While bridging fibers transmit tensile load across a crack, some load in the matrix is transferred to the rebar after cracking due to rebar-matrix interfacial bonding, which is stronger for HyFRC materials compared to conventional reinforced concrete [50, 55]. After the local cracking event, load in the HyFRC slightly increases over a limited domain of specimen strain (from $\varepsilon_{R/HyFRC}$=0.02% to 0.03%), as shown in the subplot within Figure 2-10c. The resisted R/HyFRC load increases after cracking due to a combination of further elastic deformation of the rebar and bridging fibers' load carrying capacity across cracks. This increase in specimen load resistance allows the HyFRC to reach its cracking load elsewhere, such as at section 9 (Figure 2-10d).

R/HyFRC section 9, which is where dominant cracking of the sample occurred, exhibited load softening of both the reinforced composite and HyFRC upon reaching $\varepsilon_{R/HyFRC}$=0.26%, as indicated in Figure 2-10d. Softening occurs when the fibers' peak load transmission capacity has been reached, and slipping or pull-out behavior of the fibers dominates the load resistance of the HyFRC. This value of $\varepsilon_{R/HyFRC}$=0.26% coincided with the onset of rebar strain increase at section 9, as previously shown in the subplot in Figure 2-9b, indicating that the onset of plastic deformation of the rebar section is dependent on HyFRC softening. Additional applied displacement of the sample beyond $\varepsilon_{R/HyFRC}$=0.26% revealed load resistance increases from strain hardening rebar were

not sufficient to offset load resistance decreases from softening HyFRC, resulting in overall R/HyFRC composite softening (Figure 2-11d). Consideration of a reinforcing bar composed of a steel lacking a yield plateau may more effectively mitigate early load resistance losses from softening fiber-reinforced concrete, as reported by Redaelli [56].

Enhanced ductility of R/HyFRC is dependent on the plastic deformation of rebar within multiple transverse cracks, as the high splitting crack resistance of HyFRC restricts the spread of rebar plasticity in noncracked sections. Rebar plasticity development at a transverse crack was previously mentioned to be dependent on HyFRC softening at the cracked section, which is achieved when the fibers' peak load transmission capacity has been reached. While several transverse cracks formed in the discussed R/HyFRC sample (Figure 2-6) and other R/HyFRC samples (Figure 2-8), rebar plastic deformation was concentrated at a single crack location. Because overall load softening of the R/HyFRC sample occurred after formation of the first dominant crack at section 9, other cracked sections of the sample, such as section 6, were relaxed in load (i.e., unloaded) even if the ultimate fiber bridging capacities in these other sections were not previously reached. As shown in Figure 2-10c and Figure 2-11c, the resisted HyFRC load in section 6 decreases beyond $\varepsilon_{R/HyFRC}$=0.26% despite no significant fiber pull-out action occurring at this cracked section. As will be discussed in Section 2.4.3, when the HyFRC at secondary cracks is allowed to increase in load after the first dominant crack localization, the specimen may exhibit a more ductile response.

2.4.3 Comparison to composites with greater reinforcement ratio

R/HyFRC samples in this study exhibited lower ductility compared to R/C due to strain localization within a single dominant crack and high splitting crack resistance. However, the strain capacity and fracture characteristics of R/HyFRC may be altered by modifying the rebar reinforcement ratio. Moreno et al. [44] conducted direct tensile tests of R/HyFRC with ρ=1.2%, which is designated as R/HyFRC$_{1.2}$ in this discussion section. In comparison, samples in this study were designed with ρ=0.6% and are designated as R/HyFRC$_{0.6}$ in this discussion section. Several experimental parameters were consistent between the R/HyFRC$_{0.6}$ and R/HyFRC$_{1.2}$ samples. Both experiments used the same HyFRC mix design, had the same gauge length of 813 mm, were cast with a 16 mm-diameter steel rebar, and were tested under a displacement-controlled loading protocol by applying tensile load onto high-strength steel threaded rods that were coupled onto the rebar. The primary difference between the samples was the gross cross-sectional area, as R/HyFRC$_{1.2}$ samples were fabricated with a square section with a side length of 127 mm while a side length of 178 mm was used for R/HyFRC$_{0.6}$. As a result, the HyFRC cover thickness for R/HyFRC$_{0.6}$ (81 mm) was also greater compared to R/HyFRC$_{1.2}$ (56 mm). The reinforcement ratio thus differed between samples due to changes in gross area while the rebar area remained constant between the experiments. Additionally, Moreno et al. [44] reported the tensile testing results of reinforced engineered cementitious composite (reinforced ECC, or R/ECC) with ρ=1.2%. The specimens are designated as R/ECC$_{1.2}$ in this discussion section. The ECC used was a fiber-reinforced mortar designed with 2% volume proportion of 12.7 mm-long, 0.04-mm diameter PVA fibers. Compared to HyFRC, ECC exhibits more diffuse microcracking with smaller maximum crack widths and has a greater matrix cracking strength due in part to a much lower water-binder mass ratio, which was 0.26 for ECC compared to 0.54 for HyFRC.

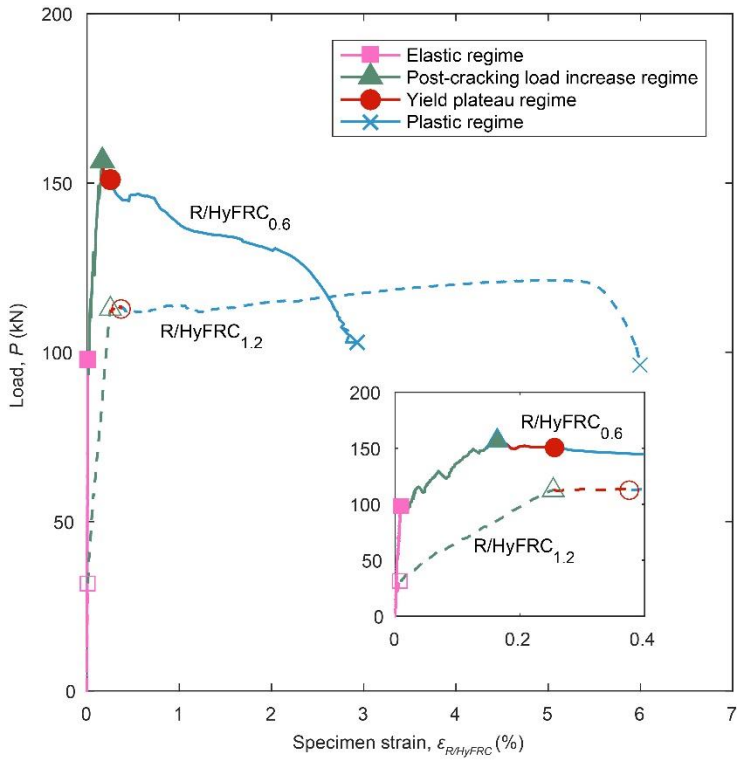


Figure 2-12: Designated tensile regimes for R/HyFRC based on representative samples. The rebar size is consistent between composite types. R/HyFRC$_{1.2}$ is reported by Moreno et al. [44]

The tensile response of R/HyFRC may be segmented into four distinct regimes, as indicated in Figure 2-12. First, the composites behave elastically and the rebar and matrix exhibit strain compatibility until the first matrix cracking event, as indicated by the square (e.g., "■") markers. Second, after matrix cracking, a composite load increase regime occurs as the rebar generally deforms elastically and fibers transmit tensile load across cracks, which allows for additional transverse cracks to form within the matrix. Tension stiffening effects are active during this regime and in succeeding regimes. Third, the composite exhibits no increase in load resistance while the rebar is strained within the yield plateau and the fibers have not yet initiated slipping or pull-out behavior. Finally, R/HyFRC either exhibits load softening (R/HyFRC$_{0.6}$) or hardening (R/HyFRC$_{1.2}$) as the plastic rebar strain hardens and fibers in the HyFRC pull out.

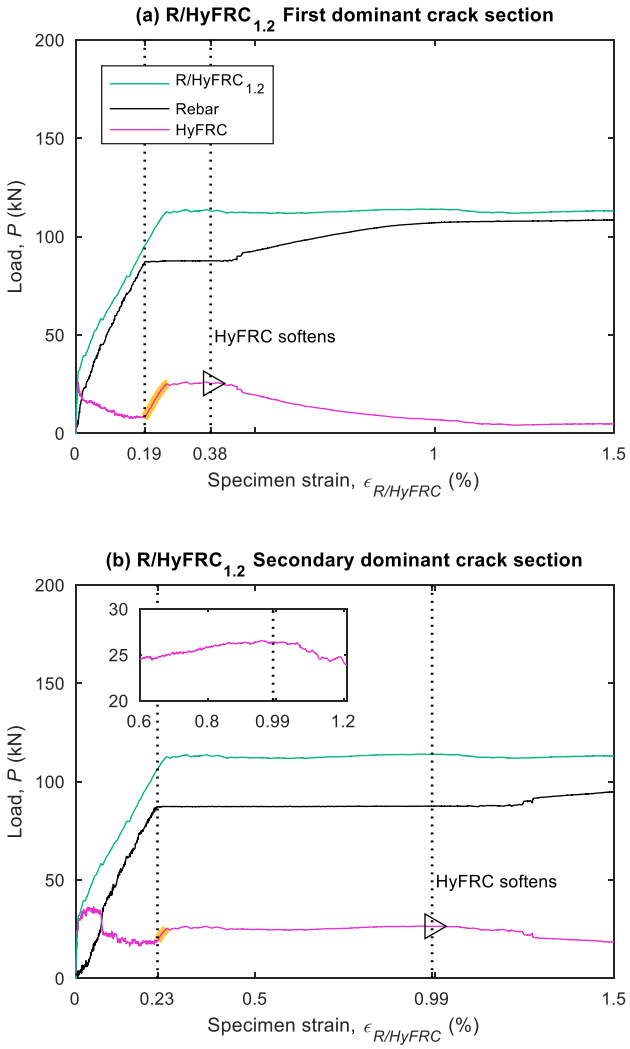


Figure 2-13: Load P distribution of materials versus average R/HyFRC specimen strain $\varepsilon_{R/HyFRC}$ (up to 1.5% strain) at select cross-sections of R/HyFRC$_{1.2}$: (a) First dominant cracking section; (b) Secondary dominant cracking section. R/HyFRC$_{1.2}$ is reported by Moreno et al. [44]

Termination of the post-cracking load increase regime, as indicated by the triangle (e.g., "▲") markers in Figure 2-12, occurred at different specimen strains between R/HyFRC sample types, with R/HyFRC$_{0.6}$ having a lower regime transition strain compared to R/HyFRC$_{1.2}$. When designed with a lower reinforcement ratio, the HyFRC cross-sectional area is greater and the total load carried by the HyFRC prior to cracking is greater. Thus, the rebar in HyFRC$_{0.6}$ receives a greater magnitude of load transfer upon cracking compared to HyFRC$_{1.2}$, and subsequently strains to a greater extent to resist the greater transferred load. This mechanism also indicates that the fibers in HyFRC$_{1.2}$ are not as intensely stressed as in HyFRC$_{0.6}$. The sectional load distribution of materials in a R/HyFRC$_{1.2}$ sample at or near the first dominant crack localization and secondary dominant crack localization are shown in Figure 2-13a and Figure 2-13b, respectively. Similar load distribution plots were previously presented for a HyFRC$_{0.6}$ sample in Figure 2-10 and Figure

2-11. The rebar and HyFRC loads presented in Figure 2-13 for $HyFRC_{1.2}$ were determined using Eqn. (1) and the method described in Section 2.4.2 for a $R/HyFRC_{0.6}$ sample with rebar strain measurements. At a specimen strain of $\varepsilon_{R/HyFRC}$=0.1%, which was within the post-cracking load increase regime for both R/HyFRC composite types, HyFRC resisted 65% of composite load for $R/HyFRC_{0.6}$ at the section nearest the first dominant crack location, while HyFRC resisted 17% of composite load for $R/HyFRC_{1.2}$ at the section nearest the first dominant crack location. Due to lower stress demand on the HyFRC in $R/HyFRC_{1.2}$, only after rebar yielding do bridging fibers in $R/HyFRC_{1.2}$ operate at peak load capacity. At a specimen strain of $\varepsilon_{R/HyFRC}$=0.19% and $\varepsilon_{R/HyFRC}$=0.23%, as indicated in Figure 2-13a and Figure 2-13b, respectively, the rebar reaches the yield load and the HyFRC load resistance increases (as highlighted in the plots), also increasing the specimen strain at which the initial load increase regime ceases. Such an increase for HyFRC after yielding was not observed for $R/HyFRC_{0.6}$, as the HyFRC hardened to peak load capacity shortly after matrix cracking, as previously discussed in section 2.4.2.

Based on the tensile response regimes designated in Figure 2-12, behavior within the plastic regime is most crucial for dictating the overall ductility of the composite. The transition from the yield plateau regime to the plastic regime is characterized by the onset of HyFRC softening at a crack due to the initiation of fiber pull out and initiation of rebar plasticity located within or near the crack, as previously detailed in Section 2.4.2. While composite load softening occurred for $R/HyFRC_{0.6}$ due to load capacity increases from rebar strain hardening being unable to offset load capacity decreases from HyFRC softening, the degradation of load-carrying capacity from HyFRC was not as severe at a reinforcement ratio of ρ=1.2% due to the lower magnitude of load carried by the HyFRC within $R/HyFRC_{1.2}$ samples. The strain hardening rebar is generally able to offset the losses of the softening HyFRC at the first dominant crack section such that other cracked sections in the sample may increase in matrix load and reach the ultimate fiber bridging load capacity, as shown in the subplot in Figure 2-13b at $\varepsilon_{R/HyFRC}$=0.99%. Moreno et al. [44] reported that the $R/HyFRC_{1.2}$ sample presented in Figure 2-13 exhibited dominant cracking at three total cracking sites, as seen in Figure 2-14. Ductility of the sample was further increased due to limited formation of splitting cracks in the sample, which were able to propagate from dominant cracking sites due to the decreased cover thickness of the samples compared to $R/HyFRC_{0.6}$ [50].



Figure 2-14: Surface observation of a $R/HyFRC_{1.2}$ specimen just prior to fracture. $R/HyFRC_{1.2}$ is reported by Moreno et al. [44]

The influence of the reinforcement ratio on the behavior of R/HyFRC within the plastic regime suggests that an adequate reinforcement ratio is necessary to prevent excessive load capacity reduction of the reinforced composite after HyFRC softening has occurred. Use of R/HyFRC at low reinforcement ratios (e.g., ρ=0.6%) may be suitable for structures where the service limit state of the load-bearing element is yielding of the reinforcement, though would likely result in poor performance for members exhibiting large deformations, such as seismic load-resisting elements. Other researchers have reported similar conclusions on the relationship between longitudinal reinforcement ratio reduction and ductility reduction for reinforced HPFRCC under tensile or flexural loading [42, 51, 57, 58].

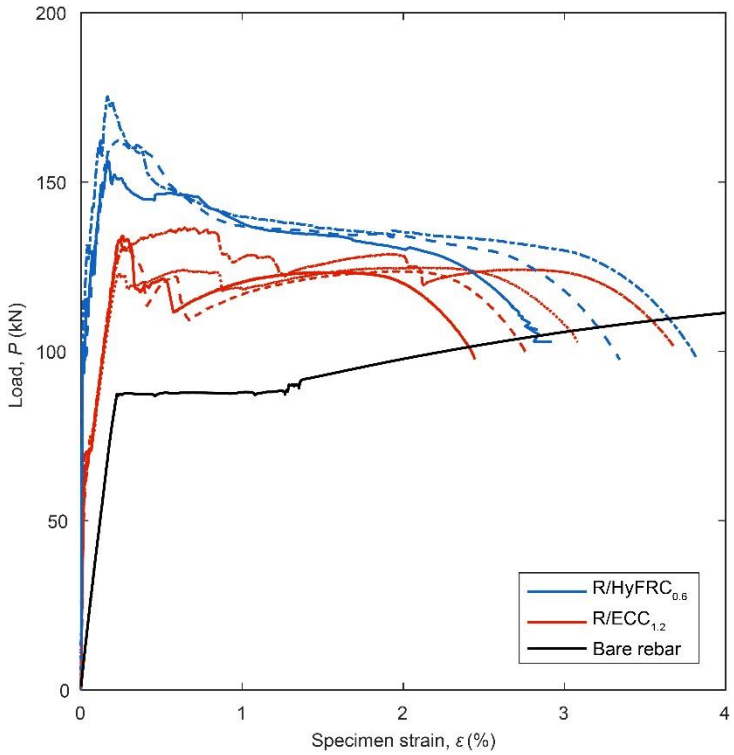


Figure 2-15: Load P versus average specimen strain ε of R/HyFRC$_{0.6}$ and R/ECC$_{1.2}$. The rebar size is consistent between composite types. R/ECC$_{1.2}$ is reported by Moreno et al. [44]

Despite being fabricated with different reinforcement ratios, R/HyFRC$_{0.6}$ and R/ECC$_{1.2}$ exhibited similar experimental characteristics. Both reinforced cementitious composites reached peak specimen load resistance prior to reaching ε=0.4% and failed at mean specimen strains within the domain of ε=3.4% to 3.5%. The comparable ultimate strain capacities coincide with observed cracking damage of the samples, as both sample types concentrated deformation within a single dominant crack and did not show significant surface splitting crack damage. Similar R/ECC crack localization characteristics were observed by Kang et al. [42] from tensile tests, which considered samples with longitudinal reinforcement ratios from ρ=0.59% to 1.64%. A noticeable difference between the responses of R/HyFRC$_{0.6}$ and R/ECC$_{1.2}$ is the shape of the softening curves after peak load resistance occurred. R/HyFRC$_{0.6}$ generally shows a smoother decrease in load resistance compared to R/ECC$_{1.2}$. This difference in softening behavior is attributed to differences in the fiber pull-out behavior of the samples. HyFRC is designed with a multiscale fiber reinforcement scheme that includes fiber lengths of 30 mm and 60 mm, while the ECC for R/ECC$_{1.2}$ contains a single

fiber type with a length of 13 mm. In the absence of steel reinforcing bars, the different designs of the cementitious composites result in ECC reaching a greater composite strain prior to dominant fiber pull out initiation compared to HyFRC, though HyFRC softens more gradually and retains more load capacity than ECC beyond a certain composite strain due to the longer fibers present in HyFRC [44, 59]. Based on Figure 2-11d, fibers in R/HyFRC$_{0.6}$ continued to carry load near the single dominant crack location to a specimen strain of at least ε=2%. For R/ECC$_{1.2}$, complete fiber pull out occurred more rapidly with increasing specimen strain, as Moreno et al. [44] reported that fibers were visually pulled out within the domain of ε=0.5% to 0.9%. Secondary hardening regimes for R/ECC$_{1.2}$ are a result of rebar strain hardening after fibers can no longer transmit forces across the dominant crack. High-performance fiber-reinforced cementitious composites with a greater residual fiber pull-out load capacity at high deformations, such as HyFRC, are advantageous for providing additional reinforced composite load capacity for a greater domain of strains, such that more gradual softening or hardening may occur within the plastic regime. To compensate for the short-length fibers of ECC, a greater reinforcement ratio compared to R/HyFRC may be necessary to promote adequate mechanical ductility of R/ECC [42, 51].

2.5 Summary and conclusions

This chapter presents the uniaxial tensile testing results of reinforced hybrid fiber-reinforced concrete (reinforced HyFRC, or R/HyFRC) designed with a low volumetric longitudinal reinforcement ratio of ρ=0.6%. Specimens were cast with a single steel reinforcing bar and subjected to direct tensile loading. Based on the experimental results, the following conclusions can be made:

1. The tensile response of R/HyFRC may be segmented into four distinct phases: (1) Elastic regime; (2) Post-cracking load increase regime; (3) Yield plateau regime; and (4) Plastic regime. Tension stiffening effects are active in the post-cracking load increase regime and succeeding regimes. The mechanisms that occur during the plastic regime are most influential on the overall ductility of R/HyFRC.
2. Upon matrix cracking, load carried by the HyFRC is redistributed to both the steel rebar and fibers bridging the cracks. This result is supported by strain measurements of rebar located near cracking sites showing discrete increases in rebar strain after a local cracking event.
3. Initiation of HyFRC material load softening and increase in rebar strain within the yield plateau are coincident events at a transverse crack. HyFRC softening occurs when the peak bridging load capacity of fibers at a crack is reached. The coincident events cause an existing transverse crack to exhibit dominant cracking behavior and allow for strain hardening of the rebar.
4. Deformation of R/HyFRC with a reinforcement ratio of ρ=0.6% was concentrated within a single dominant transverse crack. Within the cracked section, the increased load capacity of the strain hardening rebar was not sufficient to offset the load softening of HyFRC. Subsequent specimen load softening with additional applied displacement prevented secondary transverse cracks from becoming dominant cracks, limiting the strain capacity of the R/HyFRC.
5. Surface splitting cracks were suppressed in R/HyFRC, further limiting the development and spread of rebar plasticity. Control reinforced concrete (R/C) samples were able to form

splitting cracks, which allowed for distributed plasticity over greater bar lengths, leading to a greater ultimate specimen strain capacity.

6. Compared to R/HyFRC samples tested by Moreno et al. [44], which were designed with ρ=1.2%, reduction of the reinforcement ratio to ρ=0.6% resulted in reduced ultimate strain capacity and inability to exhibit hardening behavior within the plastic regime.
7. The ultimate specimen strain capacity of R/HyFRC with ρ=0.6% was similar to that of reinforced engineered cementitious composites (reinforced ECC, or R/ECC) with ρ=1.2%, which were tested by Moreno et al. [44]. R/HyFRC exhibited a more stable softening response due to the longer fiber lengths present in HyFRC compared to ECC.

3 Seismic behavior of a rocking bridge column using a precast HyFRC tube[1]

3.1 Introduction

In Chapter 1, it was reported that 9.1% of 614,000 cataloged United States bridges were classified as structurally deficient in 2016 [1]. As bridges reach the conclusion of their service lives, replacement of the structure may be required based on the severity of accumulated structural damage at the time of evaluation. Because bridge costs are directly related to the duration of onsite field operations, designs focused on accelerated bridge construction (ABC) to reduce project duration may be a worthwhile consideration [60, 61].

As the conventional design of bridges is altered to accommodate ABC, potential use of novel, damage-resisting construction materials should be considered in future bridge design revisions. To improve the damage-resisting properties of R/C columns, partial substitution of conventional concrete with HyFRC is investigated. As from Chapter 2, direct tensile testing of reinforced HyFRC, when reinforced at a steel rebar volumetric ratio of 0.6%, results in a reduction of specimen strain capacity and toughness compared to reinforced concrete caused by strain localization at an initial dominant crack location. Because bridge columns in seismic regions are expected to tolerate large displacements during an earthquake, tension stiffening effects caused by matrix fiber reinforcement may be undesirable for producing a ductile seismic response. Crack localization behavior has been reported in laterally-loaded bridge columns cast with different types of HPFRCC. Kawashima et al. [62] placed HPFRCC at the expected plastic hinge region and had localized flexural cracks develop within the hinge region between 3% to 6% drift. The HPFRCC columns of Aviram et al. [63] used supplementary dowel reinforcement in column-foundation interface and plastic hinge region to force inelastic deformations to occur away from the interface, though resulted in the formation of localized flexural cracks in the plastic hinge region as early as 1.7% to 2.6% drift (Figure 3-1). Panagiotou et al. [27] tested a column cast with HyFRC and observed localized cracking in the plastic hinge starting at 3.6% drift.



Figure 3-1: Crack localization in reinforced high-performance fiber-reinforced concrete bridge column specimen S2 at a drift of 2.6%. S2 is reported by Aviram et al. [63]

[1] Portions of this chapter appear in the article: Nguyen W, Trono W, Panagiotou M, Ostertag CP. Seismic response of a rocking bridge column using a precast hybrid fiber-reinforced concrete (HyFRC) tube. Compos Struct. 2017;174:252-62.

Controlled interface rocking of a column with its foundation and superstructure may be designed to mitigate crack localization when a plastic hinge is formed. By debonding the longitudinal reinforcing bars from the concrete matrix where the plastic hinge would normally develop and defining a rocking plane at a discontinuous joint, the concrete in the unbonded region develops minimal tensile strain. However, the concrete remains susceptible to compression damage, including spalling of concrete cover [64-66]. Reinforced HyFRC has shown higher compression damage resistance compared to conventional reinforced concrete as a shear wall boundary element subjected to direct compressive stress [29] and as bridge columns subjected to lateral loading (i.e., flexure) [27, 28].

When isolating the effects of HyFRC on compression behavior, Trono [67] tested cylindrical specimens with a longitudinal reinforcing ratio of ρ_l=1.6% and transverse reinforcing ratio ranging from ρ_s=0.3% to 1.9%. Upon direct compression testing, reinforced HyFRC was observed to form a distributed crack pattern with no dominant shear crack, while reinforced concrete showed a dominant shear crack and the onset of spalling at compressive strains of approximately 1%. Spalling and buckling were not observed for the reinforced HyFRC for strains up to 3%. Confinement provided by the spiral reinforcement did not increase the composite strength for transverse reinforcing ratios ρ_s less than 0.5%. This was in contrast to the confined strength in plain concrete samples increasing as a function of transverse reinforcing ratio. Unlike tension stiffening effects that reduce the ductility of reinforced HyFRC compared to reinforced concrete in direct tension, substitution of conventional concrete with HPFRCC for elements subjected to compressive stress results in a more ductile composite response and higher strain capacity.

The research study presented in this chapter investigates the feasibility of constructing and seismically evaluating a bridge column that synergistically adheres to the ABC and multiscale crack control methodologies. A crucial requirement is to develop a strategy of using HyFRC in a manner that professional construction engineers could easily adopt into their current practices. Use of a precast HyFRC tube element is proposed as the primary design feature to achieve an expedited construction schedule while optimizing its use in the column to where its mechanical properties are most beneficial, improving the economy of the column. The precast tube, which contains the column's longitudinal and transverse reinforcing steel, is to be installed into a foundation and then filled with cast-in-place (CIP) plain concrete afterwards. This process aims to eliminate onsite rebar assembly for the column and provides a permanent formwork for the column.

The column was subjected to static, unidirectional, cyclic loading to evaluate its seismic performance. To further increase the damage-resistance of the experimental column, a base rocking design was utilized to avoid flexural cracking associated with plastic hinge formation at the column base. The seismic response of the column is compared to a similarly sized and tested rocking column fabricated with cast-in-place HyFRC.

3.2 Materials and methods

3.2.1 Specimen design

The structural design of the column is presented in Figure 3-2. The test specimen represents the lower half of a full-height bridge column deforming in double curvature, assuming a midheight inflection point. The column's dimensions are based on a typical 15.2 m-tall column supporting a five-span box girder Californian bridge with a 1.8 m deck depth [68]. Based on the Caltrans seismic design criteria, key design parameters include the column diameter-superstructure depth ratio

(D/D_s=0.7 to 1.0) and longitudinal reinforcing ratio (ρ_l=1% to 4%) [4]. The prototype column used for the tube column was designed with diameter D=1.6m (D/D_s=1.0), 44 No. 11 (35 mm diameter) longitudinal bars (ρ_l=1.2%), No. 8 (25 mm diameter) transverse hoops spaced at 140 mm on center, resulting in a transverse reinforcing ratio of ρ_s=0.83%, and a concrete cover of 51 mm.

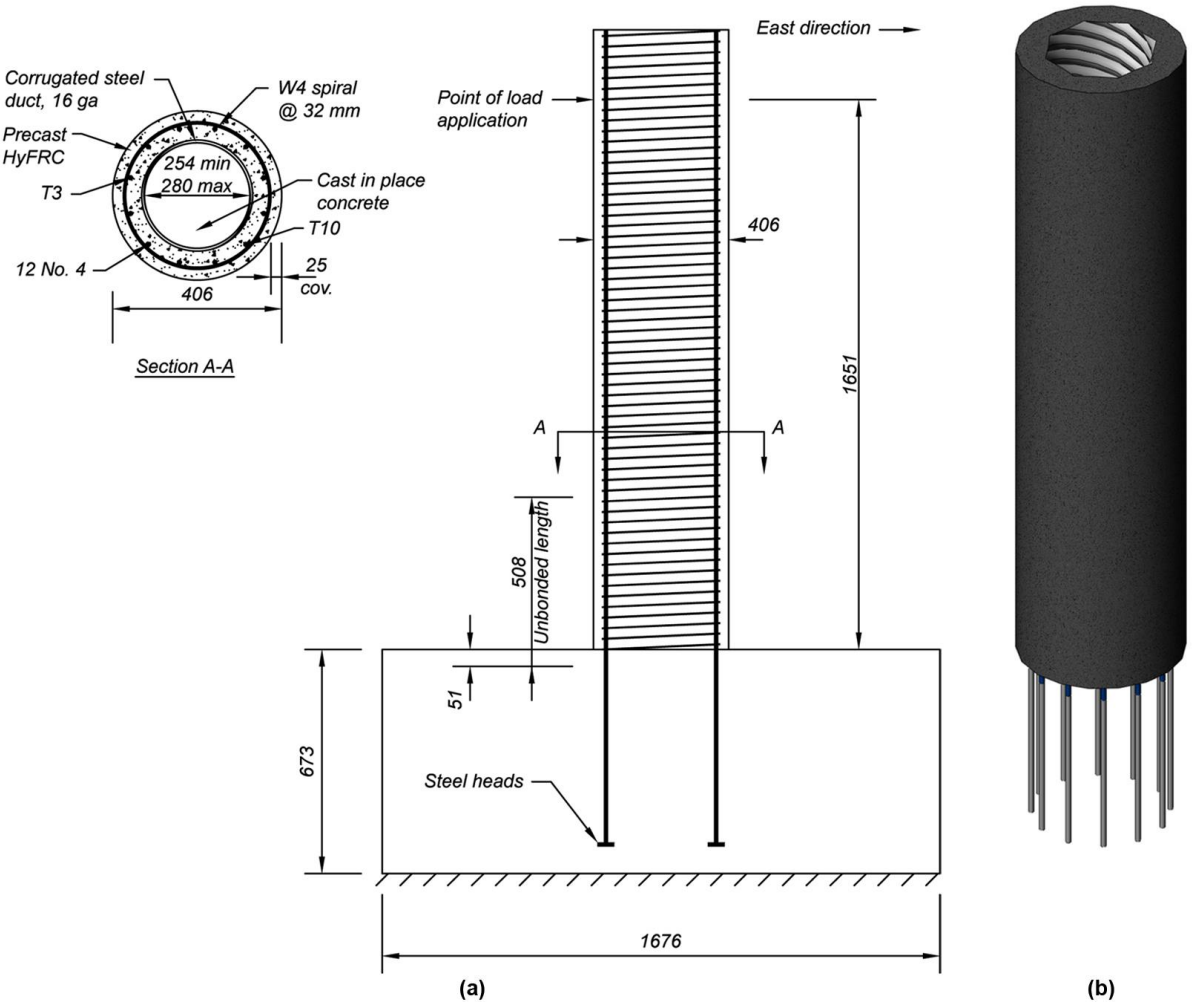


Figure 3-2: Tube column design: (a) Structural details (units in mm); (b) Representative visualization of precast tube element. Select longitudinal rebar (T3, T10) are referenced for discussion.

Table 3-1: Summary of column design parameters.

Column	Diameter, D (mm)	M/VD	Concrete	f'_c (MPa)	Cover thickness (mm)	ρ_l (%)	ρ_s (%)
Prototype Column[a]	1829	4.2	Cast-in-place plain concrete	35[b]	51	1.2	0.83
Tube Column	406	4.1	Precast HyFRC	66	25	1.2	0.87
			Cast-in-place plain concrete	44	-		

[a] Based on [68]
[b] Typical nominal compressive strength

A precast HyFRC tube, which contains the column's steel reinforcement, was determined to be the most practical method for accelerating construction. The precast tube element expedites construction by eliminating the need for rebar assembly to be done onsite for the column as well as providing permanent formwork for the interior plain concrete to be cast into. Additionally, casting of the HyFRC in a precasting facility will likely improve quality control, as cast-in-place construction of fiber-reinforced concrete is generally not common in the United States. A 16 gauge (1.6 mm thick) corrugated galvanized steel duct (ASTM A796 [70]), initially used as the inner permanent formwork of the precast tube, provided proper mechanical bond between the precast HyFRC and plain concrete. The longitudinal rebar embedded in the tube extruded 457 mm from the tube's bottom surface to allow for later installation into the foundation and were capped with steel heads for anchorage. Because HyFRC is more expensive than plain concrete, the precast tube column design improved economy by containing approximately 43% less HyFRC by volume compared to a column cast entirely with HyFRC.

The column utilized a base rocking design to avoid flexural crack localization caused by plastic hinge formation [27, 62, 63]. This design feature was achieved by allowing the longitudinal reinforcement to be unbonded in the lowest portion of the column over a length of 457 mm, with an additional 51 mm of unbonded length extending into the foundation. In a rocking column, the concrete in the unbonded region develops insignificant tensile strain. However, it remains susceptible to compression damage, including spalling of concrete cover [64-66]. To unbond the rebar, rubber mastic tape was tightly wrapped around the bars to build thickness between the ribs, such that anchorage would be negligible. A final layer of duct tape was used for additional slippage (Figure 3-6a).

3.2.2 Concrete materials

Mix proportions of the HyFRC for the precast tube element and the concrete for the filling of the tube are summarized in Table 3-2. The HyFRC was based on the self-consolidating HyFRC developed by Jen et al. [25], which is referred to herein as the baseline design. While the HyFRC for the tube column was not required to maintain the self-consolidating properties of the baseline design, a slump flow diameter of 432 mm to 483 mm was achieved on the day of casting (Figure 3-3). The concrete used 0.04 mm-diameter, 8 mm-long PVA fibers and 0.55 mm-diameter, 30 mm-long hooked-end steel fibers. The PVA fibers and steel fibers were designed at 0.2% and 1.8% fiber volume fraction, based on total concrete volume, respectively. This total fiber volume fraction of 2% is greater than the total volume fraction of 1.5% typically associated with HyFRC, which has been suggested as an upper design limit for cast-in-place construction due to the tendency of fiber clustering and fresh concrete fluidity reduction caused by the inclusion of additional fibers [25]. The HyFRC for the tube column was able to exceed this critical fiber volume fraction as vibration equipment used during laboratory casting was able to mitigate the reduced workability caused by the fibers, mirroring the expected higher quality control and more varied casting techniques available in a concrete precasting facility as opposed to a field condition. A HyFRC with a greater fiber volume fraction may simultaneously be designed with a higher compressive strength while maintaining ductile behavior [71]. Because coarse aggregates, normally having a maximum size of 9.5 mm, were removed from the mix to better accommodate casting of the fresh HyFRC material through the tube's critical thickness of 64 mm, an increase in compressive strength was expected. The strength was further increased from the baseline design by reducing the water-binder ratio from 0.45 to 0.35.

Table 3-2: Batch proportions of HyFRC and concrete.

	Mass proportions (kg/m^3)					Chemical admixture dosage (wt. % total binder)		Fiber volume fraction (vol. % composite)	
	Cement	Fly ash	Water	Coarse aggregate	Fine aggregate	SP[a]	VMA[a]	PVA	Steel (30-mm length)
HyFRC	490	163	213	-	1306	1.09	1.59	0.2	1.8
Concrete	476	-	228	693	876	-	-	-	-

[a] SP and VMA refer to superplasticizer and viscosity modifying admixture, respectively.



Figure 3-3: Slump flow test result of fresh HyFRC.

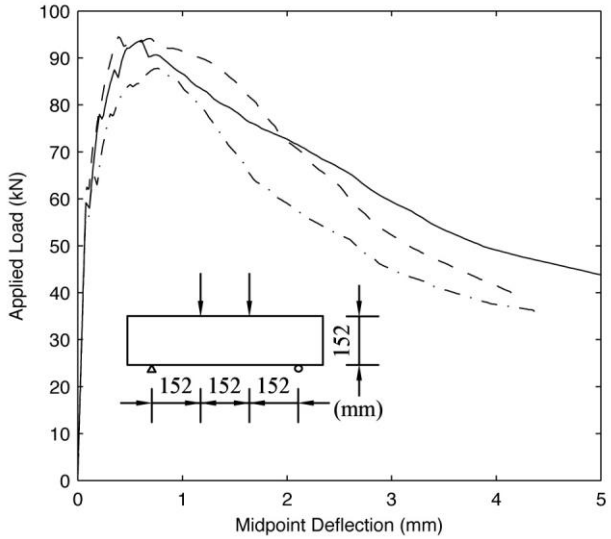


Figure 3-4: 4-point bending test results of HyFRC.

Mechanical testing of concrete materials occurred six days after large-scale structural testing of the tube column specimen. The HyFRC had a compressive strength (f'_c) of 66 MPa after 73 total days of curing. The strain at peak stress (ε_0) was -0.0042. Figure 3-4 shows 4-point beam bending test results. The beams had a square cross-section of 152 mm by 152 mm, with a length of 610 mm. The behavior of the beams satisfied the performance-based deflection-hardening criteria for HyFRC design as detailed in [24]. The plain concrete used for the interior of the column was designed with a nominal 28-day compressive strength of 35 MPa and had a water-binder ratio of 0.48. At an age of 46 days, it had a compressive strength of 44 MPa.

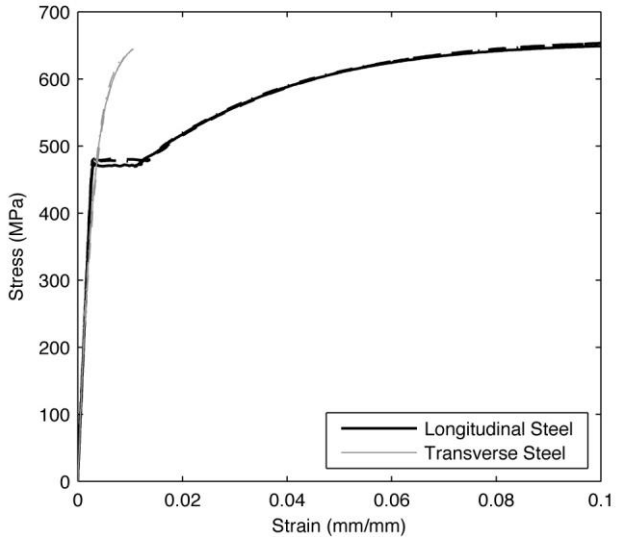


Figure 3-5: Tensile test results of reinforcing steel.

Figure 3-5 plots the stress-strain behavior of the reinforcing steel used for the column. The longitudinal reinforcement exhibited a yield stress of 480 MPa and an ultimate stress of 660 MPa. The spiral transverse reinforcement, which required straightening prior to testing, did not exhibit a yield plateau. The 0.01% proof stress of the spiral transverse reinforcement was 450 MPa at a strain of 0.0032 and the ultimate stress was found to be 640 MPa. Due to plastic deformation that occurred to allow direct tensile testing of the original spiral-shaped material, the yield strain of the spiral steel may have been overestimated.

3.2.3 Specimen construction

The tube column was constructed in the University of California, Berkeley, structural engineering laboratory in three primary stages:

1. After internal data instrumentation was applied onto the longitudinal rebar, the bars were wrapped for debonding and then assembled with the spiral reinforcement (Figure 3-6a). The tube was cast with HyFRC in a single batch with a volumetric yield of 0.26 cubic meters, which was prepared in the laboratory mixer. The corrugated steel duct provided permanent formwork for the interior surface of the tube, while removable formwork was used for the exterior surface. The HyFRC was poured from the top elevation of the tube and flowed to its base with the aid of vibration equipment. After 14 days of curing, the outer formwork was stripped, revealing no significant defects or voids.

2. The precast tube was installed into the foundation block after 18 total days of curing. A crane was used to hoist and position the tube such that the bottom surface of the tube would be coincident with the foundation's top finished surface (Figure 3-6b). Concrete for the foundation was provided by a mixing truck.
3. After the foundation cured for 9 days, the hollow tube was filled with plain concrete. Figure 3-6c shows the specimen prior to the casting of its interior. The concrete was produced in the laboratory mixer in a single batch. At the time of column testing, the tube HyFRC, foundation concrete, and column interior concrete had an age of 67 days, 49 days, and 40 days, respectively.



(a) (b) (c)

Figure 3-6: Tube column during construction: (a) Steel reinforcement prior to casting of tube, showing duct tape used for rebar debonding; (b) Precast HyFRC tube aligned prior to casting of foundation; (c) Overhead view of specimen prior to casting of its hollow interior.

3.2.4 Lateral loading

The column was tested under static, uni-directional, cyclic loading. Two horizontal actuators, inclined at 45 degrees in the direction of displacement, were used to apply lateral load to the column (Figure 6). To simulate gravity load, a constant vertical load (P=445 kN) was applied onto the column through a steel spreader beam attached to two vertical actuators. The value of vertical load was selected by setting P/f'_cA_g=0.1, using f'_c=35 MPa as the nominal compressive strength, which is common in bridge column design. A_g is the gross cross-sectional area of the column. Four post-tensioned rods were used to prevent uplifting of the foundation from the structural testing floor.



Figure 3-7: Column test setup: (a) Plan view details; (b) Global view.

The column was loaded cyclically in the east-west direction under a drift ratio-controlled protocol. The drift ratio θ is defined as the lateral displacement at the point of load application over the vertical distance from the same point to the column base. Table 3-3 summarizes the loading protocol of the column. Loading sequences up to peak drift ratio of θ=3.6% were tested in three consecutive cycles prior to increase in amplitude. All cycles after the peak drift ratio of 3.6% consisted of one cycle.

Table 3-3: Loading protocol.

Sequence (3 cycles)	Peak Drift Ratio (%)	Sequence (1 cycle)	Peak Drift Ratio (%)
1	0.15	10	4.2
2	0.30	11	4.8
3	0.44	12	6.0
4	0.60	13	7.1
5	1.2	14	8.3
6	1.8	15	9.5
7	2.4	16	11.3
8	3.0	17	13.1
9	3.6		

Strain gauges were placed along the longitudinal rebar within its unbonded length and were also placed on the transverse spiral steel near the base of the column. Within the unbonded region, linear variable displacement transducers (LVDTs) were placed in series along the column elevation on the north, south, west, and east faces. Wire potentiometers measured the translation of the column at the point of load application.

3.3 Results and discussion

3.3.1 Damage mitigation

The tube column showed excellent overall damage resistance during testing. Figure 3-8 shows the observed state of the southeast face of the column at the conclusion of select drift ratio cycles. Damage up to θ=4.8% was generally limited to hairline flexural cracks at elevations above the unbonded region and was negligible at the column base (Figure 3-8a-b). It should be noted that pens were used to trace all observed surface cracks during testing, with the pen widths not indicative of the actual crack openings produced. After θ=4.8%, no detectable crack propagation was observed for existing cracks away from the unbonded region of the column, though cracking could be detected at the column base (Figure 3-8c-d). Figure 3-9a-c shows the local observed state of the southeastern face of the column at increasing loading cycles. A splitting crack was initially observed on the southeast face of the column at θ=6.0% (b), being the first significant crack detected within the unbonded region of the column. Additional loading cycles continued to increase the crack width, which was the location of the most severe damage to the HyFRC (Figure 3-9c). On the northwest face of the column, damage consisted of very fine splitting cracks and a dominant crack was not observed (Figure 3-9d). Concrete cover spalling did not occur throughout the entirety of the test and visible lateral deformations of longitudinal rebar were also not detected at the conclusion of testing (after θ=13.1%), as shown in Figure 3-8d. A total of two longitudinal reinforcing bars was noted to have fractured, one each during the θ=11.3% and θ=13.1% cycles.

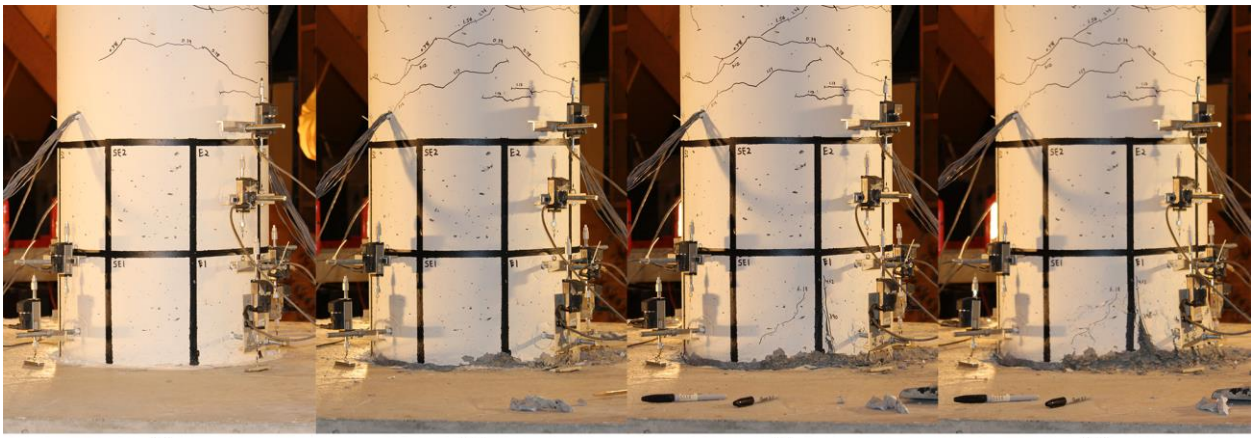


Figure 3-8: Observed state of southeast (SE) face of tube column at neutral position after completion of peak drift ratio θ: (a) θ=1.2%; (b) θ=4.8%; (c) θ=9.5%; (d) θ=13.1%. The painted gridlines on the column face are completely within the column's unbonded region. Observed cracks are traced with pens during testing.

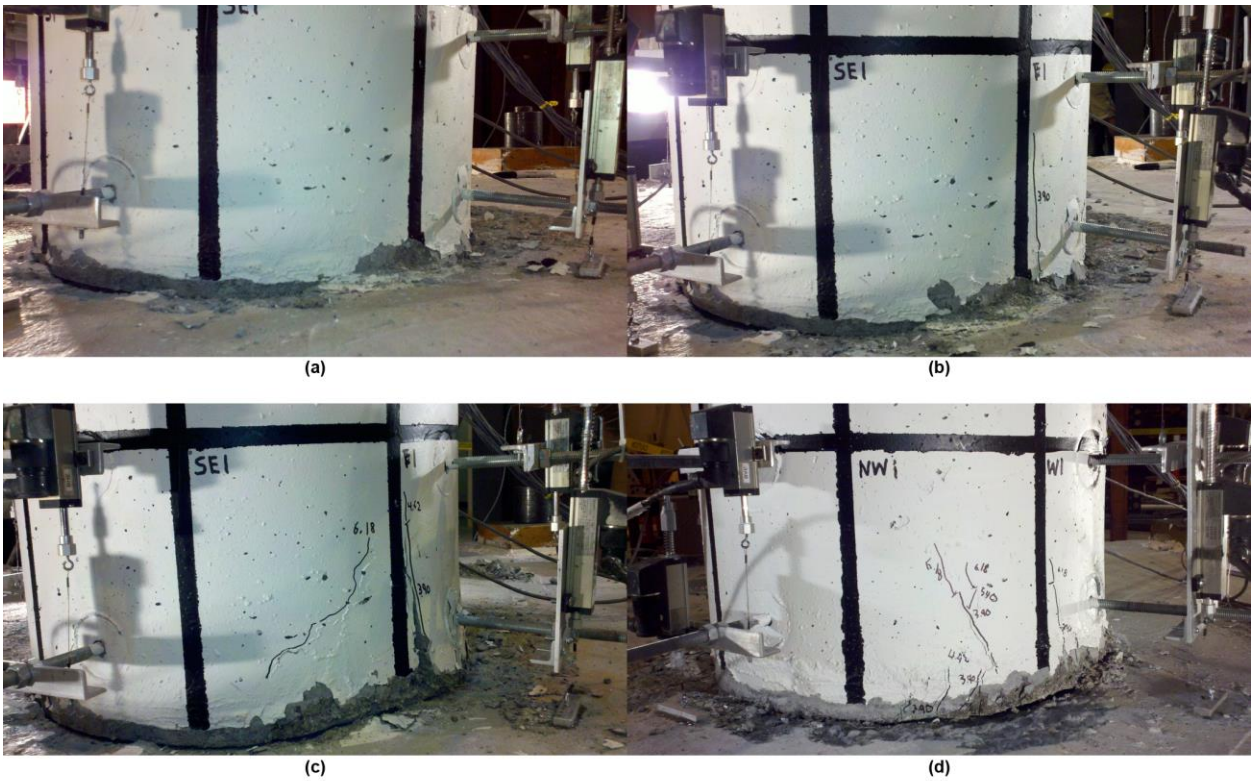


Figure 3-9: Observed local state of tube column at neutral position after completion of peak drift ratio θ: (a) Southeast (SE) face, θ=4.8%; (b) SE face, θ=6%; (c) SE face, θ=9.5%; (d) Northwest (NW) face, θ=9.5%. Observed cracks are traced with pens during testing.



Figure 3-10: Specimen Base45 after reaching a drift ratio of 3.9%. Based45 is reported by Terzic and Stojadinovic [72].

Terzic and Stojadinovic [72, 73] tested a conventionally designed and constructed bridge column (specimen Base45) with the same diameter, same longitudinal reinforcing ratio and similar transverse reinforcing ratio as the tube column. The column was tested statically, though had bi-directional lateral displacement. After the column reached a peak drift ratio of 3.9%, severe spalling was observed and cracking penetrated the concrete core, reducing its volume, as shown

in Figure 3-10. Seismic testing of Base45 ceased after this event. In statically loaded, circular RC bridge columns subjected to cyclic lateral displacement, longitudinal rebar buckling spanning several spiral spacings is expected in the load cycle immediately following the cycle in which complete cover spalling and exposure of reinforcement occurs [74]. Though the loading protocol for Base45 and the HyFRC tube column differed, the latter column was subjected to several additional cycles with peak drifts much higher than Base45's peak drift of 3.9% while having significantly less concrete damage.

3.3.2 Measured response

Figure 3-11 presents the lateral load versus drift ratio response of the tube column up to θ=6% and for the complete test. Positive lateral displacements correspond to eastward movement. The column reached a peak lateral load resistance of 120 kN during the drift cycle of θ=4.8%. The post-peak curve of the column showed only mild load resistance degradation up to θ=9.5%, revealing retention of over 90% of peak load capacity. During the sequence of θ=11.3%, the column maintained 83% of its peak resistance despite one of the 12 longitudinal bars fracturing. In conventional RC bridge columns, a general, though arbitrary, measure of column failure occurs when the lateral load resistance has reduced to 80% of its peak value [74]. The tube column did not meet this criterion until the final loading cycle, which had a maximum drift of θ=13.1%. During the entirety of the test, the applied gravity load of P=445 kN was resisted and did not significantly deviate.

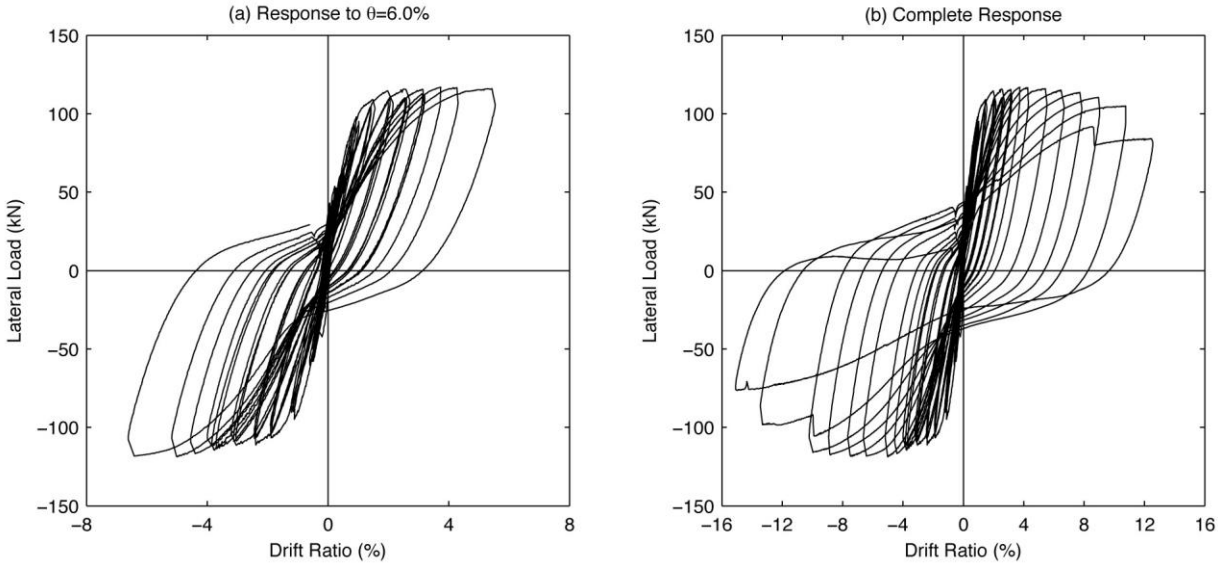


Figure 3-11: Lateral load versus drift ratio response: (a) Up to θ=6.0%; (b) Complete response.

The column base rotations, based on displacement transducer measurements located nearest the column-foundation interface, are plotted against the imposed drift ratio of the column in Figure 3-12 for drift cycles up to θ=7.1%. The response of a perfectly rigid column is shown in the plot as having drift ratios correlate to equivalent values of base rotation. The measured data shows good agreement with the idealized behavior, suggesting the debonding of the reinforcing steel was effective in producing the intended rocking behavior.

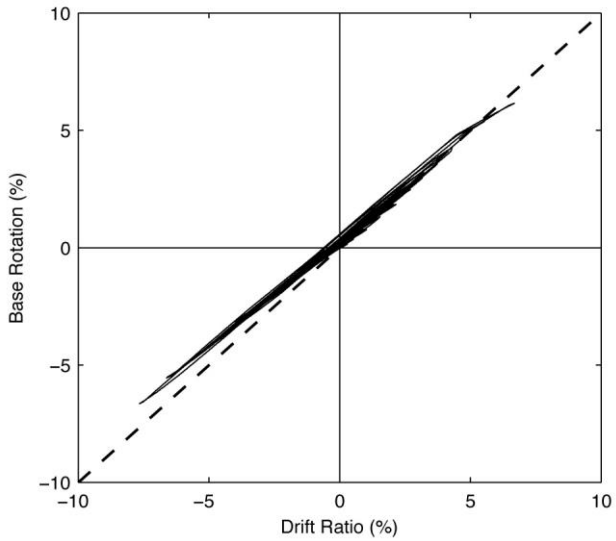


Figure 3-12: Base rotation versus drift ratio response up to θ=7.1%, with a reference line representing perfectly rigid column deformation.

Strain gauge measurements of rebar T10 are presented in Figure 3-13a. The location of the bar in the column's cross-section is identified in Figure 1a. The plot shows measurements taken at different elevations (h=102 mm and 203 mm) within the unbonded length of the rebar, showing good equivalency between the two sets approximately up to the completion of eastward movement during θ=4.8%. The similar strain values at different elevations on the bar suggest a uniform spread of plasticity in that domain, owing to the debonding of the rebar from the HyFRC matrix. During the load cycle of θ=4.8%, disparities in the minima of the measurements in rebar T10 become apparent, suggesting initial localized strain deformation. This nonuniform behavior was followed by the formation of a visible splitting crack formed near the location of rebar T10 in the next loading sequence (θ=6%) (Figure 3-9b), which coincided with softening of the lateral load resistance of the column (as shown in Figure 9). During the same cycle, the measured compressive strain of the west column face reached approximately ε=-0.0040 (Figure 3-13b), nearly matching the compressive strain at peak load of the HyFRC (ε_0=-0.0042). The results suggest the onset of lateral load softening is governed in part by macrocrack formation in the HyFRC cover.

Figure 3-14 shows the strain profile of the column's spiral transverse reinforcement at select drift ratio cycles. Strain gauges located on the western and eastern faces of the column are considered for the plot. The strain development in the spiral is minimal up to the drift ratio of θ=7.1% and the steel remains elastic up to θ=9.5% despite the column's peak lateral load occurring several load cycles prior (θ=4.8%). When a conventional RC column is in a compressive stress state, volumetric dilation of the concrete core against the transverse reinforcing steel causes a stress response in the transverse reinforcing steel, which in turn applies lateral confining stresses on the concrete core by the steel. These confining stresses improve the overall strength and ductility of the reinforced concrete [75] and the concrete core is defined as the volume of concrete enclosed by the transverse reinforcement. In the tube column, the corrugated steel duct confines and restricts volumetric dilation of the plain concrete interior, but does not confine the HyFRC. Insufficient composite material dilation perpendicular to the spiral steel's tangential direction resulted in delayed stress development in the steel, suggesting the HyFRC does not benefit from confinement by the transverse steel when the spiral steel itself is not stressed. Despite minimal strain development in the spiral steel, the high retention of residual peak lateral load, being 97% of its

peak resisted load at θ=7.1%, indicates satisfactory overall post-peak toughness with unconfined HyFRC. The result is consistent with the work performed by Trono [67], who reported that the compressive post-peak softening curves of spirally-confined reinforced HyFRC, up to transverse reinforcing ratios of ρ_s=1.0%, had the same ductile response as reinforced HyFRC lacking transverse reinforcement, suggesting unconfined HyFRC composites can exhibit similar ductility as confined HyFRC composites under compressive stress.

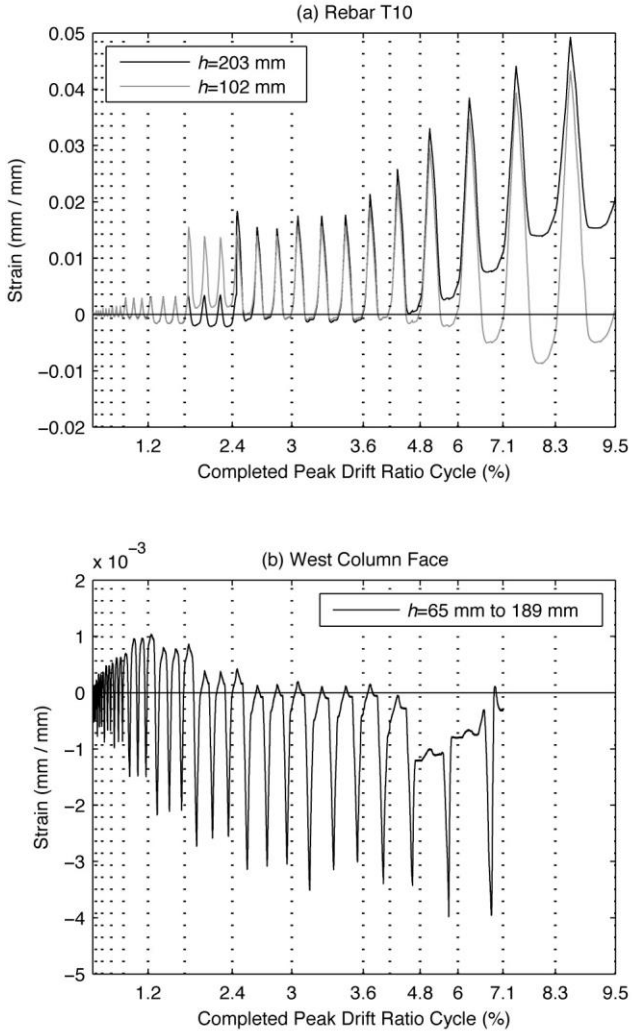


Figure 3-13: Strain measurements plotted as a function of testing time: (a) From strain gauges placed on longitudinal rebar T10; (b) From displacement transducers placed on west column face. The abscissa is labeled as the time when a sequence of drift ratio cycles has completed. Strain gauges are located at an elevation *h* above the column base. Displacement transducers have a gauge length located between indicated elevations *h* of column.

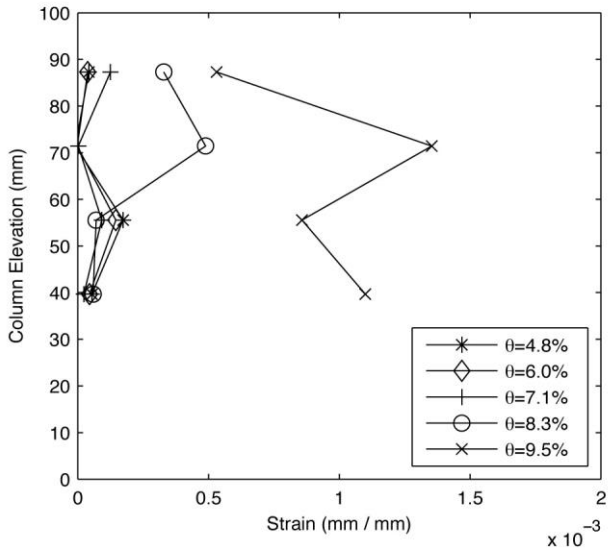


Figure 3-14: Strain profile of spiral steel transverse reinforcement. Strain measurements consider gauges located on western and eastern faces of the column, whose magnitude is taken as the greater of the strain measured during maximum lateral displacement in the westward or eastward direction.

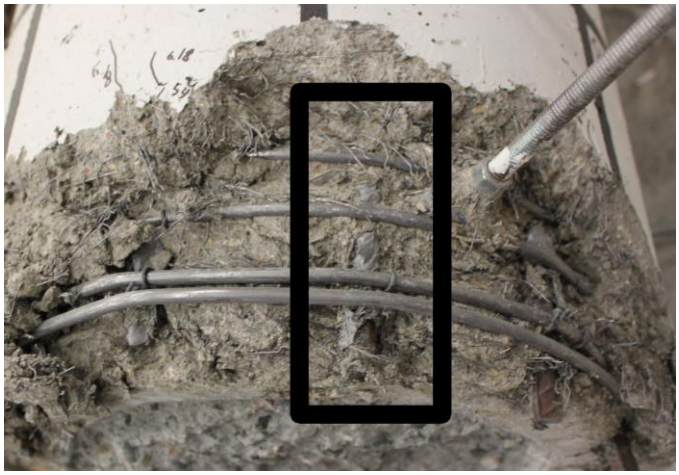


Figure 3-15: Observed final state of rebar T3 after manual removal of HyFRC cover.

Under high compressive strains, longitudinal reinforcement is susceptible to buckling after the concrete cover has cracked and spalled from a bridge column, resulting in load capacity degradation. Typically, lateral displacements of the longitudinal bars are restricted by the presence of transverse reinforcing steel. However, the aforementioned lack of measured strain in the spiral reinforcement of the tube column up to θ=7.1% further indicates insignificant lateral deformation of the longitudinal bars against the spiral reinforcement, which would otherwise produce a hoop stress in the spiral steel. It is suggested that lateral deformations of the longitudinal bars are restrained continuously along their lengths by the HyFRC, which showed no observable spalling damage due to its high crack resistance, rather than being restrained at discrete locations where the bar is in contact with the spiral steel. Figure 3-15 shows the effectiveness of the longitudinal rebar buckling restraint for rebar T3, which was located near the extreme western column face. Manual excavation of the HyFRC cover revealed the bar only having mild buckling deformation after the

conclusion of the test. Future design iterations of the tube column design may consider lowering the transverse reinforcing ratio due to the delayed contribution of the steel spiral towards concrete core confinement and longitudinal bar buckling as described.

The residual lateral load capacity of the tube column was relatively high compared to conventional RC bridge columns. The specimen designated as column 415 and tested by Lehman et al. [74] had a diameter of D=610 mm, longitudinal reinforcing ratio of ρ_l=1.5% and transverse reinforcing ratio of ρ_l=0.70%. The column was also tested under static, uni-directional cyclic lateral displacement. At the initial cycle with peak drift ratio of 5.2%, final cover spalling occurred and longitudinal rebar buckling was observed. A 20% reduction in peak lateral load capacity was measured at the third consecutive cycle with this same peak drift ratio. Use of HyFRC is thus advantageous for its spalling resistance and restraint against rebar buckling, which resulted in higher retention of peak lateral load capacity at higher drift ratios compared to column 415.

3.3.3 Comparison to a cast-in-place HyFRC rocking column

The performance of the tube column is compared to a column of similar design and loading protocol, but was cast entirely with a self-consolidating HyFRC in monolithic cast-in-place construction [27, 76]. The CIP HyFRC bridge column had the same diameter (D=406 mm), same reinforcing longitudinal reinforcing ratio (ρ_l=1.2%) and similar height (H=1708 mm) as the tube column. Additionally, the CIP column utilized a similar rocking mechanism as the HyFRC tube column by debonding of longitudinal reinforcement from the HyFRC within the expected plastic hinge region, though the length of debonding within the CIP column was 406 mm, which was 51 mm less compared to the precast HyFRC tube column. The transverse reinforcement of the tube column (ρ_s=0.87%) differed from that of the CIP column (ρ_s=0.37%). Both columns were subjected to similar seismic testing protocols, using static, uni-directional, cyclic loading at the same target peak drift values, though sequences at θ=3.0% and θ=13.1% were excluded from the testing program of the CIP column. The same magnitude of constant gravity load (P=445 kN) was also used.

The HyFRC used for the tube column had a greater fiber volume fraction (V_f=2% compared to V_f=1.5%) and greater compressive strength (f'_c=66 MPa compared to f'_c=35 MPa) than the self-consolidating HyFRC used for the CIP column. As previously described in Section 2.2, the HyFRC used for the tube column was designed with a greater total fiber volume fraction than typical HyFRC, despite a reduction in workability, due to the expected higher quality control available in a precasting facility. The strength of the HyFRC is allowed to increase due to the greater fiber volume fraction, as the composite maintained satisfactory deflection-hardening behavior. Despite differences in the HyFRC material properties between the two columns, comparison of the tube column and the CIP column is appropriate when considering how the method of column construction dictates the type of HyFRC that should be used, as a self-consolidating HyFRC is not required for fabricating precast elements, though would be beneficial for casting bridge columns at a construction site.

Use of a precast HyFRC tube appears to be an acceptable alternative construction method in lieu of conventional cast-in-place designs. Figure 3-16 shows the complete lateral load versus drift ratio response of the tube column and CIP column in superposition. The responses of the two columns are similar up to approximately θ=4.8%. The post-peak toughness of the precast HyFRC tube column is noticeably greater than that of the CIP HyFRC column, which was still ductile. At θ=7.1%, the tube column and CIP column maintained at least 97% and 80% of peak load

resistance, respectively. Further loading to θ=9.5% revealed poorer peak load capacity retention for the CIP column (61%) than the tube column (93%).

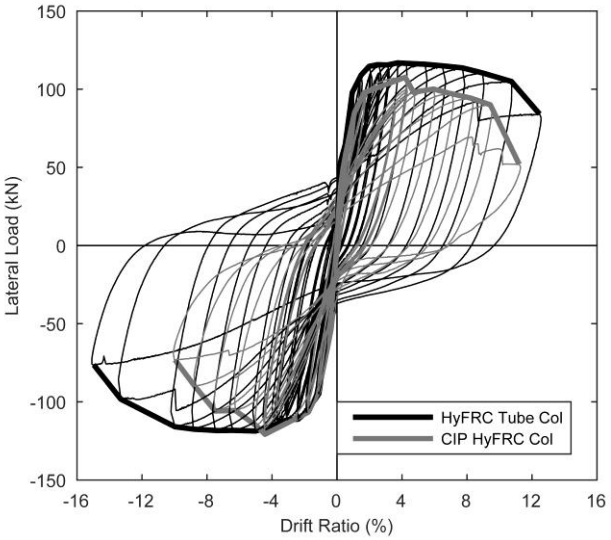


Figure 3-16: Lateral load versus drift ratio response of HyFRC tube column and cast-in-place HyFRC column [27], with envelope curves explicitly plotted.

The cover thickness of the columns appeared to influence the softening response of the columns. Because the precast tube element was designed such that the longitudinal and transverse reinforcing steel was located approximately at the tube's midthickness, the HyFRC cover in the tube column (25 mm) was greater than that of the CIP column (13 mm). During seismic testing of the CIP column, initial buckling of a longitudinal rebar was observed as early as θ=2.4%. The unexpected behavior was attributed to a construction flaw of locally thin HyFRC cover thickness (8 mm) where the buckling deformation occurred, highlighting the effect of cover thickness on buckling resistance. Four of the 12 total longitudinal reinforcing bars in the CIP column were visually observed to have some buckling deformation after reaching θ=7.1%. After completing the same drift ratio cycle, the tube column showed no visible rebar buckling behavior and the spiral reinforcement exhibited minimal strain development, indicating the HyFRC cover dominated the resistance against rebar lateral deformation. The ineffective response of the spiral steel also suggests a negligible effect of a higher transverse reinforcing ratio present in the tube column compared to the CIP column up to θ=7.1%.

Based on the load-drift ratio responses and observed damage of both the tube column and the CIP column, contribution of a deflection-hardening, spall-resistant HyFRC material to the overall toughness of a rocking bridge column is most effective when restraining longitudinal rebar buckling. The design of the tube column optimizes the use of HyFRC for this task, limiting the placement of a higher-strength HyFRC primarily around the longitudinal bars in the form of a precast tube element with an increased HyFRC cover. This optimized use of HyFRC in a precast tube, while using a plain concrete interior, may be considered a more economic and sustainable alternative due to the reduction of required HyFRC volume, while still maintaining satisfactory seismic performance. It should be noted that the CIP HyFRC column design remains a viable

option for bridge column construction due to its toughness enhancement compared to conventional RC columns, which is further detailed in [27].

3.4 Summary and conclusions

This chapter presents the seismic response of a precast hybrid fiber-reinforced (HyFRC) tube column detailed for accelerated bridge construction. The precast HyFRC tube, which contains all of the column's longitudinal and transverse reinforcement, expedites construction by eliminating onsite steel assembly for the column, eliminating temporary column formwork, and avoiding onsite casting of fiber-reinforced concrete. Compared to a monolithic column, the tube reduced HyFRC material volume consumption by 43% by specifically placing it where its damage-resisting benefits would be optimized, namely at the column base, where concrete compressive damage and rebar buckling are most likely to occur, and directly surrounding the column's steel reinforcement, for enhancing the column's resistance against steel rebar corrosion while in service. A base rocking design was used to eliminate flexural crack localization where the column's plastic hinge would typically occur, and the column was tested in under static, unidirectional, cyclic loading conditions up to θ=13.1%. The conclusions are as follows:

1. The tube column exhibited greater toughness during seismic loading compared to a monolithic cast-in-place (CIP) HyFRC column that had similar geometry, longitudinal steel reinforcing ratio, and rocking mechanism [27]. The lateral load-drift ratio response of the two columns were similar up to θ=4.8%. Continued testing at larger peak drift ratios revealed the HyFRC tube column having higher residual load capacity than the CIP HyFRC column – at θ=9.5%, the HyFRC tube column and CIP HyFRC column maintained 93% and 61% of their peak load capacity, respectively.
2. Compared to the conventionally designed reinforced plain concrete column Base45, which had similar geometry, longitudinal steel reinforcing ratio, and transverse steel reinforcing ratio [73], the HyFRC tube column exhibited superior damage resistance. The Base45 specimen had extensive spalling of cover concrete at its base after a peak drift of 3.9% had been reached. The HyFRC tube column did not show visible surface cracking at its base until θ=6%, which was in the form of minor splitting cracks. At the end of the test, the HyFRC tube column showed no spalling or visible rebar buckling.
3. The presence of an internal steel corrugated duct, which was necessary for fabrication of the precast tube element, confined and restricted the volumetric dilation of the enclosed plain concrete, resulting in a minimal strain response of the spiral transverse reinforcement up to θ=7.1%. HyFRC in the column does not receive lateral confining stresses from the transverse reinforcement to at least that drift cycle.
4. Use of HyFRC improved the overall toughness of the column by resisting longitudinal rebar buckling. The lack of strain development in the transverse spiral steel at drift ratios up to θ=7.1% further suggests lateral deformations of the rebar were restrained continuously along the HyFRC, rather than at discrete points where the longitudinal bars were in contact with the spiral reinforcement.
5. Rocking behavior eliminated flexural cracking where debonding of the longitudinal rebar from the HyFRC was defined. Strain in rebar T10 was nearly equivalent over a 102 mm unbonded length up to θ=4.8%, suggesting distributed plasticity.

4 Electrochemical polarization behavior of HyFRC composites

4.1 Introduction

In the previous chapter, the use of HyFRC in bridge columns improved the overall damage resistance and toughness of the structural element during seismic loading. However, other sources of damage exist for bridge columns, most notably long-term chemical attack, which causes substantial damage and may reduce the load capacity of a column prior to an earthquake [77-79]. While a number of environmental durability phenomena exist for reinforced concrete, the corrosion of embedded reinforcing steel is highlighted in this and succeeding chapters.

Steel corrosion requires an electrochemical cell consisting of an anode, a cathode, an electronic path, and an ionic path. The anode surface is the corroding metal surface and is where oxidation of Fe takes place. To balance the oxidation reaction, different reduction reactions may take place, depending on the pH of the electrolyte solution and the abundance of dissolved oxygen available for reduction. Table 4-1 summarizes the oxidation and common reduction reactions associated with steel corrosion. The environment of a steel reinforcing bar embedded in concrete satisfies the criteria for corrosion of the bar to occur, as shown in Figure 4-1. Concrete is a porous material which contains pores saturated with a high pH solution (ca. 13.0 to 13.5). This basic pore solution allows the concrete to act as an electrolyte, satisfying the necessary ionic pathway for ferrous ions (Fe^{2+}) to travel, while an electronic path occurs through the bulk steel. The cathodic reaction for reinforced concrete is commonly assumed to be under a basic solution with a sufficiently high dissolved O_2 content, and is given by $O_2 + 2H_2O + 4e^- \rightarrow 4OH^-$.

Table 4-1: Oxidation and reduction reactions for steel corrosion.

Reaction	Solution	Low O_2	High O_2
Oxidation	-	$Fe \rightarrow Fe^{2+} + 2e^-$	
Reduction	Acidic	$2H^+ + 2e^- \rightarrow H_2$	$O_2 + 4H^+ + 4e^- \rightarrow 2H_2O$
	Neutral / Basic	$2H_2O + 2e^- \rightarrow H_2 + 2OH^-$	$O_2 + 2H_2O + 4e^- \rightarrow 4OH^-$

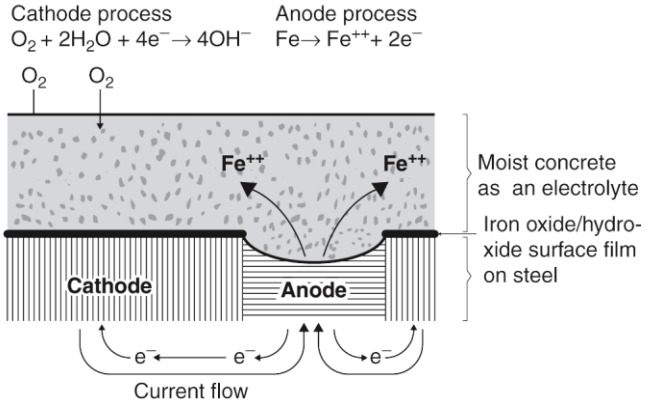


Figure 4-1: Schematic of corrosion process in reinforced concrete. Image is reported by Mehta and Monteiro [80].

While the necessary conditions for rebar corrosion are present in reinforced concrete, the high pH of the surrounding concrete pore solution results in the spontaneous formation of insoluble iron oxides. These products form what is referred to as a passive film on the steel rebar surface,

and greatly hinder corrosion damage (i.e., mass loss) of the steel. However, two primary causes have been identified to destabilize the passive film. The first cause is related to atmospheric carbon dioxide (CO_2) diffusion through the cementitious matrix. CO_2 reacts with alkalis in the concrete pore solution and lowers the pH of the solution in a process known as carbonation [81]. When the pore solution pH is reduced to a critical value, the passive film is no longer stable and corrosion may readily occur. The second, more common cause is related to chloride ion (Cl^-) diffusion through the cementitious matrix. When a sufficient amount of Cl^- is present at the steel rebar surface relative to the pH of the pore solution, the passive film may be stabilized despite the pH remaining high [6, 7]. In this dissertation, work related to chloride-induced depassivation is considered and investigated. Reinforced concrete structures vulnerable to chloride attack, such as those located near ocean saltwater or exposed to deicing salts placed on roadways during icy or snowy weather conditions, are particularly vulnerable to corrosion damage and includes bridge structures. The time from the onset of structure operation to corrosion initiation is often referred to as the corrosion initiation phase, while the subsequent phase is known as the corrosion propagation phase [82].

When steel rebar corrodes within reinforced concrete, the corrosion products that form occupy a greater volume than the volume of the parent metal [80]. This internal expansive growth of products at the rebar-matrix interface may place hoop stresses on the surrounding matrix after a sufficient volume of products has been formed. Because conventional concrete has poor crack resistance, stresses induced by corrosion product growth may exceed the cracking strength of the matrix and cause physical damage. The most basic form of protection against corrosion damage for all reinforced concrete structures is the concrete cover, which is the thickness of concrete from the surface of steel reinforcement to the nearest exterior concrete surface [83] and slows the diffusion of Cl^- and O_2 to the rebar surface. However, when the formation of corrosion products cracks the concrete cover, as shown for a reinforced concrete bridge in the state of Delaware in Figure 4-2, deleterious compounds may readily reach the rebar surface through the crack openings [9, 84, 85], maintaining or increasing the corrosion rate of the rebar. As the primary functional purpose of reinforced concrete in bridge structures is to resist load, corrosion damage is especially hazardous due to its impact on the structural capacity of the composite [86, 87].



Figure 4-2: Photograph of a reinforced concrete bridge in the state of Delaware with corrosion-induced damage. Photograph is reported by the Delaware Department of Transportation [88].

Due to the dependency of reinforced concrete durability on the cracked state of the composite, research of potential applications of novel crack-resistant construction materials has gained popularity in recent decades [89]. In particular, use of hybrid fiber-reinforced concrete (HyFRC) has been hypothesized as a method to reduce corrosion-induced cracking damage due to the mechanical toughening caused by the inclusion of different types of short, discontinuous fibers dispersed throughout the cementitious matrix [25, 34, 52]. A crack-resistant composite such as HyFRC is further desired considering the primary functional purpose of reinforced concrete is to resist mechanical loads, requiring any new implemented construction material to not only be damage-resistant towards corrosion-induced cracking, but also structural loading, especially in seismic regions [27, 28]. An increase in the time to corrosion initiation has been observed when using HyFRC over conventional concrete after subjecting samples to flexural stress [32, 33]. While a decrease in the corrosion current density i_{corr} of reinforced HyFRC was measured compared to reinforced concrete, indicating favorable performance after active corrosion has begun, electrochemical characteristics of samples were limited to corrosion potential, polarization resistance, and corrosion current density based on assumed Stern-Geary coefficients. Other corrosion-related studies with different types of fiber-reinforced concrete have employed similar techniques [90-93], making detailed information on electrochemical behavior, such as from Tafel polarization and electrochemical impedance spectroscopy (EIS), rarely available for fiber-reinforced cementitious composites.

As mentioned, i_{corr} is an experimental parameter that is often of interest when evaluating the corrosion behavior of reinforced concrete, and may be calculated using the Stern-Geary equation if the Stern-Geary coefficient B and the polarization resistance R_p are known [94]. For reinforced concrete-related research, a number of researchers have relied on the assumed values of B=52 mV and B=26 mV for passive and active steel reinforcement, respectively, referencing the paper of Andrade and González [95] published in 1978, which considered a comparison between gravimetric steel mass loss and electrochemical mass loss based on time-integration of i_{corr} measurements. While the authors did not propose values for the cathodic (β_c) or anodic (β_a) Tafel coefficients, Chang et al. [96] noted that B=52 mV may be obtained by setting β_c=120 mV/decade and allowing β_a to reach infinity. Similarly, B=26 mV may be obtained by letting both Tafel coefficients be equivalent to 120 mV/decade. Though not mentioned, the assignment of β_a=120 mV/decade may be attained by evaluating the definition of the anodic Tafel slope (Equation 4-1) under standard temperature T and setting the product $\alpha_a n$=0.5, where α_a is the anodic charge transfer coefficient and n is the number of transferred electrons involved in a rate-determining step. Additionally, R is the universal gas constant and F is the Faraday constant. A similar determination of β_c=120 mV/decade may be performed by allowing $\alpha_c n$=0.5, where α_c is the cathodic charge transfer coefficient. It is unclear whether an assumption of equivalent αn products is valid regarding the kinetics of cathodic and anodic processes in reinforced concrete.

$$\beta_a = \frac{2.303RT}{\alpha_a nF} \qquad \text{Equation 4-1}$$

Elsewhere in the literature, reported values of β_c, β_a, and B have generally been inconsistent, as surveyed in Table 4-2. Using a variety of specimen types and exposure durations, several authors have found the cathodic Tafel coefficient in active samples to be in the approximate range of 100 to 250 [97-100], as well as the greater range of 300 to 450 [100, 101]. Anodic Tafel coefficients of corroding steel have shown more skew, ranging from 230 mV/decade to values approaching

infinity [97, 100, 101]. While *B* values for active corrosion have been determined in the range of 7.1 to 14.9 [102], greater values of 43 to 86 have also been reported [97, 100]. Cracking damage of samples, if any, were not reported in several studies despite exceeding durations in excess of 2 years [99-101]. Babaee and Castel [97] noted no corrosion-induced cracks were observed around the embedded steel rebar at the conclusion of experiments while Grubb et al. [102] observed microcracking in plain mortars but no cracking in fiber-reinforced mortars. Due to the aforementioned influence of cracking on the durability of reinforced concrete, as well as varied polarization results in the literature, a study detailing the electrochemical behavior of reinforced concrete with cracking damage is warranted to better understand the processes that occur while embedded steel rebar are corroding.

Table 4-2: Survey of Tafel coefficients and Stern-Geary coefficients of reinforced concrete.

Reference	Binder type[1]	Total exposure duration	Consideration of cracks in sample	Passive			Active		
				β_c (mV/dec)	β_a (mV/dec)	*B* (mV)	β_c (mV/dec)	β_a (mV/dec)	*B* (mV)
Babaee and Castel [97]	FA, ultra-fine FA, GGBFS, NaOH solution, Na_2SiO_3 solution	336 days	Yes – No cracks found	30-45	Inf.	13-20	106-221	430-Inf.	43-69
Chang et al. [100]	C, FA	4.7 years	No	-	-	-	192-263	450-800	63-86
	C, GGBFS			-	-	-	235-480	230-295	52-62
Alonso et al. [101]	OPC	6 years	No	-	-	-	441 (Ambient) 289 (Damp)	10^{20}	-
Glass and Chadwick [99]	OPC	30 months	No	-	-	-	160	-	-
	OPC, GGBFS								
Andrade and González [95]	OPC	30 days	No	-	-	52	-	-	26
	Slag cement								
	Pozzolanic cement								
Grubb et al. [102]	OPC	22 weeks	Yes – Microcracks found in plain mortar; No microcracks found in fiber-reinforced mortar	-	-	-	-	-	7.1-9.6 (Plain)
									8.1-14.9 (Fiber-reinforced)

[1] OPC refers to ordinary portland cement, FA refers to fly ash, GGBFS refers to ground granulated blast-furnace slag, and C refers to unspecified cement.

The research presented herein investigates the long-term influence of concrete cracking on the electrochemical behavior of reinforced concrete and reinforced HyFRC in chloride environments. Prismatic samples containing a single strand of steel reinforcing bar were subjected to external NaCl solution intrusion conditions for approximately 2.5 years, during which corrosion potential measurements, linear polarization testing and Tafel polarization testing were periodically performed to monitor changes in corrosion activity. EIS was performed at the conclusion of the environmental conditioning period to evaluate changes in the impedance responses due to accumulated matrix cracking damage. To simulate the matrix cracking that may occur while reinforced concrete structures are in service, the samples were subjected to a maintained applied tensile load prior to, and during, exposure to the corrosion-inducing conditions.

4.2 Materials and methods

4.2.1 Concrete materials

The batch proportions for the HyFRC in this study are presented in Table 4-3 and is the same as the proportions used for the experiments reported in Chapter 2. The total fiber volume fraction, based on total composite volume, was 1.5% and the hybridization of fibers consisted of 0.04 mm-diameter, 8 mm-long polyvinyl alcohol (PVA) fibers, 0.55 mm-diameter, 30 mm-long hooked-end steel fibers, and 0.75 mm-diameter, 60 mm-long hooked-end steel fibers. The HyFRC was evaluated against a conventional concrete mixture having the same water-cement mass ratio of 0.54 as HyFRC but lacking fiber reinforcement. After casting of the fresh mixtures, concrete and HyFRC specimens were cured within molds for 7 days and covered with wetted burlap, demolded, and cured an additional 21 days in ambient laboratory conditions (approximately 23.5° C, 45% relative humidity), matching a similar curing method by Blunt and Ostertag [52] for the development of HyFRC. Standard compression testing of cylinders with a 100-mm diameter and 200-mm height revealed that the concrete and HyFRC had similar 28-day compressive strengths of 42.6 MPa and 44.2 MPa, respectively.

Table 4-3: Batch proportions of HyFRC.

Composite	Mass proportions (kg/m^3)				Fiber volume fraction (vol. % composite)		
	Cement	Water	Coarse aggregate	Fine aggregate	PVA	Steel (30-mm length)	Steel (60-mm length)
HyFRC	423	228	775	853	0.2	0.5	0.8

4.2.2 Specimen design

Geometric detailing of the specimen design is presented in Figure 4-3a. The rectangular prisms had a length of 610 mm and a square cross-section with side lengths of 127 mm. A single ASTM A706 [54] mild steel reinforcing bar with a nominal yield stress of 410 MPa and a nominal diameter of 16 mm was placed centrally within the specimen's cross-section. Prior to the casting of specimens, the mill scale of the rebar was removed by sandblasting to disregard variable effects of corrosion due to that layer [103]. The middle 406 mm length of rebar was defined to be the region of interest where corrosion was allowed to occur, and was bonded directly to the cementitious matrix during casting. Elsewhere, the reinforcing bar was coated with an electrically-insulating lacquer and then tightly wrapped with vinyl electrical tape to prevent physical contact with concrete. The extruded portions of the steel bar were threaded to allow for later tensile loading. A loading frame consisting primarily of light-gauge perforated tube steel was constructed such that the specimen would be allowed to remain in a stressed state while the frame would resist reactionary forces (Figure 4-3c).

Ponding of NaCl solution through the concrete cover was achieved by fixing a polyvinyl chloride ponding dam to a face of the prismatic specimens using a rubber cement adhesive, as in Figure 4-3b. All vertical concrete surfaces, along with the horizontal surface not enclosed by the adhered dam on the ponding surface, were coated with a moisture-resisting sealant to prevent leakage of sodium chloride solution during experimentation. As summarized in Table 4-4, a total of 4 specimen types were studied, varying in composite type (concrete (C) or HyFRC) and loading condition during environmental conditioning (not loaded (0) and loaded (L)).

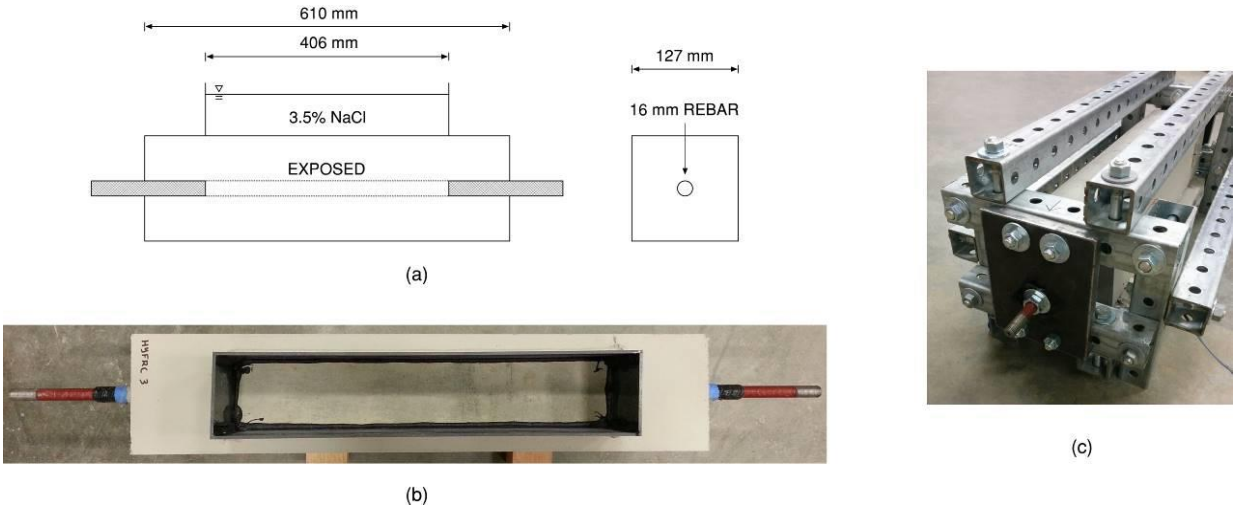


Figure 4-3: Details of specimen design: (a) Geometric drawing; (b) Plan view of specimen with ponding dam fixed to concrete surface; (c) Specimen in loading frame.

Table 4-4: Specimen type designation.

Composite	Not loaded	Maintained load
Reinforced concrete	C-0	C-L
Reinforced HyFRC	HyFRC-0	HyFRC-L

4.2.3 Tensile loading

Select specimens of each composite type were prescribed for tensile loading during chloride exposure to account for serviceability loading of reinforced concrete, which always includes gravity loading from the weight of supported structures, as well as temporary loading such as vehicle traffic and seismic events. American building design codes allow concrete cracking to occur prior to reaching the designed limit state of a structural element [83]. The setup for loading is shown in Figure 4-4a while a schematic of the loading procedure is presented in Figure 4-4b. To load the specimens, a hydraulic pump was used to longitudinally displace one end of the steel rebar, resulting in a tensile stress and strain response along the composite specimen. The other, opposite end of the extruded rebar was anchored and fixed against a steel plate. After a load of 53 kN was reached, corresponding to 65% of the reinforcing bar's nominal yield load, a nut located near the bearing plate where the hydraulic pump was positioned was tightened against the plate, transferring the point of force application on the rebar from the hydraulic pump to the nut. To prevent any effects of galvanic coupling between the extruded steel reinforcing bar and the steel loading frame, the frame's bearing plates were coated with an electrically-insulating spray solution and covered with vinyl electrical tape where the extruded rebar or bearing nut was to be in direct contact with the plate.

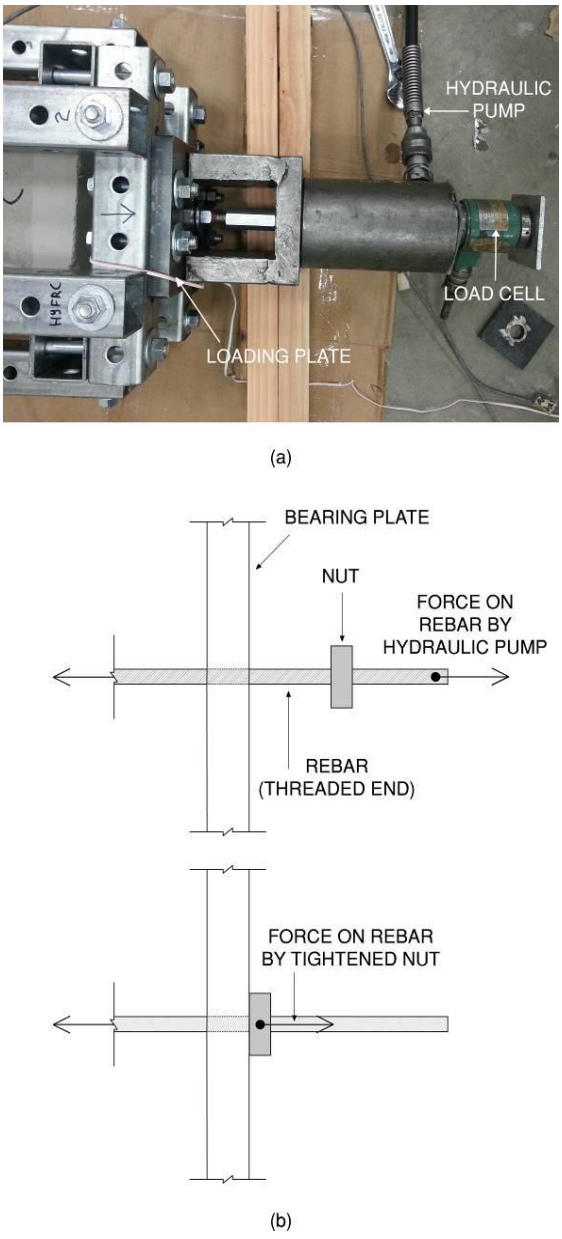


Figure 4-4: Specimen with loading frame: (a) During tensile loading, showing a hydraulic pump applying load onto the free end of the extruded reinforcing bar; (b) Loading schematic highlighting transfer of load on rebar from hydraulic pump to nut upon tightening of the nut.

4.2.4 Environmental conditioning

To allow for initial saturation of the concrete after curing in ambient laboratory conditions, specimens were externally ponded with 3.5% w/w NaCl solution for 13 consecutive weeks. Afterwards, the ponding dam was completely relieved of solution for 2 weeks, refilled with fresh solution for 2 subsequent weeks, and then repeated. This cyclic wet-dry cycling was continued to simulate field conditions where sodium chloride solution ingress into reinforced concrete is not a continuously occurring event. After 29 total weeks of environmental conditioning, the frequency

of the cycles was increased such that specimens were under drying conditions for 1 week, followed by wetting for 1 week. The total experimental corrosion monitoring time of the samples was 132 weeks, or approximately 2.5 years.

4.2.5 Electrochemical measurements

Corrosion activity measurements were taken periodically with a potentiostat in ambient laboratory conditions throughout the environmental conditioning period, with all measurements occurring while the specimen was in a ponded state. All tests utilized a 3-electrode setup, as shown in Figure 4-5, with the working electrode being the steel reinforcing bar of the specimen, the counter electrode being stainless steel, and the reference electrode being a saturated calomel electrode (SCE). The counter electrode and the reference electrode were immersed within the sodium chloride solution contained by the ponding dam. In a typical testing session, measurement of the corrosion potential E_{corr} was first performed with a duration of at least 10 minutes, during which E_{corr} was not to deviate by more than 1 mV versus SCE to ensure quasi-steady state conditions. Afterwards, linear polarization resistance tests, considering a potential domain of -10 mV to 10 mV versus E_{corr}, and Tafel polarization, considering a potential domain of -75 mV to 75 mV versus E_{corr}, were performed. The magnitude of overpotential selected for the Tafel scans was lower than the values of other researchers in reinforced concrete, which was equivalent to, or greater than, 120 mV [97, 100, 101]. Electrochemical impedance spectroscopy (EIS) was conducted at the conclusion of the environmental conditioning period. The frequency domain for testing was defined to be from 10 mHz to 100 kHz and the amplitude of the alternating current voltage was 10 mV.

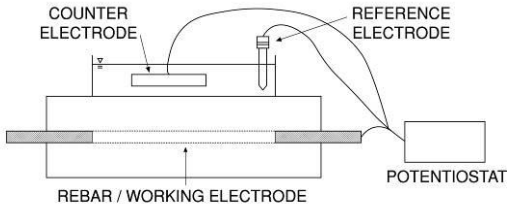


Figure 4-5: Electrochemical measurement setup using a 3-electrode setup. Stainless steel is used as the counter electrode and a saturated calomel electrode (SCE) is used as the reference electrode.

4.2.6 Destructive testing

After conclusion of the environmental conditioning phase, specimens were subjected to destructive tests to evaluate chemical, electrochemical, and physical changes caused by chloride intrusion and corrosion activity. After removing the ponding dams, cylindrical cores with a diameter of 29 mm were extracted from select samples using a coring drill press. For loaded samples, one core was taken directly over the applied load-induced macrocrack and a secondary core was taken 76 mm from the crack, as in Figure 4-6. Otherwise, a core was taken near the midlength of nonloaded samples. Coring initiated at the ponding surface and continued into the depth of the specimens, with the core drill positioned such that it would not make contact with the embedded reinforcing bar. The extracted concrete cores were cut into segments, each with a height of 25 mm, and pulverized such that the final material could pass a sieve with a maximum opening of 0.85 mm. The experimental testing standard of ASTM C1152 [104], utilizing potentiometric titration, was

performed to determine the acid-soluble chloride content of each pulverized sample, which is expected to be equivalent to the total amount of chlorides in the cementitious matrix. Because the test standard is specific to cement-based materials, steel fibers from HyFRC cores were manually removed after pulverizing to avoid possible artifacts introduced by oxidation of the steel fibers in acid solution. Remaining specimens not subjected to coring were prepared for optical cross-sectional imaging by sawing of the samples to produce a prismatic element, as schematically shown in Figure 4-7. Prior to sawing, all appreciable surface cracks were impregnated with a blue-colored, low-viscosity epoxy to maintain existing crack widths and minimize additional damage caused by the cutting process.

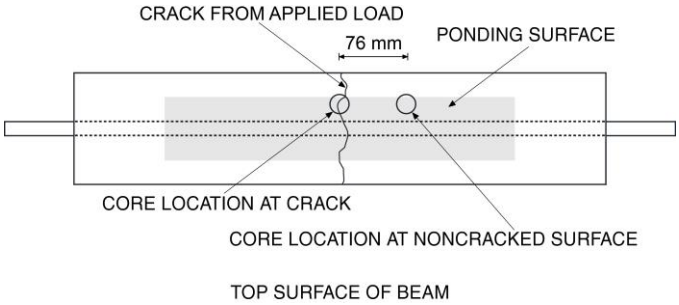


Figure 4-6: Schematic showing top, ponded surface of prism and coring locations of a loaded sample.

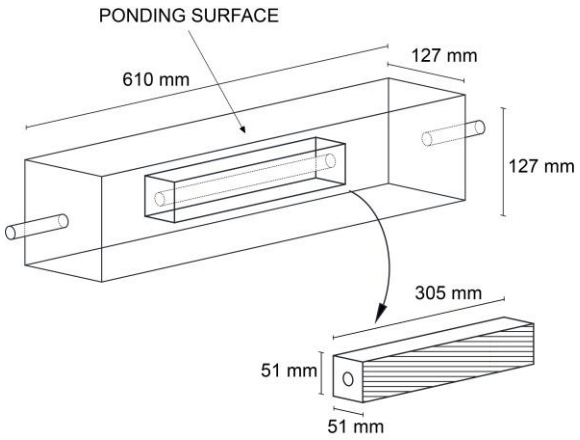
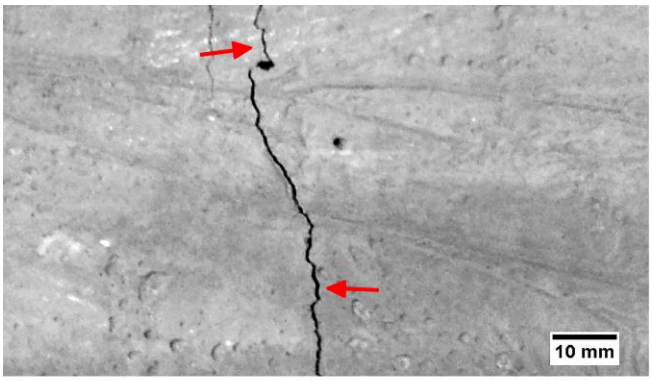


Figure 4-7: Schematic detailing prism extraction used for optical imaging. The hatched surface of the prism is the vertical surface shown as binary images in Figure 4-9 and Figure 4-10.

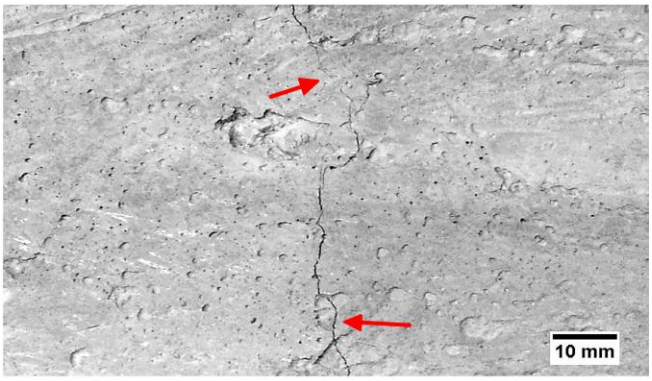
4.3 Results

4.3.1 Observed damage

Typical surface cracking of reinforced concrete and reinforced HyFRC, after application of an applied tensile load and prior to chloride exposure, is shown in Figure 4-8. Tensile macrocracks occurred near specimens' midlength with a maximum crack width of 0.42 mm and 0.22 mm for concrete and HyFRC, respectively. For the same magnitude of applied tensile load, a smaller maximum crack width in HyFRC is expected as a result of the crack control provided by hybrid fiber reinforcement [44].



(a) C-L



(b) HyFRC-L

Figure 4-8: Representative surface cracking after applied tensile loading and prior to environmental conditioning: (a) C-L; (b) HyFRC-L. Images are presented in grayscale to improve feature contrast.

Final accumulated damage of reinforced concrete and reinforced HyFRC at the conclusion of the 132-week environmental conditioning duration is shown in Figure 4-9 and Figure 4-10, respectively. The images were obtained from an extracted prism taken from a sample of each specimen type, as previously detailed in Figure 4-7. Binary images (Figure 4-9a, Figure 4-9f, Figure 4-10a, and Figure 4-10f) show a vertical surface, which was offset by 38 mm from the exterior surface of a sample. Observed macrocracks, shown in white, are contrasted from the matrix, shown in black, in these images and the mid-depth of the images coincide with the approximate mid-depth of the specimens, where the reinforcing bar were embedded. Colored lines on top of the binary images indicate the location of presented transverse section cuts. For instance, the transverse section cuts of sample C-0 are found in Figure 4-9b and Figure 4-9c and are located where the green lines occur in Figure 4-9a. In all transverse section images, surface voids and cracks are colored blue due to the impregnation of the samples with an epoxy containing a blue-colored pigment.

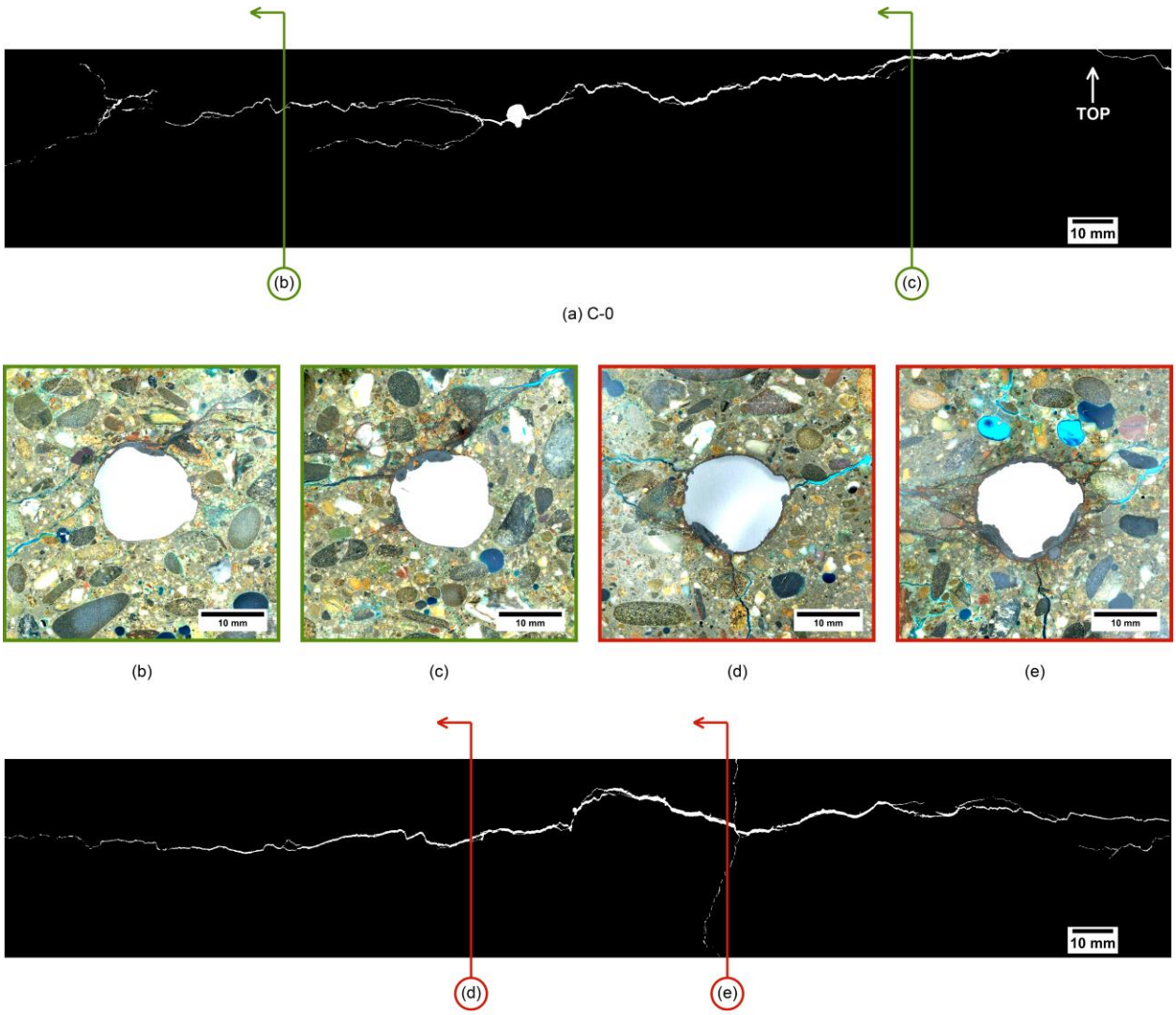


Figure 4-9: Sectional images of reinforced concrete specimens at the conclusion of environmental conditioning: (a)-(c) C-0; (d)-(f) C-L. Binary images are used to highlight crack locations on a vertical surface of the extracted prism (as in Figure 4-7). A blue-colored epoxy was used to impregnate cracks and voids in transverse section views.

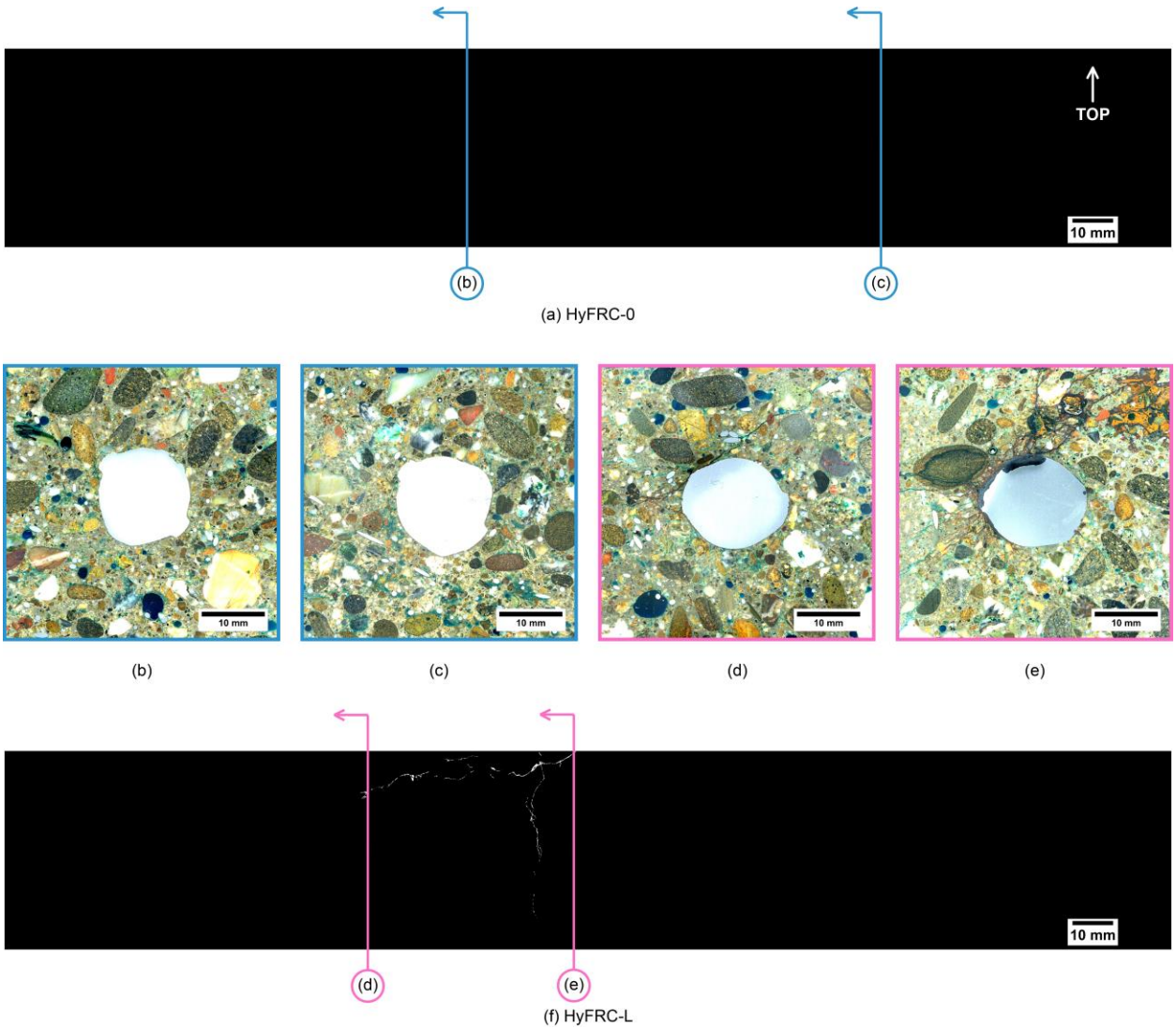


Figure 4-10: Sectional images of reinforced HyFRC specimens at the conclusion of environmental conditioning: (a)-(c) HyFRC-0; (d)-(f) HyFRC-L. Binary images are used to highlight crack locations on a vertical surface of the extracted prism (as in Figure 4-7). A blue-colored epoxy was used to impregnate cracks and voids in transverse section views.

Differences in the damage severity between concrete and HyFRC are noticeable. Matrix damage of reinforced concrete samples, regardless of applied loading state, was primarily characterized by splitting crack propagation over a considerable length of the specimens (Figure 4-9a, f). Splitting cracks are identified in a longitudinal view as cracks that form along the length of a sample and in a transverse view as cracks that form radially from the rebar. The presence of splitting cracks at a rebar surface generally coincided with a corroded rebar surface (Figure 4-9b-e), though it is unclear which event (i.e. matrix splitting crack propagation or rebar corrosion) preceded the other for a given transverse section. Regardless, the widespread propagation of these cracks allows a free path for external deleterious substances, such as NaCl solution and gaseous O_2, to reach the rebar surface away from the site of initial rebar corrosion and promote depassivation or further corrosion activity [105, 106].

In a nonloaded reinforced HyFRC-0 sample, no transverse or splitting cracks could be visually detected and rebar corrosion damage appeared negligible (Figure 4-10a-c). When loaded

and cracked, both rebar corrosion and matrix splitting cracks occurred for HyFRC-L (Figure 4-10d-f), though both the maximum splitting crack width and the extent of crack propagation along the sample length were less compared to reinforced concrete. A high splitting crack resistance is expected for HyFRC composites due to the inclusion of fibers [44, 50]. Where the splitting crack widths were fine, as in Figure 4-10d, steel mass loss was insignificant, indicating that rebar corrosion activity was generally limited to the site of the induced tensile crack near the section shown in Figure 4-10e.

4.3.2 Tafel polarization

Typical Tafel polarization curve fitting results of a passive and active specimen are presented in Figure 4-11, showing the fitted cathodic and anodic reaction curves and the net current produced by the two reaction curves. The intersection of the cathodic and anodic reaction curves is where the corrosion potential E_{corr} and the corrosion current I_{corr} occur. Generally, the most negative potentials of the raw data were ignored for fitting due to the uncharacteristically high current that occurred at these overpotentials, an experimental observation that was also noted by Chang et al. [96] Compared to an active response, a passive measurement is characterized by greater values of potential, lower values of current, and an anodic-dominated portion of the curve exhibiting a low-angle slope as plotted, which results from the passive regime of Fe exhibiting the same current for a certain domain of potential.

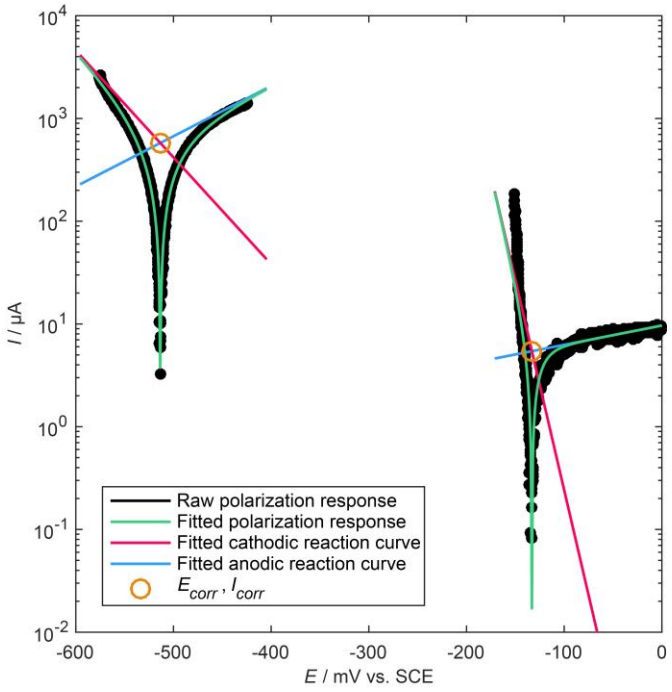


Figure 4-11: Typical fitting result of Tafel polarization curves for a passive sample (occurring at greater potentials) and an active sample (occurring at lesser potentials).

Cathodic and anodic Tafel coefficients βc and βa, respectively, are plotted in Figure 4-12 with E_{corr} labeled as the abscissa, while Table 4-5 summarizes the mean and standard deviation of βc, βc, and the Stern-Geary coefficient B. Two distinct clusters of data may be observed for each

subplot, generally separated by corrosion potentials greater than -100 mV versus SCE and lesser than -300 mV versus SCE. The former set of measurements are associated with passivated samples while the latter are associated with active samples. Determination of the cathodic Tafel coefficient for active samples revealed a mean of 102 mV/decade with a standard deviation of 9.74 mV/decade based on over 150 total measurements among all sample types. As no trend appears to exist between β_c and E_{corr} in the active regime, the same cathodic reaction likely occurred at all considered measurement periods and is assumed to be the reduction of oxygen in alkaline solution (Reaction 4-1). Correspondingly, the anodic reaction is the oxidation of Fe, as in Reaction 4-2.

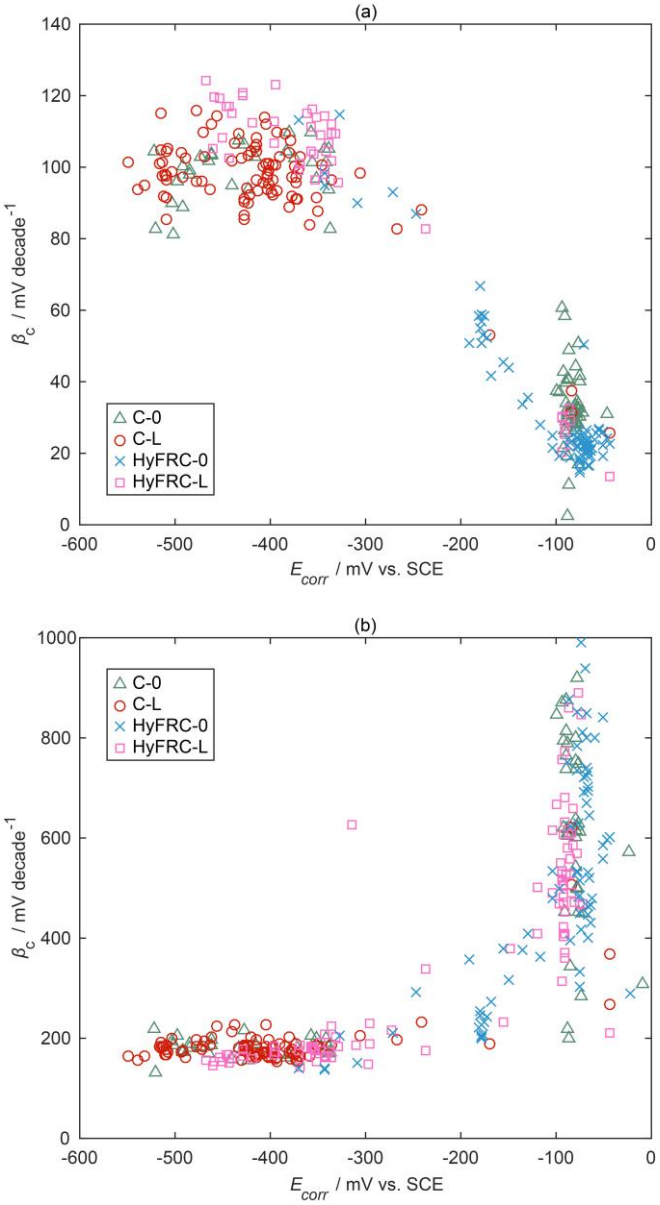


Figure 4-12: Tafel coefficients versus corrosion potential E_{corr}: (a) Cathodic Tafel coefficient β_c; (b) Anodic Tafel coefficient β_a.

Table 4-5: Summary of Tafel coefficients and Stern-Geary coefficient.

	Passive			Active		
	β_c (mV/dec)	β_a (mV/dec)	B (mV)	β_c (mV/dec)	β_a (mV/dec)	B (mV)
Mean value (standard deviation)	19.8 (4.26)	562 (201)	8.31 (1.81) 24.0[a]	102 (9.74)	180 (40.4)	28.1 (2.83)

[a] Adjusted mean value

$$\frac{1}{2}O_2 + H_2O + 2e^- \rightarrow 2(OH)^- \qquad \text{Reaction 4-1}$$

$$Fe \rightarrow Fe^{2+} + 2e^- \qquad \text{Reaction 4-2}$$

For active samples, a mean B=28.1 mV was found, which is similar to the well-cited value of B=26 mV proposed by Andrade and González [95] for reinforced concrete materials. Figure 4-13 plots the correlation between the corrosion current $I_{corr,S.G.}$ based on the Stern-Geary equation, which incorporates B directly, and the corrosion current $I_{corr,T.}$ found by extrapolation of fitted Tafel polarization responses. The dashed line in the plots is where equivalent measurements of $I_{corr,S.G.}$ and $I_{corr,T.}$ occur. For active samples, the corrosion current from both methods of derivation are similar in magnitude and the mean values showed reasonably good correlation (13.7% error). For passive samples exhibiting lower values of corrosion current, being approximately less than 10 μA based on either determination method, use of the Stern-Geary equation resulted in an underestimation of corrosion current compared to $I_{corr,T.}$ When minimizing the residual between the mean values obtained from each method, an adjusted Stern-Geary coefficient B=24.0 mV was found to be more appropriate for use regarding passivated samples.

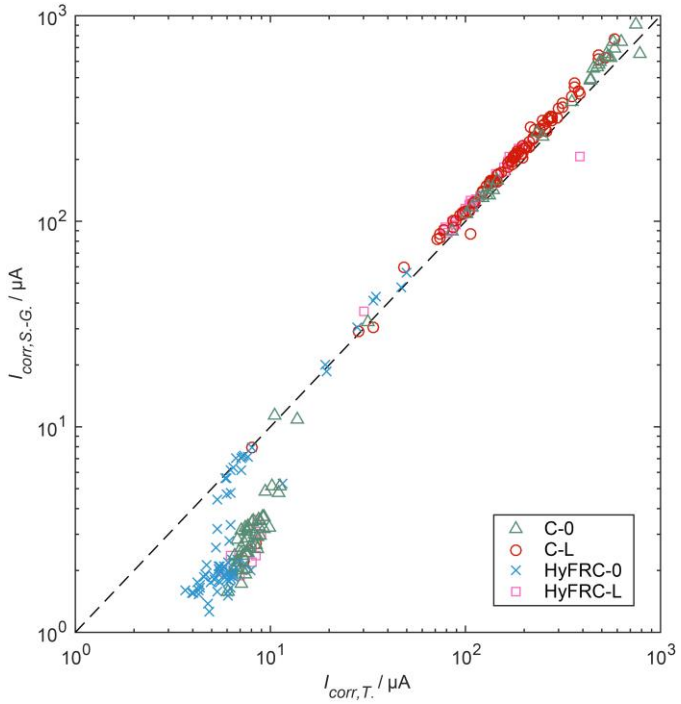


Figure 4-13: Correlation between corrosion current obtained between Stern-Geary equation $I_{corr,S.-G.}$ and Tafel polarization extrapolation $I_{corr,T.}$.

4.3.3 Corrosion rate monitoring

The averaged corrosion current I_{corr} of specimens are plotted as a function of elapsed environmental conditioning time t for the initial 12 weeks of experimentation and for the entire duration in Figure 4-14a and Figure 4-14b, respectively. The corrosion current measurements are based on $I_{corr,S.-G.}$, though presumably passive samples considered the adjusted Stern-Geary coefficient B=24.0 mV for calculation. In reinforced concrete research, the corrosion current density i_{corr} is often reported in the literature and is typically determined by normalizing I_{corr} by the nominal surface area of the rebar in contact with cementitious matrix. The actual corroding surface area of an embedded rebar is generally not known without the use of advanced materials characterization techniques. Considering the nonuniform corrosion activity of samples in this study, as previously visualized in Figure 4-9 and Figure 4-10, communication of the corrosion current density normalized by a constant active surface area may result in inaccurate interpretations of the actual corrosion current density of the samples.

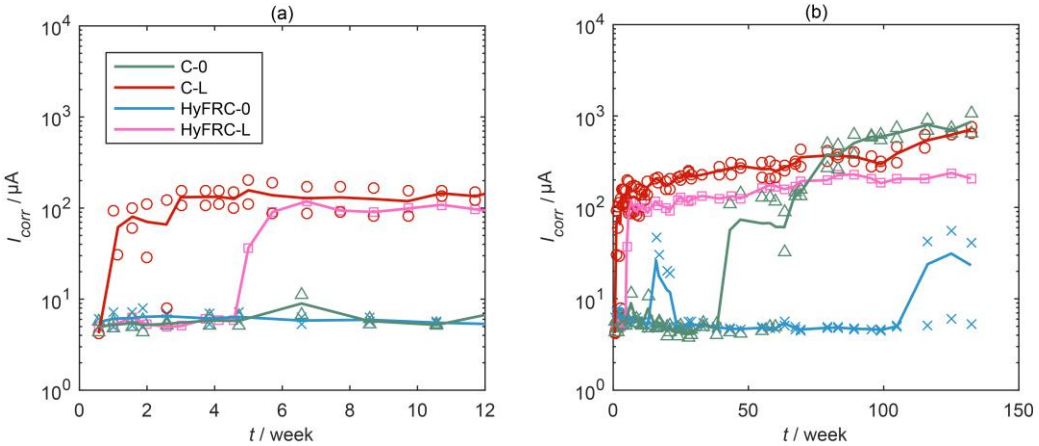


Figure 4-14: Corrosion current of samples: (a) During initial 12 weeks of environmental conditioning; (b) Complete experimental duration. Averaged responses of a specimen set are plotted as lines, while individual specimens are plotted as markers.

Initial corrosion activity of a sample was detected by an increase of I_{corr} on the order of one magnitude between consecutive measurements. Among all specimen types, loaded reinforced concrete samples (C-L) exhibited the earliest time to corrosion initiation, requiring approximately 1.0 week to become active. After 5.0 weeks, corrosion initiation was detected in loaded HyFRC-L, which was delayed compared to C-L due to the smaller crack widths produced in HyFRC upon loading. For nonloaded specimens, use of HyFRC was found to result in a significant delay in corrosion initiation time. Conventional reinforced concrete samples first exhibited active corrosion between 43.1 and 63.3 weeks, depending on the individual specimen. The additional delay of corrosion initiation for HyFRC composites was at least 41.7 weeks, equivalent to a delay factor of approximately 1.7.

Corrosion initiation time was influenced by the diffusion rate of chlorides through the cementitious matrix. Figure 4-15a and Figure 4-15b plot the chloride content C_{Cl^-} of reinforced concrete and reinforced HyFRC, respectively, as a function of depth d from the ponding surface of the specimens. The chloride content is the weight of chlorides normalized by the expected weight of cement binder in a tested sample. At the depth where the steel reinforcing bar was

centrally located (d=63.5 mm), the chloride content of C-L was 2.1% wt. binder at the cracked location and 1.7% at a noncracked location, highlighting the faster rate of chloride ingress where a crack was present and correlating with the shorter time to corrosion initiation of cracked samples compared to noncracked samples. For HyFRC specimens not containing a macrocrack, the chloride contents were found to be in the range of 0.38 to 0.61% wt. binder at the depth where the reinforcing bar was located, reduced from the chloride content found in noncracked conventional concrete at the same depth by a factor of at least 2.8. Because the concrete and HyFRC were designed with the same cement weight content and same water-cement weight ratio, differences in chloride binding from cement was likely negligible between composite types. The reduction in chloride penetration may then attributed to the presence of fiber reinforcement in sound matrices. The inclusion of PVA or steel fibers has been experimentally observed to retard the rate of chlorides in cementitious composites [107-109]. In the absence of macrocracks, use of hybrid fiber reinforcement may be used as an effective corrosion initiation retardant for its decrease in effective chloride permeation rate, though the precise influence of fibers on chloride diffusion requires further investigation.

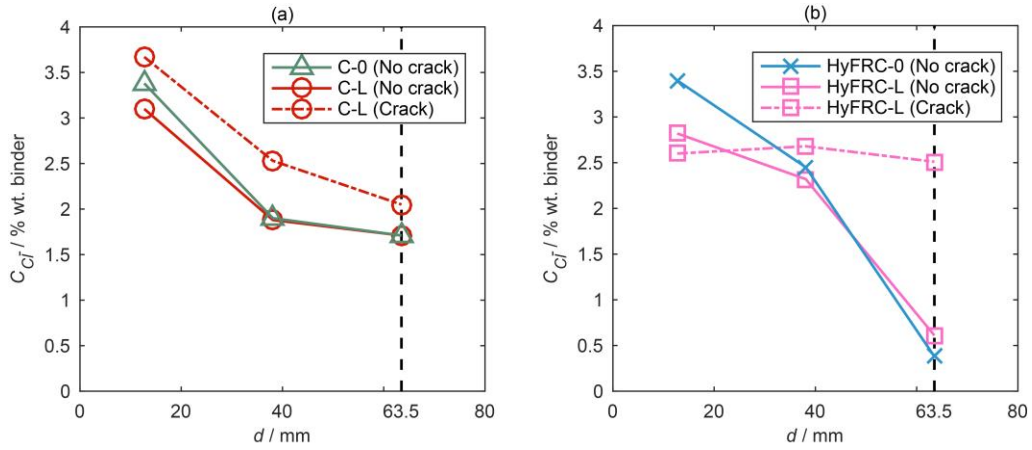


Figure 4-15: Chloride content profiles: (a) Concrete; (b) HyFRC. After specimen type designation, (Crack) refers to a core taken directly at an applied tensile load-induced crack location and (No crack) refers to a core taken at a location where no visible surface cracking at the ponding surface occurred. Dashed vertical line in plots indicates the depth where the centroid of the steel reinforcing bar occurred.

4.3.4 Electrochemical impedance spectroscopy

Selection of an appropriate equivalent circuit model for EIS results was dependent on the composite material of a sample. A circuit containing two time constants, as shown in Figure 4-16a, was suitable for modelling the behavior of conventional reinforced concrete, being similar to the models described by others in reinforced concrete-related research [110-114], though the interpretations of the individual circuit elements differ within the literature. Constant-phase elements (CPE) were used in the equivalent circuit to account for the nonideal behavior of capacitor elements. Its impedance Z_{CPE} is described by Equation 4-2:

$$Z_{CPE} = \frac{1}{Y_0(j\omega)^{\alpha}} \qquad \text{Equation 4-2}$$

Y_0 is the admittance modulus of an ideal capacitor, j is the imaginary unit, ω is the angular frequency, and α is an exponent ranging from 0 to 1. A value of 1 for α describes an ideal capacitor, while a value of 0.5 describes an infinite Warburg diffusion-controlled element. For this research, the element designated as CPE_{DL} represents the double-layer capacitance while the element R_{CT} accounts for the charge transfer resistance at the steel-solution interface. These two parallel elements are connected in series to the resistor R_{pit}, which accounts for the resistance within corrosion pits or crevices. The remaining constant phase element, CPE_{pass}, relates to the interfacial capacitance of the passive surfaces of the steel reinforcing bar. Finally, the resistance of the concrete solution within void defects such as pores and cracks is represented by the element R_{soln}. The assignments of the circuit elements are consistent with the proposed equivalent electrical circuit of Królikowski and Kuziak [112]. After unsatisfactory fitting of data from HyFRC samples to the described equivalent circuit, a constant phase element (CPE_{fiber}) was placed parallel to R_{soln} to account for steel fibers (Figure 4-16b), which act as conductive elements at intermediate to high EIS testing frequencies [115, 116]. The fitting results of the modulus of impedance and phase shift are shown in Figure 4-17, showing good correlation between the experimental and modelled results.

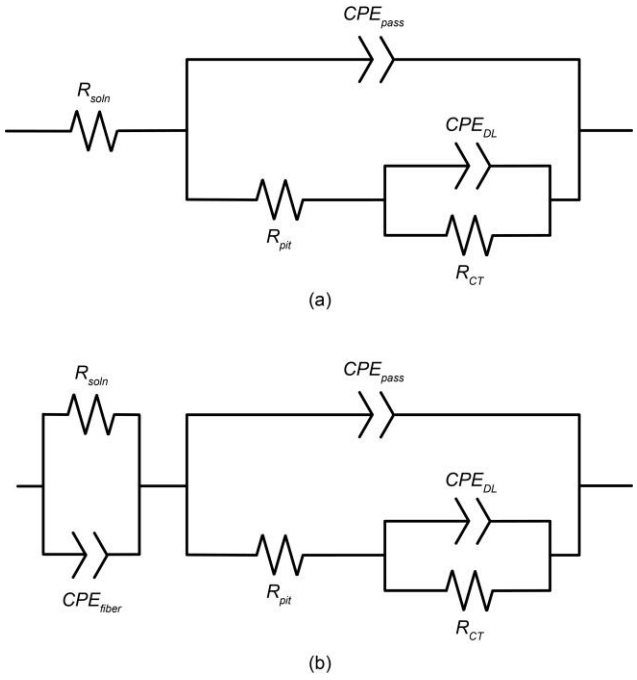


Figure 4-16: Equivalent electrical circuit model used for EIS results: (a) Reinforced concrete; (b) Reinforced HyFRC. CPE_{DL} represents the double-layer capacitance, CPE_{pass} represents the passive film interface, CPE_{fiber} represents the presence of steel fibers (in HyFRC composites only), R_{CT} represents the charge-transfer resistance, R_{pit} represents the resistance within pits, and R_{soln} represents the pore solution resistance in the matrix.

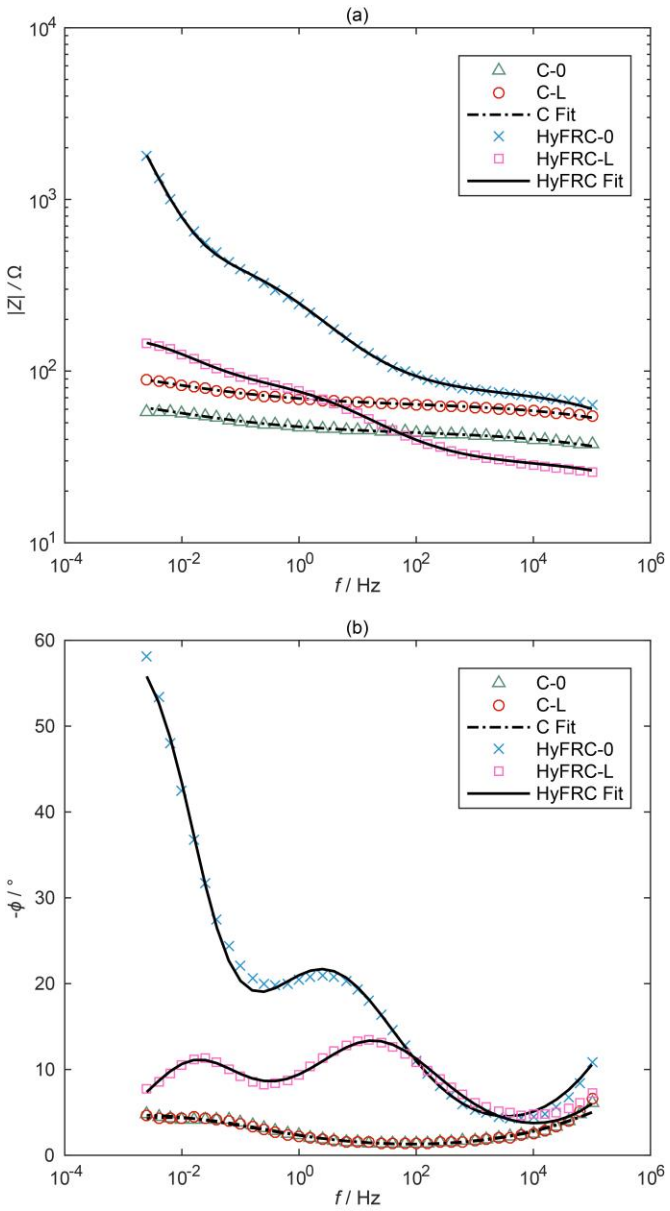


Figure 4-17: Bode plots showing EIS results and fitted results with a domain of frequency *f*: (a) Modulus of impedance |*Z*|; (b) Phase shift -*Φ*.

Values of the parameters used in the equivalent circuit modelling, in addition to corrosion current, are summarized in Table 4-6 for considered specimens at the conclusion of corrosion monitoring. Lower charge transfer resistances R_{CT} were noted for samples with greater I_{corr}. While R_{CT} of loaded samples were similar in magnitude to the nonloaded reinforced concrete sample C-0, the charge transfer resistance of HyFRC-0 was significantly greater than the other considered specimens, due to this specific specimen remaining passivated throughout the environmental conditioning period. The electrolyte solution resistance R_{soln}, determined to be 3.07 to 6.93 Ω for reinforced concrete, was greater for HyFRC-L (28.8 Ω) and was 1 order of magnitude greater for HyFRC-0. Due to the presence of longitudinal splitting cracks that reached the specimen surface in both reinforced concrete specimens, a direct path with greater void volume saturated by solution

is available from the working electrode to the surface of the concrete. Cracks within the HyFRC-L matrix were finer compared to reinforced concrete, resulting in a greater electrolyte solution resistance for the HyFRC sample.

Table 4-6: Element values for equivalent electrical circuit used for EIS results fitting.

	I_{corr}	R_{soln}	R_{CT}	CPE_{DL}-Y_0	CPE_{DL}-α	R_{pit}	CPE_{pass}-Y_0	CPE_{pass}-α	CPE_{fiber}-Y_0	CPE_{fiber}-α
	µA	Ω	Ω	mS s^{α}	-	Ω	mS s^{α}	-	mS s^{α}	-
C-0	1070	3.07	33.6	119	0.336	41.0	0.103	0.306	-	-
C-L	775	6.93	63.3	81.3	0.297	56.7	0.056	0.325	-	-
HyFRC-0	5.26	74.1	3.07 x 10^5	12.2	0.807	431	1.42	0.512	5.86 x 10^{-3}	0.493
HyFRC-L	208	28.8	77.7	73.3	0.632	61.5	2.58	0.502	5.67 x 10^{-3}	0.508

Circuit element values for the constant phase element representing the interfacial capacitance of the passive film, CPE_{pass}, were found to differ between reinforced concrete and reinforced HyFRC samples. For reinforced concrete and reinforced HyFRC samples, the exponent term α was found to be 0.306 to 0.325 and 0.502 to 0.512, respectively. As α=0.5 describes an infinite Warburg element, it is suggested that CPE_{pass} is a diffusion-controlled element for the HyFRC samples. The passive film of steel in simulated concrete pore solution was modelled by Sánchez et al. [117] as a Warburg element representing the diffusion of oxygen vacancies through the passive film. Compared to noncracked conventional concrete sections, noncracked HyFRC sections were found to exhibit a relatively low chloride content in the matrix pore solution at the depth of the reinforcing bar, as previously detailed in Figure 4-15. It is likely that the HyFRC generally maintained an insignificantly-damaged passive film at cathodic surfaces, while the higher chloride content in the pore solution of conventional reinforced concrete caused damage to the film.

Fitting of CPE_{fiber}, which accounted for the impedance contribution of embedded steel fibers in the HyFRC matrix, was determined to have an exponent term α in the range of 0.493 to 0.508. It is suggested that the steel fibers in the matrix are also best described as a Warburg diffusion element due to α nearly being equivalent to the value of 0.5 and the bulk of the fibers remaining in a passive state. The fitting results coincide with the general observation of insignificant corrosion of embedded steel fibers, except those located very near a matrix crack or directly at the ponding surface. Similar observations of the passivity of steel fibers in chloride-contaminated concrete have been summarized elsewhere [89].

4.4 Discussion

4.4.1 Early-age corrosion propagation

Changes of the Tafel polarization responses of select samples during the initial 40 weeks of active corrosion are presented in Figure 4-18. The indicated time in the plots is the elapsed active corrosion time, which is considered to be 0 weeks upon first detection of corrosion initiation. HyFRC-0 did not produce sufficient active corrosion measurements during the experiment to consider for appropriate comparison.

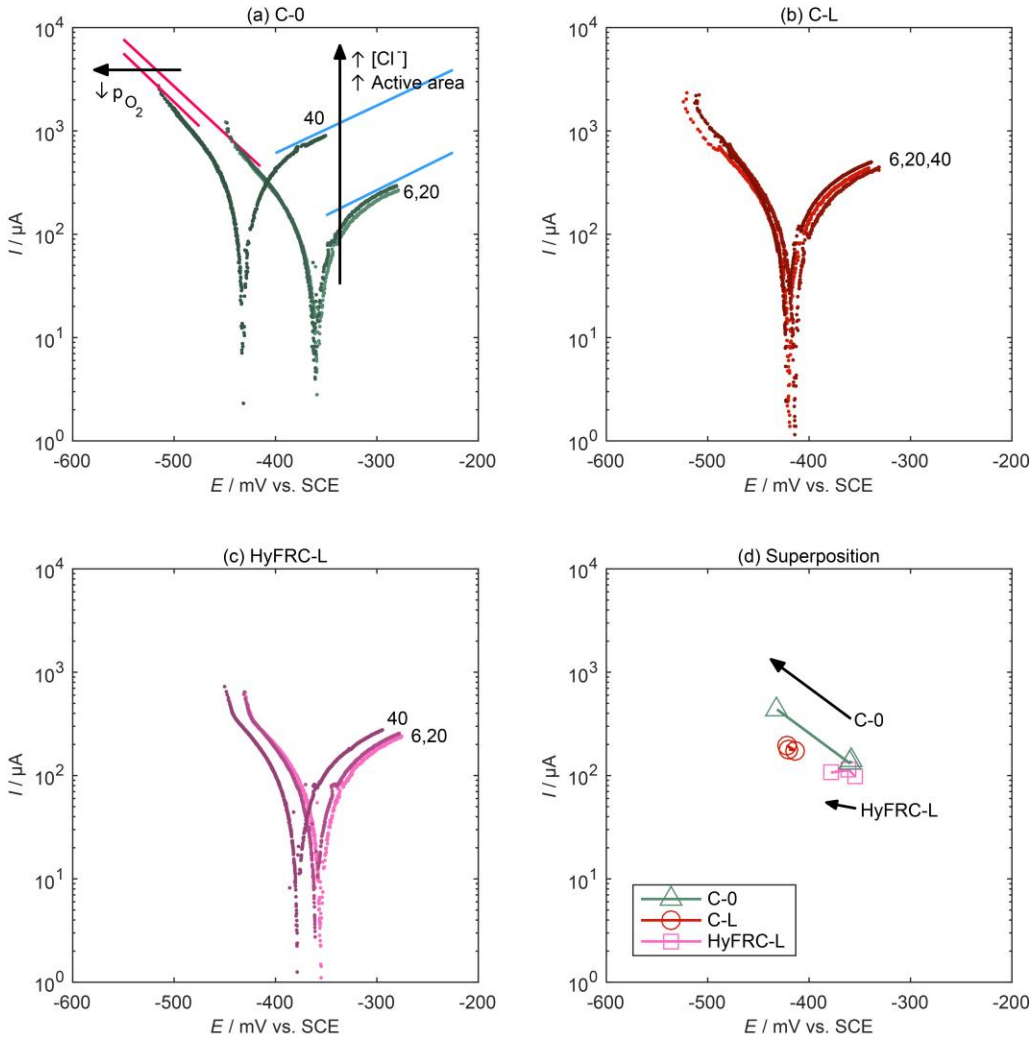


Figure 4-18: Tafel polarization responses of select specimens over elapsed active corrosion time, up to 40 weeks: (a) C-0, additionally showing influence of factors on polarization curvature; (b) C-L; (c) HyFRC-L; (d) Superposition of I_{corr}-E_{corr} relations from (a)-(c). Numbers adjacent to polarization curves indicate time, in weeks, of elapsed active corrosion time.

The early-age corrosion propagation characteristics were influenced by composite type and presence of matrix cracks. For the nonloaded sample C-0, insignificant changes are observed for the polarization curves at 6 and 20 weeks. Later, a shift in the polarization response at 40 weeks is characterized by a large current increase of the anodic reaction curve, as highlighted by the arrow in Figure 4-18a. By comparison, the cathodic reaction curve is only slightly shifted to lesser potential. An increase in anodic current may be caused by an increase of chloride concentration of the local solution at the rebar surface [118-121], an increase of the actively corroding surface area, or both. Cracking of the concrete matrix would allow both events to occur, as splitting cracks with sufficient width increase the chloride solution permeability of the concrete cover [9, 10] and subsequently cause passivated surfaces within the splitting crack wake to become active. The large shift of the anodic curve results in an increase in corrosion current from 20 to 40 weeks, as highlighted in Figure 4-18d. While loaded C-L exhibits a greater corrosion current at 6 weeks compared to C-0, the polarization response of C-L does not significantly change from 6 to 40

weeks. Because corrosion products preferentially form within defects located near the steel rebar surface [122, 123], the corrosion rate of C-L is higher due to products readily forming within empty crack openings compared to a denser rebar-matrix interface. Matrix cracking occurs when the accumulation of expansive corrosion products fills a void volume and places sufficient stresses on the matrix, which likely did not occur until after 40 weeks of active corrosion. Due to a lack of additional matrix cracking, the corrosion rate does not increase as rapidly compared to C-0 despite being initially greater.

Although HyFRC-L was exposed to a chloride environment while in a cracked and loaded condition, its corrosion current was lower compared to C-L due to the fineness of the cracks in the HyFRC matrix, resulting in a smaller initial anodic surface where the crack-rebar interface was located. A decrease of HyFRC-L corrosion potential occurs at 40 weeks and the corrosion rate (107 μA) is slightly reduced from the measurement obtained at 20 weeks (113 μA) despite an increase of the anodic reaction curve to greater current. Lowering of the corrosion rate is caused by shifting of the equilibrium potential *E* of the cathodic reaction to a more negative value of potential. Based on the Nernst equation and the oxygen reduction reaction previously presented in Reaction 4-1, a change in the equilibrium potential of the cathodic reaction may be anticipated based on changes in solution chemistry as described by Equation 4-3.

$$E = E^0 - \frac{0.0592}{z}\log\left(\frac{[(OH)^-]^2}{p_{O_2}1/2}\right) \qquad \text{Equation 4-3}$$

E^0 is the standard equilibrium potential, z is the number of electrons transferred in the cell reaction, $[(OH)^-]$ is the concentration of OH^- in solution, and p_{O_2} is the partial pressure of dissolved O_2 in solution. The equilibrium potential *E* lowers for increasing concentration of hydroxide or decreasing partial pressure of dissolved oxygen. The former change in chemistry is unlikely due to the inherently high pH of concrete pore solution (ca. 13 to 13.5) and a tendency for pH to decrease due to carbonation or calcium hydroxide leaching of the cementitious matrix. A lowering of oxygen partial pressure is more likely and may be caused by several phenomena, including the formation of corrosion product scales on the steel rebar surface, which impede the diffusion of oxygen through the scale layers [124, 125], and a greater consumption of oxygen in electrode reactions compared to replenishment [126, 127], leaving the oxygen partial pressure lowered at the time of measurement. Samples remained under activation-controlled kinetics, as a plateau in the polarization curves indicative of diffusion control was absent. While both C-0 and HyFRC-L exhibit a shifting of cathodic reaction curves from 20 to 40 weeks, the increase in anodic current is significantly greater for C-0 due to the poor crack resistance of the plain matrix compared to the fiber-reinforced matrix of HyFRC.

4.4.2 Late-age corrosion propagation

Tafel polarization diagrams showing responses for up to 90 weeks of corrosion activity for C-0 and up to 130 weeks of corrosion activity for C-L and HyFRC-L are presented in Figure 4-19. C-0 is characterized by the greatest increases in corrosion current as corrosion propagation time increases, followed by C-L then HyFRC-L. Greater corrosion current was correlated to greater splitting crack damage, which was previously mentioned to decrease the permeability of the cementitious matrix and allow for the ingress of chlorides and oxygen to the steel rebar surface through cracks. For C-0 and C-L, the maximum surface splitting crack widths were measured to

be 0.32 mm and 0.14 mm, respectively. While HyFRC-L exhibited local splitting crack damage near actively corroding rebar surfaces, as previously shown in Figure 4-10, no surface splitting cracks could be visually detected on the exterior surface of any HyFRC sample, though crack width measurements required an opening of at least 0.01 mm. Correspondingly, the corrosion rate of HyFRC-L shows small increases in corrosion rate from 40 to 70 weeks though does not significantly change after 70 weeks.

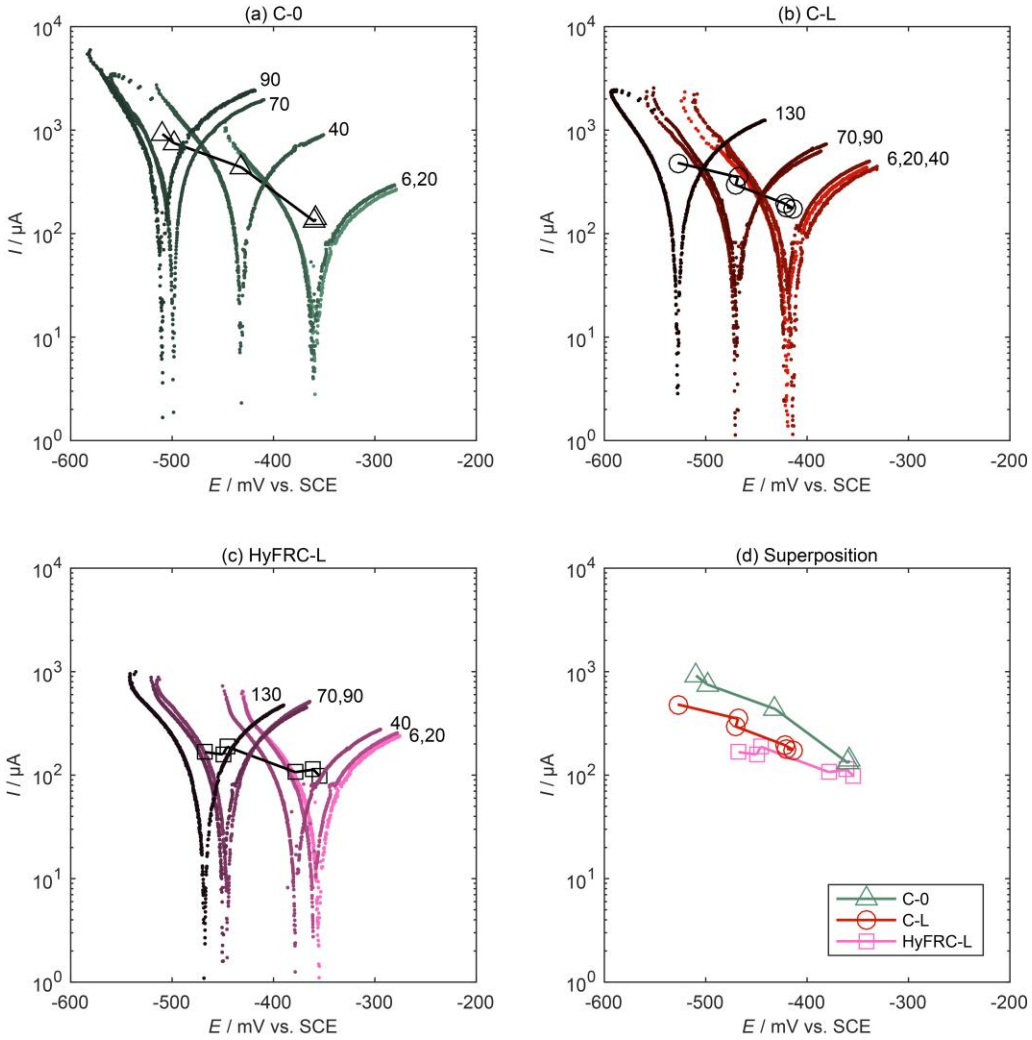


Figure 4-19: Tafel polarization responses of select specimens over elapsed active corrosion time, up to 90 or 130 weeks: (a) C-0; (b) C-L; (c) HyFRC-L; (d) Superposition of I_{corr}-E_{corr} relations from (a)-(c). Numbers adjacent to polarization curves indicate time, in weeks, of elapsed active corrosion time.

Evaluation of the fitted cathodic and anodic reaction curves from polarization responses taken at 90 weeks of active corrosion, as shown in Figure 4-20, highlight the dominating effect of the anodic response on I_{corr} compared to the cathodic response. Due in majority to the increased anodic current, the corrosion currents of C-0 and C-L are greater than the corrosion current of HyFRC-L ($I_{corr,HyFRC-L}$) by factors of 5.78 and 2.21, respectively. Use of hybrid fiber reinforcement may be regarded as a method to reduce the total corrosion current of reinforced concrete over long-

term conditions due to its effective crack control, which restricts depassivation of large surfaces of the steel rebar far from the initial site of corrosion.

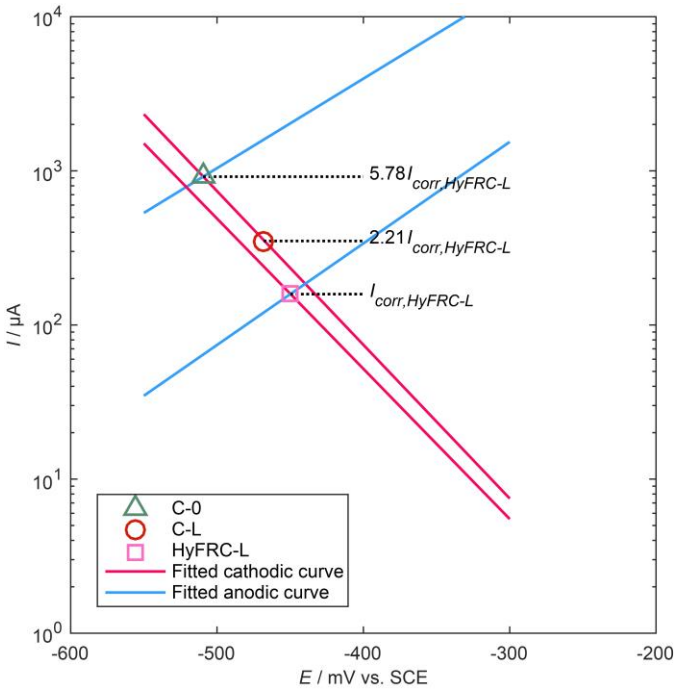


Figure 4-20: I_{corr}-E_{corr} relations at 90 weeks, showing select fitted cathodic and anodic reaction curves from Tafel polarization responses. The corrosion current of HyFRC-L in the plot is referred to as $I_{corr,HyFRC-L}$.

4.5 Summary and conclusions

The corrosion behavior of conventional reinforced concrete and reinforced hybrid-fiber reinforced concrete (HyFRC) was found to be highly dependent on the cracked state of the composite matrix. A corrosive environment was prepared by allowing 3.5% w/w NaCl solution to permeate the porous cementitious matrix of samples containing a single steel reinforcing bar (rebar) in a wet-dry cyclic manner over a 2.5-year experimental duration. To account for cracks that are present in civil engineering structures in service, subsets of specimens were subjected to the same applied tensile load during environmental exposure. Corrosion potential measurements, linear polarization tests and Tafel polarization tests were periodically conducted to monitor the electrochemical response of samples during the experiment. In addition, electrochemical impedance spectroscopy (EIS) was performed to evaluate the differences in the impedance responses between samples as a result of accumulated matrix cracking. The following conclusions are made:

1. HyFRC composites require a longer time to initiate steel rebar corrosion compared to conventional reinforced concrete. While placed under tensile stress and subsequently cracked, the delay is attributed to the crack-controlling properties of fiber reinforcement restricting the maximum opening of induced cracks, which slow the rate of external NaCl solution penetration. For nonloaded samples, the inclusion of polyvinyl alcohol (PVA) and steel fibers reduces the effective chloride diffusion rate through the matrix and lengthens

the time to achieve active corrosion by a factor of at least 1.7, though the detailed mechanism of retardation requires additional study.

2. The cathodic and anodic Tafel coefficients for actively corroding samples, regardless of composite or loading condition, were found to have mean values of β_c=102 mV/decade and β_a=180 mV/decade, respectively. A mean Stern-Geary coefficient of B=28.1 mV was also calculated, similar to the well-cited value of B=26 mV for active corrosion of reinforced concrete proposed by Andrade and González [95]. For passive samples, use of B based on fitted Tafel coefficients resulted in an underestimation of the corrosion current compared to the corrosion current extrapolated directly from Tafel polarization curves. In this case, an adjusted Stern-Geary coefficient of B=24.0 mV was used for passive samples based on empirical fitting.
3. At the conclusion of testing, matrix cracking damage was most severe for nonloaded reinforced concrete (C-0). In order of descending observed damage, loaded reinforced concrete (C-L), loaded reinforced HyFRC (HyFRC-L), and finally nonloaded reinforced HyFRC (HyFRC-0) followed. Upon initial active corrosion, stress accumulation and subsequent cracking from expansive corrosion product formation occurs more rapidly for C-0 due to the formation of such products in a dense rebar-matrix interface rather than within a crack void. Use of HyFRC was significantly more effective than conventional concrete for restricting the opening and propagation of corrosion-induced cracks.
4. Correlating to the most severe cracking damage among sample types, C-0 was associated with the lowest charge transfer resistance and lowest pore solution resistance, as well as the highest corrosion current. Correspondingly, the charge transfer and pore solution resistances were greater and the corrosion current was lower for HyFRC-L compared to reinforced concrete samples.
5. While the partial pressure of reducible oxygen of the concrete pore solution decreased over time, which would otherwise lower the corrosion rate if no other changes occurred, increasing corrosion currents occurred for reinforced concrete samples during the testing duration while active HyFRC did not significantly change in corrosion rate for the final 40 weeks of experimentation. Increases in corrosion current were primarily attributed to the formation of additional active steel rebar surfaces from the initial site of corrosion, which was possible by the formation of matrix splitting cracks along the length of the rebar and was more widespread for reinforced concrete. Control of the anodic current response is regarded as being critical for preventing increasing corrosion rates for reinforced concrete composites undergoing wet-dry cycling.

5 Corrosion behavior of HyFRC beam elements

5.1 Introduction

The work in the preceding Chapter 4 considered the case of reinforced HyFRC with a single strand of rebar under direct tensile stress. In professional practice, reinforcing bars are assembled in cage assemblies prior to casting of concrete and are in electrical contact with other bars. Furthermore, use of HyFRC is typically intended for structural elements under flexural stress, such as beam elements and beam-column elements such as the tube column presented in Chapter 3. Particular to the tested tube column, because only the plastic hinge region of the column has steel reinforcement debonded from the HyFRC, portions of the column not bound within this region exhibited some flexural cracking. Thus, study of reinforced HyFRC with flexural cracking damage under corrosive environments is proposed as a method of evaluating the performance of the composite material in a more practical engineering setting.

Several researchers have investigated the corrosion behavior of different types of fiber-reinforced cementitious composite (FRCC) beam elements, as surveyed in Table 5-1. Common to all surveyed references is the application of flexural loading prior to, or during, exposure to a chloride environment to account for matrix cracks found in real structures. Loading procedures differed between studies, as well as the specific type of FRCC investigated. When evaluating composite beams on the basis of the same magnitude of applied load, reinforced FRCC exhibited a longer time to corrosion initiation compared to reinforced concrete due to microcracking in the matrix as opposed to dominant crack localization found in plain matrices [32, 33]. However, when comparing composite beams on the basis of similar maximum surface crack opening, reinforced FRCC exhibited insignificant or only small increases in corrosion initiation time [90, 92].

Despite an interest in using crack-resistant materials for corrosion damage control, corrosion propagation behavior of reinforced FRCC has not been widely reported. Blunt et al. [32] and Jen and Ostertag [33] exposed reinforced hybrid fiber-reinforced concrete (HyFRC) samples to exposure durations of 36 weeks and 2 years, respectively, and confirmed a lower overall reduction in rebar mass loss within HyFRC composites compared to conventional reinforced concrete. The corrosion damage control of HyFRC was attributed in part to the restriction of corrosion-induced splitting crack propagation. Miyazato and Hiraishi [93] subjected reinforced high-performance fiber-reinforced cementitious composites (HPFRCC) to flexural loads sufficient to produce crack widths of at least 0.1 mm width. Lower corrosion rates in reinforced FRCC were attributed to the formation of multiple anodic sites along the steel reinforcing bar where diffuse cracking occurred, as opposed to large localized corrosion rates where a dominant crack occurred in reinforced mortar. However, the conclusions were determined after only 4 weeks of exposure. In a longer study with a duration of 89 weeks, Paul and van Zijl [91] reported that the corroded surface of rebar extracted from cracked reinforced SHCC was more localized and had similar or greater pitting depths compared to reinforced mortar. It should be noted that the reinforced SHCC was evaluated with a greater total experimental duration compared to reinforced mortar, which was tested for 65 weeks. While use of FRCC appears beneficial for reducing corrosion damage at the onset of propagation, its behavior over long-term conditions has yet to be thoroughly evaluated.

Table 5-1: Survey of select studies on the corrosion behavior of reinforced fiber-reinforced cementitious composite beam elements subjected to applied flexural loading prior to, or during, chloride exposure. References are listed in ascending order of exposure duration.

Reference	Exposure duration	Exposure conditions[1]	Loading conditions[2]	Reinforcement of interest and concrete cover details	Cementitious composite[3] (total fiber volume fraction, % vol. compos.)	Maximum observed flexural crack width (mm)	Corrosion initiation time	Physical validation of rebar corrosion damage
Michel et al. [92]	3.4 weeks	Continuous wetting with 3% NaCl solution	3-point bending to target extent of rebar-matrix interfacial slip; Sustained loading only	(2) ø 12 mm bars, one being hollowed, instrumented, and segmented; 60 mm cover	SFRC (1.0%)	0.068	1 day	Not reported
					SFRC (0.5%)	0.139	1.5 days	
					Concrete	0.069	<1 day	
Miyazato and Hiraishi [93]	4 weeks	Wet-dry cycling: Wetting cycle with 3% NaCl solution for 2 days; Drying cycle for 5 days	3-point bending to target load; Sustained loading only, for HPFRCC	Single ø 9 mm bar, segmented; 20 mm cover	HPFRCC (1.5%)	0.1	0-4 weeks	Not reported
					Mortar	0.3-0.4	0-4 weeks	
			3-point bending to match max. crack width of mortar; Sustained loading only		HPFRCC (1.5%)	0.3-0.4	0-4 weeks	
Blunt et al. [32]	36 weeks	Continuous wetting with NaCl solution under 50 °C	4-point bending to target load, 5 total cycles	Single ø 9.5 mm bar, electrically connected to 2 ø 12.7mm bars; 25 mm cover	HyFRC (1.5%)	0 (not detectable)	6-17 weeks	Gravimetric mass loss of rebar, normalized by entire surface area of bar: 26.3-51.3 mg/cm^2
					Concrete	0.3-0.4	0-1 week	124-140 mg/cm^2
Berrocal et al. [90]	67 weeks	Wet-dry cycling: Wetting cycle with 16.5% NaCl solution for 2 weeks; Drying cycle for 2 weeks	3-point bending to target maximum crack widths; Preloaded: 1 or 5 total cycles; Sustained loading	(3) ø 10 mm bars; 30 mm cover	Synthetic fiber-reinforced concrete (0.75%)	Preloaded: 0.02-0.06; Sustained loading (Steel fiber-reinforced concrete and concrete): 0.1-0.4	No loading: 54.9-(>66.7) weeks; Preloaded: 20-70 days	Not reported
					Hybrid fiber-reinforced concrete (0.5%)		No loading: 51.6-(>66.7) weeks; Cyclically preloaded: 10-30 days Preloaded: 7-30 days	
					Steel fiber-reinforced concrete (0.5%)		Not loaded: 28.7-(>66.7) weeks; Sustained loading: 0-1 day Cyclically preloaded: 0-70 days Preloaded: 10-70 days	

Table continued on next page.

Reference	Exposure duration	Exposure conditions[1]	Loading conditions[2]	Reinforcement of interest and concrete cover details	Cementitious composite[3] (total fiber volume fraction, % vol. compos.)	Maximum observed flexural crack width (mm)	Corrosion initiation time	Physical validation of rebar corrosion damage
Berrocal et al. [90] (cont.)	67 weeks	Wet-dry cycling: Wetting cycle with 16.5% NaCl solution for 2 weeks; Drying cycle for 2 weeks	3-point bending to target maximum crack widths; Preloaded: 1 or 5 total cycles; Sustained loading	(3) ø 10 mm bars; 30 mm cover	Concrete	Preloaded: 0.02-0.06; Sustained loading (Steel fiber-reinforced concrete and concrete): 0.1-0.4	Not loaded: 28.7-(>66.7) weeks; Sustained loading: 0-1 day Cyclically preloaded: 1-20 days Preloaded: 4-30 days	Not reported
Paul and van Zijl [91]	89 weeks for SHCC	Wet-dry cycling: Wetting cycle with 3.5% NaCl solution for 3 days; Drying cycle for 4 days	3-point bending to target midpoint disp. based on composite: SHCC – 3.5 mm; Mortar – 1.5 mm	1 or 2 ø 10 mm bars; 15, 25, or 35 mm cover	SHCC with fine sand (26 kg/m^3 fiber dosage)	0.100-0.174	Not reported	Mean and maximum pitting corrosion depth of rebar: 0.21-0.24 mm (mean); 0.30-0.59 mm (max.)
					SHCC with coarse sand (26 kg/m^3 fiber dosage)	0.050-0.274	Not reported	0.29-0.30 mm (mean); 0.32-0.50 mm (max.)
	65 weeks for mortar			Single ø 10 mm bar; 15 mm cover	Mortar with fine sand	0.375-0.400	Not reported	0.23 mm (mean); 0.28 mm (max.)
					Mortar with coarse sand	0.225-0.249	Not reported	No measured validation
Jen and Ostertag [33]	104 weeks[4] (2 years)	Continuous wetting with 3.5% NaCl solution for initial 1 year under 50 °C, followed by cont. drying for 1 year under 50 °C and 50% relative humidity	4-point bending to target load, 5 total cycles	Single ø 9.5 mm bar, electrically connected to a ø 19 mm bar; 25 mm cover	SC-HyFRC (1.5%)	0 (not detectable)	Preloaded: 1-2 years Not preloaded: 1-2 years	Gravimetric mass loss of rebar: Preloaded: 4 g Not preloaded: 2 g
					Concrete	0.2-0.3	Preloaded: 0-1 week Not preloaded: 1-2 years	Preloaded: 12 g Not preloaded: 8 g

[1] Assumed under ambient laboratory conditions, unless noted otherwise

[2] Unloading occurs after reaching target load or deformation, unless noted otherwise

[3] Nomenclature per reference: HPFRCC (high-performance fiber-reinforced cementitious composite); HyFRC (hybrid fiber-reinforced concrete); SC-HyFRC (self-consolidating hybrid fiber-reinforced concrete); SFRC (steel fiber-reinforced concrete); SHCC (strain-hardening cementitious composite)

[4] Estimated time in weeks, per reference

The research presented in this chapter evaluates the long-term influence of hybrid fiber reinforcement on the corrosion behavior of reinforced concrete beam elements. Samples were exposed to a chloride environmental for 2.2 years, which was sufficiently long to allow HyFRC composites to exhibit corrosion damage of embedded steel reinforcement. To account for the effects of existing cracks in reinforced concrete structures, beam elements were flexurally preloaded prior to chloride exposure. After periodically measuring the corrosion rate of samples throughout the entirety of the experiment, specimens were evaluated for electrochemical and physical damage, chloride permeation, and residual mechanical properties.

5.2 Materials and methods

5.2.1 Concrete materials

Batching proportions for the HyFRC used in this study are presented in Table 5-2 and are the same as the proportions presented in Chapter 2. A plain concrete lacking fiber reinforcement was also investigated, and was batched with the same cement and aggregate material types and designed with the same water-cement mass ratio as the HyFRC. After casting with fresh concrete or HyFRC, samples were cured within molds for 7 days and covered with wetted burlap, demolded, and then cured in ambient laboratory conditions (approximately 23.5° C, 45% relative humidity) for 21 additional days prior to mechanical preloading, if prescribed. A similar curing method was performed by Blunt and Ostertag [52] for the development of HyFRC. The 28-day compressive strength f'_c of the HyFRC or concrete was required to reach a minimum value of 35 MPa, which is a typical nominal design strength in the United States. The HyFRC reached this criterion with a compressive strength of f'_c=47 MPa. Samples cast with plain concrete required two separate batches, resulting in compressive strengths of f'_c=45 MPa and f'_c=53 MPa for nonloaded samples and preloaded samples, respectively.

Table 5-2: Batch proportions of HyFRC.

Composite	Mass proportions (kg/m^3)				Fiber volume fraction (vol. % composite)		
	Cement	Water	Coarse aggregate	Fine aggregate	PVA	Steel (30-mm length)	Steel (60-mm length)
HyFRC	423	228	775	853	0.2	0.5	0.8

5.2.2 Specimen design

Beam elements were selected for study due to the expected use of deflection-hardening HyFRC in flexural load applications [52]. Figure 5-1a shows the specimen design, which is similar to the test specimen detailed in ASTM G109 [128] and contains two ASTM A615 [129], United States grade 60 steel longitudinal reinforcing bars positioned at different specified depths. The cover thickness of either bar to the nearest concrete surface was 25 mm. The primary steel rebar of interest for monitoring and analysis of corrosion behavior had a 9.5 mm nominal diameter (United States size 3) and was cast at higher elevation than a secondary bar with a 19 mm nominal diameter (United States size 6). The two bars in the sample were connected by an insulated copper wire to simulate the effects of galvanic corrosion caused by the nonuniform depassivation of tied reinforcement sections extending to different depths from an exposed concrete surface (Figure 5-1c). Corrosion of steel was limited to a defined region of interest, being the middle 508 mm of the bar, which was

sandblasted to remove its mill scale. Elsewhere, the bar surface was insulated and prevented from being in direct contact with the cementitious matrix. After application of an electrically insulating lacquer onto the bar surface, the rebar was coated by vinyl tape and then polyolefin tubing for physical protection.

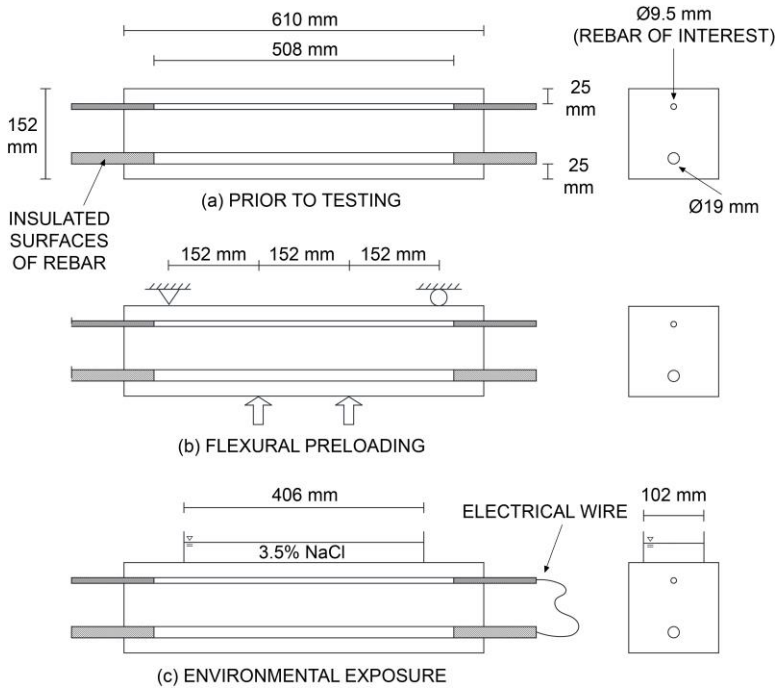


Figure 5-1: Preparation and testing of specimen: (a) Sample after casting and prior to any testing; (b) Schematic for 4-point flexural preloading, with rebar of interest placed under tensile stress during preloading; (c) Sample during environmental exposure, with rebar of interest located near adhered ponding dam. An insulated copper wire electrically connected the two bars in the sample during environmental exposure.

5.2.3 Flexural preloading

Prior to environmental exposure, select samples were subjected to 4-point bending with equidistant lengths between loading points, as schematically shown in Figure 5-1b. The beams were orientated to stress the 9.5 mm-diameter rebar of interest in tension. While preloading of reinforced FRCC in corrosion-related studies has occurred under conditions of constant magnitude of applied load [32, 33, 93] or loading until a target maximum surface crack width was attained [90, 93, 130], the loading protocol utilized for this research was dictated by the formation of intended surface crack characteristics to evaluate the effect of crack morphology on both corrosion initiation and propagation behavior. The targeted crack characteristics were selected based on progressive damage states expected upon loading a reinforced concrete or reinforced HyFRC member to its ultimate bending capacity. Table 5-3 summarizes differences between specimen groups for study. After a peak load was identified to produce the desired cracking damage, samples were cyclically loaded and unloaded a total of 5 instances with the same peak load. Two specimens were tested for each experimental group.

Reinforced concrete composites were loaded such that one set of samples exhibited only flexural cracks while the other set showed more severe damage in the form of splitting cracks in addition to flexural cracks. Splitting cracks are caused by interfacial slipping of the steel rebar ribs

from the surrounding matrix when the composite is stressed [40]. A peak load of 42 kN was selected for producing flexural cracks, while the range of 42 kN to 54 kN allowed for surface splitting cracks to form. Damage of reinforced HyFRC beams loaded to 54 kN primarily consisted of flexural microcracking due to the crack-controlling properties of the fibers. To induce surface cracks with widths similar to those observed for reinforced concrete (i.e. greater than 0.10 mm), a load of 89 kN was required for HyFRC composites. The high magnitude of load, which was equivalent to 85% of the peak monotonic flexural capacity of the HyFRC beam, is representative of inelastic loading from a high-intensity event such as an earthquake. Regardless of applied load level, all reinforced HyFRC samples showed no observable surface splitting cracks, which is a characteristic damage-resisting property of the composite [44, 55].

Table 5-3: Specimen name designation and intended preload damage characteristics.

Specimen type[1]	Composite	Intended surface cracking pattern	Peak applied load
C-0	Concrete	-	-
C-f	Concrete	Flexural cracks	42 kN
C-fs	Concrete	Flexural and splitting cracks	42 kN or 54 kN
HyFRC-0	HyFRC	-	-
HyFRC-m	HyFRC	Microcracks	54 kN
HyFRC-f	HyFRC	Flexural cracks	89 kN

[1] Abbreviation for specimen name designations: 0 – no preload; f – flexural crack formation; fs – flexural and splitting crack formation; m – microcrack formation.

5.2.4 Environmental conditioning

A corrosion-inducing environment was prepared for samples by first adhering a polyvinyl chloride ponding dam onto the beam surface nearest the rebar of interest, as shown in Figure 5-1c. The dam was filled with 3.5% w/w NaCl solution. For preloaded samples, the ponding surface coincided with the cracked surface. The dam was continuously filled with solution for the initial 11 weeks of experimentation to allow for chloride solution saturation of the matrix. Afterwards, wet-dry cycling was performed by relieving the ponding dam of solution for 1 week, then refilling the dam with fresh solution for 1 additional week. The procedure was then repeated. To prevent leaking of solution from defects on the concrete surface, all vertical beam surfaces and the top horizontal surface that was not enclosed by the dam were coated with a moisture-resistant sealant. The exposed bottom horizontal surface acted as an evaporation sink for the ponded solution, driving the solution from the top surface of the sample towards the bottom surface [32].

5.2.5 Electrochemical measurements

Electrochemical measurements were periodically acquired throughout the entire environmental conditioning period of 116 weeks (2.2 years). Figure 5-2 shows the typical setup for corrosion potential and linear polarization resistance testing for the rebar of interest. All measurements were performed using a saturated calomel electrode (SCE) as the reference electrode while stainless steel was used as the counter electrode. Both electrodes were immersed in the NaCl ponding solution during testing. The corrosion potential E_{corr} was measured for at least 10 minutes, during which the corrosion potential value was not to deviate by more than 1 mV to ensure quasi-steady state conditions. To obtain the polarization resistance R_p, the bar was subjected to a linear polarization test that considered an overpotential domain of -10 mV to 10 mV versus E_{corr}.

Determination of the corrosion current I_{corr} requires the Stern-Geary coefficient B [94], which was assumed to be B=26 mV/decade for actively corroding rebar and B=52 mV/decade for passive rebar embedded within concrete [95, 131]. While values of B=28.1 mV and B=24.0 mV for active and passive samples, respectively, were determined in Chapter 4, the experiments in this chapter occurred concurrently with those described in Chapter 4. Therefore, a conservative approach was taken in the analysis of the corrosion current for experiments in this chapter and the well-cited assumed values were used. The difference between the proposed Stern-Geary coefficient from Chapter 4 and the coefficient proposed by Andrade and González [95] only differed by 8.1%, however. For samples exhibiting a corrosion potential value greater than -277 mV versus SCE, which has been attributed to a 90% probability of passive behavior [132], the passive B value was selected. Otherwise, B was assumed based on active conditions. The galvanic current between the two steel reinforcing bars was determined by connecting the counter electrode terminal to the larger, secondary embedded rebar and measuring the current flow between the two bars. Additionally, the corrosion potential of the secondary rebar was also measured using similar methods as for the primary rebar of interest.

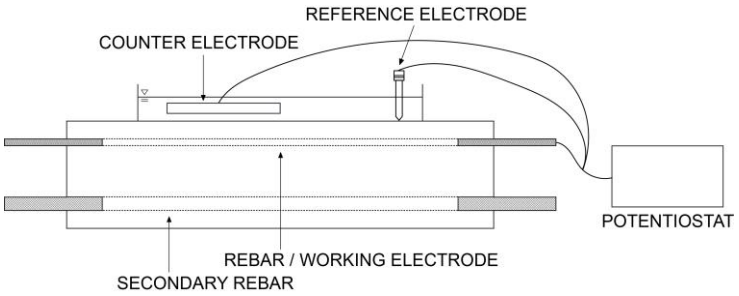


Figure 5-2: Typical electrochemical measurement setup for corrosion potential and linear polarization resistance. Stainless steel was used as the counter electrode and a saturated calomel electrode (SCE) was used as the reference electrode.

5.2.6 Destructive testing

At the conclusion of environmental conditioning, select samples were subjected to 4-point bending, using the same setup schematically shown in Figure 5-1b, to evaluate mechanical properties after accumulation of corrosion-induced damage. The loading procedure consisted of 5 total cycles with a peak applied load of 42 kN, regardless of composite type or previous preload history. To determine the chloride content of the same samples, a coring drill press extracted 29 mm-diameter cylindrical cores from the beam depth. For samples with flexural macrocracks induced by mechanical preloading, core sampling was positioned both over a flexural crack and over a noncracked surface, as shown schematically in Figure 5-3. If no observed flexural cracks were present from preloading, coring occurred near the midlength of the beam. Because the steel reinforcing bar was required to be intact for additional analysis, coring was offset from the middle of the beam. The extracted cores were sawed into 25 mm-tall segments and pulverized such that the material could pass a sieve with openings of 0.85 mm. Determination of the acid-soluble chloride content was based on the potentiometric titration method detailed in ASTM C1152 [104], which is expected to yield the total chloride content in the cementitious matrix. Due to possible artifacts introduced by the oxidation of steel in acid solution, steel fibers were manually removed from pulverized HyFRC samples prior to chloride content testing. After coring, the 9.5 mm-

diameter steel bars of interest were extracted from the beams, stripped of protective coatings, cleaned of adhered corrosion products using a hydrochloric acid-based solution [133], and measured for gravimetric mass loss due to corrosion.

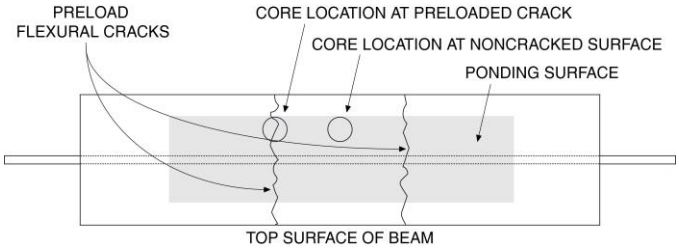


Figure 5-3: Schematic showing top, ponded surface of beam. Core extraction locations were based on the preload-induced flexural surface cracking characteristics, if any.

Specimens not subjected to the described destructive tests were prepared for optical imaging of the transverse section of the beam to visualize electrochemical damage of the corroded rebar and physical damage of the cracked surrounding matrix. Prior to cutting of the samples, surface cracks were impregnated with a low-viscosity, blue-colored epoxy to maintain existing crack widths. The process for producing slices for transverse section imaging is shown in Figure 5-4. From a beam specimen, a 51 mm-wide, 64 mm-deep, and 305 mm-long prism containing the rebar of interest was extracted. The top surface of this prism was a portion of the ponding surface of the beam. Rectangular plates with a thickness of approximately 13 mm were then sawed from the prism. When not being prepared for imaging, the cut samples were placed into a vacuumed desiccator to prevent further oxidation of the steel or corrosion products. After covering the surfaces with additional epoxy to fill matrix pores, the plates were polished and then optically imaged. Sawing of the prism and polishing of the plates were performed using kerosene as a lubricant to minimize the dissolution of cement paste or corrosion products that could otherwise occur with water.

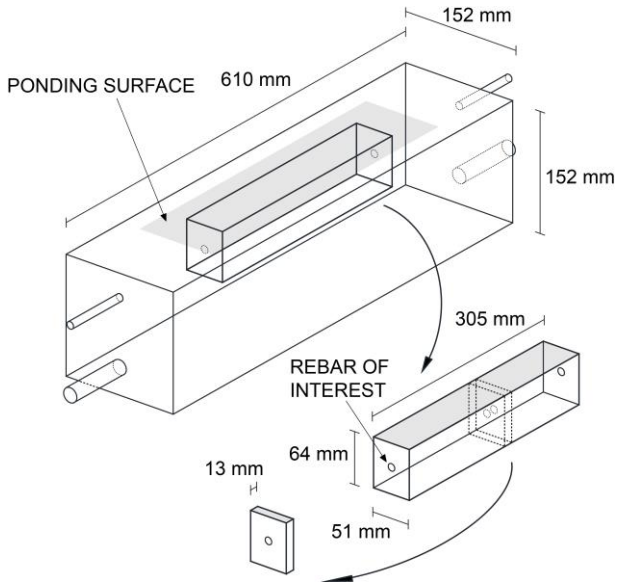


Figure 5-4: Schematic showing the extraction of transverse section slices of rebar of interest and surrounding matrix from the beam sample. The top surface of the slice coincides with the ponding surface of the beam.

5.2.7 X-ray diffraction

X-ray diffraction (XRD) was performed on the corrosion products of select specimens to evaluate any effect, if any, of hybrid fiber reinforcement on the composition of products. Such XRD information is rarely reported in the literature for fiber-reinforced cementitious composites. After manually extracting the steel rebar from select composite samples, visible corrosion products were immediately scraped from the bulk metal, deposited into a container, and placed into a vacuumed desiccator prior to characterization. X-ray powder diffraction was performed at room temperature with a step size of 2θ=0.02° and a range of 2θ=3° to 100°. A Co anode was used with an energy of 40 keV and a current of 40 mA.

5.3 Results

5.3.1 Mechanical preloading

Flexural preloading responses are presented in Figure 5-5. After reinforced concrete specimens exceeded the matrix cracking load, a nonlinear ascending curve characterized by discrete load reductions was observed. These reductions are indicative of macrocrack formations, as shown in Figure 5-6a. Flexural cracks are identified as cracks that cross the beam width, while splitting cracks propagate longitudinally along the beam length. In contrast to reinforced concrete, stable cracking behavior in HyFRC composites resulted in a smooth post-elastic ascending curve with no apparent loss in load resistance. A summary of deformation and cracking characteristics from individual beam samples is presented in Table 5-4. The maximum flexural crack width is measured within the center 102 mm of the beam width, coinciding with the portion of the crack directly enclosed by the ponding dam. These crack widths ranged from 0.09 mm to 0.17 mm for reinforced concrete and required the application of peak loads from 42 kN to 54 kN. Application of a significantly greater peak load of 89 kN for reinforced HyFRC produced crack widths of the same magnitude (0.12 to 0.14 mm) as cracked reinforced concrete. As HyFRC-m samples exhibited some residual midpoint displacement but had no detectable flexural cracks based on the scanned image resolution of 11 μm per pixel, permanent deformation was caused primarily by microcracking. Splitting cracks were not observed in any HyFRC sample, as in Figure 5-6b.

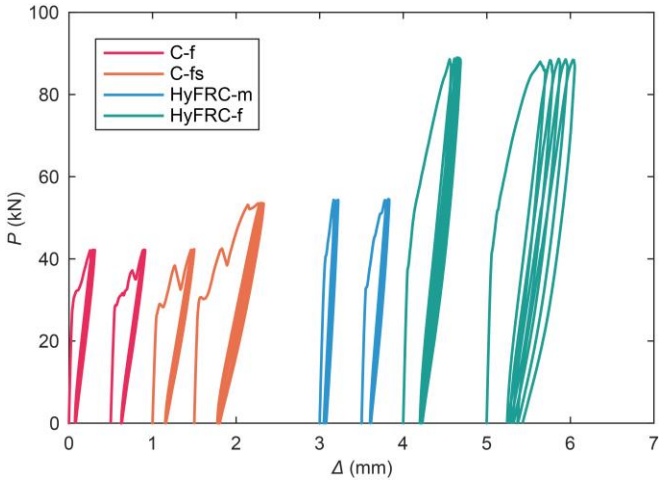
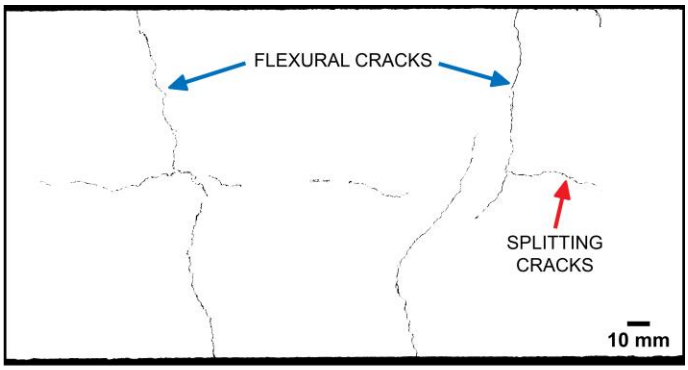


Figure 5-5: Flexural preloading response prior to environmental conditioning: Applied load P versus midpoint deflection Δ. Specimen responses are offset by 0.5 or 1 mm for clarity.



(a) C-fs



(b) HyFRC-f

Figure 5-6: Observed representative surface crack characteristics after preloading: (a) C-fs; (b) HyFRC-f. The images are presented as binary images to highlight crack features. Crack widths are enlarged for clarity.

Table 5-4: Summary of specimen deformation and cracking characteristics.

Specimen	Peak load	Residual midpoint disp. (mm)	Max. flexural crack width (mm)[1]	Max. splitting crack width (mm)
C-f-1	42	0.08	0.09	-
C-f-2	42	0.13	0.12	-
C-fs-1	42	0.15	0.13	0.10
C-fs-2	54	0.30	0.17	0.11
HyFRC-m-1	54	0.07	-	-
HyFRC-m-2	54	0.11	-	-
HyFRC-f-1	89	0.23	0.12	-
HyFRC-f-2	89	0.42	0.14	-

[1] Measured within middle 102 mm of specimen width

5.3.2 Chloride permeation

The chloride content C_{Cl^-} of the cementitious matrix varied as a function of sample depth d from the ponding surface, where C_{Cl^-} is expressed as a proportion of chloride weight normalized by binder weight. Figure 5-7a plots the chloride content profiles of one sample from each specimen testing type. The plot considers cores taken at a noncracked surface, though microcracks may have been present in the matrix. Among reinforced concrete samples, C-0-1 exhibited the greatest

chloride content at each considered depth due to its greater matrix porosity, as indicated by the lower compressive strength (f'_c=45.0 MPa) of its concrete compared to that of preloaded specimens (f'_c=52.8 MPa). Generally, HyFRC exhibited lower chloride contents than plain concrete at the same depth from the ponding surface, with differences in C_{Cl^-} between the two composites more apparent at increased depths. Due to preloading, cores taken from HyFRC-m and HyFRC-f contained microcracks, the presence of which did not seem to be impactful on the chloride ingress compared to HyFRC-0. Because the compressive strength of HyFRC was either less than or similar to plain concrete, the lower diffusion rate of HyFRC was likely not due to a significant decrease in matrix porosity and the presence of embedded fibers may have slowed the rate of chloride diffusion. Steel and PVA fibers in a cementitious matrix have been reported to slow chloride transport though the composite [108], with steel fibers being attributed to act as chloride settling surfaces [107].

Figure 5-7b shows the influence of flexural cracking, as a result of mechanical preloading, on the chloride ingress of concrete and HyFRC. The plot reveals that cracked sections of C-fs-2 and HyFRC-f-1 showed greater chloride contents than corresponding cores taken where flexural macrocracks did not occur, indicating the faster rate of chloride transport within cracks. The chloride profiles of C-f-1 showed less sensitivity to the presence of cracks. As the surface flexural crack width of this sample (0.09 mm) was the lowest among all preloaded samples, its value was likely below a critical crack width threshold to cause significant effects on the NaCl solution ingress rate [9, 134].

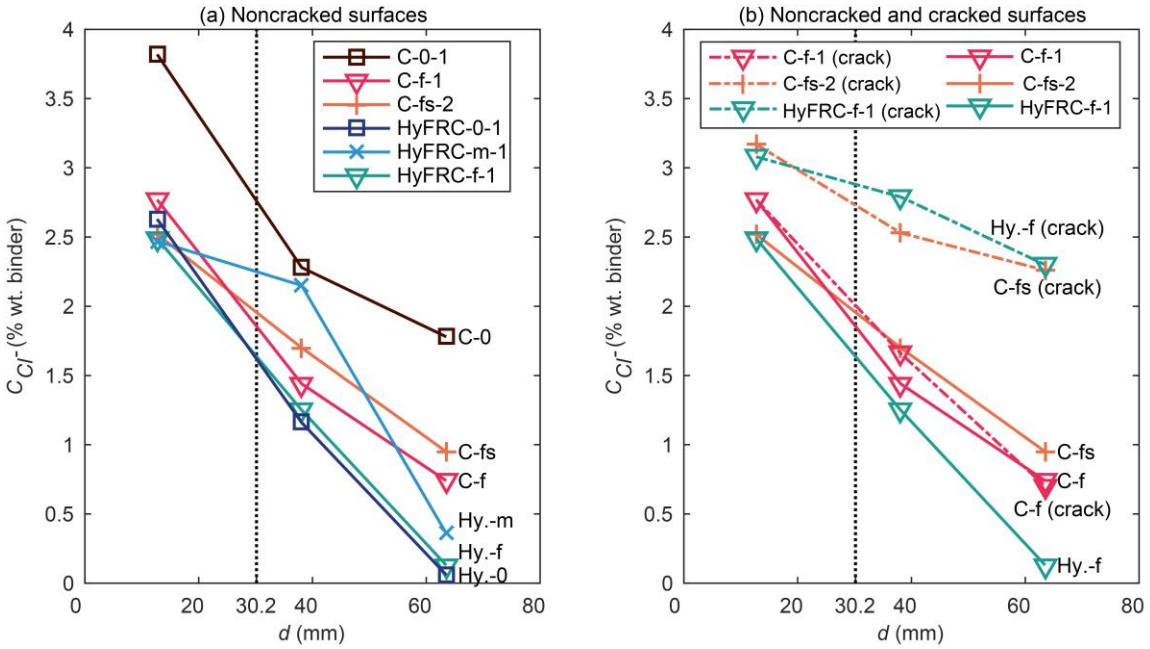


Figure 5-7: Chloride content C_{Cl^-} determined at depth d from beam ponding surface: (a) Considering all sample types, taken at noncracked surfaces only; (b) Considering only sample types with preload-induced flexural macrocrack, with chloride contents reported at cracked and noncracked surfaces for each considered sample. The centroid of the steel reinforcing bar is expected to occur at d=30.2 mm.

5.3.3 Corrosion rate monitoring

Results of the corrosion current I_{corr} monitoring of samples without and with preload-induced macrocracks are presented in Figure 5-8a-b and Figure 5-8c-d, respectively. While corrosion current density, which is the corrosion current normalized by the anodic surface area of the steel rebar, is often reported in the literature, the actual surface area of the specimens could not be determined nondestructively considering the limitations of the experiment. As will be discussed in Section 5.4, the active surface area of the rebar generally does not remain constant during the exposure duration. The plots include the responses of samples until corrosion initiation detection (Figure 5-8a and c), which is recognized by a sharp increase in I_{corr} between consecutive measurement times. Considering the nonloaded condition, use of HyFRC compared to plain concrete resulted in a corrosion initiation time that was longer by a factor of at least 1.7. The delay is attributed to a slower rate of chloride diffusion through the fiber-reinforced matrix, as mentioned in Section 5.3.2. Because there were no appreciable differences in corrosion initiation time between HyFRC-0 and HyFRC-m, preload-induced microcracking in the HyFRC matrix may be tolerated with no apparent effect on the depassivation of the steel rebar. The result correlates with the marginal effect of microcracking on the chloride diffusion of HyFRC. Cracked specimens belonging to the sample types of C-fs and HyFRC-f showed active corrosion behavior within the initial 18 weeks of ponding, with the specific sample HyFRC-f-1 showing active corrosion after 2 weeks of exposure. Preloaded reinforced concrete samples lacking splitting cracks (C-f) exhibited corrosion initiation after 30 weeks, showing a delay compared to reinforced concrete samples with splitting cracks (C-fs). Further discussion of corrosion initiation behavior for both composite types is detailed in Section 5.4.1.

Corrosion current measurements from the complete experimental duration are presented in Figure 5-8b and Figure 5-8d, with the mean I_{corr} response based on specimen type explicitly plotted. For all specimen types with flexural macrocracks present prior to exposure (Figure 5-8d), the mean corrosion current at the conclusion of experimentation was in the range of 240 μA to 310 μA. As shown in Figure 5-8b, the final mean I_{corr} for nonloaded specimen groups C-0 and HyFRC-0, which exhibited the greatest and lowest corrosion rate of all sample types, respectively, differed by an order of magnitude.

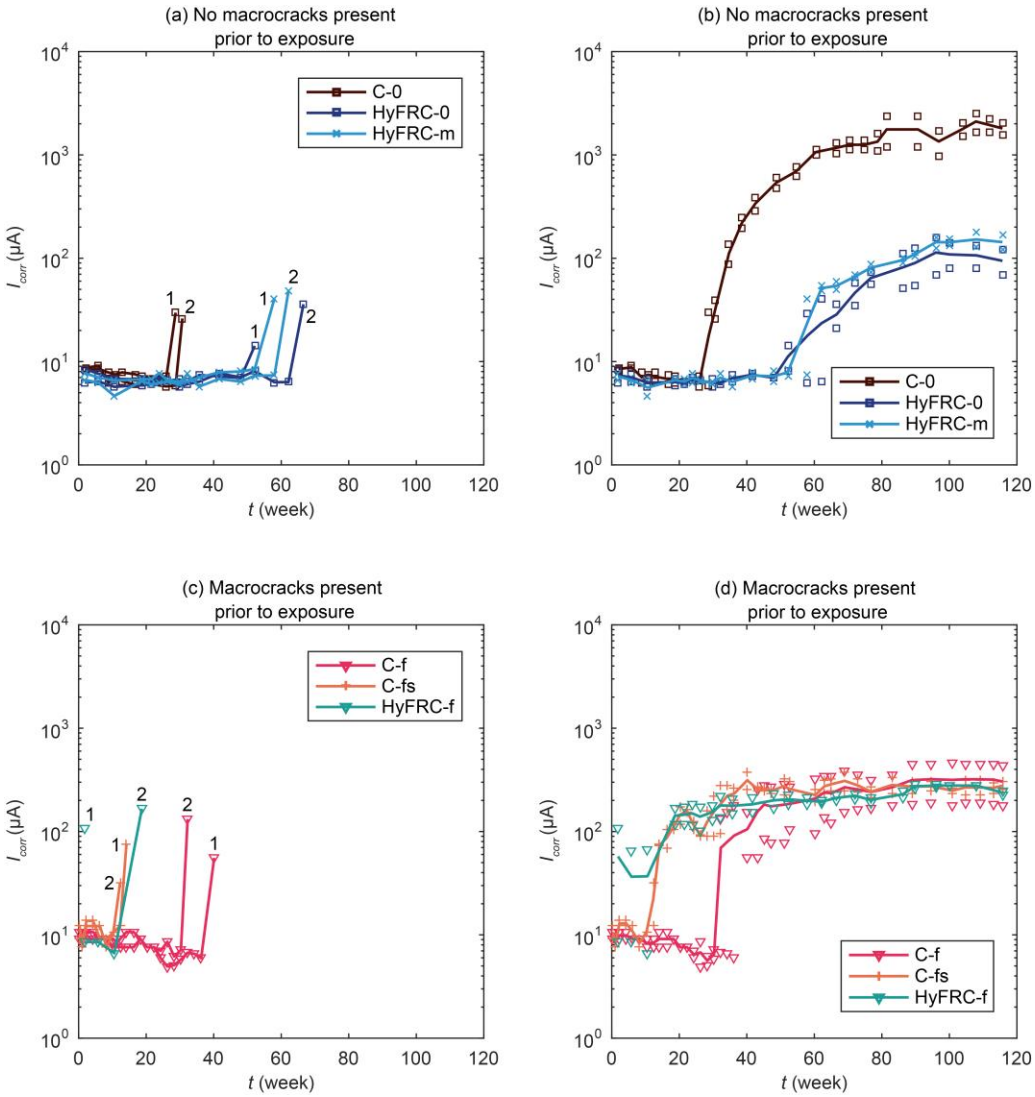


Figure 5-8: Corrosion current I_{corr} of the rebar of interest versus environmental conditioning time t: (a) -(b) Response of samples without macrocracks prior to exposure; (c)-(d) Response of samples with macrocracks prior to exposure. (a) and (c) plot the responses until corrosion initiation occurs. Numbers in the plots indicate the specimen name suffix. (b) and (d) plot the complete mean response.

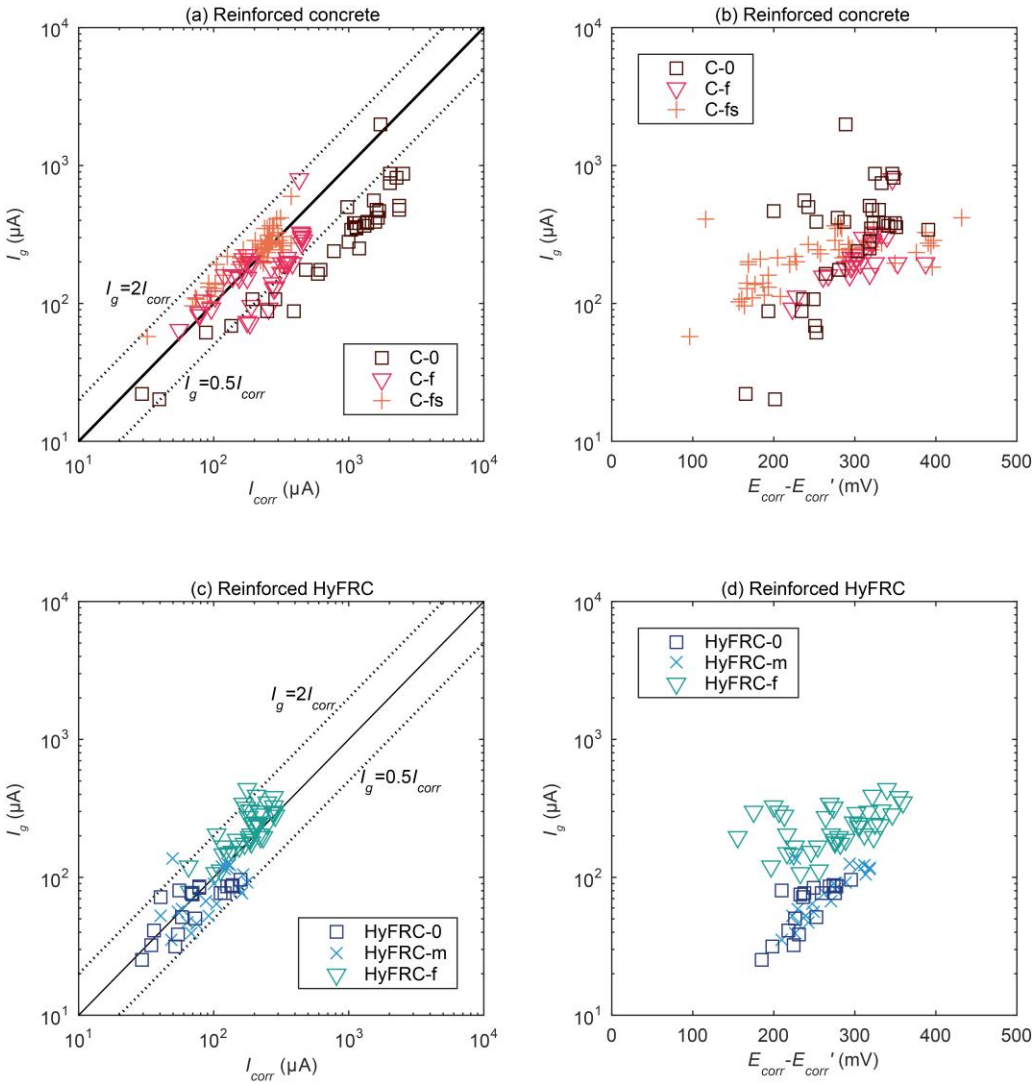


Figure 5-9: Galvanic current I_g versus electrochemical parameter: (a) and (c) versus corrosion current I_{corr} of the rebar of interest in C and HyFRC samples, respectively; (b) and (d) versus the difference between corrosion potential of the rebar of interest E_{corr} and corrosion potential of secondary rebar E_{corr}' in C and HyFRC samples, respectively. The solid black lines in (a) and (c) occur where I_g=I_{corr}.

Electrical connection of the 9.5 mm-diameter steel reinforcing bar of interest to a 19 mm-diameter secondary bar within the composite sample caused a galvanic, or macrocell, current to flow between the bars. Figure 5-9a and c plot the relationship between the magnitude of the galvanic current I_g and the corrosion current I_{corr} of the rebar of interest for reinforced concrete and reinforced HyFRC samples, respectively. The plots consider I_{corr} measurements greater than 10 μA, which are indicative of actively corroding samples at the time of testing. Measurements of galvanic current and corrosion current were generally on the same order of magnitude and were mostly bound between the relationships of I_g=0.5I_{corr} and I_g=2I_{corr}, suggesting that both I_{corr} and I_g should both be considered when evaluating the overall corrosion activity of steel reinforcing bars in electrical contact with other rebar in a cementitious composite. Hansson et al. [135] investigated reinforced concrete beam samples containing a single steel rebar of interest electrically connected to two steel bars located at a different depth within the beam and found that the galvanic current

and the corrosion current of the rebar of interest were also comparable on the same order of magnitude. For I_{corr} values greater than 10^3 μA, I_g measurements in this experiment tended to be less than $0.5I_{corr}$, indicating a high I_{corr} dominates the corrosion activity of the rebar of interest compared to galvanic corrosion. This condition only affected C-0 samples. A greater difference between the corrosion potential of the rebar of interest E_{corr} and the corrosion potential of the secondary rebar E_{corr}' is expected to result in a greater galvanic current between the two rebar. As shown in Figure 5-9b, C-0 samples exhibited similar I_g values as C-f and C-fs samples when the corrosion potential difference was also similar, indicating the magnitude of the corrosion current I_{corr} of the rebar of interest may not necessarily provide an accurate prediction of I_g. A comparable relationship between corrosion potential difference and galvanic current may be observed for reinforced HyFRC samples as well (Figure 5-9d).

Using I_{corr} and I_g measurements, the expected total rebar mass loss ΔM_{total} of select specimens may be calculated based on Faraday's first law of electrolysis (Equation 5-1) and compared against the gravimetric mass loss ΔM_{grav}. The gravimetric mass loss is the actual, physical mass loss and was determined by finding the difference between the measured rebar mass prior to specimen fabrication and the measured rebar mass at the conclusion of experimentation.

$$\Delta M_{total} = \frac{Qm}{zF} \qquad \text{Equation 5-1}$$

Table 5-5: Comparison of expected and actual mass loss of rebar of interest.

Specimen	ΔM_{icorr} (g), expected based on i_{corr}	ΔM_{ig} (g), expected based on i_g	ΔM_{total} (g), expected total ($\Delta M_{icorr}+\Delta M_{ig}$)	ΔM_{grav} (g), gravimetric[1]	Estimation factor ($\Delta M_{grav}/\Delta M_{total}$)
C-0-1	20.9	7.91	28.8	23.9	0.83
C-f-1	2.02	1.93	3.96	4.6	1.16
C-fs-2	3.70	4.14	7.84	8.0	1.02
HyFRC-0-1	0.655	0.604	1.26	0.4	0.32
HyFRC-m-1	1.08	0.952	2.04	1.0	0.49
HyFRC-f-1	3.80	3.81	7.60	3.8	0.50

[1] Measured to nearest 0.1 g.

In Equation 5-1, ΔM_{total} is the expected steel mass loss, Q is the total electric charge exchanged by the rebar of interest and is estimated by summation of the trapezoidal integrations of I_{corr} and I_g responses against t (as in Figure 5-8b), m is the molar mass of iron (m=55.9 g/mol), z is the valence of the oxidation reaction of iron (z=2), and F is Faraday's constant. Comparisons of the accumulated expected mass loss ΔM_{total} and gravimetric mass loss ΔM_{grav} are summarized in Table 5-5. An estimation factor ($\Delta M_{grav}/\Delta M_{total}$) is also reported to quantify disparities between the expected and actual mass loss measurements, with the factor varying from 0.83 to 1.16 for reinforced concrete and from 0.32 to 0.50 for reinforced HyFRC. A nonunity factor is reasonable, considering the Stern-Geary coefficient was assumed as B=26 mV/decade and has an intrinsic error factor of 2, which would impact the magnitude of the I_{corr} measurements [131]. In addition, I_{corr} is sensitive to the local relative humidity of the cementitious matrix while the samples undergo wet-dry cycling. Babaee and Castel [97] reported that the corrosion rate of reinforced concrete during a 2-week drying cycle reduced to as low as 25% of the measurement value taken at the end of a preceding wetting cycle. All electrochemical measurements obtained in this study occurred

during a wetting cycle and did not consider changes in corrosion rate during a drying cycle. The lower estimation factors of reinforced HyFRC compared to reinforced concrete suggest that corrosion activity monitoring of the former composite may lead to overestimations of the overall mass loss of steel reinforcing bar under wet-dry cyclic conditions, which would result in a conservative estimate of rebar mass loss.

5.4 Discussion

5.4.1 Corrosion initiation

For preloaded samples, corrosion initiation time was dependent on an individual sample's retention of flexural elastic stiffness, quantified as the ratio of the cracked flexural stiffness K_{cr} to the elastic flexural stiffness K_{el}. The cracked flexural stiffness was based on the mean residual stiffness of a preloaded beam considering the second to fifth cycles of the 5-cycle set. Figure 5-10 plots the relationship between K_{cr}/K_{el} and corrosion initiation time t_{int}. Stiffness retention values less than 35% generally correlated to a shorter corrosion initiation time, as highlighted by the explicitly plotted segmented line, which disregards the outlying data point of specimen HyFRC-f-1. During preloading of conventional reinforced concrete, the formation of matrix splitting cracks degrades the rebar-matrix bond strength and allows for greater slippage of the rebar from the concrete [136], resulting in reduction of the flexural stiffness of a beam. The presence of surface splitting cracks in C-fs samples, indicative of high rebar-matrix interfacial damage, resulted in the shortest corrosion initiation time. Similar effects of interfacial damage were reported by Michel et al. [92]

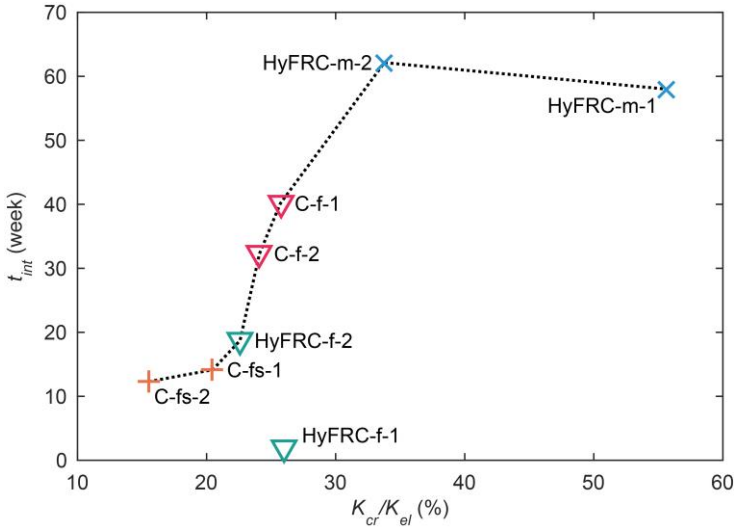


Figure 5-10: Corrosion initiation time t_{int} versus flexural stiffness retention K_{cr}/K_{el}.

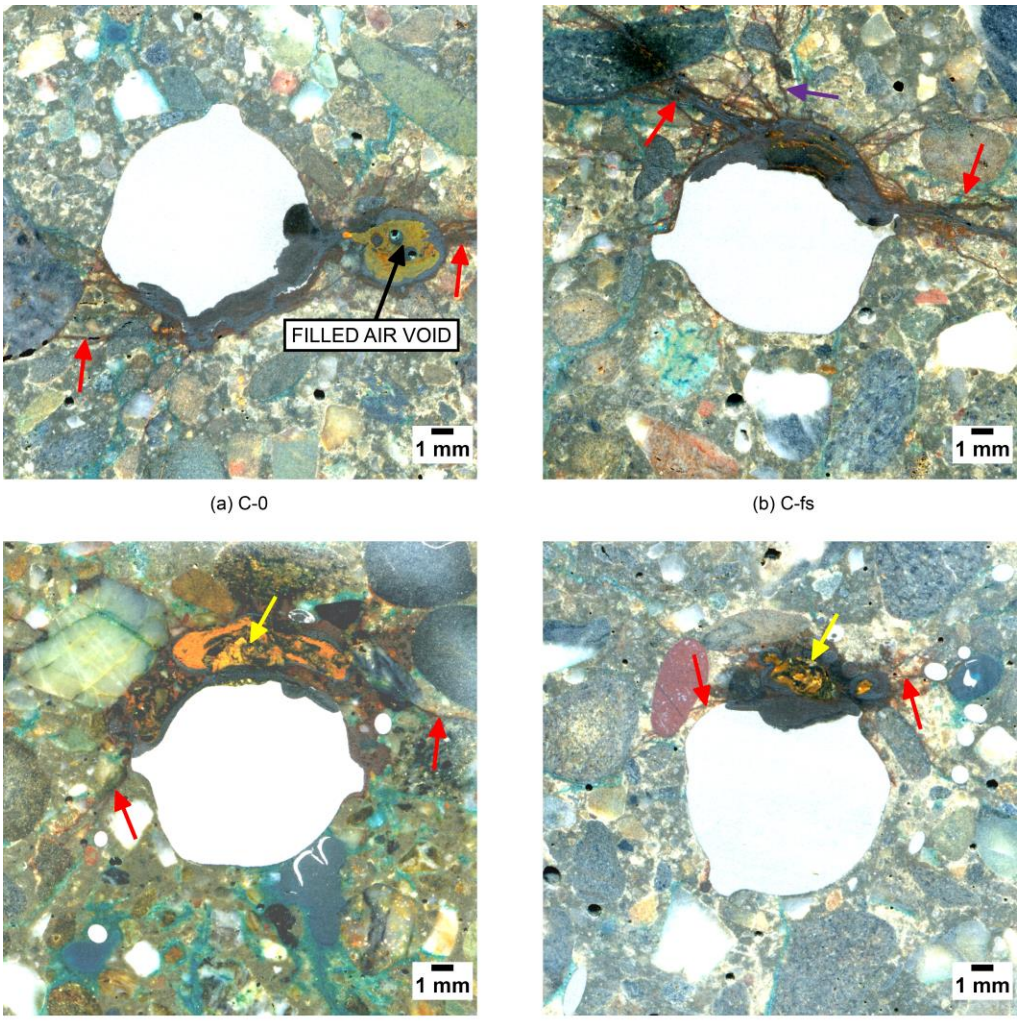
Considering the results of HyFRC-m samples, which ranged in stiffness retention values from 34% to 56%, a difference of only 4 weeks between t_{int} of the samples was measured. The corrosion initiation times of these samples were also previously found to be similar to nonloaded reinforced HyFRC (Figure 5-8a), suggesting that above a threshold of approximately K_{cr}/K_{el}=35%, t_{int} becomes insensitive to preload damage of reinforced HyFRC. Because HyFRC has considerably greater splitting crack resistance [44, 55] and greater rebar-matrix bond strength [50] than plain concrete, microcrack damage in the HyFRC cover dominated the reduction in flexural

stiffness over splitting cracks that may have initiated at the rebar-matrix interface, if any. However, when HyFRC is further damaged, t_{int} is significantly reduced. The stiffness reduction of HyFRC-f-2 was likely dictated by flexural macrocracks that propagated within the matrix during loading, which opened to a maximum surface width of 0.14 mm. To produce such crack damage during preloading, this sample was subjected to a high peak midpoint displacement (1.05 mm) and high peak load (89 kN). In comparison, the greatest peak midpoint displacement and peak load exhibited by any preloaded reinforced concrete sample was 0.83 mm and 54 kN, respectively. Surface splitting cracks could not be observed on any HyFRC-f beam surface and may not have contributed significantly to the flexural stiffness reduction. While mechanical enhancements from hybrid fiber reinforcement exist for reaching greater deflection and load resistance levels, severe loading of HyFRC composites results in marginal benefits with regard to corrosion initiation delay when its flexural stiffness retention is reduced to approximately K_{cr}/K_{el}=26% and less.

5.4.2 Corrosion products

The process of corrosion product formation in noncracked conventional reinforced concrete has been attributed to a three-phase process, as detailed by Liu and Weyers [137]. First, corrosion products occupy local pores at the rebar-matrix interfacial zone with no exertion of stress on the matrix. Second, after empty pores are filled, additional expansive growth initiates the accumulation of stress on the matrix. Finally, splitting cracks form when the accumulated stress exceeds the matrix cracking strength. Corrosion products may then occupy the splitting cracks and migrate from the rebar surface, as shown in transverse sections for reinforced concrete samples in this study (Figure 5-11a-b). Where preload-induced crack tips reach the rebar surface, corrosion products may freely form in the open cracks in addition to the rebar-matrix interfacial zone. However, reinforced concrete samples still remain susceptible to corrosion-induced splitting crack damage. Considering the presented cross-section of C-fs, the wider product-filled cracks (as indicated by red arrows in Figure 5-11b) were likely caused by corrosion activity due to preload-induced splitting cracks typically forming directly above the location of the reinforcing bar. The purple arrow in the section indicates the splitting crack that reached the surface of the beam, matching the location of the surface splitting crack formed after preloading.

The inclusion of fiber reinforcement altered the manner of corrosion product growth accommodation at the rebar-matrix interface. As shown in Figure 5-11c-d, corrosion products noticeably permeated into the bulk cement paste matrix, as indicated by yellow arrows in the images. While some penetration of corrosion products into the matrix is expected for conventional reinforced concrete [138], the depth of penetration was observed to be much more significant in HyFRC than plain concrete. Corrosion products in HyFRC composites are expected to exert stresses to initiate splitting cracks, however, crack widening and propagation is highly restricted due to crack closure stresses imposed by the fibers. After occupying the limited volume of splitting cracks in HyFRC, corrosion products then migrate into the porous cement paste matrix, locally densifying it.



(a) C-0 (b) C-fs

(c) HyFRC-0 (d) HyFRC-f

Figure 5-11: Optical imaging of representative transverse sections of rebar of interest and surrounding matrix: (a) C-0; (b) C-fs; (c) HyFRC-0; (d) HyFRC-f. A blue-colored epoxy impregnated surface voids and cracks. Red arrows indicate the location of observable cracks, purple arrows (reinforced concrete samples only) indicate preload-induced splitting cracks, yellow arrows (reinforced HyFRC samples only) indicate corrosion products located within cement paste or voids. The images are orientated such that the ponding surface occurs above the location of the rebar, as presented.

Powder X-ray diffraction was performed on one sample from each sample type. Representative X-ray powder diffractograms of C-0 and HyFRC-0 are presented in Figure 5-12, while Table 5-6 summarizes identified corrosion products present in considered samples. All sample types contained goethite (α-FeOOH), magnetite (Fe_3O_4), and ferrihydrite ($Fe_5HO_8 \cdot 4H_2O$). The presence of these rust minerals in reinforced concrete has been reported by others [139, 140].

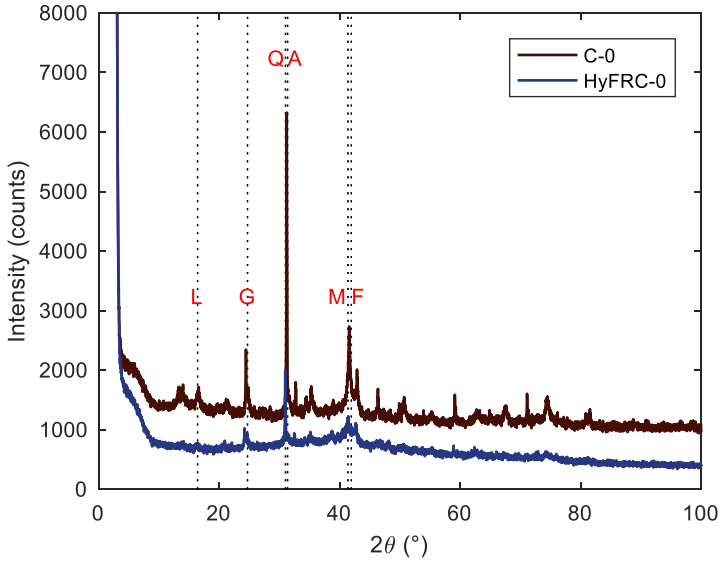


Figure 5-12: X-ray powder diffractograms of C-0 and HyFRC-0. Diffraction peaks correspond to compounds: A (Akaganéite), F (Ferrihydrite), G (Goethite), L (Lepidocrocite), M (Magnetite), Q (Quartz).

Table 5-6: Presence of corrosion products on rebar surface as identified by XRD.

Sample	Gravimetric mass loss (g)[1]	Goethite	Akaganéite	Lepidocrocite	Magnetite	(2-line) Ferrihydrite
		α-FeOOH	β-FeOOH	γ-FeOOH	Fe_3O_4	$Fe_5HO_8{\cdot}4H_2O$
C-0	23.9	Yes	Yes	Yes	Yes	Yes
C-f	4.6	Yes	Yes	Yes	Yes	Yes
C-fs	8.0	Yes	Yes	Yes	Yes	Yes
HyFRC-0	0.4	Yes	-	-	Yes	Yes
HyFRC-m	1.0	Yes	Yes	-	Yes	Yes
HyFRC-f	3.8	Yes	Yes	-	Yes	Yes

[1] Measured to nearest 0.1 g.

Akaganéite (β-FeOOH) was detected in all samples except for HyFRC-0. While this compound is typically found in Cl-rich environments [141], its absence in HyFRC-0 does not necessarily indicate lower chloride contents near the site of corrosion in that sample. HyFRC-0 was previously noted to have similar chloride contents as preloaded HyFRC composites when macrocracking was not present (Figure 5-7a) and noted to have a similar corrosion initiation time as HyFRC-m (Figure 5-8a), suggesting the chloride content in HyFRC-0 was sufficiently high to form akaganéite if the rust mineral could also be formed in HyFRC-m. The previous results also indicated that microcracks have marginal effects on the time for corrosion initiation to occur, however, such microcracks may be influential on corrosion propagation behavior. After corrosion products fill local pores and voids at or near the rebar-matrix interface, stresses are exerted on the matrix due to the volumetric growth of the products, which causes reactionary stresses to be placed on the products from the matrix, which may densify the products. Šavija et al. [122] reported that the confinement of products by fiber reinforcement resulted in greater measured elastic moduli of corrosion products, with the confinement effect producing both uniform mechanical and chemical rust layers. For HyFRC samples in this study, the confinement effect may have been most effective for the nonloaded, sound HyFRC-0 samples compared to preloaded HyFRC samples due to matrix

cracking damage in the latter sample sets, as previously quantified by degradation of elastic flexural stiffness (Figure 5-10). Presumably, a greater confinement effect would result in greater densification of corrosion products at the rebar-matrix interface, which may impede the transport of chlorides or oxygen from reaching the rebar steel surface [125, 142]. The resistance towards chloride transport may have prevented local formation of akaganéite in HyFRC-0.

Another rust mineral whose presence differed between samples types was lepidocrocite (γ-FeOOH), which was found in all reinforced concrete samples but was absent in all reinforced HyFRC samples. Lepidocrocite is a corrosion product that is formed through a green rust intermediate, and transforms into the more thermodynamically stable goethite over time [143]. Lepidocrocite may not have formed in reinforced HyFRC due to the confinement effect imposed on the corrosion products by the fiber-reinforced matrix, which may have hindered the transport of oxygen through the confined rust layers and slow the rate of green rust oxidation. Rather than transforming into lepidocrocite, magnetite transformation is preferred when a low oxidation rate of green rust occurs [143].

5.4.3 Electrochemical and physical damage

Use of hybrid fiber reinforcement was found to be effective for reducing total steel rebar mass loss compared to conventional concrete. Figure 5-13 plots the adjusted predicted steel mass loss $\Delta m_{total}'$ of individual samples as a function of corrosion propagation time t_{prop}. The adjusted predicted mass loss at any time is given by (2):

$$\Delta m_{total}' = \Delta m_{total} \left(\frac{\Delta M_{grav}}{\Delta M_{total}}\right) \qquad \text{Equation 5-2}$$

All predicted steel mass loss values Δm_{total} at a given time, using Faraday's first law of electrolysis, are adjusted by the estimation factor $\Delta M_{total}/\Delta M_{grav}$ of a specimen's testing group that was previously presented in Table 5-5. When considering the mass loss of the entire rebar, HyFRC-0 and HyFRC-m samples were more effective than concrete for reducing total damage at a given corrosion propagation time. After 40 weeks, HyFRC-f samples also exhibited lower total mass loss compared to any conventional reinforced concrete sample.

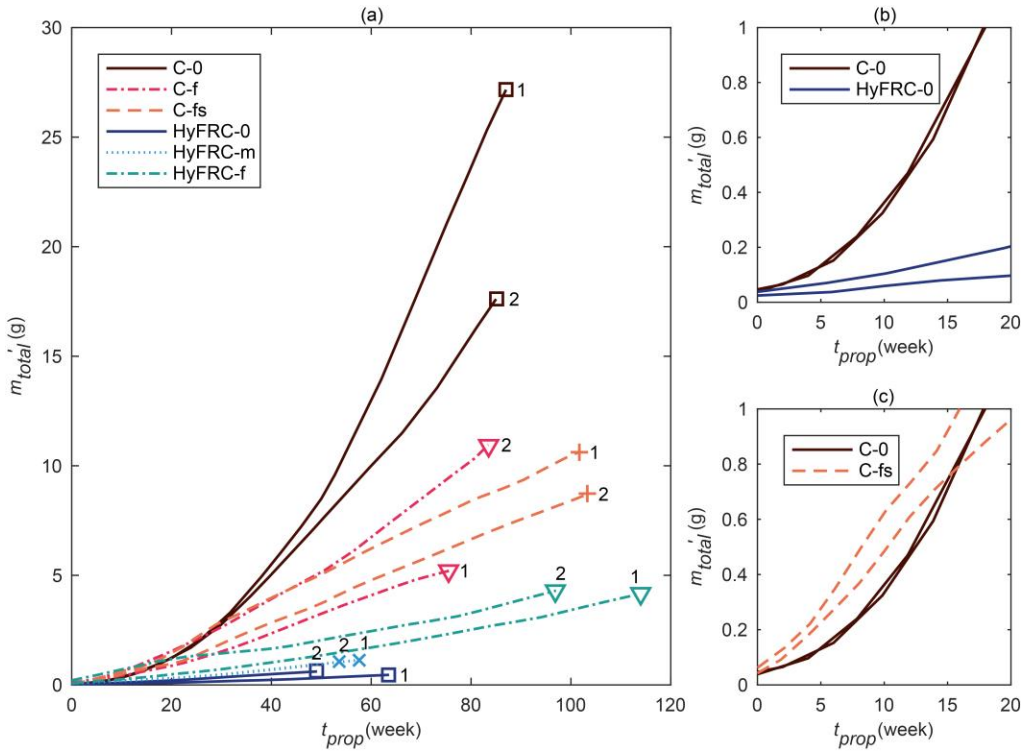
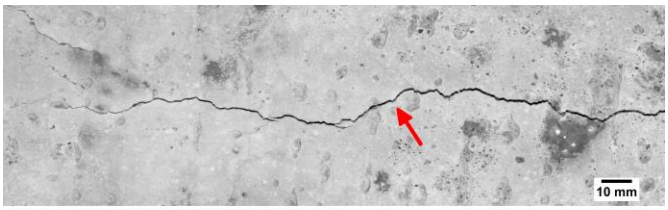


Figure 5-13: Adjusted expected steel mass loss $\Delta m'$ versus corrosion propagation time t_{prop}: (a) All samples for entire experimental duration; (b) Nonloaded samples C-0 and HyFRC-0 for initial 10 weeks of corrosion propagation time; (c) Reinforced concrete samples C-0 and C-fs for initial 10 weeks of corrosion propagation time. Note that corrosion propagation time is defined herein to begin at the time when the active corrosion is first detected for a sample.

Differences in the total mass loss of samples may be related to the propagation of corrosion-induced splitting cracks. Figure 5-14 shows a representative ponding surface of C-0 and HyFRC-0 samples at the conclusion of environmental conditioning. Because both samples were not preloaded, all surface macrocracking was corrosion-induced. A prominent splitting crack propagated along a considerable length of C-0, while cracking damage could not be detected on the HyFRC-0 surface. The restriction of splitting cracks by hybrid fiber reinforcement is impactful for reducing total rebar mass loss, as these cracks originate from the rebar-matrix interface and provide a free path for externally transported Cl^- to depassivate rebar surfaces within a splitting crack wake. In Figure 5-15a, widespread corroded surfaces may be observed on the rebar extracted from a C-0 sample at the conclusion of experimentation. In contrast, rebar corrosion damage of a HyFRC-0 sample was more localized (Figure 5-15b), owing to a lack of splitting crack propagation from the initial site of active corrosion. Correspondingly, the rate of rebar mass loss for C-0 samples was significantly greater than HyFRC-0 samples, as shown in Figure 5-13b. Due to the nonuniform distribution of corroded surfaces of rebar in cementitious composites, as visualized in Figure 5-11 and Figure 5-15, some caution should be considered when interpreting corrosion activity using corrosion current density, which is often normalized by the nominal surface area of rebar in contact with cementitious matrix and which may lead to inaccurate evaluations of actual corrosion rate.



(a) C-0

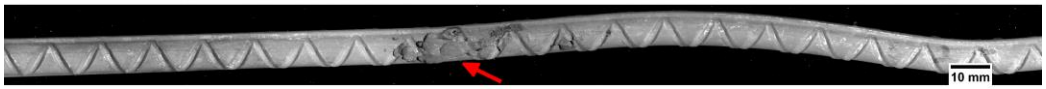


(b) HyFRC-0

Figure 5-14: Observed representative ponding surfaces of samples lacking preload damage at conclusion of environmental conditioning: (a) C-0, showing a corrosion-induced splitting crack; (b) HyFRC-0, showing no observable surface splitting cracks. Dark features on HyFRC surface are steel fibers with some rust formation at the surface only. Images are presented in grayscale to improve feature contrast.



(a) C-0



(b) HyFRC-0

Figure 5-15: Observed representative surfaces of extracted steel rebar of interest after manual extraction from specimens and removal of corrosion products: (a) C-0; (b) HyFRC-0. Deformations in the bars are due to process of manual extraction. Images are presented in grayscale to improve feature contrast.

Despite containing cracks prior to chloride exposure and having similar or longer active corrosion durations, preloaded C-f and C-fs samples exhibited less total rebar mass loss than nonloaded C-0 samples after test completion (Figure 5-13a). At the conclusion of environmental conditioning, the measured mean maximum surface splitting crack widths of C-fs, C-f, and C-0 samples were 0.18 mm, 0.20 mm, and 0.39 mm, respectively. Previously, the maximum splitting crack widths of C-fs samples after flexural preloading were measured in the range of 0.10 to 0.11 mm (Table 5-4). The measurements indicate that the impact of corrosion product formation on splitting crack widening is greatest when no or less cracks are present upon initial corrosion product formation. As previously mentioned, corrosion products freely occupy empty cracks at an actively corroding rebar surface. This action does not initially place stresses on the matrix, allowing preloaded, cracked samples to exhibit a retardation in corrosion-induced cracking, though the initial mass loss is greater within the initial 20 weeks of propagation behavior, as in Figure 5-13c. Similar influences of defects on delayed corrosion-induced cracking have been reported by Zhang et al. [123]

5.4.4 Post-corrosion composite mechanical properties

As a primary design purpose of HyFRC composites is to resist applied mechanical loading, structural evaluation of reinforced HyFRC with corrosion damage is of interest for serviceability determination. Figure 5-16 plots the results of residual flexural loading, which consisted of 5 cycles of loading to a peak load of 42 kN, regardless of composite type and prior preloading history. For samples subjected to preloading, the preload response is also included in the plots. Pertinent details of the mechanical responses are summarized in Table 5-7, which includes the cracked stiffness after corrosion $K_{cr,corr}$. This parameter was the mean of residual stiffness considering the second to fifth cycles of loading.

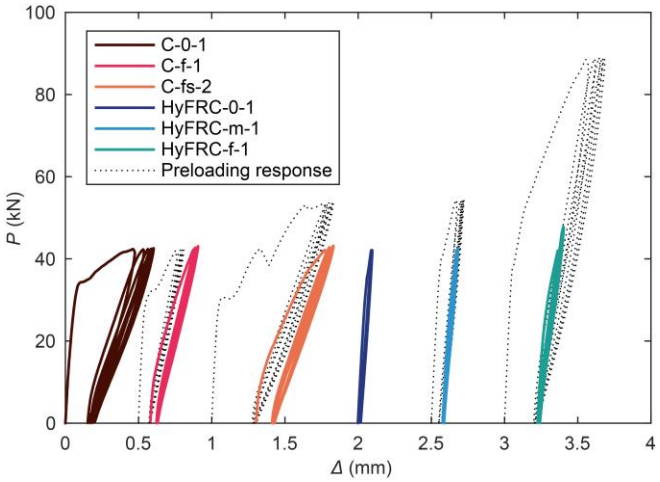


Figure 5-16: Residual flexural loading response after environmental conditioning: Applied load P versus midpoint deflection Δ. Preloading responses are included, if conducted. Specimen responses are offset by 0.5 mm or 1 mm for clarity.

Table 5-7: Summary of specimen mechanical characteristics after residual flexural loading.

Specimen	Preloading characteristics			Residual loading characteristics, after exposure		Residual midpoint disp. (mm)[3]
	K_{el} (kN/mm)	K_{cr} (kN/mm)	K_{cr}/K_{el} (%)	$K_{cr,corr}$ (kN/mm)	$K_{cr,corr}/K_{el}$ (%)	
C-0-1[1]	596-731[2]	-	-	107	14.6-17.9	0.20
C-f-1	731	189	25.8	146	20.0	0.05
C-fs-2	645	100	15.5	102	15.8	0.12
HyFRC-0-1[1]	719-791[2]	-	-	522	66.0-72.6	0.02
HyFRC-m-1	719	400	55.6	415	57.8	0.01
HyFRC-f-1	791	206	26.1	264	33.3	0.02

[1] Samples did not undergo preloading prior to exposure
[2] Based on response of 4 C or 4 HyFRC preloaded specimens
[3] Considers loading response after environmental conditioning only and does not consider residual midpoint displacement caused by preloading, if any

After 2.2 years of chloride exposure, initially nonloaded sample C-0-1 was reduced in flexural stiffness to approximately 14.6% to 17.9% of the elastic response of a pristine reinforced concrete sample. The retention in elastic stiffness is lower than preloading the sample to a load level of 42 kN in pristine condition (K_{cr}/K_{el}=25.8% for C-f-1), highlighting the reduction in rebar-

matrix bond caused by corrosion-induced splitting cracks. Corrosion damage also reduced the cracked stiffness of C-f-1 from K_{cr}=189 kN/mm to $K_{cr,corr}$=146 kN/mm. The stiffness of C-fs-2 did not significantly differ as the rebar-matrix bond in this sample, as a result of preload-induced splitting cracks, was already severely degraded such that additional corrosion damage was not able to further reduce the composite stiffness.

In contrast, preloaded samples HyFRC-m-1 and HyFRC-f-1 exhibited slight increases in cracked flexural stiffness. The increase in stiffness is attributed to an enhanced rebar-matrix bond due to corrosion product densification of the interfacial zone between the two materials [144]. Correspondingly, reloading of preloaded HyFRC resulted in marginal additional midpoint deflection of 0.01 mm to 0.02 mm, being noticeably less than the 0.05 mm to 0.12 mm residual midpoint displacements exhibited by preloaded reinforced concrete. Excessive deformation has been regarded as an issue for maintaining serviceability of prestressed reinforced concrete box girder bridges [145]. Use of HyFRC is not intended as a material to prevent corrosion of steel reinforcement, but rather, as a material to reduce damage caused by this phenomenon which would otherwise affect the mechanical performance of a structure. Its high crack resistance is crucial for maintaining rebar-matrix bond strength and allowing the composite to behave with little to no apparent degradation to stiffness properties within the considered testing load limits.

5.5 Summary and conclusions

In this chapter, reinforced concrete and reinforced hybrid fiber-reinforced concrete (HyFRC) beam elements were monitored for corrosion activity over a total duration of 116 weeks (2.2 years). To account for cementitious matrix cracking that occurs due to mechanical loading in field conditions, samples were flexurally preloaded prior to 3.5% w/w NaCl solution exposure to produce crack characteristics typical of increasing composite damage severity. Reinforced concrete was evaluated for corrosion behavior under conditions of no loading (C-0 sample type), surface flexural crack damage (C-f), and both surface flexural and splitting crack damage (C-fs), while reinforced HyFRC was evaluated under conditions of no loading (HyFRC-0), microcrack damage (HyFRC-m), and surface flexural crack damage (HyFRC-f). The following conclusions may be formulated based on the results:

1. Considering nonloaded samples and samples with only microcrack damage, use of HyFRC compared to conventional concrete resulted in a longer time to corrosion initiation by a factor of at least 1.7. The longer period coincided with lower chloride contents found in HyFRC, which is hypothesized to occur due to fiber reinforcement retarding the bulk diffusion rate of chlorides through the matrix. Where a surface macrocrack of width 0.12 mm or greater was present in either concrete or HyFRC, the local chloride diffusion rate was faster compared to a noncracked condition.
2. For preloaded samples, a lower residual stiffness factor (K_{cr}/K_{el}) was strongly associated with shorter corrosion initiation times. A lower retention of elastic stiffness for reinforced concrete was related to rebar-matrix interfacial damage, which was most severe for samples with splitting cracks. For reinforced HyFRC, a lower retention of elastic stiffness was related to flexural macrocracking. Above a threshold value of K_{cr}/K_{el}=35%, corrosion initiation time of HyFRC composites was not impacted compared to nonloaded samples despite the presence of microcracks in the matrix.

3. Hybrid fiber reinforcement altered the manner of corrosion product diffusion from the steel rebar surface compared to reinforced concrete. Because conventional concrete forms extensive splitting cracks after a sufficient amount of corrosion products has formed at the rebar-matrix interface, products may migrate away from the active rebar surface through cracks. The high crack resistance of HyFRC restricts splitting crack propagation, resulting in the diffusion of corrosion products into the porous bulk cement paste matrix.
4. Flexural and splitting cracks at the steel rebar surface provide an empty volume for corrosion products to feely migrate into after formation, resulting in initially greater rebar mass loss compared to noncracked samples. However, this action delays the stress accumulation on the matrix from expansive corrosion product formation, which would otherwise occur at a denser rebar-matrix interface in a noncracked condition. Particular to reinforced concrete samples, corrosion-induced splitting crack widening was less severe for samples already containing preload-induced cracks due to the stress accumulation retardation.
5. Propagation of corrosion-induced splitting cracks in reinforced concrete caused widespread formation of actively corroded rebar surfaces, resulting in increased total rebar mass loss compared to HyFRC composites. Due to the restriction of splitting crack propagation by fiber reinforcement, rebar corrosion was generally localized and the total mass loss was reduced. For samples not subjected to flexural preloading, the actual, gravimetric mass loss of the rebar from a reinforced concrete sample and a reinforced HyFRC sample were measured to be 23.9 g and 0.4 g, respectively.
6. Corrosion products in reinforced concrete were identified to include goethite (α-FeOOH), akaganéite (β-FeOOH), lepidocrocite (γ-FeOOH), magnetite (Fe_3O_4) and ferrihydrite ($Fe_5HO_8 \cdot 4H_2O$). Reinforced HyFRC samples contained the same rust species, except for lepidocrocite, which was absent from all HyRC composites. Mechanical confinement of corrosion products from the HyFRC may have densified the rust scales such that oxygen transport was hindered, resulting in the formation of magnetite over lepidocrocite when a low oxidation rate of a green rust intermediate occurs.
7. Residual mechanical loading of corroded samples revealed HyFRC did not degrade in flexural stiffness. In contrast, corrosion-induced splitting cracks further reduced the flexural stiffness of reinforced concrete if splitting crack damage was not already present in the sample.

6 Corrosion behavior of microfiber-reinforced cementitious composites using by X-ray micro-computed tomography

6.1 Introduction

The multiscale crack resistance approach of HyFRC is dependent on the hybridization of fiber materials and sizes in a single cementitious composite. HyFRC includes 0.04-mm diameter, 8-mm length polyvinyl alcohol (PVA) fibers to resist the initial propagation of matrix microcracks, which are the first type of cracks to form. Based on their function, these fibers are often referred to as microfibers to explicitly indicate the scale of cracks that are most effectively resisted. Proper microcrack control within fiber-reinforced cementitious composites is a critical precursor to achieving deflection- or strain-hardening behavior [146]. A conventional fiber-reinforced concrete (FRC) utilizing only long (e.g. length of 30 mm or greater) fibers will exhibit crack localization after the matrix cracking stress has been reached, as shown schematically in Figure 6-1a. Fibers for this composite are most effective at improving post-peak mechanical toughness but have less influence prior to the formation of a dominant crack. When microfibers are included into a conventional long fiber-reinforced concrete (Figure 6-1b), as in HyFRC, diffuse microcracking occurs after the matrix cracking stress has been reached. The distributive cracking behavior, which increases both the peak flexural load and deflection where the peak load occurs, is possible due to microfibers restricting the propagation of microcracks and placing closure stresses on the cracks at the onset of damage initiation. As additional flexural load is resisted by the composite and beam deformation increases, formation of new matrix microcracks is preferred and occurs at a lower stress than the propagation of existing, fiber-bridged microcracks. The toughness enhancement provided by microfibers in a hybrid fiber-reinforced concrete composite is not limited to flexural stress states, and may be extended to shear stress [147, 148], compressive stress [26, 149], and hoop stress about a longitudinal steel rebar [55, 150]. The latter stress state is similar to corrosion-induced hoop stress caused by corrosion product formation at a rebar-matrix interface.

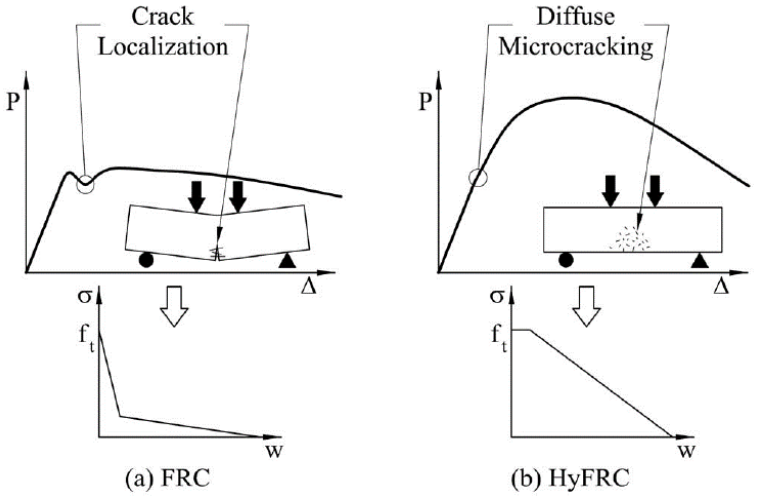


Figure 6-1: Effect of microfibers on HyFRC flexural response compared to conventional FRC. σ is stress, f_t is the concrete modulus of rupture, and w is the crack width. Schematic is reported by Blunt and Ostertag [24].

Observable microcracking of fiber-reinforced cementitious composites is often restricted to surface features. Damage caused by internal durability-related stresses, such as steel corrosion within reinforced concrete, is notably difficult to characterize using typical experimental methods due to the uncertainty of damage sites within the composite volume and the long experimental times required to induce such damage. Destructive testing may be used to evaluate accumulated damage, though provides limited information on the rate of damage. Specific to corrosion damage, determination of the actual corroded surface of the rebar in a nondestructive manner is often not performed, and the nominal surface area of the rebar in contact with the cementitious matrix is often assumed as the active corrosion surface when calculating the corrosion current density i_{corr}. Such assumptions may lead to inaccurate interpretations of the actual corrosion rate considering the nonuniform corrosion behavior that was visually observed for corroded samples presented in Chapter 4 and Chapter 5.

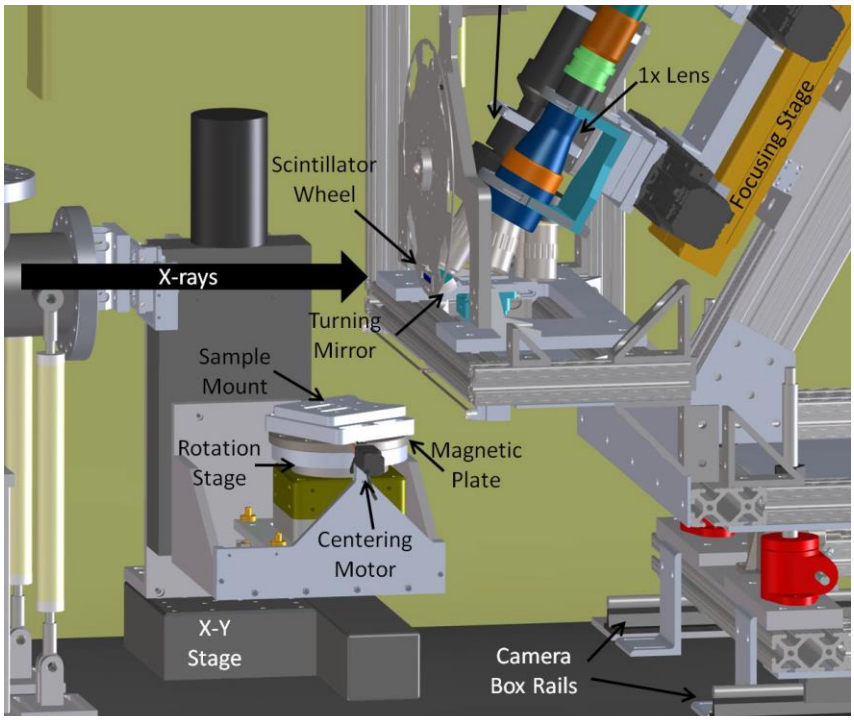


Figure 6-2: Microtomography experimental setup at beamline 8.3.2 at Advanced Light Source. Schematic is reported by the Advanced Light Source [151].

To address the aforementioned issues in experimental methods related to internal corrosion damage characterization of reinforced concrete, X-ray micro-computed tomography (microtomography or μCT) may be utilized. Microtomography experiments can be performed at beamline 8.3.2 at the Advanced Light Source synchrotron of the Lawrence Berkeley National Laboratory. A schematic of the experimental setup at the beamline is shown in Figure 6-2. In this characterization technique, a horizontal X-ray beam typically penetrates a sample of interest and a series of projection images are acquired as the sample is rotated about the axis perpendicular to the horizontal plane. The transmitted intensity is detected by a charge couple device (CCD) area detector. When monochromatic light is used in absorption mode, the transmitted intensity I is based on the initial intensity I_0, the linear attenuation coefficient μ_i of a material phase i, and the thickness x_i of a material phase i, as described by Beer's Law (Equation 6-1):

$$I = I_0 \exp(-\Sigma \mu_i x_i)$$ Equation 6-1

The attenuated value $P(t, z)$ for each pixel (t, z) on the detector is described by Equation 6-2 and Figure 6-3 schematically shows a representation of the coordinate system for an object at z:

$$P(t, z) = -\ln\left(\frac{I(t,z)}{I_0}\right)$$ Equation 6-2

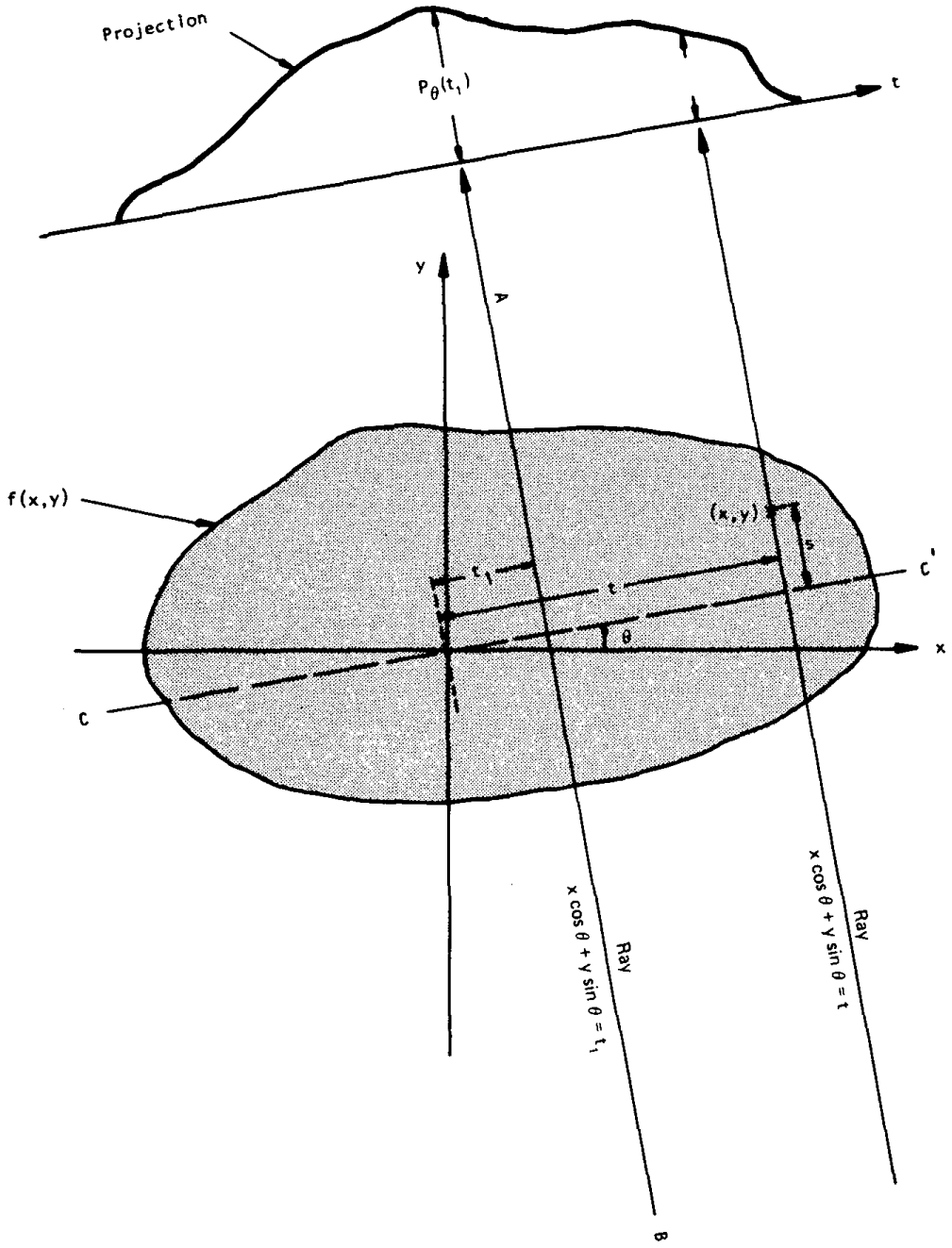


Figure 6-3: Schematic showing an object and its projection, as reported by Kak and Slaney [152].

Acquired parallel beam projection images are based on the transmitted intensity of the X-ray beam passing through the sample at a certain rotational angle φ, as indicated in Figure 6-4. The attenuation $P(\varphi, x', z)$ may also be described as the Radon transform of the linear attenuation field $\mu(x, y, z)$ (Equation 6-3):

$$P(\varphi, t, z) = \iint_{\Omega} \mu(x, y, z)\delta(x\cos\varphi + y\sin\varphi - t)dxdy \qquad \text{Equation 6-3}$$

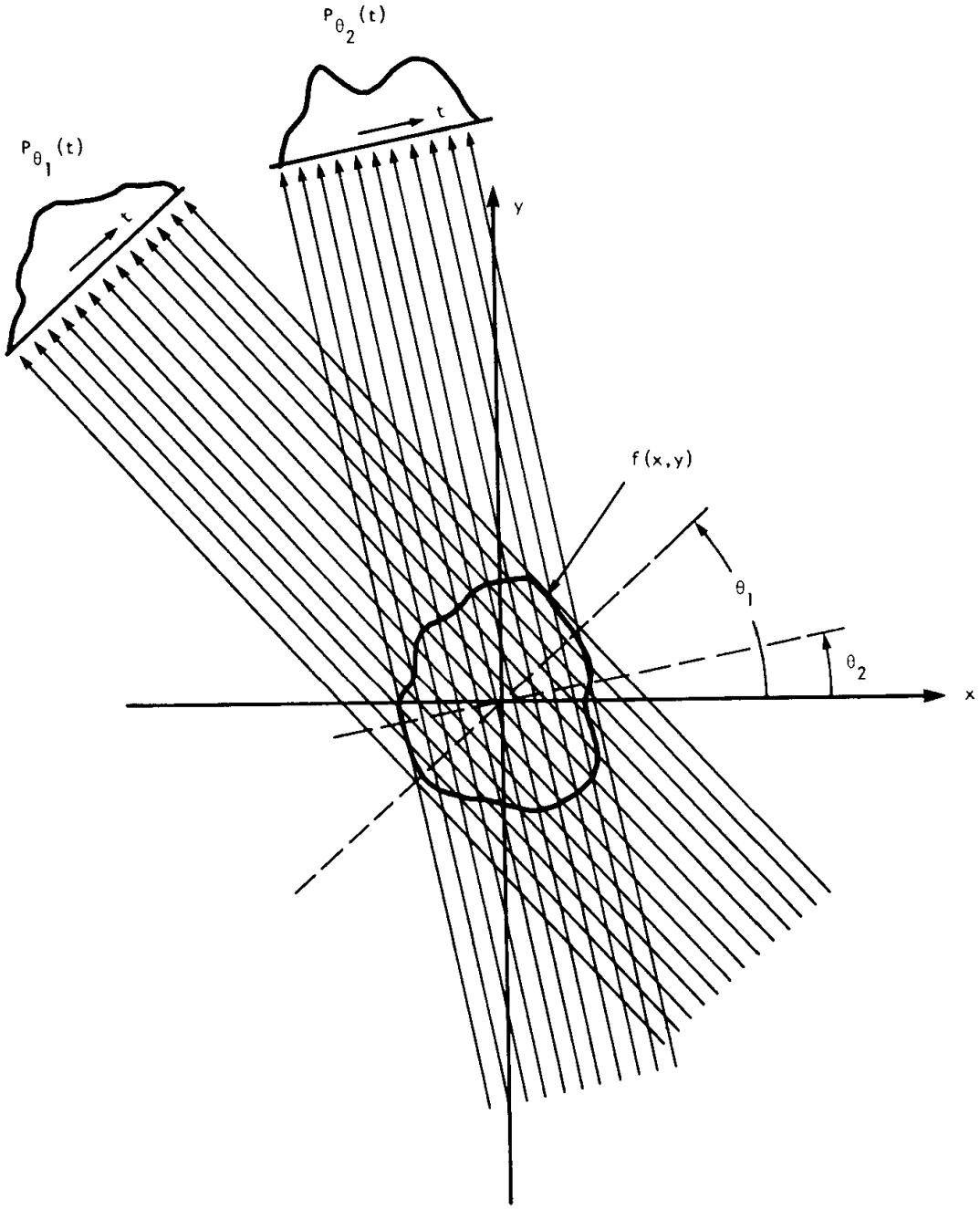


Figure 6-4: Schematic of projections taken at different angles, as reported by Kak and Slaney [152].

In Equation 6-3, the δ function describes the path of X-rays through the sample. To obtain $\mu(x, y, z)$, the Fourier slice theorem must be used to invert the expression of $P(\varphi, t, z)$ in a process typically referred to as reconstruction, which is detailed further by Kak and Slaney [152]. The resulting tomograms describe information of the material of interest by assigning each voxel in an image stack of tomograms with an absorbance value. For concrete materials, which may contain many different phases within a single composite, use of µCT techniques is thus advantages for identifying individual phases within a sample, assuming the phase contrast is sufficiently high. Figure 6-5 shows a possible image analysis sequence possible with µCT for fiber-reinforced cementitious composites.

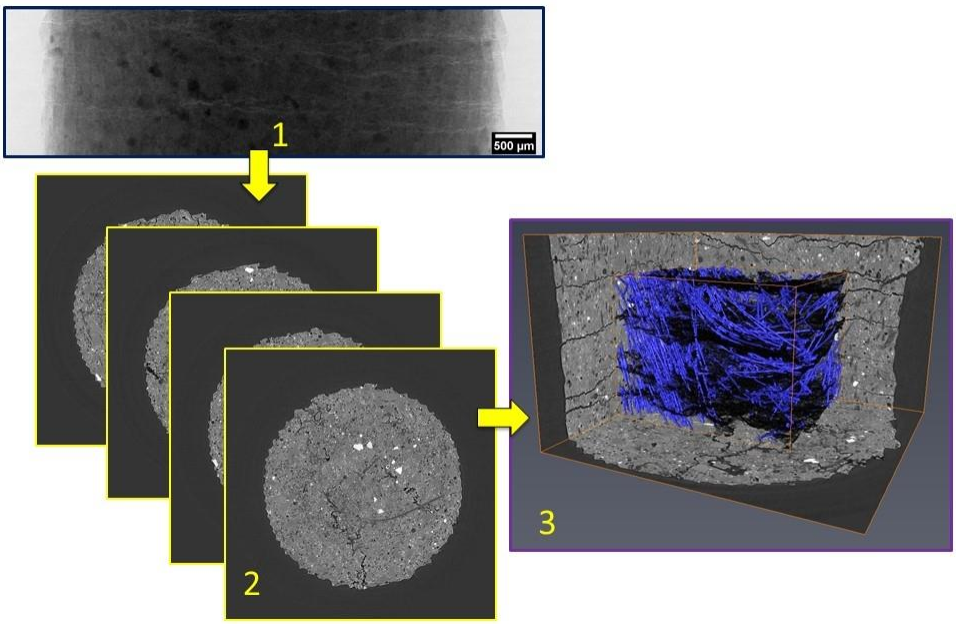


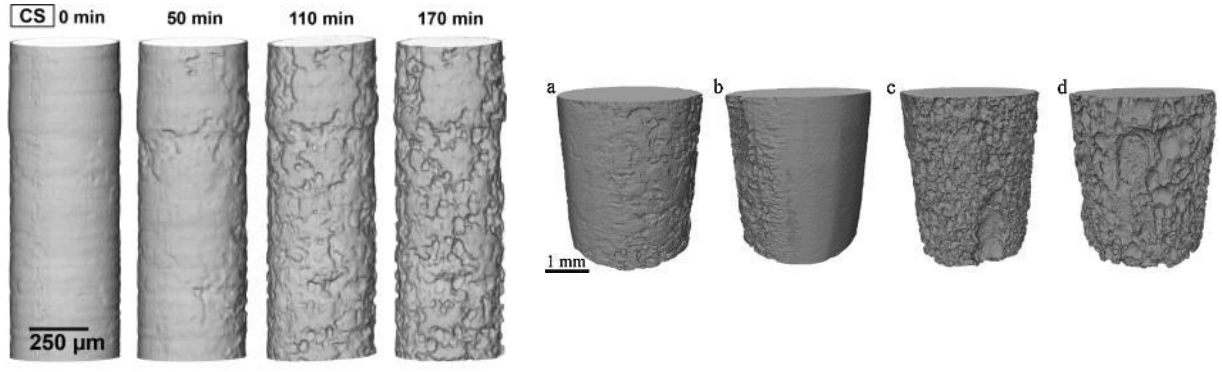
Figure 6-5: Possible image analysis sequence: (1) Obtain X-ray radiographs from µCT experimentation; (2) Reconstruct radiographs into horizontal cross-section tomograms; (3) Use tomogram image stack to obtain 3D information.

X-ray micro-computed tomography has been validated as an effective technique for characterizing internal degradation processes that result from environmental exposure of cement-based materials. In-situ visualizations of alkali-silica reaction gel formation [153-156], ice formation within matrix voids [157], matrix cracking from sulfate attack [158], and erosion due to bacterial weathering [159] have been reported in the literature. Monitoring of corrosion damage in cementitious composites using µCT has also been investigated, as surveyed in Table 6-1. All of the surveyed studies [122, 160-163] relied on the use of an impressed current to artificially accelerate corrosion as opposed to allowing corrosion to occur naturally under ambient conditions. Accelerated corrosion methods provide a user with corrosion damage information in a significantly reduced experimental duration at the cost of possible introduction of experimental artifacts, including altered corrosion product chemical composition, acidification at the rebar-matrix interface, larger crack widths for the same amount of mass loss, and more uniform corrosion in contrast to localized corrosion [164, 165]. Visualizations of the corroded bar from the studies of Itty et al. [163] and Sun et al. [162] show generally nonlocalized corrosion damage characteristics when using an impressed current.

Table 6-1: Survey of X-ray computed tomography studies on corrosion behavior of reinforced cementitious composites. References are listed in descending order of total environmental exposure duration.

Reference	Composite materials	Corrosion method[1]	Exposure duration	Steel region of interest dimensions[2] (l_{scan}/d)	CT experimental parameters
Beck et al. [160]	Unspecified cement mortar; S 235 JR G2 steel	Stepwise galvanostatic; i_g=5 to 25 μA/cm^2	40 days	d=9 mm; l_{scan}=10 mm; l_{scan}/d=1.1	45 μm/pixel; 200 kV; 100 μA
Van Steen et al. [161]	CEM I 42.5 R HES cement mortar; ST37-2K steel	Galvanostatic; i_g=100 μA/cm^2	514.4 hours (21.4 days)	Steel diameter not reported; l_{scan}=30 mm;	12.7 μm/pixel; 135 V; 200 μA
Šavija et al. [122]	CEM I 42.5 N cement mortar; CEM I 42.5 N cement mortar with 2% vol. PVA fiber (SHCC); Unspecified carbon steel	Stepwise potentiostatic; V_g=3 to 30V	202 hours (8.4 days) for mortar; 340 hours (14.2 days) for SHCC	d=6 mm with 4.2 mm inner diameter cavity; l_{scan}=36 mm; l_{scan}/d=6	16 μm/pixel; Energy and current not reported
Sun et al. [162]	PII 42.5 cement paste; Unspecified steel	Galvanostatic; i_g=469 to 464 μA/cm^2 or i_g=4222 to 4231 μA/cm^2	24 hours (1 day), regardless of i_g magnitude	d=3 mm; l_{scan}=3 mm; l_{scan}/d=1	4.5 μm/pixel; 150 kV; 65 μA 13 μm/pixel; 120 kV; 82 μA
Itty et al. [163]	Type II cement paste; A36 low-carbon steel; UNS S41000 low-nickel ferritic stainless steel	Galvanostatic; i_g=5000 μA/cm^2	170 to 180 minutes	d=0.5 mm; l_{scan}=2 mm; l_{scan}/d=4	3.3 μm/pixel; 43 kV; Current not reported

[1] Reports impressed galvanostatic current i_g or potentiostatic potential V_g.
[2] Steel bar diameter d and length of steel bar scanned under tomography experimentation l_{scan}



(a) **(b)**

Figure 6-6: 3D visualization of corroded steel within reinforced cementitious composites in the literature. Images are reported by: (a) Itty et al. [163]; (b) Sun et al. [162]. Both studies utilized an impressed current to induce corrosion activity.

To complement the medium- and large-scale corrosion studies conducted in Chapter 4 and Chapter 5, respectively, microscale corrosion studies are reported in this chapter to further elucidate the influence of fiber reinforcement and crack control on the corrosion behavior of reinforced cementitious composites. X-ray micro-computed tomography is used to visualize progressive corrosion damage of samples over an environmental exposure duration of 43.6 weeks. The work described in this chapter differs from the studies surveyed in Table 6-1 due to the long experimental time and the method of induced corrosion, which was based on intrusion of a 3.5% w/w NaCl solution and did not utilize impressed current techniques. The high image resolution afforded by μCT experimentation (e.g. 3.2 μm per pixel length) at beamline 8.3.2 of the Advanced Light Source allowed for detection of matrix microcrack damage, resulting in the study of microfiber-reinforced cementitious composites rather than direct study of the HyFRC composite material. Similar to the experiments described in Chapter 4 and Chapter 5, samples for μCT experimentation were also subjected to preload-induced cracking to account for cracks that exist in reinforced concrete structures in service.

6.2 Materials and methods

6.2.1 Mortar materials

A microfiber-reinforced mortar utilizing a binder blend of 45% type II/V portland cement and 55% class F fly ash was studied, with the batching proportions summarized in Table 6-2. The composite was designed with the inclusion of fine aggregates with a maximum size of 0.13 mm and a water-binder mass ratio of 0.28. To produce strain hardening properties, as shown in Figure 6-7, the fiber volume fraction of 0.04-mm diameter, 8-mm long polyvinyl alcohol (PVA) fibers was set to 3.5%, based on total composite volume. The PVA fibers are of the same type found in HyFRC. Strain-hardening fiber-reinforced mortars with a cement-fly ash binder blend and PVA fiber inclusions are often categorized within the class of construction materials known as strain-hardening cementitious composites (SHCC) or engineered cementitious composites (ECC) [20], with the former term used to designate the studied material in this chapter. A plain cementitious composite (PCC) having the same matrix proportions as the SHCC but lacking fiber reinforcement was also investigated.

Table 6-2: Batch proportions of SHCC and PCC.

Composite	Mass proportions (kg/m^3)				Chemical admixture dosage (wt. % total binder)		Fiber volume fraction (vol. % compos.)
	Cement	Fly ash	Water	Fine aggregate	SP[a]	VMA[a]	PVA
SHCC	559	670	334	318	0.69	0.33	3.5
PCC	579	694	346	329	0.69	0.33	-

[a] SP and VMA refer to superplasticizer and viscosity modifying admixture, respectively.

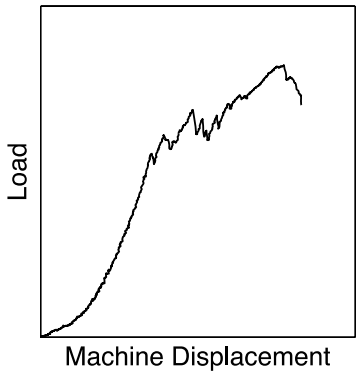


Figure 6-7: Typical load-machine displacement response of SHCC, showing strain-hardening behavior.

6.2.2 Specimen design

To induce precrack damage, the experiment required specimens that could be loaded in direct uniaxial tension. For fiber-reinforced cementitious composites, such testing is commonly conducted on dogbone-shaped samples [166], which concentrates cracking and fracture within a known region of interest while the remainder of the sample is expected to deform elastically. A similar approach was utilized for this experiment, as shown in Figure 6-8. Hourglass-shaped specimens were designed with a minimum, critical diameter of 6 mm, which occurred over a 3-mm height. A circular cross-section maintained a uniform thickness upon rotation about the specimen's longitudinal axis and was favorable for reducing possible artifacts introduced upon μCT imaging. To avoid premature cracking as a result of geometric stress concentrations, the cross-sectional area of the specimen gradually increased from the midheight. 3D-printed molds were fabricated to cast samples within and to ensure high accuracy of detailed specimen geometry.

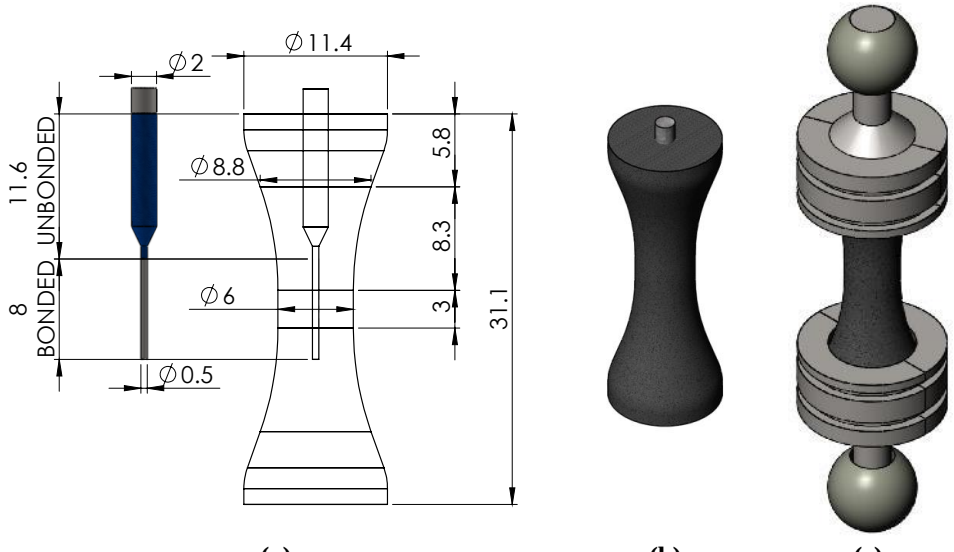
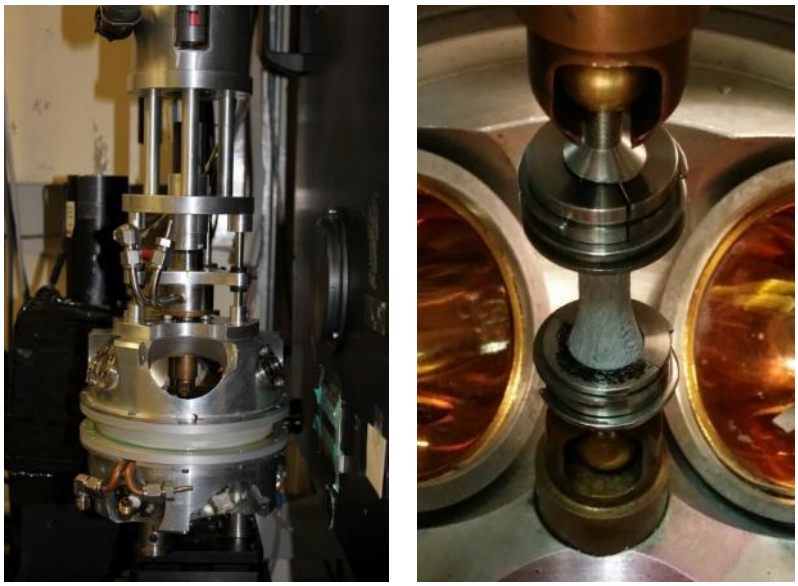


Figure 6-8: Specimen design: (a) Geometric detailing (units in mm); (b) Visualization of sample; (c) Visualization of sample with loading encasements.

A single steel reinforcing bar was centrally embedded along the specimen height. The bar was lathed from a strand of 9.5-mm diameter (United States size 3), ASTM A615 [129] steel reinforcing bar, which was of the same size and alloy were used in large-scale corrosion experiments detailed in Chapter 5. The thinnest section of the rod was machined to a maximum diameter of 0.5 mm, with an approximate 8-mm long region of interest where scanning of corroded surfaces was to occur. A long region of interest compared to the bar diameter (approximately l_{scan}/d=16) was designed to account for possible nonuniform corrosion activity along a single bar length. Outside this region, the steel bar was restricted from corroding by coating the steel surface with an electrically-insulating lacquer and then wrapping the surface with polytetrafluoroethylene (PTFE) tape.

6.2.3 Tensile preloading

Specimens were preloaded to induce microcracks prior to corrosion activity to simulate the cracks existing in the concrete cover, similar to the motivation of studying reinforced HyFRC with preexisting cracks in Chapter 4 and Chapter 5. Direct tensile testing of samples, regardless of material composition, occurred under a displacement-controlled loading protocol at a rate of 1.3 μm per second. Figure 6-9a and b show the loading apparatus used to apply uniaxial tensile load onto samples and the sample within the apparatus, respectively. As schematically shown in Figure 6-8c, two parts of stainless steel were machined to fit the specimen at each end, and were held in place by retaining rings (not shown). Removable brass spheres were required to fit the specimen into the loading machine's ball and socket connection, which allowed the specimen to be placed in direct tension. This testing setup resulted in some slip between components once loading initiated. Load was applied by a stepper motor while displacement was measured by a linear variable differential transformer (LVDT) that was positioned between an elevating loading stage displaced by the motor and a fixed stage of the testing apparatus.



(a) **(b)**

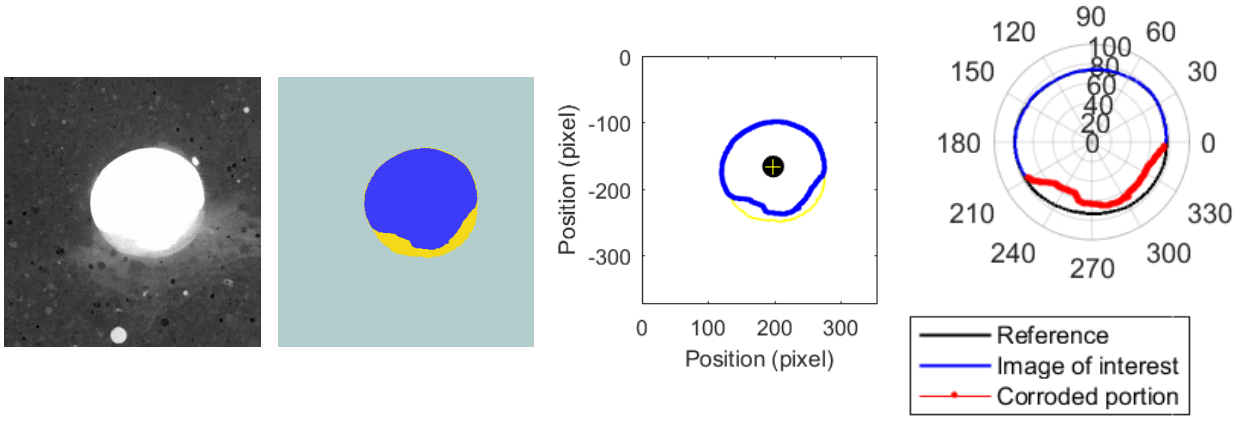
Figure 6-9: Mechanical test setup: (a) Loading apparatus; (b) Specimen within apparatus, showing ball and socket connection.

One reinforced SHCC (R/SHCC) sample and one reinforced PCC (R/PCC) sample were preloaded. The severity of induced damage was dependent on the type of cementitious composite. The reinforced PCC sample was loaded until the formation of a dominant crack, which caused a significant decrease in load resistance, and then completely unloaded. The SHCC sample was loaded until the matrix cracking load was reached, which was detectable by a discrete decrease in the load resistance, and then allowed to be displaced an additional 100 μm to allow for multiple cracking prior to unloading. It should be noted that imaging of these specimens occurred only after the conclusion of applied load, and did not include sequential scanning during mechanical testing.

6.2.4 X-ray micro-computed tomography

Hard X-ray micro-computed tomography experiments were performed at the Advanced Light Source synchrotron on beamline 8.3.2. The X-ray beam is allowed to penetrate an area of interest and the transmitted intensity is measured by a charge couple device area detector, as previously described in Section 6.1. During a scan, the sample is rotated about an axis perpendicular to the horizontal plane over 180°, with 1025 radiographs obtained over this rotation. After image processing, a stack of cross-sectional images is obtained for analysis. With the synchrotron ring current set at 500 mA, an energy level of 43 keV was prescribed to allow for satisfactory minimum intensity transmission (e.g. at least 20 to 30%). The PCO.edge camera with a magnification factor of 2 was used, which yielded a pixel resolution of 3.2 μm and allowed for an approximate 8.3 mm horizontal field of view.

6.2.5 Image analysis



(a) **(b)** **(c)** **(d)**

Figure 6-10: Method of quantifying μCT data: (a) Reconstructed tomogram; (b) Phase segmentation of steel (blue) and corrosion products occupying original steel volume (yellow); (c) Conversion to geometric object for MATLAB analysis; (d) Determination of corroded surface of section after centroid alignment with reference images taken prior to environmental exposure.

Using μCT results directly, several pertinent corrosion parameters (e.g. steel mass loss, corroded steel surface area) that are not typically available in reinforced concrete research become available for analysis. Figure 6-10 shows the general methodology of quantifying steel corrosion damage. After producing a stack of tomograms and segmenting the steel and corrosion product phases, the latter of which only includes products occupying the original volume of steel and does not include

products diffused into voids or matrix, the images were imported into MATLAB [167] and analyzed as geometric objects. The centroid of the corroded steel was based on its estimated original cross-section and was aligned with the centroid of the same section of the reference image stack obtained prior to environmental exposure. Surfaces affected by corrosion could then be detected and measured, as in Figure 6-10d.

6.3 Results and discussion

6.3.1 Preload response

Tensile responses from sample preloading are presented in Figure 6-11. Due to the design of the testing apparatus, measured displacement of the sample included contributions of slip from loading components (e.g. sample loading encasements) at the onset of testing, resulting in an initial nonlinear response, though slipping became less influential at testing loads greater than approximately 50 N. The curve of the PCC sample suggests an elastic response prior to formation of a dominant tensile crack upon reaching approximately 180 N. Immediately after the cracking event, a considerable decrease in composite load resistance occurred. In contrast, the SHCC sample exhibited strain hardening behavior. After first cracking, which is indicated by a small, partial unloading of the composite near 190 N, the bridging action of fibers strengthened the cracked section, allowing the composite to increase in load resistance despite the presence of cracks. The SHCC sample was manually unloaded after being displaced an additional 100 µm past the displacement where first cracking occurred and significant decreases in load resistance were not observed for the considered domain of displacements.

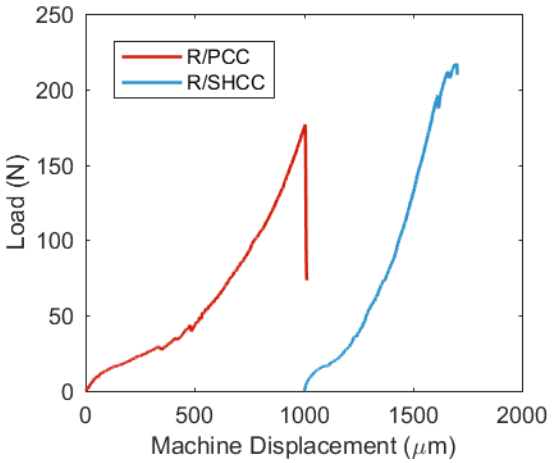
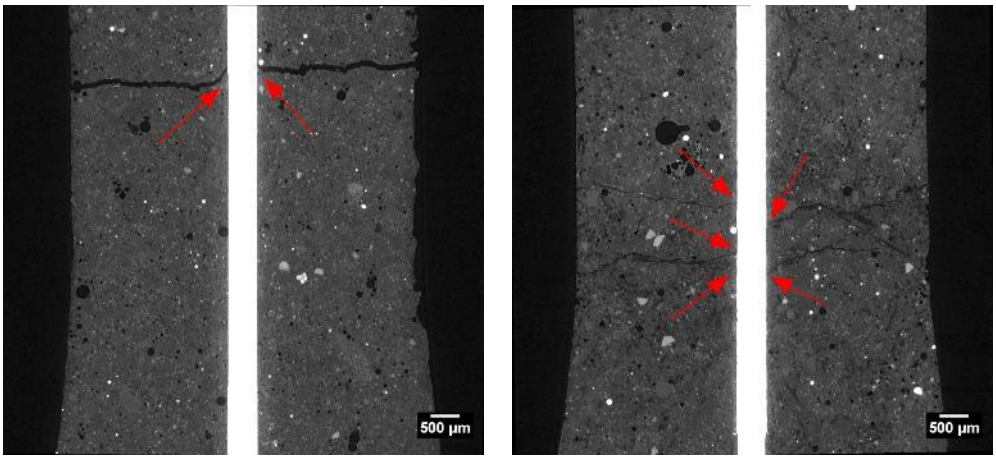


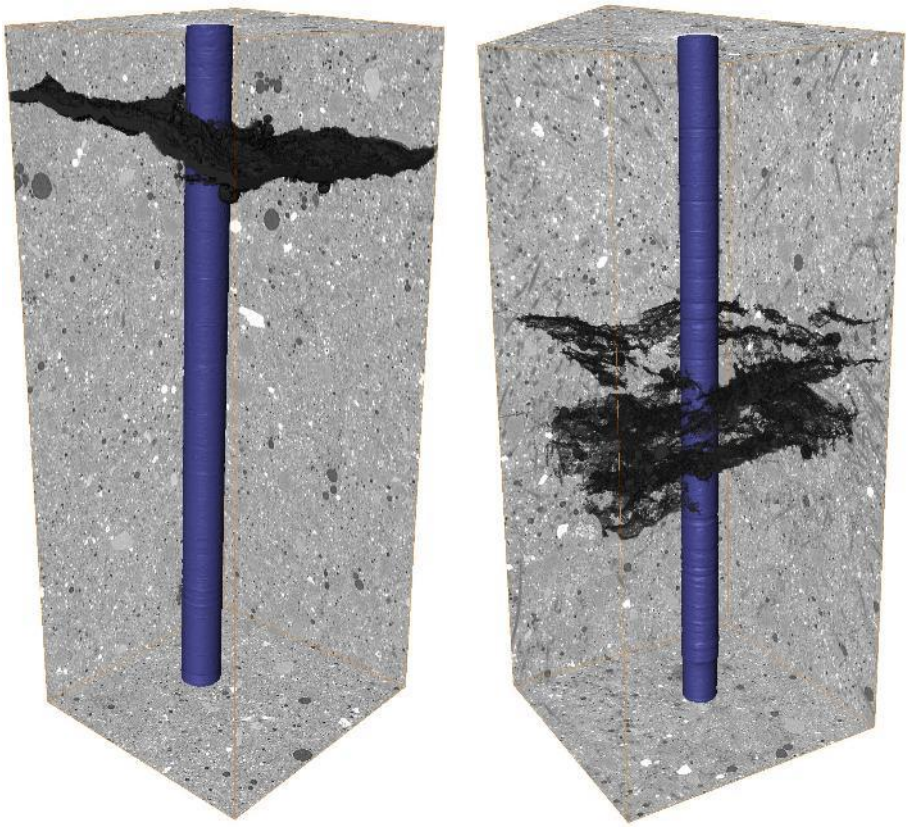
Figure 6-11: Tensile preloading response of samples.

The preload-induced cracking damage of the samples are shown as vertical-section tomograms in Figure 6-12 and as 3D visualizations in Figure 6-13. Correlating to the previously presented load-displacement responses, damage of PCC was characterized by a single crack with a maximum opening of approximately 100 µm. No additional microcracks were detected in the sample. Multiple tensile cracks were observed in the SHCC sample with a maximum opening of approximately 15 µm. Rather than concentrating damage within a single location, SHCC cracking was distributed over a greater height of the sample and is typical of damage under tensile stress [166].



(a) PCC **(b) SHCC**

Figure 6-12: Tomograms of preload-induced cracking prior to environmental conditioning: (a) PCC; (b) SHCC.



(a) PCC **(b) SHCC**

Figure 6-13: 3D visualization of preload-induced cracking prior to environmental conditioning: (a) PCC; (b) SHCC. The bounding box of the PCC and SHCC visualizations represents dimensions of 4.2 mm by 4.0 mm by 8.0 mm and dimensions of 4.1 mm by 3.9 mm by 8.4 mm, respectively.

6.3.2 Visualized corrosion damage

Visualizations of progressive corrosion damage of the steel bar in the PCC samples are shown in Figure 6-14 up to 43.6 weeks of elapsed exposure duration. Corrosion products are also visualized, though some products that have diffused into the matrix may not be shown. The initial site of corrosion damage, as determined by detectable rebar mass loss within the limits of the image resolution (3.2 µm), occurred where the tensile crack intersected the steel bar no later than after 5.3 weeks of environmental conditioning. Figure 6-15 highlights this damage. After 13.1 weeks of exposure, corrosion generally intensified at the initial site, though additional corrosion activity occurred on the lower portion of the sample between 13.1 weeks to 25.0 weeks. By 43.6 weeks, corrosion was noticeably widespread and affected a majority of the bar height.

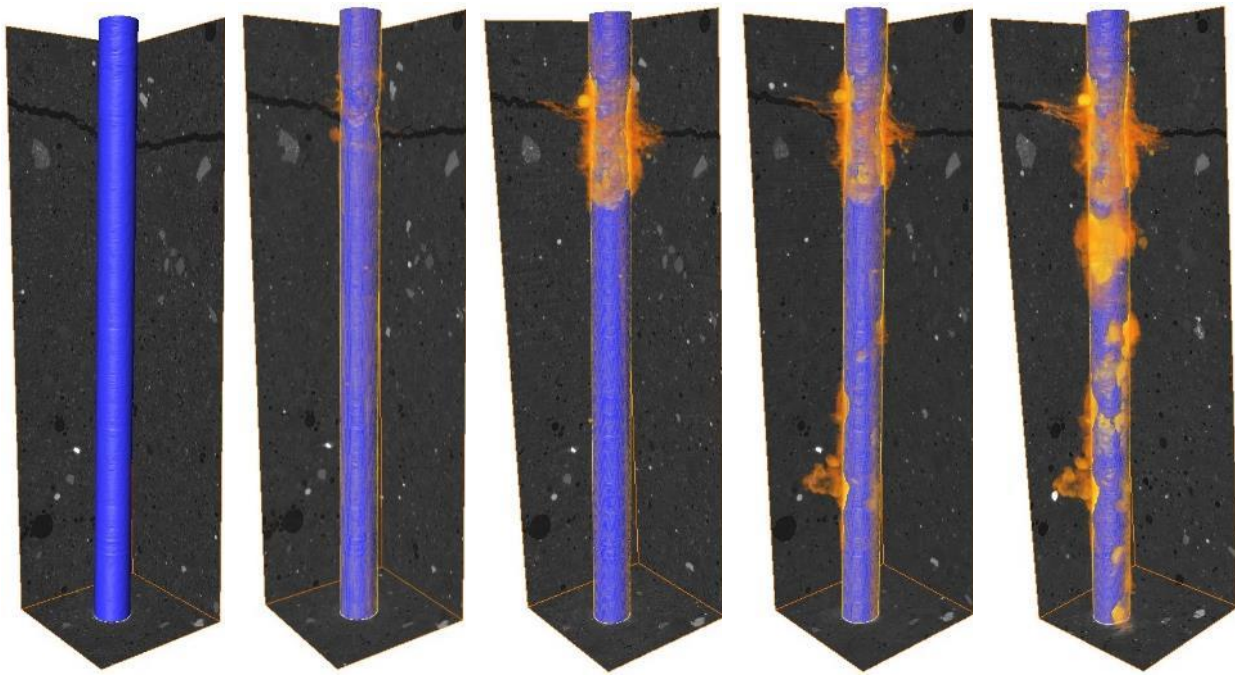


Figure 6-14: 3D visualization of steel bar and corrosion products in PCC sample at increasing exposure durations: (a) 0 weeks; (b) 5.3 weeks; (c) 13.1 weeks; (d) 25.0 weeks; (e) 43.6 weeks. The bounding box of each visualization represents dimensions of 1.92 mm by 1.92 mm by 7.68 mm.

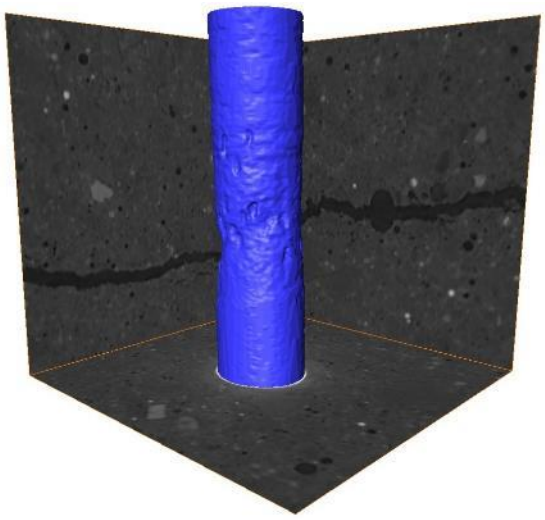


Figure 6-15: 3D visualization of steel bar in PCC sample at 5.3 weeks, showing corrosion damage of the bar at the matrix crack location. The bounding box of each visualization represents dimensions of 1.92 mm by 1.92 mm by 1.92 mm.

The corrosion behavior of R/SHCC differed in both corrosion initiation and propagation, as shown in Figure 6-16. While steel mass loss could be detected at 5.3 weeks for the PCC sample, no such observation could be made for the SHCC sample at the same elapsed duration, indicating a longer time required to initiate rebar mass loss for fiber-reinforced cementitious composites with more diffuse, but finer microcracks. Between 13.1 weeks and 25.0 weeks, the R/SHCC sample initiated active corrosion in the microcracked region of the sample. Despite the microcracks in SHCC had little to negligible influence on external solution ingress of the cracked matrix due to the maximum opening of the cracks (approximately 15 μm) being under a reported critical crack threshold of 50 μm for matrix permeability increase [9, 168], the presence of microcracks promoted preferential active corrosion sites. Air void defects at a steel reinforcing bar-cementitious matrix interface have been noted to act as preferred sites for steel rebar corrosion activity [122, 123]. Microcracks in SHCC behaved similarly, allowing an unoccupied volume for corrosion products to form within and migrate into, rather than typical formation at a denser rebar-matrix interface. Additional exposure to NaCl solution after 25.0 weeks and 43.6 weeks generally resulted in additional damage near the vicinity of the initial corrosion site. Unlike the R/PCC sample, the approximate upper third of the steel bar in SHCC showed negligible corrosion activity.

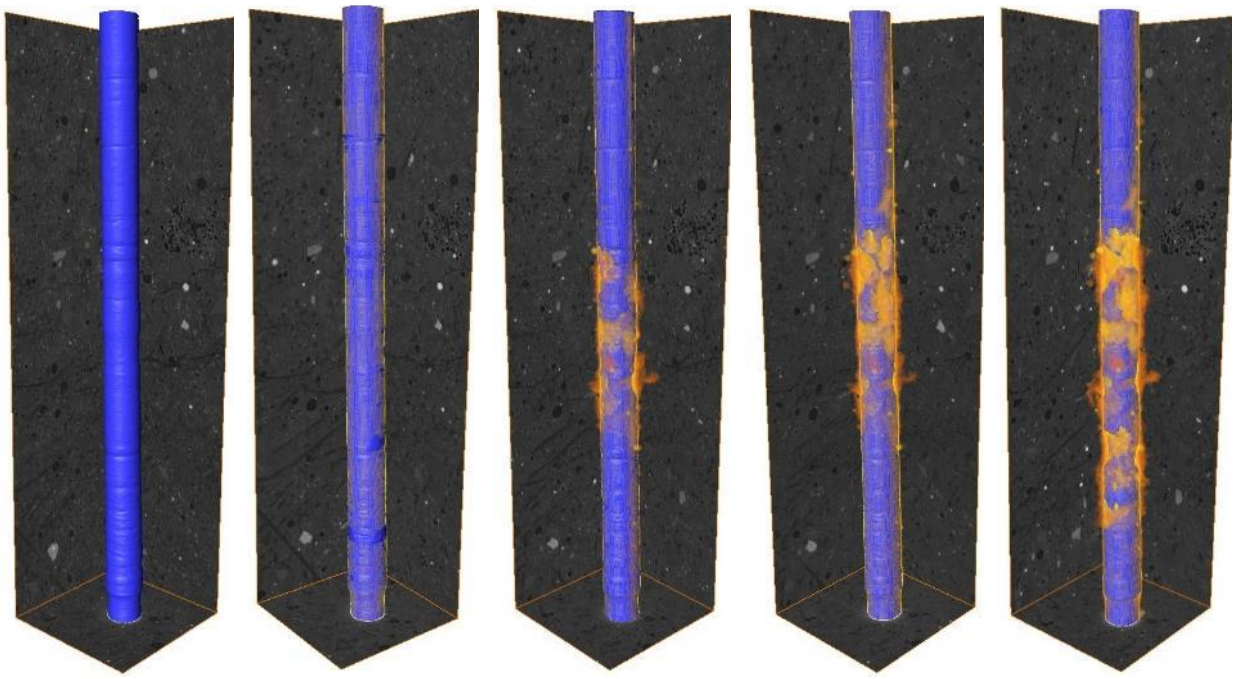


Figure 6-16: 3D visualization of steel bar and corrosion products in SHCC sample at increasing exposure durations: (a) 0 weeks; (b) 5.3 weeks; (c) 13.1 weeks; (d) 25.0 weeks; (e) 43.6 weeks. The bounding box of each visualization represents dimensions of 1.92 mm by 1.92 mm by 7.68 mm.

6.3.3 Corrosion propagation behavior

The measured cross-section areas *A* of the steel bar in the R/PCC sample are shown in Figure 6-17a for a given specimen height *h*, while the changes in steel bar cross-section shape are shown for select sections in Figure 6-17b-e. Corresponding with observed damage based on 3D visualization of the steel rod, sectional area loss was detected in the steel bar after 5.3 weeks of exposure at or near Section (b), which was where the tensile crack in the sample was located. At this section, corrosion occurred on the entire circumference of the cross-section. In contrast, other corroded sections of the sample, including Sections (c), (d), and (e), showed greater heterogeneity of corrosion surfaces. The preference of active corrosion sites of the steel bar is strongly influenced by the presence of matrix cracking in the reinforced sample. At Section (b), steel bar radius reduction is more uniform as the bar cross-section is located within a through-thickness crack void, which allows for chloride attack and depassivation of the bar section circumference from all angles. No volumetric restriction of corrosion products is imposed on the cracked section from the cementitious matrix, allowing for free corrosion.

At 25.0 weeks, corrosion was first detected in noncracked sections, with the section area loss greatest near Section (e). Two general areas of corrosion can be identified, located near 0° and 225° (as oriented in Figure 6-17e). The tomogram of this section at 25.0 weeks is presented in Figure 6-18a, showing fine splitting cracks emanating near the two corrosion sites. Matrix splitting cracks were previously identified in Chapter 4 and Chapter 5 of this dissertation as being highly influential on increasing the overall corrosion rate of steel rebar due to the widespread active corrosion of surfaces located within splitting crack wakes. It is unclear if corrosion product formation at this section induced splitting cracks at this section, or if the cracks formed prior to

corrosion of the steel section. Regardless, additional environmental exposure up to 43.6 total weeks resulted in widening of the cracks (Figure 6-18b). The propagation of the splitting cracks towards Section (c) coincided with steel bar corrosion of that section where the splitting cracks were located (Figure 6-18d), further validating the detrimental effect of splitting cracks on steel rebar corrosion damage. As shown in Figure 6-17f, splitting cracks in the sample propagated over a significant height of the sample and coincided with active corrosion surfaces where the crack faces reached the steel bar surface.

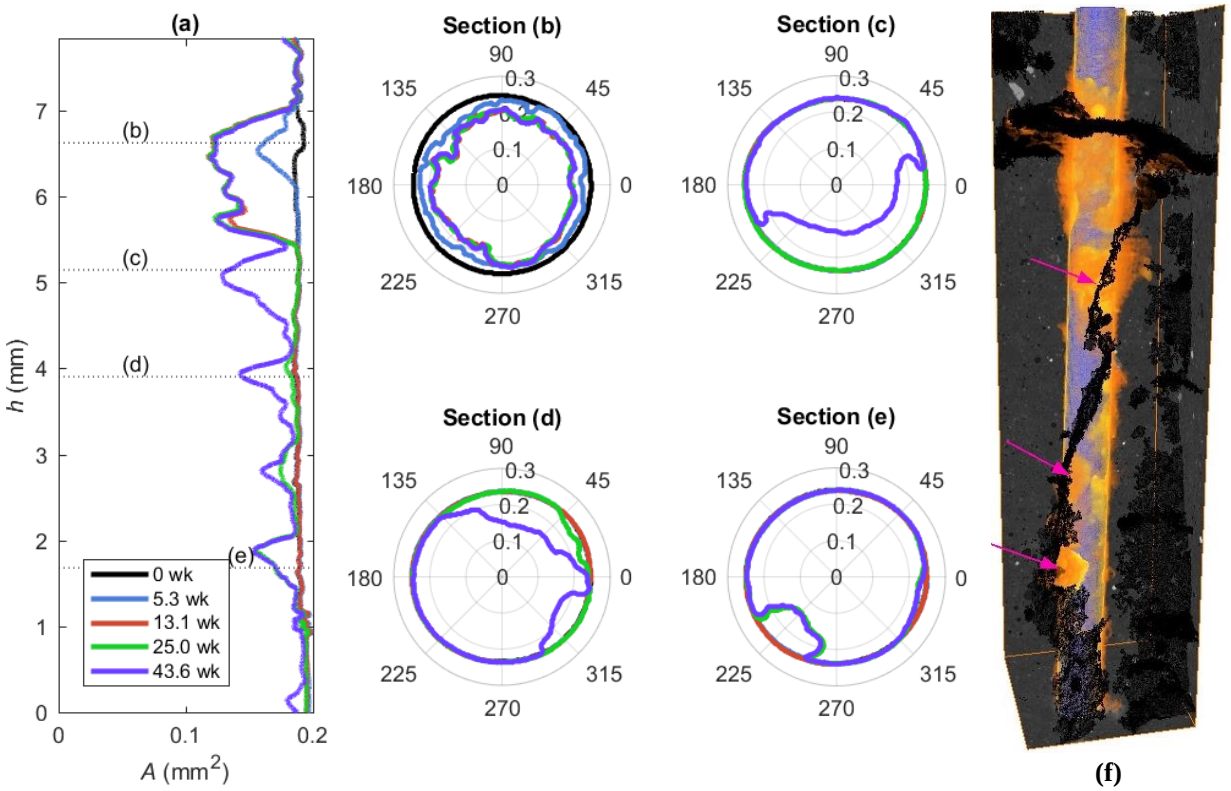
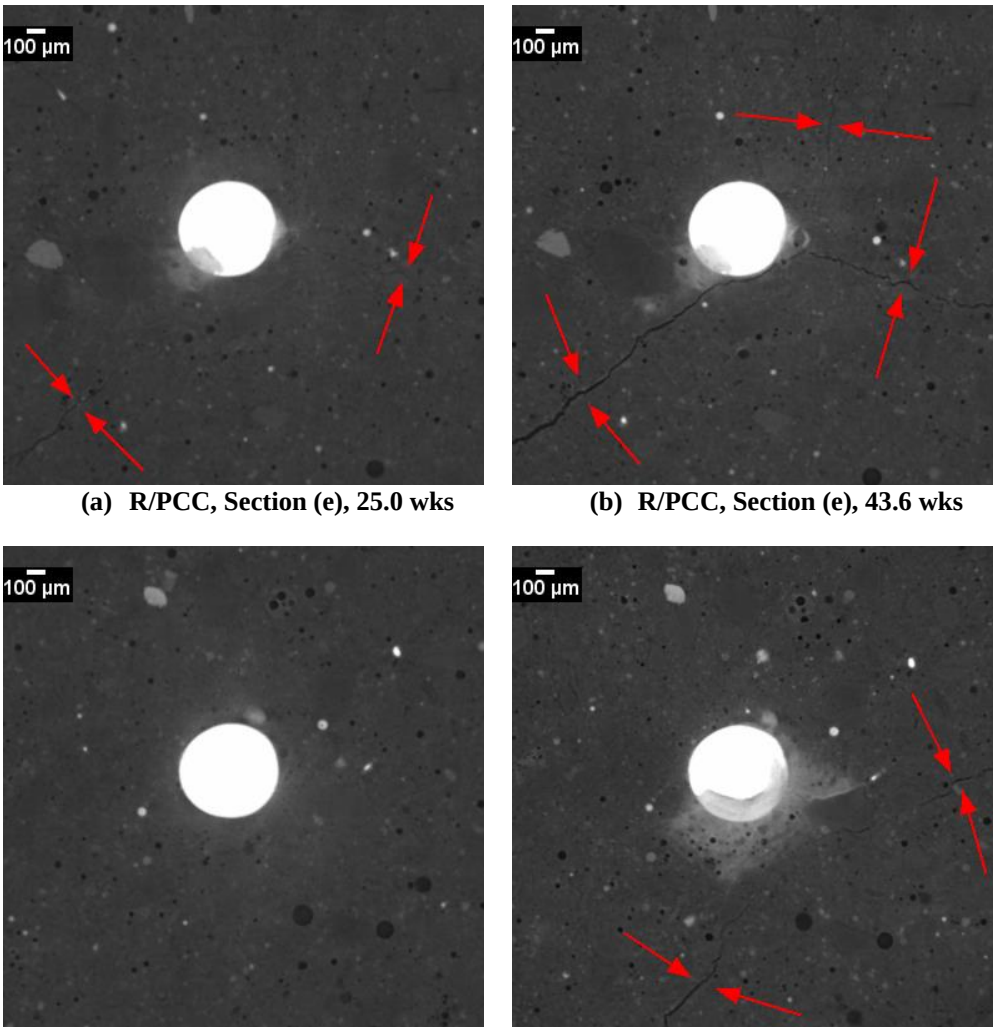


Figure 6-17: Corrosion propagation of R/PCC: (a) Steel bar cross-section area *A* at steel bar height *h*; (b)-(e) Change in steel bar cross-section area, with section locations designated in (a). Angular coordinates are expressed in degrees (°) and radial coordinates are expressed in mm. (f) 3D visualization of sample at 43.6 weeks, including visualization of cracks. The bounding box represents dimensions of 1.92 mm by 1.92 mm by 7.68 mm.



(a) R/PCC, Section (e), 25.0 wks **(b) R/PCC, Section (e), 43.6 wks**

(c) R/PCC, Section (c), 25.0 wks **(d) R/PCC, Section (c), 43.6 wks**

Figure 6-18: Tomograms of select cross-sections. Section locations were previously designated in Figure 6-17.

For the R/SHCC sample, the cross-section area of the steel bar is plotted for a given height in Figure 6-19a while changes in the cross-section geometry of select bar cross-sections are presented in Figure 6-19b-e. For heights approximately greater than h=6 mm and lower than h=1 mm, steel mass loss was negligible for the maximum considered exposure duration of 43.6 weeks, as highlighted in the undamaged cross-section of Section (b). Due to a lack of significant splitting crack propagation, corrosion damage of the bar was generally localized and maintained where microcracking of the SHCC matrix was present.

The corrosion propagation behavior of R/SHCC differed from R/PCC in part due to the crack resistance of SHCC. Figure 6-20a shows a tomogram of Section (c), which had corrosion damage at 25.0 weeks. Additional environmental exposure up to 43.6 weeks resulted in additional area reduction of the bar cross-section, though the maximum pitting depth did not significantly increase on existing pits. Rather, other surfaces of the bar exhibited corrosion damage, as shown by superimposed cross-section geometry changes in Figure 6-19c and by the yellow arrow in Figure 6-20b. Splitting cracks could not be detected at this section considering the resolution of the images. Due to fiber inclusion, splitting cracks in SHCC materials are highly restrained from

propagating [42, 44]. While additional corrosion surfaces in the R/PCC generally occurred where a splitting crack was present, further propagation of active corrosion surfaces for the steel bar in SHCC could occur without significant splitting cracks, though these new surfaces were formed only within the local vicinity of the initial corrosion site, as in Section (e) at 43.6 weeks (Figure 6-20d).

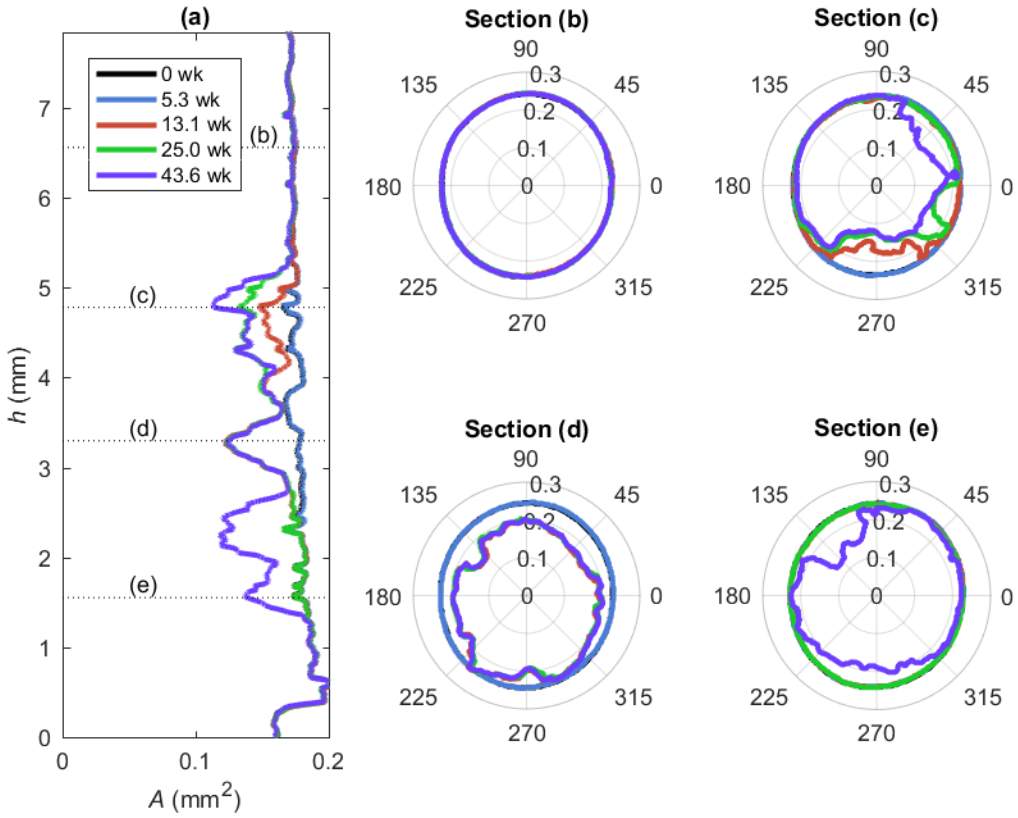
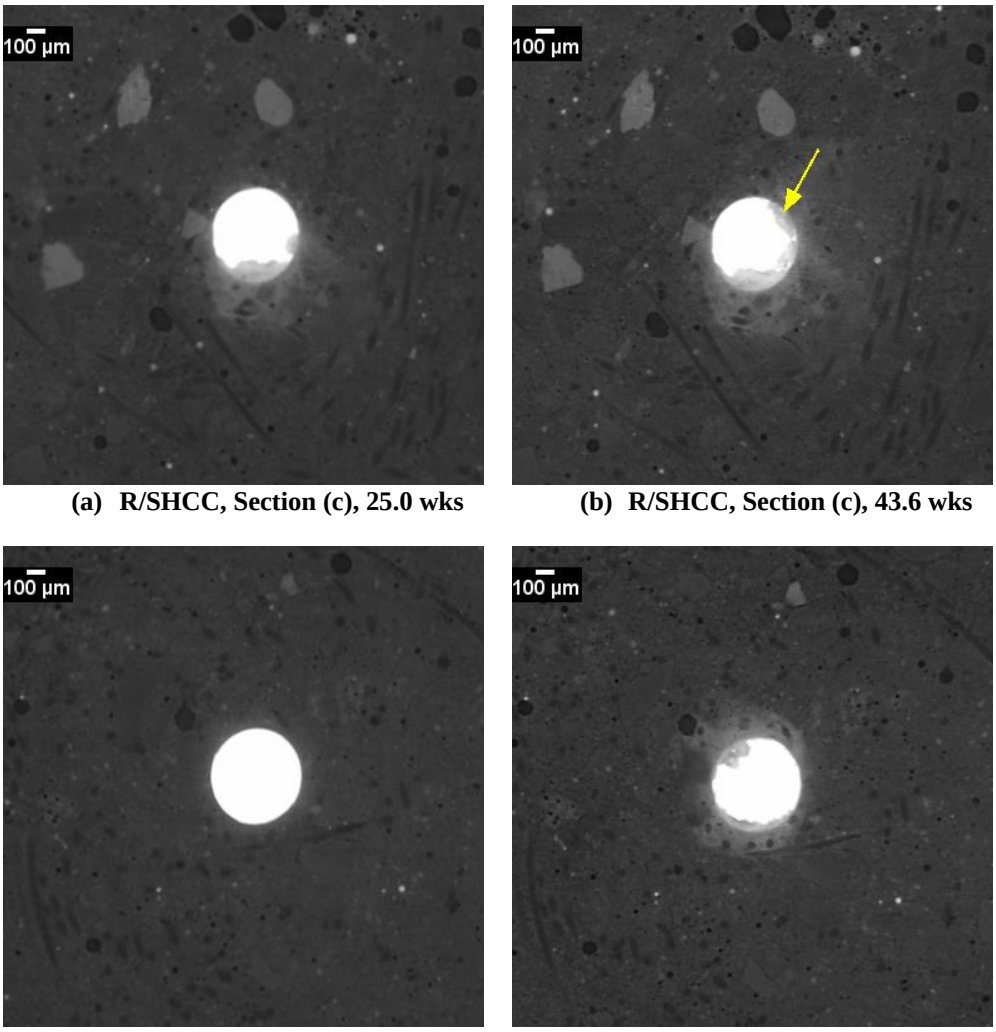


Figure 6-19: Corrosion propagation of R/SHCC: (a) Steel bar cross-section area *A* at steel bar height *h*; (b)-(e) Change in steel bar cross-section area, with section locations designated in (a). Angular coordinates are expressed in degrees (°) and radial coordinates are expressed in mm.



(a) R/SHCC, Section (c), 25.0 wks **(b) R/SHCC, Section (c), 43.6 wks**

(c) R/SHCC, Section (e), 25.0 wks **(d) R/SHCC, Section (e), 43.6 wks**

Figure 6-20: Tomograms of select cross-sections. Section locations were previously designated in Figure 6-19.

Differences in the corrosion propagation between plain cementitious composites and strain-hardening cementitious composites may be further realized in Figure 6-21. In the plot, the proportion of corroded steel bar height h_{corr}/H is plotted against the elapsed exposure time t. A corroded steel section to defined to have a cross-section area loss of at least 1% compared to the same section found in reference images obtain prior to corrosion. Because the multiple cracking behavior of SHCC distributes cracking damage over a greater height of the sample, rather than concentrating damage within a single crack as in R/PCC, steel bar corrosion within SHCC is also affected over a greater height, as indicated by the difference in h_{corr}/H between the two samples at 13.1 weeks. Miyazato and Hiraishi [93] reported that the influence of multiple cracks in fiber-reinforced cementitious composites caused the corrosion of embedded steel rebar to affect a greater surface area compared to conventional reinforced concrete within a 4-week experimental testing duration. Kobayashi and Kojima [169] also related the presence of a greater number of cracks in SHCC to a greater rebar corrosion surface area upon initial corrosion propagation. Due to the presence of splitting cracks, h_{corr}/H increased at a noticeably greater rate after 13.1 weeks for R/PCC than R/SHCC.

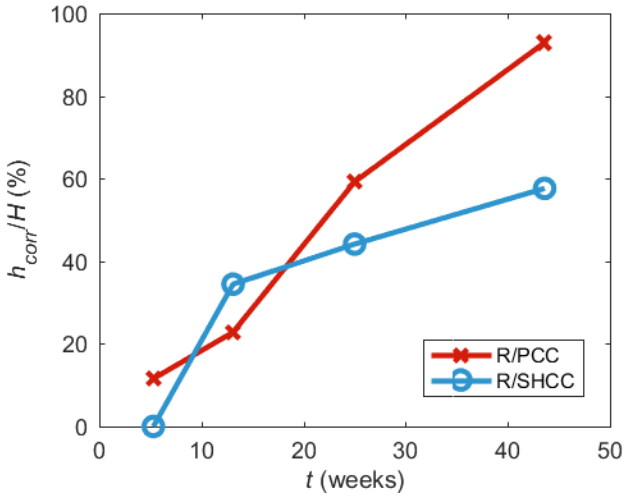


Figure 6-21: Proportion of corroded height h_{corr}/H versus elapsed exposure time t.

6.3.4 Corrosion rate

In reinforced concrete research, the corrosion current I_{corr} is often normalized by the nominal surface area of the steel reinforcing bar of interest to report the corrosion current density i_{corr}. Because μCT provides information on the actual mass loss and corroded surface area, considering the resolution limits of acquired images, these parameters were evaluated for each cross-sectional tomogram to determine the mean corrosion current density $i_{corr,mean}$ between μCT experiment dates. Figure 6-22 plots $i_{corr,mean}$ for each considered height h of the steel bar. An absence of points for a particular period of time at a certain value of h indicates that cross-section had a negligible corrosion rate (e.g. less than 10^{-1} μA/cm^2). Corrosion rates less than 0.1 to 0.2 are often cited as a minimum threshold range for active corrosion of embedded steel reinforcement [131].

For the R/SHCC sample, i_{corr} was generally greater than 10 μA/cm^2 between 5.3 weeks and 13.1 weeks, coinciding with the period of exposure time when rebar mass loss initially occurred. As expected, significant corrosion rates were first detected within and near the multiple crack region of sample, which was bound between approximately h=3.1 mm to 4.4 mm. After 13.1 weeks, the local corrosion rate was generally lower than 10 μA/cm^2. The greater corrosion rates initially exhibited within or near the multiple crack region were produced in part by the presence of microcracks, which provide a free volume for products to form within or migrate into. Corrosion rates of approximately 20 μA/cm^2 or greater have been observed for steel immersed within simulated concrete pore solution contaminated with chlorides [170-172]. Such experiments of steel immersed within solution would have no influence of the physical barrier of the cementitious matrix against corrosion product growth, and would be similar to the influence of an open crack at the steel bar surface. With the presence of a concrete cover, Poursaee and Hansson [173] reported corrosion rates of 6 to 10 μA/cm^2 based on area normalization by observed corroded surface area of rebar. These values are generally consisted with the corrosion rates exhibited by noncracked regions of the R/SHCC sample.

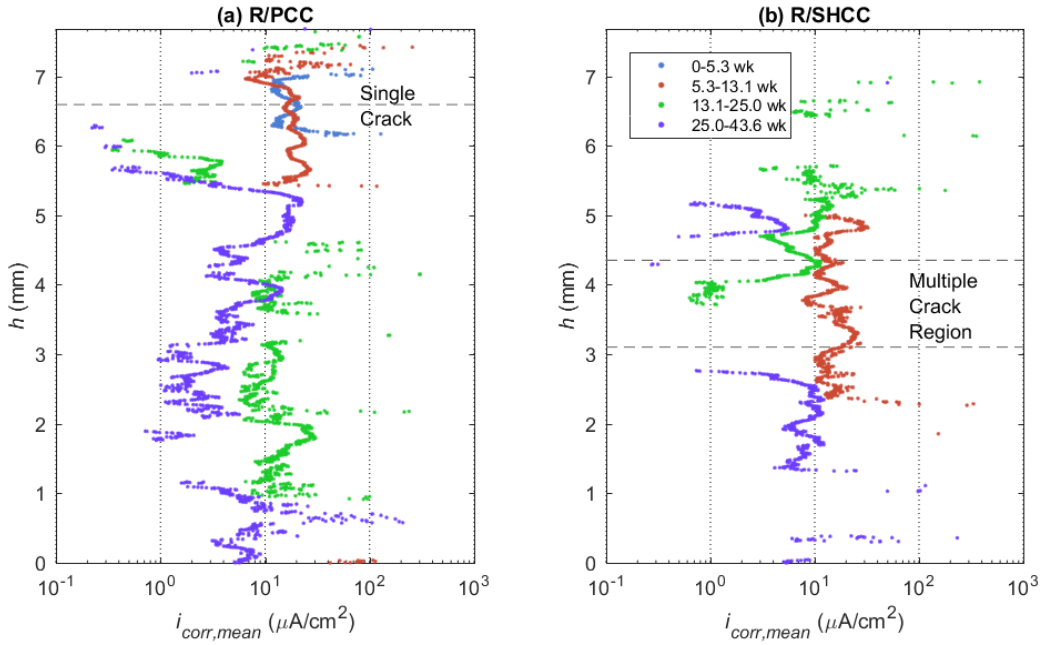


Figure 6-22: Mean corrosion current density $i_{corr,mean}$ of steel cross-section at height h. Current density measurement is based on steel mass loss between indicated experimental times.

Corrosion rates in excess of 10 μA/cm^2 were also determined for the R/PCC steel bar near the location of the preload-induced matrix crack. Unlike the R/SHCC sample, initially noncracked sections of the sample could still exhibit corrosion rates greater than 10 μA/cm^2 due to the propagation of corrosion-induced splitting cracks. The formation of these types of cracks in SHCC was previously mentioned to be negligible, indicating a durability benefit of SHCC is related to lower initial corrosion rates on secondary corrosion initiation sites after first corrosion initiation.

After initial corrosion activity, sections of either the R/PCC or R/SHCC sample generally exhibited reduced or negligible corrosion rates. For instance, sections of the R/SHCC sample between h=3 mm and 3.5 mm had corrosion rates reduced to lower than 0.1 μA/cm^2 from at least 10 μA/cm^2 after 13.1 weeks. The corrosion rate of steel may be retarded after the formation of corrosion products on the steel bar surface, which may impede the diffusion of chlorides and oxygen to the steel bar surface [125, 142] and may also be related to the restricted liberation of ferrous ions from the bulk metal surface due to the mechanical confinement of corrosion products on the steel surface. Grubb et al. [102] postulated that a confinement effect occurs in fiber-reinforced concrete when expansive corrosion products form at the rebar-matrix interface.

6.4 Summary and conclusions

In this chapter, X-ray micro-computed tomography (μCT) was used to visualize the in-situ corrosion damage progression in reinforced strain-hardening cementitious composites (reinforced SHCC, or R/SHCC) and reinforced plain cementitious composites (reinforced PCC, or R/PCC). Samples were monitored and exposed to a 3.5% w/w NaCl solution bath for 43.6 weeks. Similar to experiments conducted in Chapter 4 and Chapter 5, samples in this study were precracked prior to environmental exposure, with the SHCC sample exhibiting multiple cracking with finer crack

widths while the PCC sample was characterized by a single crack with greater opening. The following conclusions are made based on the experimental results:

1. X-ray micro-computed tomography is a viable materials characterization technique for visualizing corrosion damage in reinforced cementitious composites. Considering the parameters of the specimen design and the μCT experimental parameters, corrosion of the steel and cracking of the matrix could be identified within the resolution limits (3.2 μm per pixel length) of the acquired images.
2. Corrosion initiation of the steel bar occurs where matrix cracks reach the bar surface. Because the multiple cracking of SHCC occurs over a greater height of the sample, a greater proportion of the steel bar height was corroded compared to the reinforced PCC sample, which initially exhibited more localized corrosion damage. Despite the fine crack widths found in SHCC (e.g. less than 15 μm opening), steel bar corrosion was preferential near these cracks due to the open volume available for products to form within and migrate into.
3. Corrosion-induced splitting cracks formed in the R/PCC sample while such cracks were negligible in the R/SHCC sample. The splitting cracks coincided with the locations of corrosion propagation away from the first corrosion initiation site, indicating the influence of this crack morphology on the overall corrosion damage of embedded steel bars in cementitious composites. Corrosion propagation in SHCC was limited near the vicinity of the initial corrosion site due to a lack of splitting crack development. At the end of the experiment, 93% of the monitored bar height in R/PCC exhibited as least 1% reduction in cross-section area loss due to corrosion, while 58% of the bar height in R/SHCC was affected by corrosion damage.
4. The local corrosion rate was greater than approximately 10 $\mu A/cm^2$ where matrix cracks were near the corroding steel bar surface, while the rate was less than this value where cracking was negligible. At a given corroded steel section, the corrosion rate may decrease to an inconsequential rate (e.g. less than 0.1 $\mu A/cm^2$) after sufficient generation of corrosion products in both R/PCC and R/SHCC. The corrosion products are hypothesized to hinder the diffusion of chlorides and oxygen to the steel bar surface and restrict the liberation of ferrous ions from the bulk steel surface, greatly limiting further corrosion activity.

7 Final remarks

7.1 Conclusions

In this dissertation, hybrid fiber-reinforced concrete (HyFRC) was investigated for use in reinforced concrete infrastructure in seismic and corrosive environments. While the HyFRC material has greater crack resistance and mechanical toughness than conventional concrete, its use may be optimized based on its damage characteristics such that resulting reinforced HyFRC (R/HyFRC) structures gain a substantial service life enhancement.

Performance of HyFRC for seismic load-resisting structural elements is highly dependent on the structural design of the member, including its tensile longitudinal reinforcement. Direct substitution of concrete with HyFRC for test elements subjected to direct tensile stress results in a pronounced tension stiffening effect, which allows R/HyFRC to achieve a greater maximum load capacity than R/C, though at the cost of reduced strain capacity (i.e. reduced ductility). The high splitting crack resistance of HyFRC and strain localization of the steel reinforcing bar (rebar) within a tensile crack causes this behavior, which is generally undesirable for structural elements that are expected to withstand high deformations during an earthquake. To increase the tensile ductility of R/HyFRC, additional longitudinal reinforcement may be included such that the strain-hardening contribution of steel more effectively offsets load softening from fiber pull out processes at a crack.

To take advantage of the crack-resisting properties of HyFRC, its compressive damage resistance can be emphasized. A novel rocking bridge column design using a precast HyFRC tube element was proposed and evaluated. The precast tube contained all of the column's steel rebar and was intended to accelerate bridge construction. By debonding the longitudinal steel reinforcing bars from the HyFRC within the expected plastic hinge region of the column, a base-rocking mechanism occurs, which relieves the HyFRC of tension stiffening effects. The high post-peak toughness of the column, which retained 93% of its peak load capacity at 9.5% drift, was strongly dictated by the high compression damage resistance of HyFRC. The HyFRC cover did not spall and was able to greatly restrict buckling deformations of longitudinal bars. Use of HyFRC specifically for its compressive damage resistance appears to be an effective strategy for improving the toughness and serviceability of bridge columns located in seismic regions, and may be extended to other types of structural elements.

Corrosion of embedded steel in reinforced concrete structures is a major source of infrastructure damage, and is generally partitioned into a corrosion initiation phase (i.e., time from operation start to onset of active corrosion) and a corrosion propagation phase (i.e., time after onset of active corrosion). Experiments in this dissertation considered the application of load prior to, or during, corrosive environment exposure to account for cracks that may be present in reinforced concrete structures under service loading prior to significant corrosion activity. During the corrosion initiation phase, in the absence of crack widths greater than approximately 0.09 mm, HyFRC was experimentally observed to retard the chloride ingress rate compared to plain concrete lacking fibers. In two independent experiments, the time to corrosion initiation was greater for reinforced HyFRC compared to reinforced concrete by a factor of at least 1.7. When R/HyFRC beam elements in this dissertation were flexurally loaded such that their flexural stiffness was reduced to 26% or less of their elastic stiffness, the benefits of HyFRC on corrosion initiation is less impactful compared to reinforced concrete beams that exhibit a similar reduction in stiffness. For reinforced HyFRC, such a reduction in stiffness is also accompanied by surface crack widths

exceeding 0.10 mm. Crack localization behavior should thus be avoided for corrosion-induced loading, paralleling the detrimental effects of crack localization on the ductility of reinforced HyFRC under tensile stress. To maintain the service life enhancement of HyFRC during the corrosion initiation phase, cracking damage of the HyFRC should be designed to have an upper limit based on flexural stiffness and maximum crack width opening for beam elements.

During the corrosion propagation phase, the restriction of corrosion-induced splitting cracks in HyFRC composites compared to widespread formation of splitting cracks in conventional reinforced concrete was most influential on lowering overall corrosion activity of embedded steel rebar and lowering total rebar mass loss. This inherent property of HyFRC occurs regardless of the damage state of the HyFRC at the time of corrosion initiation. Splitting cracks that propagate over a considerable length of samples provide a direct path for external chlorides and oxygen to readily reach the rebar surface, forming additional actively corroding surfaces away from the initial site of corrosion. By restricting the propagation of these cracks with hybrid fiber reinforcement, corrosion in reinforced HyFRC was visually observed to be more localized. The restriction of corrosion-induced splitting cracks in reinforced HyFRC is crucial for maintaining high rebar-matrix interfacial bond, which prevents the composite stiffness from severely degrading, even with some corrosion damage. In contrast, reinforced concrete with splitting cracks exhibited high loss of rebar-matrix bond, which may cause issues with unexpected additional deflections and deformations that may not have been accounted for in design calculations.

X-ray micro-computed tomography (μCT), a non-destructive, 3D imaging technique, was used to monitor the progressive corrosion damage of reinforced microfiber-reinforced cementitious composites. Conclusions drawn from this study correlate well to medium- and large-scale corrosion studies performed in this dissertation. The benefits of crack control on corrosion initiation delay were confirmed by quantifying the actual steel bar mass loss of samples, while the influence of splitting cracks formed within plain cementitious composites were additionally confirmed to cause widespread formation of actively corroding surfaces of the steel bar. The microfiber-reinforced cementitious composite exhibited negligible splitting crack damage and its corrosion behavior was generally localized near the site of corrosion initiation.

7.2 Recommendations for future research

This dissertation attempted to thoroughly evaluate the HyFRC material under two loading cases detrimental to reinforced concrete infrastructure. However, further work related to the themes of this report are recommended for further study.

The overall toughness of R/HyFRC under tensile stress is influenced by the longitudinal rebar reinforcing ratio and the presence of a yield plateau for typical low-carbon construction steel. Experiments considering more robust parameters, including the investigation of steels with no yield plateau and more varied reinforcing ratios, are suggested for study to determine optimal material selection for structural design and to also further validate the mechanisms proposed in this report.

By using a rocking bridge column design, the toughness of the HyFRC precast tube column was governed by the compression damage resistance of the HyFRC, which did not spall during lateral loading. To further identify the processes related to this damage resistance, isolated experiments related to pure compression are proposed. Such experiments may consider the effect of HyFRC on core confinement and longitudinal rebar buckling resistance.

R/HyFRC was found to exhibit a significant delay in corrosion initiation time compared to conventional R/C when both composites were not subjected to any mechanical loading prior to environmental exposure. In addition, chloride contents were generally lower in noncracked HyFRC than noncracked concrete. Because the primary difference between the sample types are the inclusion of fibers in HyFRC, a study identifying the precise effect of fibers on chloride transport through a cementitious matrix is proposed. Both polyvinyl alcohol and steel fibers should be considered for experimentation.

Finally, the large-scale corrosion experiments in this dissertation considered the effects of multiple lengths of steel rebar, though did not explicitly account for the effect of transverse reinforcing steel bars in specimen design. For future study, a R/HyFRC beam element should be designed per professional code standards and include both longitudinal and transverse steel reinforcement in a scaled structural element. Samples should then be exposed to a corrosive environment to observe behavior more representative of a beam in field conditions. Such an experiment may consider the effects of partially debonded or smooth steel longitudinal reinforcement, which would be designed to relieve the element of tension stiffening effects.

8 References

[1] Federal Highway Administration. Tables of frequently requested NBI information. Washington, DC, USA: Federal Highway Administration; 2017.
[2] U.S. Department of Transportation. 2010 Status of the Nation's Highways, Bridges, and Transit: Conditions and Performance. Washington, United States: Federal Highway Administration; 2010.
[3] Koch GH, Brongers MPH, Thompson NG, Virmani YP, Payer JH. Corrosion costs and preventive strategies in the United States. McLean, VA: Turner-Fairbank Highway Research Center; 2002.
[4] Caltrans. Seismic design criteria version 1.7. Sacramento, CA2013.
[5] Schoettler M, Restrepo J, Guerrini G, Duck DE, Carrea F. A full-scale, single-column bridge bent tested by shake-table excitation. Center for Civil Engineering Earthquake Research: University of Nevada, Reno, NV; 2012.
[6] Gouda VK. Corrosion and corrosion inhibition of reinforcing steel: I. Immersed in alkaline solutions. Br Corros J. 1970;5(5):198-203.
[7] Hausmann DA. Steel corrosion in concrete-How does it occur? Mater Prot. 1967;6(11):19-23.
[8] Andrade C, Alonso C, Molina FJ. Cover cracking as a function of bar corrosion: Part I-Experimental test. Mater Struct. 1993;26(8):453-64.
[9] Li Y, Chen X, Jin L, Zhang R. Experimental and numerical study on chloride transmission in cracked concrete. Constr Build Mater. 2016;127:425-35.
[10] Ye H, Jin N, Jin X, Fu C. Model of chloride penetration into cracked concrete subject to drying–wetting cycles. Constr Build Mater. 2012;36:259-69.
[11] Yuan W, Guo A, Li H. Seismic failure mode of coastal bridge piers considering the effects of corrosion-induced damage. Soil Dyn Earthq Eng. 2017;93:135-46.
[12] Ou Y-C, Nguyen ND. Influences of location of reinforcement corrosion on seismic performance of corroded reinforced concrete beams. Eng Struct. 2016;126:210-23.
[13] Ou Y-C, Tsai L-L, Chen H-H. Cyclic performance of large-scale corroded reinforced concrete beams. Earthq Engin Struct Dyn. 2012;41(4):593-604.
[14] Çağatay İH. Experimental evaluation of buildings damaged in recent earthquakes in Turkey. Eng Fail Anal. 2005;12(3):440-52.
[15] Werner S, McCullough N, Bruin W, Augustine A, Rix G, Crowder B, et al. Seismic Performance of Port de Port-au-Prince during the Haiti Earthquake and Post-Earthquake Restoration of Cargo Throughput. Earthq Spectr. 2011;27(S1):S387-S410.
[16] Ruiz-Pinilla JG, Adam JM, Pérez-Cárcel R, Yuste J, Moragues JJ. Learning from RC building structures damaged by the earthquake in Lorca, Spain, in 2011. Eng Fail Anal. 2016;68:76-86.
[17] Pakravan HR, Latifi M, Jamshidi M. Hybrid short fiber reinforcement system in concrete: A review. Constr Build Mater. 2017;142:280-94.
[18] Anandamurthy A, Guna V, Ilangovan M, Reddy N. A review of fibrous reinforcements of concrete. J Reinf Plast Compos. 2017;36(7):519-52.
[19] Afroughsabet V, Biolzi L, Ozbakkaloglu T. High-performance fiber-reinforced concrete: a review. J Mater Sci. 2016;51(14):6517-51.
[20] Li VC. On engineered cementitious composites (ECC) a review of the material and its applications. J Adv Concr Technol. 2003;1(3):215-30.

[21] Yoo D-Y, Banthia N. Mechanical properties of ultra-high-performance fiber-reinforced concrete: A review. Cem Concr Compos. 2016;73:267-80.
[22] Yi CK, Ostertag CP. Strengthening and toughening mechanisms in microfiber reinforced cementitious composites. J Mater Sci. 2001;36:1513-22.
[23] Naaman AE, Reinhardt HW. Proposed classification of HPFRC composites based on their tensile response. Mater Struct. 2006;39(5):547-55.
[24] Blunt J, Ostertag CP. Performance-based approach for the design of a deflection hardened hybrid fiber-reinforced concrete. J Eng Mech. 2009;135(9):978-86.
[25] Jen G, Trono W, Ostertag CP. Self-consolidating hybrid fiber reinforced concrete: Development, properties and composite behavior. Constr Build Mater. 2016;104:63-71.
[26] Rambo DAS, Silva FdA, Filho RDT. Effect of steel fiber hybridization on the fracture behavior of self-consolidating concretes. Cem Concr Compos. 2014;54:100-9.
[27] Panagiotou M, Trono W, Jen G, Kumar P, Ostertag CP. Experimental seismic response of hybrid fiber-reinforced concrete bridge columns with novel longitudinal reinforcement detailing. J Bridge Eng. 2014;20(7):04014090.
[28] Trono W, Jen G, Panagiotou M, Schoettler M, Ostertag CP. Seismic response of a damage-resistant recentering posttensioned-HYFRC bridge column. J Bridge Eng. 2014;20(7):04014096.
[29] Williams ID, Arteta CA, Ostertag CP. Experimental response of a HyFRC boundary element under pure compression. 16th World Conference on Earthquake Engineering (16WCEE 2017). Santiago, Chile2017. p. 1092.
[30] Hay R, Ostertag CP. Innovative double skin facade (DSF) with high performance green hybrid fiber-reinforced concrete (HP-G-HyFRC) for resilient and sustainable buildings. In: Raebel CH, editor. AEI 2015. Milwaukee, WI: American Society of Civil Engineers; 2015. p. 120-33.
[31] Hay R, Ostertag C. Development and application of high performance green hybrid fiber-reinforced concrete (HP-G-HyFRC) for sustainable and energy-efficient buildings. Key Eng Mater. 2014;629-630:299-305.
[32] Blunt J, Jen G, Ostertag CP. Enhancing corrosion resistance of reinforced concrete structures with hybrid fiber reinforced concrete. Corros Sci. 2015;92:182-91.
[33] Jen G, Ostertag CP. Experimental observations of self-consolidated hybrid fiber reinforced concrete (SC-HyFRC) on corrosion damage reduction. Constr Build Mater. 2016;105:262-8.
[34] Duncan JF, Nguyen W, Ostertag CP. Effect of hybrid fiber reinforcement on corrosion induced degradation of reinforced concrete columns. 14th International Conference on Durability of Building Materials and Components. Ghent, Belgium2017.
[35] Jen GGT. Development of self-consolidating hybrid fiber-reinforced concrete and assessment of its durability performance [PhD thesis]. Berkeley, CA: University of California, Berkeley; 2014.
[36] Hay R. Development, durability studies and application of high performance green hybrid fiber-reinforced concrete (HP-G-HyFRC) for sustainable infrastructure and energy efficient buildings. Berkeley, CA: University of California, Berkeley; 2015.
[37] Blunt J. The effect of fiber reinforcement on the corrosion controlled degradation of reinforced concrete flexure elements. Berkeley, CA: University of California, Berkeley; 2008.
[38] U.S. Department of Transportation. HPC Bridges, Building Bridges for the 21st Century, Publication No. FHWA-SA-98-084. Washington D.C.: Federal Highway Administration; 1998.
[39] Considère A. Influence des armatures metalliques sur le propriétés des mortiers et bétons. Le Génie Civ. 1899;34(15):229-33.
[40] Goto Y. Cracks formed in concrete around deformed tension bars. ACI J Proc. 1971;68(4):244-51.

[41] Abrishami HH, Mitchell D. Influence of splitting cracks on tension stiffening. ACI Struct J. 1996;93(6):703-10.
[42] Kang S-B, Tan KH, Zhou X-H, Yang B. Influence of reinforcement ratio on tension stiffening of reinforced engineered cementitious composites. Eng Struct. 2017;141:251-62.
[43] Tiberti G, Minelli F, Plizzari G. Cracking behavior in reinforced concrete members with steel fibers: A comprehensive experimental study. Cem Concr Res. 2015;68:24-34.
[44] Moreno DM, Trono W, Jen G, Ostertag C, Billington SL. Tension stiffening in reinforced high performance fiber reinforced cement-based composites. Cem Concr Compos. 2014;50:36-46.
[45] Deluce JR, Vecchio FJ. Cracking behavior of steel fiber-reinforced concrete members containing conventional reinforcement. ACI Struct J. 2013;110(3):481-90.
[46] Jansson A, Flansbjer M, Löfgren I, Lundgren K, Gylltoft K. Experimental investigation of surface crack initiation, propagation and tension stiffening in self-compacting steel–fibre-reinforced concrete. Mater Struct. 2012;45(8):1127-43.
[47] Yuguang Y, Walraven JC, den Uijl JA. Combined effect of fibers and steel rebars in high performance concrete. HERON. 2009;54(2/3):205-24.
[48] Bischoff PH. Tension stiffening and cracking of steel fiber-reinforced concrete. J Mater Civ Eng. 2003;15(2):174-82.
[49] Fischer G, Li VC. Influence of matrix ductility on tension-stiffening behavior of steel reinforced engineered cementitious composites (ECC). ACI Struct J. 2002;99(1):104-11.
[50] Bandelt MJ, Billington SL. Bond behavior of steel reinforcement in high-performance fiber-reinforced cementitious composite flexural members. Mater Struct. 2014;49(1-2):71-86.
[51] Bandelt MJ, Billington SL. Impact of reinforcement ratio and loading type on the deformation capacity of high-performance fiber-reinforced cementitious composites reinforced with mild steel. J Struct Eng. 2016;142(10):04016084.
[52] Blunt J, Ostertag CP. Deflection hardening and workability of hybrid fiber composites. ACI Mater J. 2009;106(3):265-72.
[53] Khabaz A. Monitoring of impact of hooked ends on mechanical behavior of steel fiber in concrete. Constr Build Mater. 2016;113:857-63.
[54] ASTM International. ASTM A706 / A706M-13, Standard specification for low-alloy steel deformed and plain bars for concrete reinforcement. West Conshohocken, PA2013.
[55] Lin A, Ostertag CP. Multi-scale pull-out resistance of steel reinforcing bar embedded in hybrid fiber reinforced concrete (HyFRC). 9th International Conference Fibre Concrete 2017. Prague, Czech Republic2017.
[56] Redaelli D. Testing of reinforced high performance fibre concrete members in tension. In: Vogel T, Mojsilović N, Marti P, editors. 6th International PhD Symposium in Civil Engineering. Zurich, Switzerland: fib; 2006.
[57] Dancygier AN, Berkover E. Cracking localization and reduced ductility in fiber-reinforced concrete beams with low reinforcement ratios. Eng Struct. 2016;111:411-24.
[58] Yang IH, Joh C, Kim B-S. Structural behavior of ultra high performance concrete beams subjected to bending. Eng Struct. 2010;32(11):3478-87.
[59] Moreno DM, Trono W, Jen G, Ostertag C, Billington SL. Tension-stiffening in reinforced high performance fiber-reinforced cement-based composites under direct tension. In: Parra-Montesinos GJ, Reinhardt HW, Naaman AE, editors. High Performance Fiber Reinforced Cement Composites 6 (HPFRCC 6). Bagneux, France: RILEM; 2012. p. 263-70.

[60] Hieber DG, Wacker JM, Eberhard MO, Stanton JF. State-of-the-art report on precast concrete systems for rapid construction of bridges. University of Washington, Seattle, WA: Washington State Transportation Center; 2005.
[61] Culmo MP. Accelerated Bridge Construction. Springfield, VA: Federal Highway Administration; 2011.
[62] Kawashima K, Zafra RG, Sasaki T, Kajiwara K, Nakayama M, Unjoh S, et al. Seismic performance of a full-size polypropylene fiber-reinforced cement composite bridge column based on E-defense shake table experiments. J Earthq Engin. 2012;16(4):463-95.
[63] Aviram A, Stojadinovic B, Parra-Montesinos GJ. High-performance fiber-reinforced concrete bridge columns under bidirectional cyclic loading. ACI Struct J. 2014;111(2):303-12.
[64] Wang J-C, Ou Y-C, Chang K-C, Lee GC. Large-scale seismic tests of tall concrete bridge columns with precast segmental construction. Earthq Engin Struct Dyn. 2008;37(12):1449-65.
[65] Ou Y-C, Wang P-H, Tsai M-S, Chang K-C, Lee GC. Large-scale experimental study of precast segmental unbonded posttensioned concrete bridge columns for seismic regions. J Struct Eng. 2010;136(3):255-64.
[66] Sideris P, Aref AJ, Filiatrault A. Quasi-static cyclic testing of a large-scale hybrid sliding-rocking segmental column with slip-dominant joints. J Bridge Eng. 2014;19(10):04014036.
[67] Trono WD. Earthquake resilient bridge columns utilizing damage resistant hybrid fiber reinforced concrete [PhD thesis]. Berkeley, CA: University of California, Berkeley; 2014.
[68] Ketchum M, Chang V, Shantz T. Influence of design ground motion level on highway bridge costs. University of California, Berkeley, Berkeley, CA: Pacific Earthquake Engineering Research Center; 2004.
[69] ASTM International. ASTM A82 / A82M-07, Standard specification for steel wire, plain, for concrete reinforcement. West Conshohocken, PA2007.
[70] ASTM International. ASTM A796 / A796M-13, Standard practice for structural design of corrugated steel pipe, pipe-arches, and arches for storm and sanitary sewers and other buried applications. West Conshohocken, PA2013.
[71] Naaman AE. Strain hardening and deflection hardening fiber reinforced cement composites. In: Naaman AE, Reinhardt HW, editors. High Performance Fiber Reinforced Cement Composites (HPFRCC-4). Ann Arbor, USA: RILEM Publications; 2003. p. 95-113.
[72] Terzic V, Stojadinovic B. Post-earthquake traffic capacity of modern bridges in California. University of California, Berkeley, Berkeley, CA: Pacific Earthquake Engineering Research Center; 2010.
[73] Terzic V, Stojadinovic B. Evaluation of post-earthquake axial load capacity of circular bridge columns. ACI Struct J. 2015;112(1):23-34.
[74] Lehman D, Moehle J, Mahin S, Calderone A, Henry L. Experimental evaluation of the seismic performance of reinforced concrete bridge columns. J Struct Eng. 2004;130(6):869-79.
[75] Mander JB, Priestley MJN, Park R. Observed stress‐strain behavior of confined concrete. J Struct Eng. 1988;114(8):1827-49.
[76] Kumar P, Jen G, Trono W, Panagiotou M, Ostertag CP. Self compacting hybrid fiber reinforced concrete composites for bridge columns. Berkeley, CA: Pacific Earthquake Engineering Research Center; 2011.
[77] Azad AK, Ahmad S, Azher SA. Residual strength of corrosion-damaged reinforced concrete beams. ACI Mater J. 2007;104(1):40-7.
[78] El Maaddawy T, Soudki K, Topper T. Long-term performance of corrosion-damaged reinforced concrete beams. ACI Struct J. 2005;102(5):649-56.

[79] Al-Sulaimani GJ, Kaleemullah M, Basunbul IA, Rasheeduzzafar. Influence of corrosion and cracking on bond behavior and strength of reinforced concrete members. ACI Struct J. 1990;87(2):220-31.
[80] Mehta PK, Monteiro PJM. Concrete: Microstructure, properties, and materials. 4th ed. New York NY: McGraw-Hill Professional; 2013.
[81] Parrott LJ. A review of carbonation in reinforced concrete. Cement and Concrete Association; 1987.
[82] Tuutti K. Corrosion of steel in concrete. Stockholm: Swedish Cement and Concrete Institute; 1982.
[83] ACI Committee 318. Building code requirements for structural concrete (ACI 318-14). Farmington Hills, Mi: American Concrete Institute; 2014.
[84] Djerbi A, Bonnet S, Khelidj A, Baroghel-bouny V. Influence of traversing crack on chloride diffusion into concrete. Cem Concr Res. 2008;38(6):877-83.
[85] Win PP, Watanabe M, Machida A. Penetration profile of chloride ion in cracked reinforced concrete. Cem Concr Res. 2004;34(7):1073-9.
[86] Andisheh K, Scott A, Palermo A. Seismic behavior of corroded RC bridges: Review and research gaps. Int J Corros. 2016;2016:1-22.
[87] Zhou Y, Gencturk B, Willam K, Attar A. Carbonation-induced and chloride-induced corrosion in reinforced concrete structures. J Mater Civ Eng. 2015;27(9):04014245.
[88] Delaware Departement of Transportation. Interstate Bridge Maintenance, South (BR 1-701, 703, 703A). 2017.
[89] Berrocal CG, Lundgren K, Löfgren I. Corrosion of steel bars embedded in fibre reinforced concrete under chloride attack: State of the art. Cem Concr Res. 2016;80:69-85.
[90] Berrocal CG, Löfgren I, Lundgren K, Tang L. Corrosion initiation in cracked fibre reinforced concrete: Influence of crack width, fibre type and loading conditions. Corros Sci. 2015;98:128-39.
[91] Paul SC, van Zijl GPAG. Crack formation and chloride induced corrosion in reinforced strain hardening cement-based composite (R/SHCC). J Adv Concr Technol. 2014;12(9):340-51.
[92] Michel A, Solgaard AOS, Pease BJ, Geiker MR, Stang H, Olesen JF. Experimental investigation of the relation between damage at the concrete-steel interface and initiation of reinforcement corrosion in plain and fibre reinforced concrete. Corros Sci. 2013;77:308-21.
[93] Miyazato S, Hiraishi Y. Durability against steel corrosion of HPFRCC with bending cracks. J Adv Concr Technol. 2013;11(4):135-43.
[94] Stern M, Geary AL. Electrochemical polarization I. A theoretical analysis of the shape of polarization curves. J Electrochem Soc. 1957;104(1):56-63.
[95] Andrade C, González JA. Quantitative measurements of corrosion rate of reinforcing steels embedded in concrete using polarization resistance measurements. Mater Corros. 1978;29(8):515-9.
[96] Chang Z-T, Cherry B, Marosszeky M. Polarisation behaviour of steel bar samples in concrete in seawater. Part 1: Experimental measurement of polarisation curves of steel in concrete. Corros Sci. 2008;50(2):357-64.
[97] Babaee M, Castel A. Chloride-induced corrosion of reinforcement in low-calcium fly ash-based geopolymer concrete. Cem Concr Res. 2016;88:96-107.
[98] Garcés P, Andrade MC, Saez A, Alonso MC. Corrosion of reinforcing steel in neutral and acid solutions simulating the electrolytic environments in the micropores of concrete in the propagation period. Corros Sci. 2005;47(2):289-306.

[99] Glass GK, Chadwick JR. An investigation into the mechanisms of protection afforded by a cathodic current and the implications for advances in the field of cathodic protection. Corros Sci. 1994;36(12):2193-209.
[100] Chang Z-T, Cherry B, Marosszeky M. Polarisation behaviour of steel bar samples in concrete in seawater. Part 2: A polarisation model for corrosion evaluation of steel in concrete. Corros Sci. 2008;50(11):3078-86.
[101] Alonso C, Andrade C, Izquierdo M, Nóvoa XR, Pérez MC. Effect of protective oxide scales in the macrogalvanic behaviour of concrete reinforcements. Corros Sci. 1998;40(8):1379-89.
[102] Grubb JA, Blunt J, Ostertag CP, Devine TM. Effect of steel microfibers on corrosion of steel reinforcing bars. Cem Concr Res. 2007;37(7):1115-26.
[103] Ghods P, Isgor OB, McRae GA, Li J, Gu GP. Microscopic investigation of mill scale and its proposed effect on the variability of chloride-induced depassivation of carbon steel rebar. Corros Sci. 2011;53(3):946-54.
[104] ASTM International. ASTM C1152/C1152M - 04, Standard test method for acid-soluble chloride in mortar and concrete. West Conshohocken, PA2004.
[105] Fu C, Jin N, Ye H, Jin X, Dai W. Corrosion characteristics of a 4-year naturally corroded reinforced concrete beam with load-induced transverse cracks. Corros Sci. 2017;117:11-23.
[106] Dasar A, Hamada H, Sagawa Y, Yamamoto D. Deterioration progress and performance reduction of 40-year-old reinforced concrete beams in natural corrosion environments. Constr Build Mater. 2017;149:690-704.
[107] Frazão C, Camões A, Barros J, Gonçalves D. Durability of steel fiber reinforced self-compacting concrete. Constr Build Mater. 2015;80:155-66.
[108] Kim B, Boyd AJ, Kim HS, Lee SH. Steel and synthetic types of fibre reinforced concrete exposed to chemical erosion. Constr Build Mater. 2015;93:720-8.
[109] Abbas S, Soliman AM, Nehdi ML. Chloride ion penetration in reinforced concrete and steel fiber-reinforced concrete precast tunnel lining segments. ACI Mater J. 2014;111(6):613-22.
[110] Feng X, Lu X, Zuo Y, Zhuang N, Chen D. Electrochemical study the corrosion behaviour of carbon steel in mortars under compressive and tensile stresses. Corros Sci. 2016;103:66-74.
[111] Wei J, Fu XX, Dong JH, Ke W. Corrosion evolution of reinforcing steel in concrete under dry/wet cyclic conditions contaminated with chloride. J Mater Sci Technol. 2012;28(10):905-12.
[112] Królikowski A, Kuziak J. Impedance study on calcium nitrite as a penetrating corrosion inhibitor for steel in concrete. Electrochim Acta. 2011;56(23):7845-53.
[113] Ababneh A, Sheban M. Impact of mechanical loading on the corrosion of steel reinforcement in concrete structures. Mater Struct. 2010;44(6):1123-37.
[114] Andrade C, Keddam M, Nóvoa XR, Pérez MC, Rangel CM, Takenouti H. Electrochemical behaviour of steel rebars in concrete: influence of environmental factors and cement chemistry. Electrochim Acta. 2001;46:3905-12.
[115] Suryanto B, McCarter WJ, Starrs G, Ludford-Jones GV. Electrochemical immittance spectroscopy applied to a hybrid PVA/steel fiber engineered cementitious composite. Mater Des. 2016;105:179-89.
[116] Torrents JM, Mason TO, Peled A, Shah SP, Garboczi EJ. Analysis of the impedance spectra of short conductive fiber-reinforced composites. J Mater Sci. 2001;36(16):4003-12.
[117] Sánchez M, Gregori J, Alonso C, García-Jareño JJ, Takenouti H, Vicente F. Electrochemical impedance spectroscopy for studying passive layers on steel rebars immersed in alkaline solutions simulating concrete pores. Electrochim Acta. 2007;52(27):7634-41.

[118] Liu G, Zhang Y, Ni Z, Huang R. Corrosion behavior of steel submitted to chloride and sulphate ions in simulated concrete pore solution. Constr Build Mater. 2016;115:1-5.
[119] Ye C-Q, Hu R-G, Dong S-G, Zhang X-J, Hou R-Q, Du R-G, et al. EIS analysis on chloride-induced corrosion behavior of reinforcement steel in simulated carbonated concrete pore solutions. J Electroanal Chem. 2013;688:275-81.
[120] Jiang L, Huang G, Xu J, Zhu Y, Mo L. Influence of chloride salt type on threshold level of reinforcement corrosion in simulated concrete pore solutions. Constr Build Mater. 2012;30:516-21.
[121] Liu T, Weyers RW. Modeling the dynamic corrosion process in chloride contaminated concrete structures. Cem Concr Res. 1998;28(3):365-79.
[122] Šavija B, Luković M, Hosseini SAS, Pacheco J, Schlangen E. Corrosion induced cover cracking studied by X-ray computed tomography, nanoindentation, and energy dispersive X-ray spectrometry (EDS). Mater Struct. 2014;48(7):2043-62.
[123] Zhang R, Castel A, François R. Concrete cracking due to chloride-induced reinforcement corrosion – influence of steel–concrete interface defects due to the 'top-bar effect'. Eur J Environ Civ Eng. 2012;16(3-4):402-13.
[124] Burger E, Monnier J, Berger P, Neff D, L'Hostis V, Perrin S, et al. The long-term corrosion of mild steel in depassivated concrete: Localizing the oxygen reduction sites in corrosion products by isotopic tracer method. J Mater Res. 2011;26(24):3107-15.
[125] Yuan Y, Ji Y, Jiang J. Effect of corrosion layer of steel bar in concrete on time-variant corrosion rate. Mater Struct. 2009;42(10):1443-50.
[126] Ji Y-s, Wu M, Tan Z, Gao F, Liu F. Process control of reinforcement corrosion in concrete. Part 2: Time-dependent dominating factors under different environmental conditions. Constr Build Mater. 2014;73:214-21.
[127] Raupach M. Investigations on the influence of oxygen on corrosion of steel in concrete—Part I. Mater Struct. 1996;29(3):174-84.
[128] ASTM International. ASTM G109-07(2013) Standard Test Method for Determining Effects of Chemical Admixtures on Corrosion of Embedded Steel Reinforcement in Concrete Exposed to Chloride Environments. West Conshohocken, PA: ASTM International; 2013.
[129] ASTM International. ASTM A615/A615M-14 Standard specification for deformed and plain carbon-steel bars for concrete reinforcement. West Conshohocken, PA: ASTM International; 2014.
[130] Shaikh FUA, Mihashi H, Kobayakawa A. Corrosion durability of reinforcing steel in cracked high-performance fiber-reinforced cementitious composite beams. J Mater Civ Eng. 2015;27(8):04014228.
[131] Andrade C, Alonso C. Corrosion rate monitoring in the laboratory and on-site. Constr Build Mater. 1996;10(5):315-28.
[132] ASTM International. ASTM C876-15 Standard Test Method for Corrosion Potentials of Uncoated Reinforcing Steel in Concrete. West Conshohocken, PA: ASTM International; 2015.
[133] ASTM International. Standard practice for preparing, cleaning, and evaluating corrosion test specimens. West Conshohocken, PA2003.
[134] Sahmaran M, Yaman IO. Influence of transverse crack width on reinforcement corrosion initiation and propagation in mortar beams. Can J Civ Eng. 2008;35(3):236-45.
[135] Hansson CM, Poursaee A, Laurent A. Macrocell and microcell corrosion of steel in ordinary Portland cement and high performance concretes. Cem Concr Res. 2006;36(11):2098-102.

[136] Desnerck P, Lees JM, Morley CT. Bond behaviour of reinforcing bars in cracked concrete. Constr Build Mater. 2015;94:126-36.
[137] Liu Y, Weyers RE. Modeling the time-to-corrosion cracking in chloride contaminated reinforced concrete structures. ACI Mater J. 1998;95(6):675-81.
[138] Zhao Y, Zhang X, Jin W. Influence of environment on the development of corrosion product-filled paste and a corrosion layer at the steel/concrete interface. Corros Sci. 2017:https://doi.org/10.1016/j.corsci.2017.03.026.
[139] Dehoux A, Bouchelaghem F, Berthaud Y. Micromechanical and microstructural investigation of steel corrosion layers of variable age developed under impressed current method, atmospheric or saline conditions. Corros Sci. 2015;97:49-61.
[140] Vera R, Villarroel M, Carvajal AM, Vera E, Ortiz C. Corrosion products of reinforcement in concrete in marine and industrial environments. Mater Chem Phys 2009;114(1):467-74.
[141] Rémazeilles C, Refait P. On the formation of β-FeOOH (akaganéite) in chloride-containing environments. Corros Sci. 2007;49(2):844-57.
[142] Marcotte TD, Hansson CM. The influence of silica fume on the corrosion resistance of steel in high performance concrete exposed to simulated sea water. J Mater Sci. 2003;38(23):4765-76.
[143] Cornell RM, Schwertmann U. The Iron Oxides: Structure, Properties, Reactions, Occurences and Uses. 2 ed. Federal Republic of Germany: WILEY-VCH Verlag GmbH & Co. KGaA, Weinheim; 2003.
[144] Berrocal CG, Fernandez I, Lundgren K, Löfgren I. Corrosion-induced cracking and bond behaviour of corroded reinforcement bars in SFRC. Compos Part B Eng. 2017;113:123-37.
[145] Bažant ZP, Yu Q, Li G-H. Excessive long-time deflections of prestressed box girders. I: Record-span bridge in Palau and other paradigms. J Struct Eng. 2012;138(6):676-86.
[146] Ostertag CP, Yi CK. Crack/fiber interaction and crack growth resistance behavior in microfiber reinforced mortar specimens. Mater Struct. 2006;40(7):679-91.
[147] Banthia N, Majdzadeh F, Wu J, Bindiganavile V. Fiber synergy in Hybrid Fiber Reinforced Concrete (HyFRC) in flexure and direct shear. Cem Concr Compos. 2014;48:91-7.
[148] Chasioti SG, Vecchio FJ. Shear behavior and crack control characteristics of hybrid steel fiber-reinforced concrete panels. ACI Struct J. 2017;114(1).
[149] Chasioti SG, Vecchio FJ. Effect of fiber hybridization on basic mechanical properties of concrete. ACI Mater J. 2017;114(3).
[150] Huang L, Chi Y, Xu L, Chen P, Zhang A. Local bond performance of rebar embedded in steel-polypropylene hybrid fiber reinforced concrete under monotonic and cyclic loading. Constr Build Mater. 2016;103:77-92.
[151] Advanced Light Source. Beamline 8.3.2 manual. Lawrence Berkeley National Laboratory2015.
[152] Kak AC, Slaney M. Principles of Computerized Tomographic Imaging: Society of Industrial and Applied Mathematics; 2001.
[153] Hernández-Cruz D, Hargis CW, Dominowski J, Radler MJ, Monteiro PJM. Fiber reinforced mortar affected by alkali-silica reaction: A study by synchrotron microtomography. Cem Concr Compos. 2016;68:123-30.
[154] Hernández-Cruz D, Hargis CW, Bae S, Itty PA, Meral C, Dominowski J, et al. Multiscale characterization of chemical–mechanical interactions between polymer fibers and cementitious matrix. Cem Concr Compos. 2014;48:9-18.

[155] Voltolini M, Marinoni N, Mancini L. Synchrotron X-ray computed microtomography investigation of a mortar affected by alkali–silica reaction: a quantitative characterization of its microstructural features. J Mater Sci. 2011;46(20):6633-41.
[156] Marinoni N, Voltolini M, Broekmans MATM, Mancini L, Monteiro PJM, Rotiroti N, et al. A combined synchrotron radiation micro computed tomography and micro X-ray diffraction study on deleterious alkali-silica reaction. J Mater Sci. 2015.
[157] Monteiro PJM, Kirchheim AP, Chae S, Fischer P, MacDowell AA, Schaible E, et al. Characterizing the nano and micro structure of concrete to improve its durability. Cem Concr Compos. 2009;31(8):577-84.
[158] Qian C, Nie Y, Cao T. Sulphate attack-induced damage and micro-mechanical properties of concrete characterized by nano-indentation coupled with X-ray computed tomography. Struct Concr. 2016;17(1):96-104.
[159] De Graef B, Cnudde V, Dick J, De Belie N, Jacobs P, Verstraete W. A sensitivity study for the visualisation of bacterial weathering of concrete and stone with computerised X-ray microtomography. Sci Total Environ. 2005;341(1-3):173-83.
[160] Beck M, Goebbels J, Burkert A, Isecke B, Bäßler R. Monitoring of corrosion processes in chloride contaminated mortar by electrochemical measurements and X-ray tomography. Mater Corros. 2009;61(6):475-9.
[161] Van Steen C, Wevers M, Verstrynge E. X-ray computed tomography for the detection of corrosion-induced damage at the reinforcement-concrete interface. 7th Conference on Industrial Computed Tomography (iCT 2017). Leuven, Belgium2017.
[162] Sun H, Zhao D, Gu Y, Memon SA, Ren Z, Liu B, et al. Three-dimensional characterization of steel corrosion embedded in cement paste. Constr Build Mater. 2017;143:24-32.
[163] Itty P-A, Serdar M, Meral C, Parkinson D, MacDowell AA, Bjegović D, et al. In situ 3D monitoring of corrosion on carbon steel and ferritic stainless steel embedded in cement paste. Corros Sci. 2014;83:409-18.
[164] El Maaddawy TA, Soudki KA. Effectiveness of impressed current technique to simulate corrosion of steel reinforcement in concrete. J Mater Civ Eng. 2003;15(1):41-7.
[165] Poursaee A, Hansson CM. Potential pitfalls in assessing chloride-induced corrosion of steel in concrete. Cem Concr Res. 2009;39(5):391-400.
[166] van Zijl GPAG, Slowik V, Toledo Filho RD, Wittmann FH, Mihashi H. Comparative testing of crack formation in strain-hardening cement-based composites (SHCC). Mater Struct. 2015;49(4):1175-89.
[167] The Mathworks Inc. MATLAB® 2017a. Natick, Massachusetts, USA2017.
[168] Wang K, Jansen DC, Shah SP, Karr AF. Permeability study of cracked concrete. Cem Concr Compos. 1997;27(3):381-93.
[169] Kobayashi K, Kojima Y. Effect of fine crack width and water cement ratio of SHCC on chloride ingress and rebar corrosion. Cem Concr Compos. 2017;80:235-44.
[170] Jiang S, Jiang L, Wang Z, Jin M, Bai S, Song S, et al. Deoxyribonucleic acid as an inhibitor for chloride-induced corrosion of reinforcing steel in simulated concrete pore solutions. Constr Build Mater. 2017;150:238-47.
[171] Yu H, Chiang K-TK, Yang L. Threshold chloride level and characteristics of reinforcement corrosion initiation in simulated concrete pore solutions. Constr Build Mater. 2012;26(1):723-9.
[172] Criado M, Sobrados I, Sanz J, Bastidas JM. Steel protection using sol–gel coatings in simulated concrete pore solution contaminated with chloride. Surf Coat Technol. 2014;258:485-94.

[173] Poursaee A, Hansson CM. The influence of longitudinal cracks on the corrosion protection afforded reinforcing steel in high performance concrete. Cem Concr Res. 2008;38(8-9):1098-105.